THE HENRYK NIEWODNICZAŃSKI
INSTITUTE OF NUCLEAR PHYSICS
POLISH ACADEMY OF SCIENCES

Studies of three-nucleon force effects in the ^{1}H(d,pn)p breakup reaction at 160 MeV

Bogusław Włoch

A dissertation submitted for the degree of
Doctor of Philosophy in Physics

Prepared under the supervision of
Thesis supervisor: dr hab. Adam Kozela
Axuiliary supervisor: dr hab. Izabela Ciepał

Kraków, 2021

Contents

Abstract

This doctoral dissertation is devoted to the study of the few-nucleon system dynamics in deuteron-proton collisions at 160 MeV deuteron beam energy. The collected experimental data allowed for the determination of differential cross sections for the deuteron breakup reaction. Contrary to previous analyses, this one focuses on direct detection of the proton-neutron pairs. This allowed to reach phase space regions which have not yet been studied in previous experiments and to test theoretical predictions including various aspects of nuclear interactions, such as three-nucleon force (3NF) or Coulomb interaction.

The experiment was carried out in 2011 at the KVI in Groningen (the Netherlands), by a group of physicists from Poland and the Netherlands. A deuteron beam of the energy of 160 MeV was impinging on a liquid hydrogen target. The reaction products were registered with the BINA detection system. The detector was originally designed to reconstruct the final states of two charged particles. In this thesis, however, we exploit its ability to detect neutrons.

The analysis was aimed at determination of the differential cross sections of the ^{1}H(d,pn)p deuteron breakup reaction by measuring the proton-neutron coincidences. We have developed methods allowing for direct reconstruction of neutron observables in the BINA detector. We used the asymmetry of signals from a thick detector to determine the position of the neutrons, and the time of flight to determine their energy. The registered protons are used to calculate the reaction time. This required an extensive use of Monte Carlo simulation to accurately determine the particle energy losses in the detector. The efficiency of neutron detection and the efficiency of the detection of the proton-neutron pair were also calculated. Finally, a set of differential cross section of the deuteron breakup reaction for a number of angular configurations was obtained.

The results were compared with a set of theoretical models of the three-nucleon system. These calculations are based on the so-called realistic nucleon-nucleon potentials like Argonne v18 and Charge-Dependent Bonn. They were supplemented with additional elements of 3N dynamics, such as the Tucson-Melbourne 99 and Urbana-IX three-nucleon forces, or the Coulomb interactions. The most important and somewhat surprising result was that adding the TM99 three-body forces only, regardless of the selected potential, deteriorates the agreement between the theoretical calculations and the experimental data. In addition, for a few selected angular configurations, the results have been compared to the latest calculations based on the chiral theory.

The obtained results enriched the database of breakup cross section with 765 new experimental points, which may help in the verification and further development of theoretical predictions. The methods developed can be used in a planned experiments with the BINA detector, which in 2015 has been transferred and installed in Krakow, at the Cyclotron Center Bronowice.

Streszczenie

Niniejsza rozprawa doktorska poświęcona jest badaniom dynamiki systemów kilkunukleonowych, w zderzeniach deuteron-proton, przy energii wiązki deuteronowej 160 MeV. Zebrane dane doświadczalne pozwoliły na wyznaczenie różniczkowych przekrojów czynnych na reakcję rozbicia (breakupu) deuteronu. Prezentowana analiza wyróżnia się spośród wcześniejszych tym, że skupiono się w niej na kanale reakcji z bezpośrednią detekcją pary proton-neutron. Umożliwiło to zbadanie dotąd nie eksploatowanych w naszych pomiarach obszarów przestrzeni fazowej. Pozwoliło to następnie na przetestowanie obliczeń teoretycznych uwzględniających różne aspekty oddziaływań jądrowych takich jak siła trójnukleonowa czy oddziaływanie kulombowskie.

Eksperyment został przeprowadzony w 2011 r. w ośrodku KVI w Groningen w Holandii, przez grupę fizyków z Polski i Holandii. Wiązka rozpędzonych do energii 160 MeV deuteronów zderzana była z tarczą z ciekłego wodoru. Produkty wytworzone w tych reakcjach, rejestrowane były przy pomocy układu detekcyjnego BINA. Detektor pierwotnie był zaprojektowany z myślą o rekonstrukcji zdarzeń w których rejestrowano dwie naładowane cząstki. W prezentowanej pracy postanowilismy wykorzystać jego zdolnośc do detekcji neutronów.

Analiza danych miała na celu wyznaczenie różniczkowych przekrojów czynnych na reakcję breakupu deuteronu ^{1}H(d,pn)p poprzez pomiar koincydencji proton-neutron. Udało nam się opracować metody pozwalające na rekonstrukcję tak energii jak i kierunku emisji neutronów w detektorze BINA. W tym celu użyto asymetrii sygnałów rejestrowanych w detektorze do wyznaczenia pozycji rejestrowanego neutronu oraz czas przelotu do wyznaczenia jego energii. Do obliczenia czasu reakcji wykorzystane zostały protony, rejestrowane w standardowy sposób, tj. za pomocą metody strat energii. Wymagało to przeprowadzenia symulacji Monte Carlo układu detekcyjnego, w celu dokładnego wyznaczenia strat energii cząstek w detektorze. Została również wyznaczona wydajność na detekcję neutronów oraz wydajność na detekcję pary proton-neutron. W rezultacie uzyskany został zestaw przekrojów czynnych dla reakcji rozbicia deuteronu dla szeregu konfiguracji kątowych proton-neutron.

Uzyskane wyniki zostały porównane z zestawem modeli teoretycznych układu trzech nukleonów. Obliczenia te bazują na tzw. realistycznych potencjałach nukleon-nukleon, Argonne v18 (Av18) i Charge-Dependent Bonn (CDB). Wzbogacone są one o dodatkowe elementy dynamiki 3N, takie jak modele siły trójnukleonowej Tucson-Melbourne 99 (TM99) i Urbana-IX (UIX) czy oddziaływania kulombowskie. Najważniejszym i nieco zaskakującym wynikiem tej pracy było to, że uwzględnienie siły trzynukleonowej TM99, niezależnie od wybranego modelu, pogarsza zgodność obliczeń teoretycznych z danymi eksperymentalnymi. Ponadto dla kilku wybranych konfiguracji kątowych, porównaliśmy otrzymane wyniki z najnowszymi obliczeniami bazującymi na teorii chiralnej.

Otrzymane wyniki wzbogacają bazę danych przekrojów czynnych dla reakcji breakupu o kolejne punkty eksperymentalne, co może pomóc w weryfikacji i dalszym rozwoju przewidywań teoretycznych. Uzyskane przez nas metody mogą zostać użyte w planowanych eksperymentach wykorzystujących detektor BINA, który w 2015 roku został przeniesiony i zainstalowany w Krakowie, w Centrum Cyklotronowym Bronowice.

Chapter 1

Introduction

The most fundamental questions in nuclear physics are related to the forces binding nucleons together to form nuclei. Already in 1935, following successfull desription of electromagnetical interaction as the exchange of masless photon between charged particles, Yukawa proposed to describe the nucleon-nucleon (NN) force with an exchange of a mezon [1]. Since the range of the nuclear force is very short, about 2 fm, Yukawa predicted the mass of the mediating particle as about 200 times the mass of the electron. Yukawa's meson was found in 1947 by Powell [2], and came to be known as the pion.

On a basis of this theory, models of NN forces were created [3, 4]. Nowadays, since quantum chromodynamics (QCD) cannot yet be solved in the non-perturbative regime, the realistic two-nucleon (2N) potentials, together with the more sophisticated approaches like coupled-channels (CC) method [5] and the fundamental one based on Chiral Perturbation Theory (ChPT) [6], constitute a rich theoretical basis for the description of the nucleon-nucleon interaction. The new generation of realistic NN potentials such as Argonne v18 (Av18) [7], Charge Dependent Bonn (CDB) [8], Nijmegen I and II [9] reproduce the scattering data (proton-proton, proton-neutron) with an impressive precision, expressed by a χ^2 per degree of freedom very close to one.

Few-nucleon systems are ideal testing ground for the study of the details of nucleon-nucleon force models and, what follows this, the properties and interaction mechanisms of the nuclei. Their theoretical and experimental investigation started from simple NN systems and gradually evolved into more complicated environments. The natural step forward was to test whether 2N potentials describe the experimental properties of systems consisting of more than two nucleons. In order to investigate this problem, the simplest laboratory, the three-nucleon (3N) system was chosen. As it turned out, even the most fundamental properties, like the binding energies of ^{3}H and ^{3}He [10], have not been reproduced with expected precision. This experimental fact was the first clue for existence and significance of additional dynamics appearing in the presence of the third nucleon, which is referred to as three-nucleon force (3NF). A well-known example of the realization of such a force is the Fuijta-Miyazawa force [11] in which all three nucleons interact via a 2π-exchange mechanism with an intermediate excitation of one of the nucleons (see Fig 1.1). Further and richer indications of 3NF existence came from the nucleon-deuteron high precision scattering data for the differential cross sections and spin observables [12, 13, 14].

Especially the breakup reaction, where the deuteron disintegrates into proton and neutron, with its final state of three particles, provides kinematically rich environment for verification of the interaction models. Unprecedented increase of computer power as well as the progress in the development of new mathematical methods provided numerically exact solutions of the 3N problem. This allowed one to calculate all relevant observables in both elastic scattering and breakup processes in deuteron-nucleon interaction, selectively

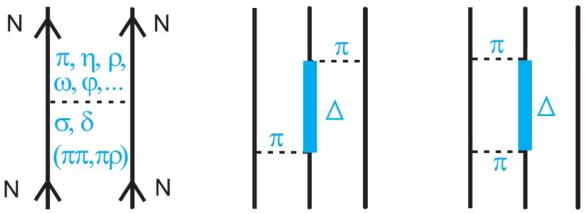

Figure 1.1: *Left Panel:* A diagram describing the interaction of a pair of nucleons through the exchange of intermediary mesons. *Center and Right Panel:* Two diagrams showing the three-nucleon interaction in terms of the Fuijta-Miyazawa theory [15].

accounting for most important parts of the nuclear interaction. Though the full calculations including all relevant contributions (3NF, relativistic effects and the Coulomb force) are still hardly available, it appeared rather early that even adding only a 3NF to the pairwise interactions dramatically improves elastic scattering cross section and in general leads to a better description of the breakup data (see Fig. 2.5). Discrepancy at energy below 100 MeV can mostly be removed by adding 3NF. However, at higher energies current 3NF models only partially improve description of elastic cross section data and the discrepancies increase with the energy. Also in the case of the nucleon-deuteron breakup, the significance of 3NF was confirmed.

Remarkable disagreement observed at low relative energies between the cross-section data at 130 MeV [16] and the theoretical predictions was interpreted as a manifestation of the Coulomb force. This discovery and further dedicated experiments at Forschungszentrum Julich, Germany [15], led to incorporation of electromagnetic interaction which were neglected, initially, in the mentioned above predictions. Further measurements of the ^{2}H(p,pp)n reaction carried out at Kernfysich Versneller Instituut (KVI), Groningen, the Netherlands, using the BINA detector at 135 [17] and 190 MeV [18] indicated at some deviations between the measured differential cross sections and currently available calculations, even when 3NF and electromagnetic interaction were included. Part of the discrepancies, especially at a higher energy region, could be accounted by relativistic effects. Nevertheless it is clear that some missing part of the dynamic still escapes the theoretical description.

In addition to nuclear interactions in the few-nucleon systems, in recent years, 3NF models have found application in other areas of physics. They are successfully used in the calculation of the binding energy of light nuclei (Fig. 1.3). Calculations based on the Green's Function Monte Carlo (GFMC) and using the Av18 potential with the Illinois-7 3NF very accurately reproduce the binding energies of the ground states and many of the excited states of light nuclei up to $A = 12$ [20]. The 3NF models also find application in the *abinitio* calculations of the structure of an atomic nucleus. The measured lifetimes of the second excited states 2^+ of ^{20}O and ^{16}C can currently be only explained by the theory with the 3N interactions [21]. Another very interesting example comes from the equation of state of nuclear matter. The use of 2N + 3NF potentials allows for recreation of the nuclear matter saturation point (see Fig. 1.3, left). The addition of a repulsive 3NF contribution increases the "stiffness" of nuclear matter. This, in turn, has found an application in the astrophysics. Due to the stiffer equation of state it is possible to form a more massive neutron stars (see Fig. 1.3, right). Recent discoveries of neutron stars with a mass greater than 2 times the mass of the Sun, such as J0348+0432 [22], J0740+6620 [23] GW170817 [24], seem to support suitability of using the 3NF models.

This work is a continuation of the previous systematic studies of a few-nucleon system dynamics performed in a collaboration of Institute of Nuclear Physics Polish Academy of

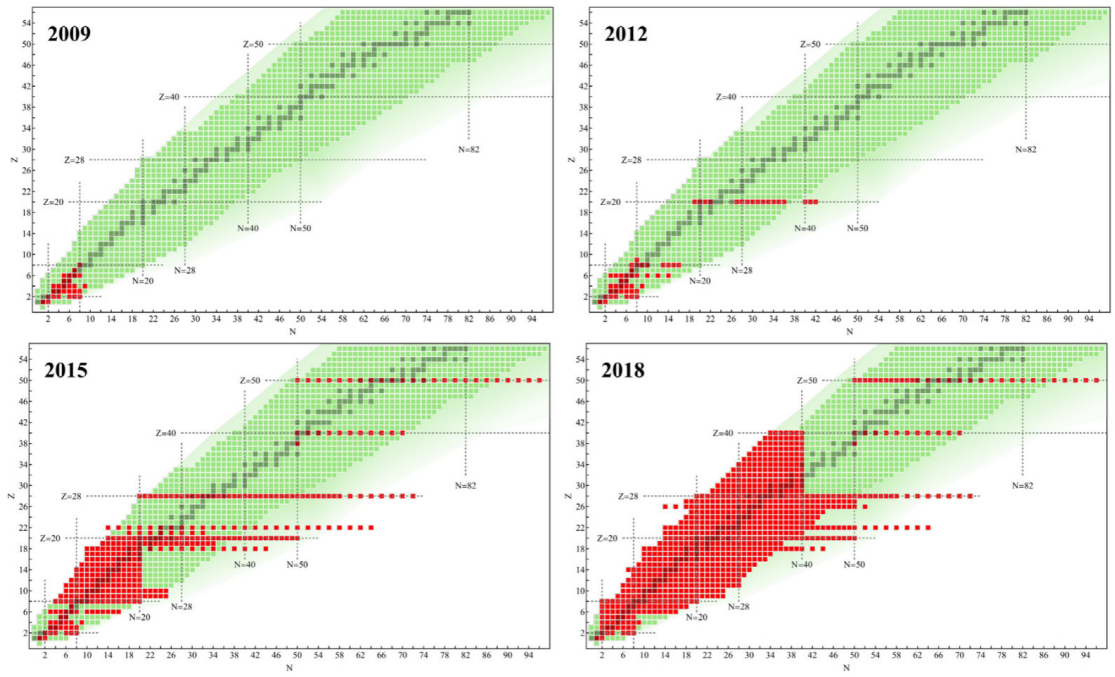

Figure 1.2: The illustration of a progress of ab initio many-body calculations of nuclei from the 2009 to 2018, using 2N and 3N interactions. Studied nuclei are presented in red [19].

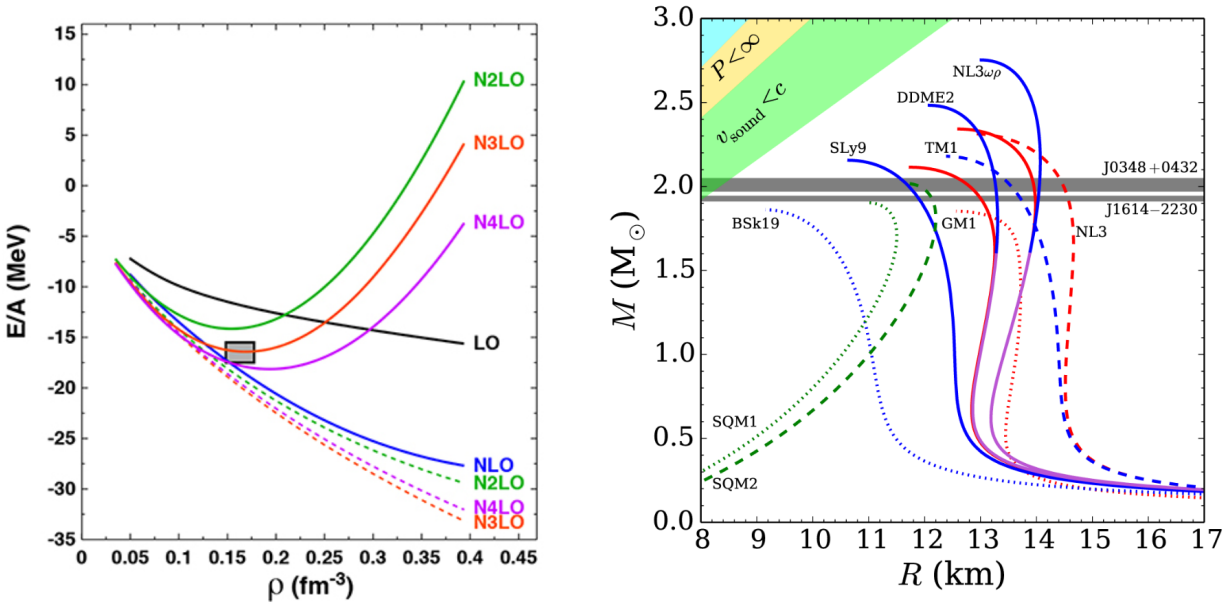

Figure 1.3: *Left panel:* Energy per particle as a function of density of symmetric nuclear matter. Solid lines represent equations of state including three-body interactions, while dashed with only pairwise interaction. The grey box approximate the empirical saturation energy and density. Due to the repulsive behavior of 3NF, energy per particle reaches its saturation point at about 0.17 fm^{-3}. Adopted from [25]. *Right panel:* Mass to radius relation for neutron stars. Each line represents solution based on different EoS. Figure taken form [26].

Science, Jagiellonian University, University of Warsaw, University of Silesia, KVI and University of Groningen, using the BINA detector. The thesis is focused on detecting proton-neutron pairs from deuteron breakup reaction. The neutron detection in the BINA setup is

challenging and required introducing of a time of flight technique. This new approach was successfully used in this thesis to analyze the dp breakup reaction and can also be applied to study the dd (4N system) reaction. The ability to detect neutron, in the same experimental setup as for charged particles analysis, gives a great opportunity for comparing $dp \to (pp)n$ and $dp \to (pn)p$ or $dd \to (dp)n$ and $dd \to (dn)p$ reaction channels at the same kinematical conditions. In addition, the applied method allows for the registration of neutrons with lower energies than charged particles. Lowering the detection threshold extends the available reaction phase space. For some of proton-neutron configurations, these regions show rapid changes in the cross section and relatively large differences between the available models. This may give new insight into the various aspects of few-nucleon system dynamics, like the Coulomb interaction or isospin dependence of 3NF.

The outline of the thesis is as follows. In the second chapter we introduce the theoretical aspects of 3-nucleon systems. Chapter 3 presents the BINA experimental setup. In chapter 4 the details of conducted data analysis for charged particles and neutrons is described. The last chapter is devoted to breakup reaction analysis and the discussion of the obtained cross section and their comparison with the theoretical calculations.

Chapter 2

Theoretical and experimental background

In this chapter theoretical background of the few-nucleon system dynamics is discussed. First, a short description of kinematical properties of elastic scattering and three-body breakup reaction is presented. Understanding of the *dp* reaction kinematics and its observables is particularly important for the following experimental sections. It is followed by the discussion of some basic aspects of the existing models of nucleon-nucleon interaction and three-nucleon forces. The latest developments in the field of chiral effective field theory are described at the end of this chapter.

2.1 Reaction kinematics

2.1.1 Reference frame

Two types of reference frames are used in the analysis of the experimental data. First one is the center of mass system (CM). It is best suited for the two-body elastic scattering, which can be fully described with a single variable like the θ_{CM} angle. The second, is the laboratory frame of reference (LAB). The experiment described in this dissertation used a fixed target. Due to the symmetry of the considered problem and the symmetry of the detector structure, a convenient coordinate system to use is a right-handed spherical one. The center of the system is placed in the center of the target, while the beam direction defines the Z axis. The XY plane, perpendicular to the Z axis, is oriented so that the Y axis is vertical, pointing upwards. The polar angle θ is defined as an angle between the beam (Z) axis and the direction of the outgoing particle. The azimuthal angle, ϕ, is measured between the projection of the particle's trajectory on the XY plane and the X axis. The presented analysis is mostly focused on the detection of two particles in a coincidence. This situation is shown in Fig. 2.1. In order to describe such an event, the polar angles (θ_1, θ_2) of both particles, and the their relative azimuthal angle defined as $\Delta\phi_{12} = |\phi_1 - \phi_2|$ are used, and in the following will be referred to as a geometrical configuration $\xi = \{\theta_1, \theta_2, \Delta\phi_{12}\}$.

2.1.2 Elastic dp scattering

In the case of elastic scattering, in the input and output channels, both colliding particles remain intact, only their momenta are changed. The law of momentum conservation impose a coplanarity condition to registered elastically scattered particles, which means that their relative azimuthal angle $\Delta\phi_{12} = 180°$. Only one kinematic variable is needed to fully describe

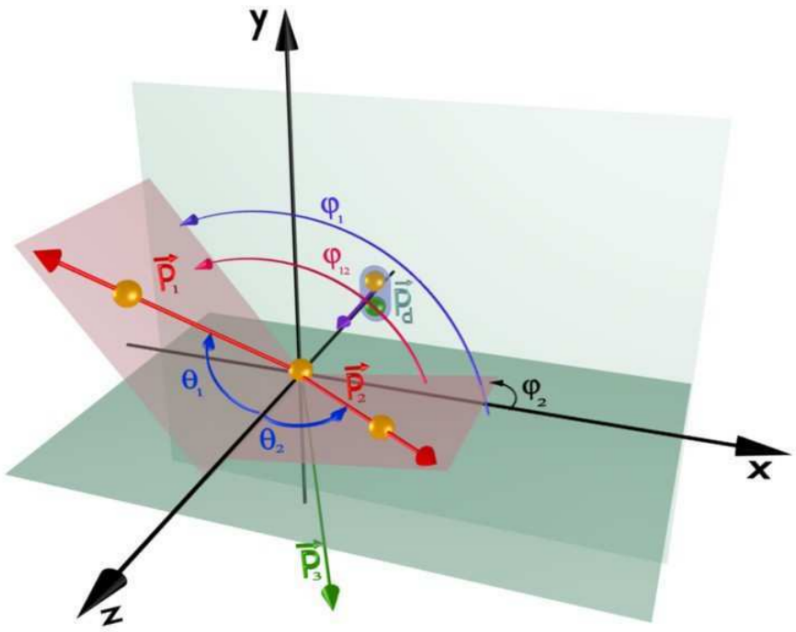

Figure 2.1: Diagram showing deuteron breakup reaction in the LAB system. The direction of the beam is along the Z axis, while θ_1, θ_2 are the polar scattering angles of protons with respect to the beam axis and $\Delta\phi_{12}$ is the relative azimuthal angle between them.

the final state of this reaction. Determining this variable (for example θ_1 angle) strictly determines the momenta of both particles.

In this experiment fixed proton target and deuteron beam were used, thus the projectile was heavier than the target. This relation between masses of reacting particles leads to the so-called inverse kinematics in which the reaction products are confined in the forward hemisphere and in the case of the elastically scattered deuterons, there is a maximum emission angle in the LAB frame (about 30°). A relatively large part of the available phase space covered by the forward part of the BINA detector allowed for registration of both elastically scattered particles in coincidence, see Fig. 2.2. As a consequence the study of this scattering provides an excellent tool for testing the geometry of the experimental system, as well as for the detector energy calibration.

2.1.3 Three-body breakup

In the breakup case, as a result of the collision, three free nucleons are produced, two protons and one neutron. Each of these particles can be described by its momentum $\mathbf{p_1}, \mathbf{p_2}, \mathbf{p_3}$. However, from the experimental point of view, it is more convenient to switch to the other set of variables which were directly measured in the detectors, namely the kinetic energies E and the emission angles: polar θ and azimuthal ϕ. In both cases this gives in total 9 kinematical variables. These number can be reduced to 5 by applying the energy and momentum conservation laws:

$$E_d = E_1 + E_2 + E_3 + E_B,$$
$$\mathbf{p_d} = \mathbf{p_1} + \mathbf{p_2} + \mathbf{p_3},$$

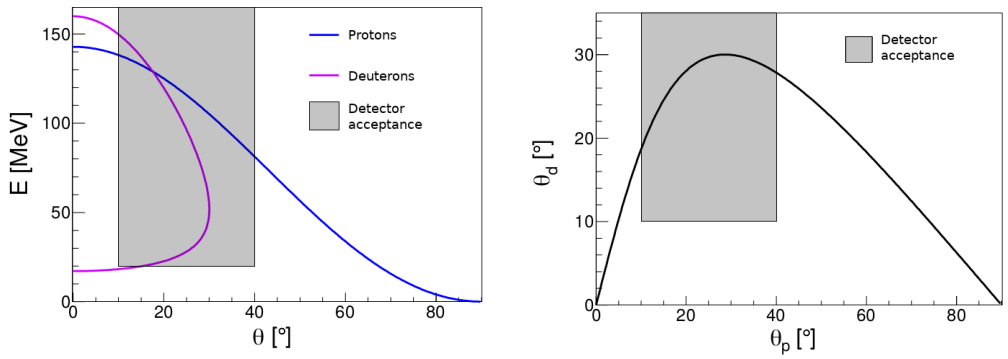

Figure 2.2: Kinematic relations describing *dp* elastic scattering. The angular and energy acceptance of the Forward Wall (see details in Chapter 3) is shown as a black rectangle. *Left panel:* The energy of particle (protons and deuterons) as a function of its polar angle θ *Right panel:* Relation between the polar angles of protons and deuterons.

where E_d, $\mathbf{p_d}$ are the kinetic energy and momentum of the deuteron beam, E_i, $\mathbf{p_i}$ are the kinetic energy and momenta of the three particles in the final state and E_B is the biding energy of deuteron, which equals to 2.224 MeV. In this experiment 6 variables were measured. This eliminates the need of the detection of third particle, as the information obtained from the two particles is sufficient. The redundant information have been used to improve events selection by means of cuts on kinematical relations.

Relation between E_1 and E_2 in the non-relativistic framework is given as:

$$\frac{-(E_d + E_B)}{2} = E_1 + E_2 - \sqrt{2E_dE_1}\cos\theta_1 - \sqrt{2E_dE_2}\cos\theta_2 + \sqrt{E_1E_2}\cos\Theta_{12}, \qquad (2.1)$$

where $\cos\Theta_{12} = \cos\theta_1\cos\theta_2 + \sin\theta_1\sin\theta_2\cos(\Delta\phi_{12})$. In general these relation spans a 5 dimensional surface (the phase space) in the 9 dimensional space. For a given angular configuration θ_1, θ_2 and $\Delta\phi_{12}$ the relation describes a single curve on the E_1 vs E_2 plane, the so-called kinematical curve or simple "kinematics". Examples of such kinematics for the ^{1}H$(d, pn)p$ breakup reaction are shown in Figure 2.3. In this figure we also introduce the S variable, commonly used in the description of a breakup reaction and defined as an arc-length along the kinematical curve. This variable is expressed in energy units with a starting point $S = 0$ chosen arbitrary at the minimum of E_2 and anticlockwise orientation. Due to the limited resolution of the detector, in both the energy and angular measurement, the experimental points do not follow strictly the kinematics but are spread over a certain area around the curve.

2.2 Few-nucleon interactions

Properties of few-nucleon systems at intermediate energies [1] are determined mainly by the nucleon-nucleon (2N) interaction, described with the 2N potentials. In general, the long-range component is expressed by the meson-exchange theory, while the short-range part is described phenomenologically, based on elastic 2N scattering data.

[1] Energies from a few tens MeV up to pion production threshold at about 200 MeV/A.

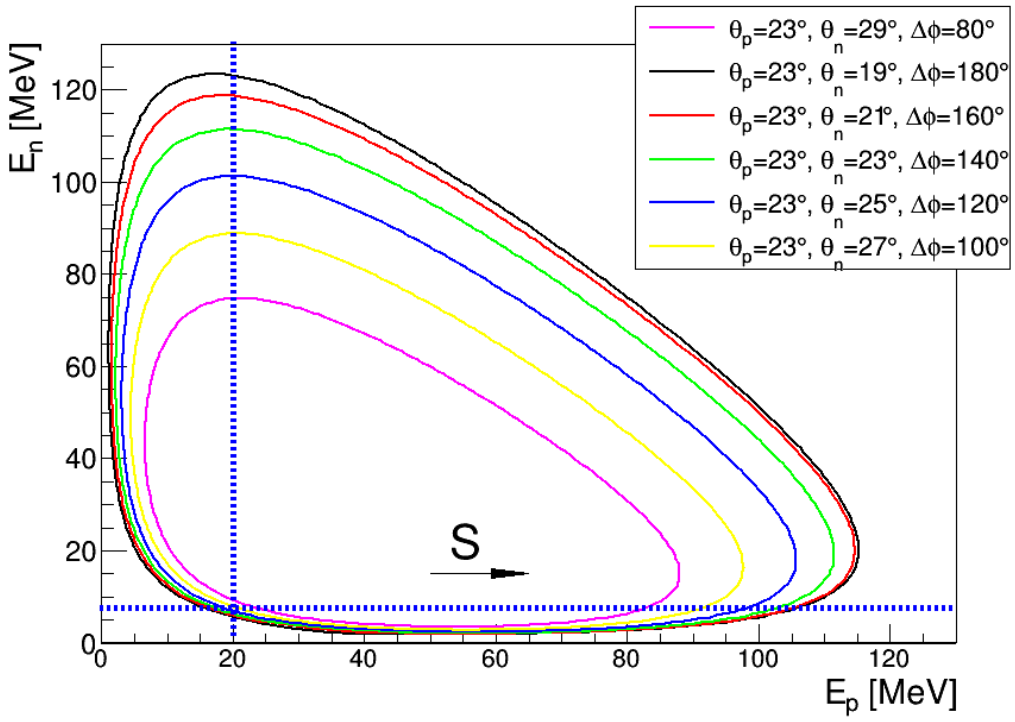

Figure 2.3: Set of kinematic curves for selected proton-neutron angular configurations for the deuteron breakup reaction at 160 MeV. The energy thresholds for particle detection are shown as a vertical and horizontal lines.

2.2.1 Scattering formalism

Since nuclear systems are microscopic objects, it is necessary to use quantum mechanics to correctly describe scattering processes. The initial state consists of elementary particles or bound states that are sufficiently well separated so that their interactions with each other can be ignored. Physical process is modeled as a scattering process of these well separated bound states. This process is described by the full Hamiltonian H, but once it's over, all of the new elementary particles or bound states separate again and one finds a new non-interacting state. In the non-relativistic regime, scattering can be described by the Lipmann-Schwinger equation (LSE):

$$|\Psi^{\pm}\rangle = |\phi\rangle + G_0 V |\Psi^{\pm}\rangle, \tag{2.2}$$

where $G_0 = (E - H_0 \pm i\epsilon)^{-1}$ is called the free-particle propagator, related to the resolvent of a Green's function. The Hamiltonian of a free particle is denoted by H_0 while V is the interaction potential. At large distance the wave function $\langle x|\Psi\rangle$ can be written as the sum of the incident and outgoing waves corresponding to the positive solution. The LSE is equivalent to the Schrödinger equation with the boundary conditions typical for scattering processes, thus the solution of LSE must also fulfill the Schrödinger equations. Because the Schrödinger equation conserves probability, only solutions of the LSE, which contain both the incident and outgoing waves, exist.

Now we can define the operator t:

$$V|\Psi^{\pm}\rangle \equiv t|\phi\rangle, \tag{2.3}$$

which describes the transition of the initial state to the scattering state by means of a given potential. The cross section of scattering process is directly related to the operator t as it is proportional to the square of t-matrix elements $|t|^2$.

By multiplying the LSE (Eq. 2.2) by V on the left one obtains:

$$t = V + VG_0t. \tag{2.4}$$

In this equation t is on the both sides, so it can be evaluated iteratively using the Born approximation:

$$t = V + VG_0V + VG_0VG_0V + VG_0VG_0VG_0V + \cdots . \tag{2.5}$$

Three nucleon scattering

The Hamiltonian of the 3N system can be written as:

$$H = -\sum_{i=1}^{3} \frac{\hbar^2}{2m_i}\nabla_i^2 + \sum_{i>j=1}^{3} v_{ij} + \sum_{i>j>k=1}^{3} v_{ijk}, \tag{2.6}$$

where the v_{ij} represents 2N and v_{ijk} 3N potentials, respectively. The magnitude of the 3N potential is usually much smaller than the 2N one. Let us now treat the 3N system with only pairwise nucleon-nucleon interaction with the 3N potential added separately. We can choose the Jacobi coordinate system [27] in which the 3N system is treated as a two-nucleon subsystem plus the third nucleon acting as a spectator. Using this coordinate and applying additional boundary conditions one can rewrite the LSE (Eq. 2.2):

$$|\Psi_i^{\pm}\rangle = \delta_{il}|\Phi_i\rangle + G_l(V_j + V_k)|\Psi_i^{\pm}\rangle, \tag{2.7}$$

where the permutation of ljk is cyclic and $l = i, j$ or k. By the convention, the V_i is the potential of jk pair. In fact, Eg. 2.7 corresponds to three separate equations called Lippman-Schwinger triad. Similar to 2N scattering, the transition operator T is given as:

$$T = V + VG_0T. \tag{2.8}$$

To solve this problem, we can adopt the Faddeev approach [28] and splits this into three equations:

$$T = (V_1 + V2 + V3) + (V_1 + V_2 + V_3)G_0T = \sum_{i=1}^{3}(V_i + V_iG_0T) \equiv \sum_{i=1}^{3} T_i. \tag{2.9}$$

The Eq. 2.9 can be then rearranged as:

$$T_i = t_i + t_iG_0(T_j + T_k), \tag{2.10}$$

where t_i is a two-body t-matrix from Eq. 2.4 in three-body space. Eq. 2.10 is one of the form of Faddeev equation [28].

2.2.2 Realistic NN potentials

To calculate observables one needs to know the nucleon-nucleon potential. Different 2N potentials have been developed in the past decades, for example Reid93 [9], Nijmegen I, Nijmegen II [9], Argonne V18 (av18) [7] or CDBonn (CDB) [8]. Each of these models uses different parameterization and is fitted to the experimental nucleon-nucleon database. Shapes of the 2N potentials are presented in Fig. 2.4. The potential must be invariant under rotation, reflection and time reversal. A long-range part of these potentials are constructed based on the meson-exchange theory, while for the short range each model uses different, phenomenological approaches. In this thesis calculations based on the Av18 and CDB potentials are presented and are described briefly in the following sections.

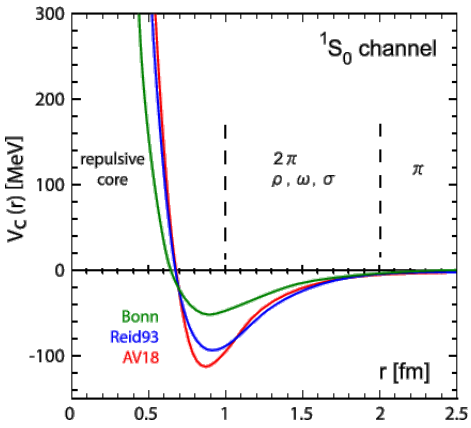

Figure 2.4: Two-nucleon potentials for various models Reid93 [9], Argonne [7] and Bonn [8].

Charge-dependent Bonn potential

The CDBonn is a charge dependent (CD), one boson exchange, non-local 2N potential [8]. Contrary to full-Bonn potential, which is the successor, the CDB potential is energy independent, making practical calculation easier. The CDB models use scalar mesons with masses below the nucleon mass, like π, ω and ρ. In the CDB model, the π-meson determines the long-range part and the ω-meson determines the short-range repulsive and the spin-orbit interaction. The intermediate range is described by a 2π-exchange mechanism. It is one of the high-quality potentials which reproduces the pp and np scattering data with $\chi^2/d.o.f \approx 1$.

Argonne v18 potential

The Argonne potentials [7] are a series of modern phenomenological 2N potentials which are developed by a group of theoreticians at Argonne National Laboratory. The last version of these series is called Argonne version 18 (AV18). The long-range part has a shape which we expect from the Yukawa potential. In the intermediate range, the most dominant process is Two-Pion-Exchange (TPE). The short-range part is phenomenological and has a Woods-Saxon shape whereby the parameters are taken from the Urbana model [29]. The AV18 potential is an updated version of AV14 with three additional charge-dependent and one charge-asymmetric operators.

2.2.3 Three-nucleon force models

Historically the first model of 3N potential was developed by Fujita and Miazawa [11]. They described the interaction by two-pion exchange, with the intermediate excitation of one nucleon. Nowadays there are many models of the 3NF. In this paper, we focus on three of them, Tucson-Melbourne 99 (TM99) [30], Urbana IX (UIX) [20] and the Coupled-Channel (CC) approach [3, 4]. The most prominent examples of 3NF effects in the Nd elastic scattering and the breakup reactions is presented in Fig. 2.5.

Tucson-Melbourne

Tucson-Melbourne 3NF [30] is one of the most popular models of 3NF. It is based on the Two-Pion exchange approach. The latest version, TM99, was introduced by Coon and Han [30]. It includes the pion-nucleon scattering with the off-shell mass of pion. Unlike the original Fujita-Miazawa approach, the TM99 model covers also other possibilities of π-N scattering than Δ excitation. This model has one free cut-off parameter, Λ_{TM}, which is the

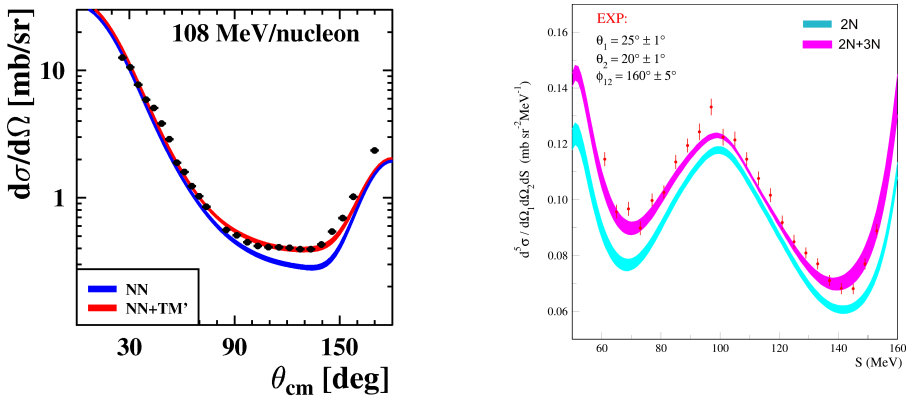

Figure 2.5: *Left panel:* Comparison of the differential cross-section data with the theoretical predictions for the Nd elastic scattering at 108 MeV/nucleon. The dark blue band presents theoretical calculation based on the realistic 2N potentials, whereas the red one shows the predictions of the NN potentials combined with the TM99 3NF. The experimental results (black circles) are the Nd elastic scattering data [13]. *Right panel*: Comparison of the differential cross-section data (red points) with the theoretical predictions (with and without 3NF included) for the ^{1}H(d,pp)n breakup at 130 MeV [16] for one selected angular configuration.

effective mass of the pion. The value of this parameter is chosen in a way to reproduce the tritium binding energy.

Urbana-Illinois

Urbana-Illinois X (UIX) potential has been developed by the Urbana-Argonne collaboration, mainly to describe the properties of the nuclear matter and the light nuclei. It is used together with the AV18 potential. As in the most of 3NF models, this one also includes the nucleon-Δ excitation. The UIX model is based on the two- and three-pion exchanges in a closed ring configurations and includes phenomenological short-range part.

The Urbana-Illinois model is used in the ab initio Green's Function Monte Carlo (GFMS) calculations [20]. In this approach the binding energy of light nuclei up to mass of A=12 are successfully reconstructed. As one can see in Fig. 2.6, taking into account 3NF significantly improves the agreement of theoretical predictions with experimental data.

Coupled-Channel approach

The Coupled-Channel (CC) [3, 4] formalism follows a different approach than more conventional models, like e.g. the UIX or TM99 potential. It is based on the CDB potential with the Δ-isobar excitation. In this model Δ resonance is treated as a stable particle and it is created via two-nucleon scattering with the internal excitation of the nucleon, see Fig. 2.7. The two nucleon channels are coupled with those in which nucleon is excited and forms Δ. The CC approach naturally incorporates effective 3NF in the form of Fujita-Miazawa interaction, together with the so-called di-baryon dispersion, see Fig. 2.8. These two components act in opposite way and in a consequence the netto effect of including Δ isobar in 3N systems is usually smaller than for approaches with other 3NF models.

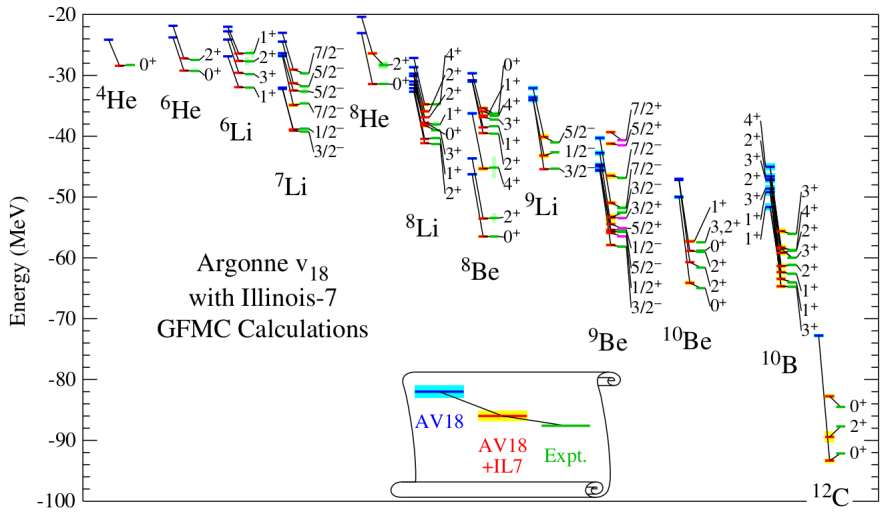

Figure 2.6: Energies of ground and excited states of light nuclei calculated with the Argonne v18 potential with the Illinois 7 3NF, based on the Green's function Monte Carlo (GFMC) method. Figure adapted from [20].

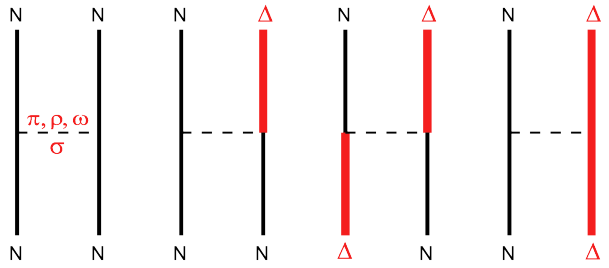

Figure 2.7: Sample channels considered in construction of the potential within the CC approach. Single Δ-isobar degrees of freedom are explicitly taken into account.

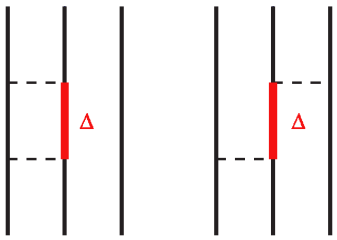

Figure 2.8: Three-baryon dispersion effect within the CC approach: two-baryon dispersion (left) and the effective three-body force (right).

2.2.4 Chiral effective field theory

The nuclear forces are a manifestation of the more fundamental interaction described by the Standard Model of particle physics. They are understood as a residual effect of the strong interaction between quarks and gluons inside the nucleons, or more general, in hadrons. The strong interaction is governed by the quantum chromodynamics (QCD). Unfortunately, due to color confinement phenomenon, QCD becomes non-perturbative at low energies. In order to overcome this problem, an approach based on effective field theory has been proposed by Weinberg in 1990 [31]. In this theory, pions - the Goldstone boson of this theory, and nucleons, become the effective degrees of freedom instead of quarks and gluons. The general Lagrangian is consistent with the symmetries of QCD, including the approximate

chiral symmetry. This approach is known as a chiral efective field theory (ChEFT) [32, 33]. Applying it to the nucleon-nucleon scattering results in an infinite number of Feynmann diagrams. They include the meson exchanges responsible for the long-range part, and the so-called hard core which is described by the contact interaction between nucleons. The nuclear interaction potential is developed in a series as a function of the variable $\left(\frac{Q}{\Lambda}\right)^v$, where Q is the nucleon momentum and the constant $\Lambda \approx 1GeV$ is related to the magnitude of chiral symmetry breaking. Each successive v-th expansion contains contributions from increasingly more complex higher orders interactions. For the next-to-next-to-leading order (N^2LO, $v = 3$), the first terms responsible for the 3NF interaction appear. This is shown in the Fig. 2.9. The significant advantages of ChEFT over other methods used so far is that the 3NF effects appear naturally and in a consistent way. What is more, it allows to estimate the uncertainty of theoretical calculations.

In recent years, there has been significant progress in the construction of the potential describing the few-nucleon interaction developed by LENPIC [34] (Low Energy Nuclear Physics International Collaboration). A new regularization approach in the coordinate space (semilocal coordinate space regularization, SCS) has been introduced [35]. It allows to maintain the long-range part of the interaction as well as to better control over the cutoff parameters, and thus a better uncertainty control. For 2N systems potential is now available up to N^4LO+, which includes additionally four N^5LO short-range operators which are needed to describe certain proton-proton scattering observables. The new method of regularization has also been implemented in the semilocal momentum space regularization (SMS) [36]. This allowed for the expansion to N^2LO order for 3N systems and to estimate the role of selected N^4LO operators, however, without fully incorporated N^3LO order.

In Sec. 5.5.3, we present the very first comparison of the latest calculations based on ChEFT (SMS) with the ^{1}H(d,pn)p experimental data at 160 MeV, for a few selected angular configurations.

2.2.5 Coulomb interaction

In contrast to the three-nucleon or even the nucleon-nucleon interaction, the Coulomb interaction is very well understood, both theoretically and experimentally. In 3N systems, we usually have a situation where two of nucleons are charged due to the much easier detection of charged particles and the absence of any neutron target. However, introduction of the Coulomb interaction between two protons in such a system is very challenging from the theoretical point of view. Because the Coulomb potential depends on distance like $1/r$, interaction does not satisfy mathematical requirements for the standard scattering theory.

For many years, the influence of the Coulomb interaction was not included in the theoretical calculations. The efforts to overcome these problems have long history and only as late as in the late 2000's some important progress has been achieved [38]. The general idea of applying the Coulomb force was that the Coulomb potential was screened and renormalized with the screening radius much larger than the range of the nuclear potential. This allowed for the to use of the standard methods for the short-range forces and the obtained results were later corrected to match the unscreened limit.

The Coulomb interaction has been incorporated for the first time in the CC approach [38]. Later also in calculations with the Av18 [39] and TM99 [40]. Currently, these calculations are the most complete as they contain both the 3NF force and the Coulomb force. The importance of the Coulomb interaction in 3N system has been observed in the *dp* breakup experiments at 130 MeV [41]. The clear demonstration of the Coulomb effects in the breakup data is presented in Fig. 2.10. Out of all available theoretical models, only those with the Coulomb force included correctly reproduce the decline in the experimental cross section for

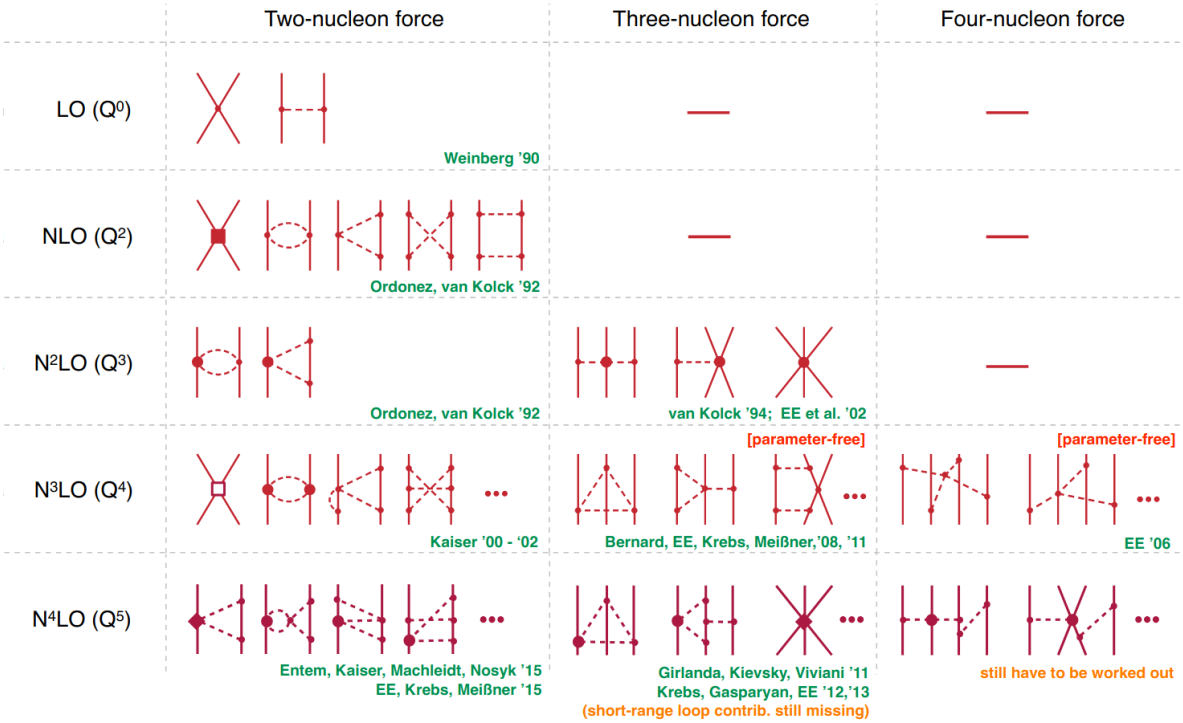

Figure 2.9: The table shows hierarchy of the graphs contributing to the nuclear forces in ChEFT theory. The solid and dashed lines represent nucleons and pions, respectively. Figure adopted from [37].

configurations with small relative angle $\Delta\phi_{12}$ between the two protons and the excess in the configurations with large $\Delta\phi_{12}$.

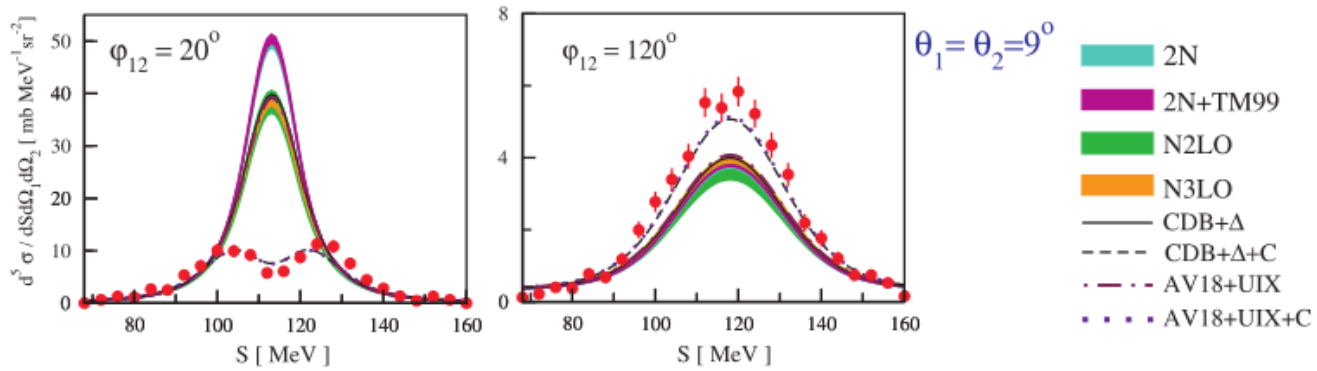

Figure 2.10: Sample of the differential breakup cross section [41] for the angular configuration specified in the picture. Theoretical predictions are shown as bands and lines, as specified in the legend.

2.2.6 Relativistic effects

The first exact calculations with relativistic contribution were developed by H. Witała theoretical group from Jagiellonian University. The relativistic treatment of the breakup reaction in 3N system was developed using NN potential [44]. This approach has also been extended for calculations including 3NF [45]. From the theoretical point of view, the relativistic effects

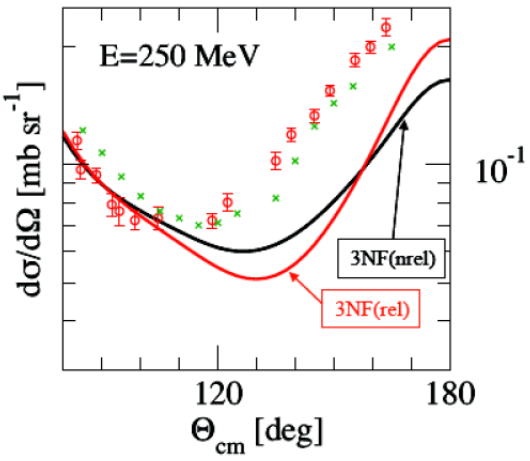

Figure 2.11: Relativistic effects in *pd* (red circles) and *nd* (green crosses) elastic scattering [42] [43]. Clear discrepancies between the both, relativistic and non-relativistic predictions can be observed.

include the Lorentz-boosted 2N potential, relativistic form of Lippmann-Schwinger equation and proper treatment of boost effects and Wigner rotations of spin states. Also kinematical effects coming from relativistic phase space factor are taken into account. The relativistic effects reveal at different parts of the phase-space with various magnitude. The relativity can increase or decrease the cross section, depending on the phase-space region, and magnitude of the effect increases with the nucleon energy. While at 65 MeV the influence of relativistic effects are rather moderate, at 200 MeV they can change the non-relativistic cross section even by 60% [45].

So far, experiments were not fully conclusive. The experimental data presented in [45] seems to confirm the theoretical findings. However, the used database for deuteron breakup at 156 MeV and 200 was limited. On the other hand, Fig. 2.11 shows the distribution of the cross section of the proton-deuteron [42] and neutron-deuteron [43] elastic scattering at the energy of 250 MeV. In this case taking into account the 3NF effects and relativistic effects together does not improve the description of the experimental data. Also the results of the WASA@COSY *dp* breakup experiment at the energy of 170 MeV/A and at the forward scattering angles do not support the relativistic calculations [46]. However, in this case considerable 3NF and Coulomb effects were observed. On the other hand, in the case of scattering at larger angles, the obtained results may suggest that under certain angular configurations, relativistic effects were actually relevant [47]. In order to test these theoretical predictions, a new experiment was proposed in which the author of this dissertation is involved, (see. Sec. 2.3).

2.3 Experimental overview

In 1998, after 41 years since Fujita-Miyazawa theory, the existence of 2π3NF was confirmed in the experimental data. Adding 2π3NF resolved problem with discrepancy at 2N elastic scattering cross section minima [48] and also reproduced 3N binding energies. This discovery started a new chapter in few-body physics.

There were many laboratories around the world which have delivered high precision data using polarized and unpolarized neutron, proton and deuteron beams. Most of the data at low energies (up to 30 MeV) have been produced at TUNL (Durham, USA) [49]. In the intermediate energy range (50-200 MeV/A) the beams have been delivered by cyclotrons or

accelerated in a ring at KVI Groningen (60-190 MeV/A, The Netherlands), RIKEN (70-140 MeV/A, Japan), RCNP (250 MeV/A, Japan), PSI (65 MeV/A), IUCF (70-200 MeV/A, USA), SATURN (95-200 MeV/A, France), Forschungszentrum Jülich (100-1300 MeV/c, Germany), or recently also Cyclotron Center Bronowice (CCB) IFJ PAN (70-200 MeV, Poland).

Our experimental group in a Polish-Dutch collaboration has initiated an extensive program on measurement of the ${}^1H(\vec{d}, pp)n$ breakup reaction in a wide phase-space region with the use of the SALAD [50] and BINA detectors [51] at KVI. Before this some systematic studies [52], [53], [54], limited to a few selected configurations were performed by Kraków-Zürich group at proton beam energy of 65 MeV.

The first measurement of the breakup reaction in a wide phase-space region was performed at 65 MeV/A and it was focused on studies of 3NF effects in cross sections and later also in analyzing powers. The results, when compared with the theoretical predictions showed not only the significance of the 3NF in the experimental cross section data [16], but also revealed new unexpected effects. In a certain part of the phase space characterized by small polar angles of the emitted protons and at large relative azimuthal angles $\Delta\phi_{12}$, significant discrepancies between the data and predictions have been observed. The effects were interpreted as manifestation of a new part of the dynamics-the action of the electromagnetic Coulomb force (neglected in theories). Then, the problem of the Coulomb interaction was studied more precisely in a dedicated experiment at very forward polar angles ($4^\circ - 14^\circ$) with the use of the Germanium Wall detector at FZ Jülich, Germany [15].

Further measurements were focused on polarization observables. The results of the vector and tensor analyzing powers of the deuteron-proton breakup reaction at 65 and 50 MeV/nucleon [55] [51] were well reproduced by 2N calculations in the whole studied phase space. In case of the tensor analyzing powers certain discrepancies were observed what suggests an existence of some missing dynamics in the spin part of the 3NF model. Moreover, the tensor analyzing powers measured at 50 MeV/nucleon [51] turned out to be sensitive to the Coulomb force influence.

Studies of the breakup reaction performed with the BINA detection system at relatively high proton beam energies of 135 MeV [56] and 190 MeV [18] reveal local discrepancies between the data and the calculations, even when 3NF models are included. Part of the discrepancies could be due to the relativistic effects.

This part of the dynamics was investigated in a dedicated experiment with a WASA@COSY facility at FZ Jülich, Germany [46]. A set of differential cross sections of elastic scattering and breakup reactions was measured at deuteron beam energies of 340, 380 and 400 MeV. The calculations [45] predict quite high magnitude of the relativistic and 3NF effects. These studies indicate that only consistent theoretical study, the 3N relativistic calculations which include 3NF, should be utilized at higher energies. Recently published results on *dp* breakup at 80 MeV/A measured with BINA [57] revealed also some discrepancies in the cross section distributions when compared to the set of theoretical calculations.

In 2014, the BINA detector was moved to the newly opened Cyclotron Center Bronowice (CCB) in the Institute of Nuclear Physics PAS, Kraków. After the reassembly and a preparation phase, the detector has been commissioned in 2016 and is still operational. The experimental program focuses on measuring the cross section for the proton-deuteron elastic and breakup reactions at 108 [58], 135 and 160 MeV. The proton beam is provided by the isochronous cyclotron C-235 Proteus. Further expansion of this program, including a dedicated neutron detector is planned.

Another activity related to few-nucleon physics carried out at the Institute is a new experiment aimed at determining the relativistic effects in the *pd* system [59]. The measurements are planned for 2021. The proton-induced deuteron breakup reaction at 200 MeV will be

investigated. The outgoing protons will be measured at a few, specially selected angular configurations. The studied region of the phase space was selected in a way that the relativistic effect are dominant while the influence from the 3N force and the Coulomb interaction are negligible. This measurement will be the final test of the relativistic predictions [45]. The experimental studies of few-nucleon systems are summarized in Tab. 2.1.

Facility	Detector	Reaction	Energy [MeV/A]	Effects
KVI	SALAD	*dp*	65[16], **65**[55]	Coulomb, 3NF
	BINA	*dp*	80[57], **50**[51], **65**[60]	3NF
		dd	80[100], **65**[61]	3NF
		pd	**190**[18][62], **135**[63][64]	3NF, Relativistic
FZ-Jülich	Ge-Wall	*dp*	**65**[15]	Coulomb
	WASA	*dp*	150, 170[46], 190, 200	3NF, Relativistic
CCB	BINA	*pd*	108[58], 135, 160	3NF
	KRATTA	*pd*	200 (planned)	Relativistic

Table 2.1: Experiments performed by our group. Experiments with polarized beams shown in bold.

It is a general agreement that in order to draw the final conclusion concerning the role of the different parts of the few nucleon system dynamics, its is crucial to observe their evolution with energy in the whole available reaction phase space and also for as wide as possible observables (cross sections, analyzing powers, polarization transfer coefficients, spin correlation coefficients). More can be found in review articles [65] [66].

Following these guidelines this thesis enlarges the existing database by completely new regions of the phase space accessible in forward part of the BINA detector in the measurement of proton-neutron coincidences.

Deuteron breakup reaction with neutron detection

Measurements of the proton-neutron coincidence in deuteron-proton breakup reactions are rare. We found only a few such measurement attempts in the 1970s, limited to in the reaction energy range and only for a few selected angular configurations [68] [69] [70]. Usually, detection of proton-neutron coincidences was used almost exclusively in the neutron-deuteron reactions. These important experiments allowed the study the properties of the three-nucleon force with respect to the reaction isospin and charge symmetry. They were used to determine neutron-neutron scattering length a_{nn} [71][72] and they contributed to the discovery of the so-called Space Star Anomaly at low energies [73].

Space Star (SST) is a special breakup configuration in which all three nucleons in the CM frame outgoing in a plane perpendicular to the neutron beam, forming an equilateral triangle with equal momenta magnitude. SST anomaly is a discrepancy between measured five fold differential cross section for the SST and the theoretical predictions (see Fig. 2.12). The measured data were systematically higher than theory for all measured energies [74][75]. Contrary, the experimental cross sections for proton-deuteron SST were below the theoretical ones [76].

The cited measurements differ significantly from the presented in this thesis in terms of used experimental techniques. Measurements of this type (proton-neutron coincidence) were mainly carried out for low particle energies and for selected angular configurations such as the previously mentioned SST or for the configurations close to quasi-free scattering. In

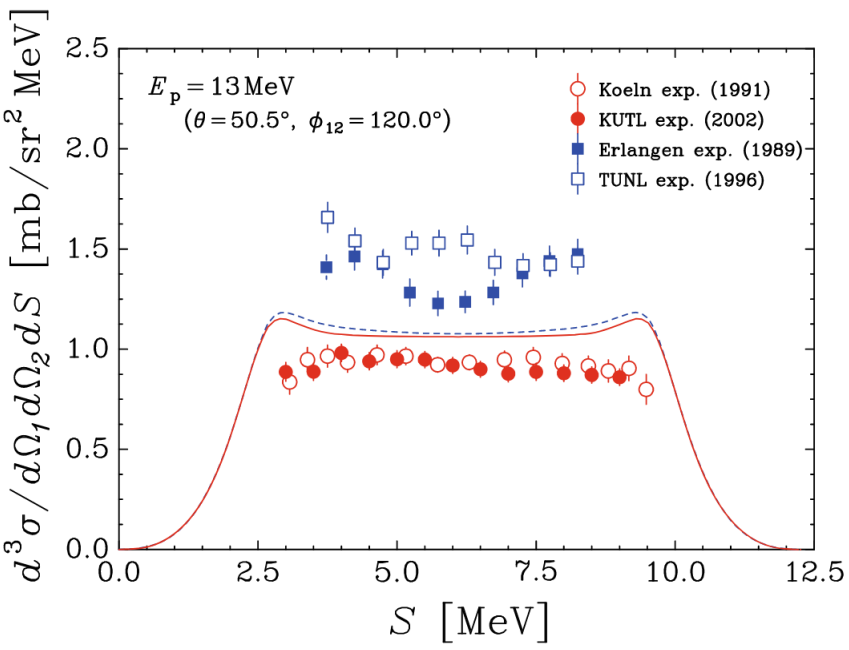

Figure 2.12: The Space Star Anomaly. Both the proton-deuteron (red circles) and neutron-deuteron (blue squares) breakup reaction cross section for Space Star configuration are not reproduced by the theoretical calculations. Figure adopted from [74]. Clear discrepancies between the both *pd* and *nd* experimental data and the theory are visible.

most cases, a dedicated liquid scintillator-based neutron detectors were used together with another charged particle detectors.

Chapter 3

Experimental setup

In this chapter, crucial parts of the detection setup used in the experiment will be presented and discussed. The experiment has been performed in 2011 in KVI-Center for Advanced Radiation Technology (KVI-CART), Groningen, the Netherlands. The AGOR cyclotron provided the deuteron beam, accelerated up to 90 MeV/nucleon, which then was transported through a beamline to the experimental hall, where the BINA detector was situated.

3.1 AGOR cyclotron

The AGOR (Accelerateour Groningen-O'Rsay) is a superconducting cyclotron. The accelerator started to operate in 1996. The AGOR is a three-segment, compact size cyclotron, with a pole diameter of 1.88 m. The superconducting magnet coils can produce magnetic fields up to 4 T. The cyclotron was designed for the acceleration of light and heavy ions. For this purpose, the cyclotron was equipped with different, exchangable external ion sources. The one used in this measurement, POLarized Ion Source (POLIS), has the ability to offer both, polarized and unpolarized beams. In the case of presented measurement, unpolarized deuteron beam was used. More information about the cyclotron can be found in [17].

3.2 BINA detector

The BINA detection system (Big Instrument for Nuclear polarization Analysis) was constructed in 2004 at the University of Groningen and it was in operation there until 2011. Recently it was moved to the Institute of Nuclear Physics in Kraków, where it was installed in the experimental hall of the Cyclotron Center Bronowice (CCB).

The detection setup can be divided into two main parts, the Forward Wall and the Backward Ball. The forward part consists of Multi-Wire Proportional Chamber (MWPC) and a hodoscope of vertically arranged thin ΔE and the horizontally-placed thick E scintillators. Together, the ΔE and E detectors form rectangular array of 120 virtual telescopes. The Wall covers scattering polar angles from 10° up to 40°, with the full azimuthal angle coverage up to 32°. A circular hole for the beam line was foreseen in the center of each component of the Forward Wall. Present thesis uses solely information from Forward Wall, however for completeness also the backward part (Backward Ball), which acts as a scattering chamber and detector at the same time will be presented.

Due to its good time-of-flight and angular resolution, and wide range of available phase space, this experimental system is an excellent tool for testing elastic scattering and deuteron breakup in deuteron-deuteron, deuteron-proton and proton-deuteron reactions.

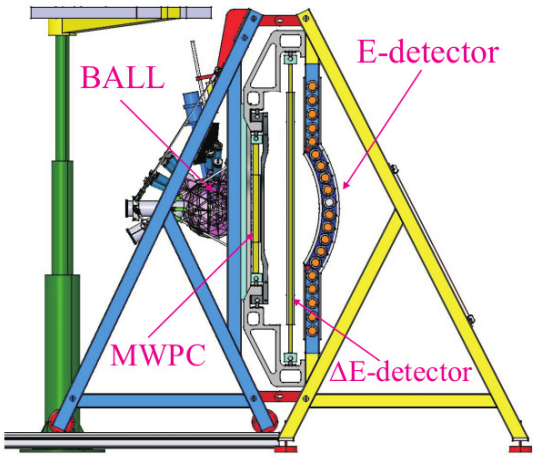

Figure 3.1: Schematic side view of the BINA detector system.

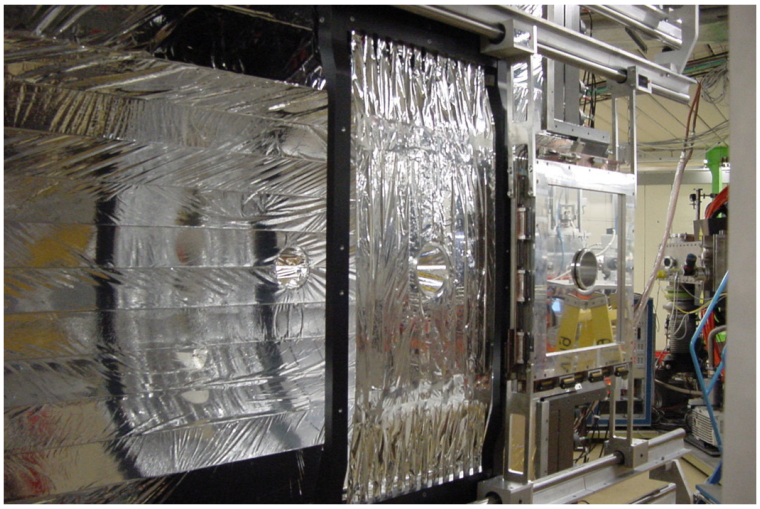

Figure 3.2: A photography of a Forward Wall during the preparation phase. The main components were displaced for a better visibility. Note the lack of the beamline pipe and cabling for the MWPC.

3.2.1 E detector

The E detector was designed to measure the energy of scattered particles. It was made of 20 horizontally placed scintillation detectors, out of which 10 central were arranged in the shape of a cylinder shell with a center of curvature placed in the target position. The individual detectors have dimensions of 9x12x220 cm. During the experiments presented in this work only 10 central elements were used. The rest of the detector, placed above and below the central part, was intended for the polarization-transfer measurement, which has not been attempted at KVI. The cylindrical shape of the central part reduced the number of particles producing a detectable signal simultaneously in two adjacent elements (the so-called "cross-over events"). Such events have nevertheless been observed due to insufficient light isolation and light leakage between segments. The E bars are made of BICRON BC-408 plastic scintillator, and their thickness allow for stopping protons of energy up to 140 MeV. Photomultiplier tubes (PMTs) were attached directly to scintillator at both ends of each, individual segment of the detector. The central hole, approximate. 12 cm in diameter, prepared for the beamline passage, resulted in a significantly different behavior of two central

scintillators. The most significant effect was a large increase if left-right asymmetry as a consequence of hindered light transport to the photomultiplier attached to the more distant PMT and additional light reflected from this cut in the direction of the closer PMT.

3.2.2 ΔE detector

Information about specific energy losses of the detected particles was provided by the ΔE detector. It consisted of 24, 2 mm thick BICRON BC-408 scintillator stripes arranged vertically, 12 covering the upper and 12 the lower part of the detector. The central stripes were trimmed in a way to allow passage of the beamline (see Fig. 3.3). Unlike in the case of E hodoscope the light readout was provided by photomultipliers attached via properly shaped optical light guide to only one, upper or lower end of each stripes, respectively. The energy loss of a particle passing through a detector depends on the particle type, its energy and the length of the trajectory inside scintillation material. The combined information from the E and ΔE detectors allowed for the identification of particles (PID), which in the case of *dp* scattering experiment was reduced to the distinction between protons and deuterons. The details of the PID method used in this experiment are presented in Sec. 4.1.3.

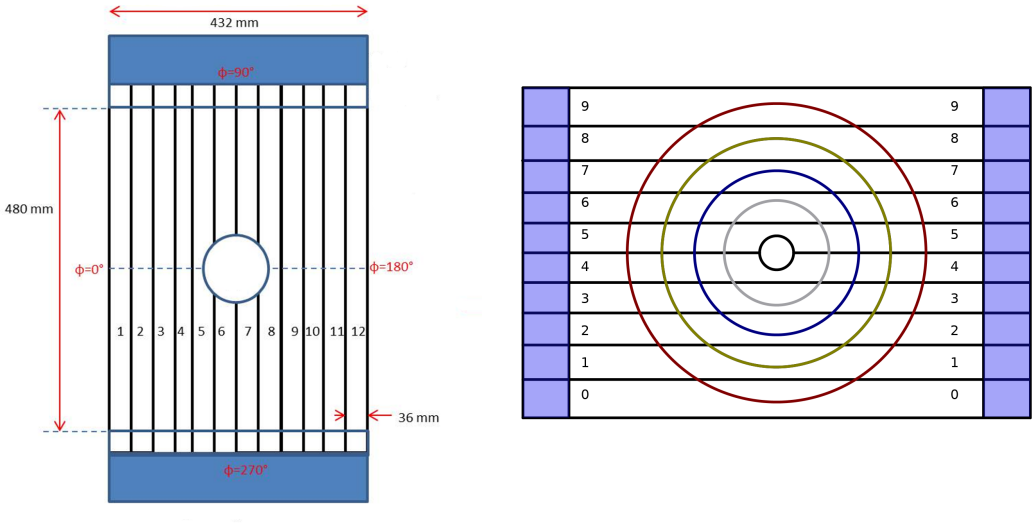

Figure 3.3: Schematic view of the ΔE (left panel) and E (right panel) detectors.

3.2.3 MWPC

The Multi-Wire Proportional Chamber was used in this experiment to measure the position of scattered particles, which in turn allowed to reconstruct their trajectories. MWPC was placed at a distance of about 30 cm from the target. Its active area was 38x38 cm^2. It was composed of three detection planes, X and Y containing 236 wires each; for x- and y-component measurement, and U plane, consisting of 296 wires inclined by 45° with respect to the other planes. The U plane allowed one to resolve the ambiguity inevitable for the cases in which more than one particle was registered in the same event and have also been used to improve the positional resolution of the MWPC.

In the center of the wire chamber there was a hole for the beamline passage. For this reason, the wires passing through the center of the chamber must have been divided into two

parts. They were electrically separated from each other and operated independently. From a data acquisition point of view they must be considered as a separate detection channels. The part of wires that was read from the opposite side to the rest of the wires in this plane is called a hub (See Fig. 3.4).

For anode wires gold-plated tungsten of 20 µm diameter, stretched by a force of 1 N, was used. Cathode electrodes were realized by conductive, grounded foils. The wires in the plane were arranged at uniform, 2 mm intervals and were grouped in two to electronic readout channels, resulting in a final 4 mm granularity of this detector. Each plane was supplied separately with high voltage of value between 3000 and 3500 V, specific for the gas mmixture used. The MWPC used mixture of 80% CF4 and 20% isobutane, which is known from its high electron drift velocity and from a very good aging properties [77]. The detector operated at atmospheric pressure which allowed for application of 25 μm thin mylar foils for the chamber windows. The gas flow through the chamber was about 150cm^3/min, which ensured constant gas refreshment in the detector.

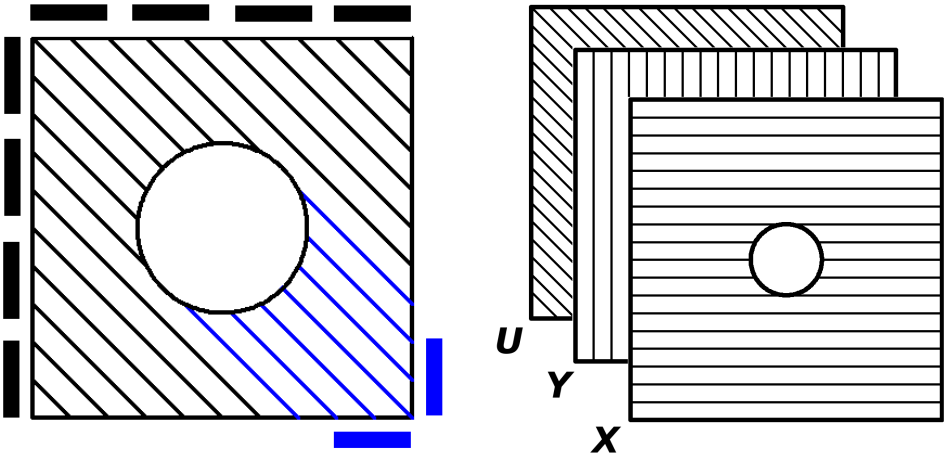

Figure 3.4: *Left panel:* Simplified diagram showing the arrangement of the wires in the U plane. The wires passing through the beamline opening, are in blue. Black and blue rectangles around the chamber symbolize the position of corresponding readout connections. *Right panel:* Arrangement of X, Y and U planes.

3.2.4 Backward Ball detector

The rear part of the detector was made of a structure of 149 scintillation elements which were glued together forming the walls of the scattering vacuum chamber. Each individual scintillator element had a shape of truncated pyramid and was made of two optically coupled scintillators with different properties: fast BICRON BC-408 scintillator constituting its main part and slow BICRON BC-444 scintillator, whose 2 mm thin layer was glued onto the internal surface of the detector. The use of two scintillators characterized by significantly different light emission times is known as a phoswich detector and allows for identification of particles registered in such detector, applying E-ΔE method, using single photomultiplier readout. An appropriately shaped optical lightguide connected each scintillator with its photomultiplier. This construction allowed for maximal reduction of the overall material budget of the whole detector and minimized value of the energy threshold for the Ball part. The vacuum chamber was closed from the front with a 40 µm thick Aramid foil window, reinforced with a Kevlar fabric, which ensured separation of the vacuum from atmospheric

pressure outside the detector.

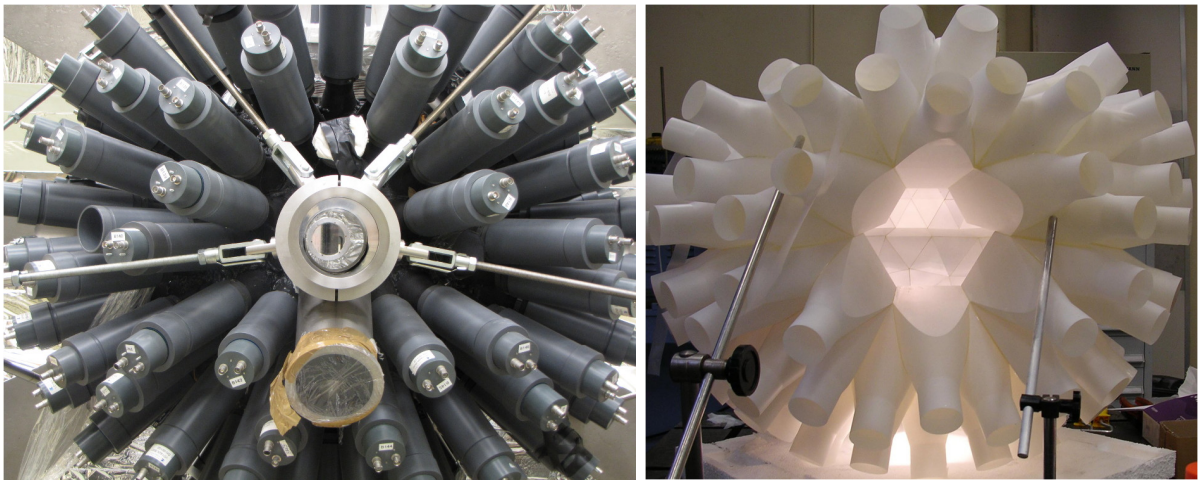

Figure 3.5: *Left panel:* The photography of Backward Ball with attached photomultipliers, but without cabling. *Right panel:* Scintillators glued together at the early stage of Backward Ball construction.

3.2.5 Target

The BINA system was designed for the use of a liquid deuterium and hydrogen cryogenic targets (see Fig. 3.6). The target cell was made of pure aluminum, to assure good thermal conductivity, and the windows were made of 4.5 µm Aramid foil. The cell diameter was 10 mm and its thickness was 3.3 mm. However, the thickness increased by about 0.6 mm, measured in the cell center, due to window bulging caused by pressure inside the cell. The target system was equipped with cooling system, a gas supply system, a pressure and temperature sensors and with a heater. The liquid target was kept at a pressure of about 250 mbar. The working temperature was 17 K for liquid deuterium and 15 K for hydrogen. A thin cylindrical aluminum shield around the cell protected the cryogenic part from the ambient thermal radiation.

In addition to the liquid target, the experiment also used two others, a solid CH_2 and zinc-sulfide target. The CH_2 target was mainly used to check the experimental setup and to determine the geometry of the system, while the luminescence of ZnS target, together with an online camera, were used to control the beam position and focus. Both solid targets were mounted vertically on a holder below the liquid cell. The whole target system was mounted inside the Backward Ball part through a system of pneumatic actuators that allowed for remote selection of target used, without access to the vacuum chamber.

3.3 Readout Electronic

Signals generated in individual detectors of the BINA experimental setup were transmitted to the computer's memory through the data acquisition system (DAQ). In this system we can distinguish four components: a readout electronics dealing with digitization of information collected from detectors, a trigger system which starts acquisitions for specific types of events, a back-end computer controlling and collecting the incoming data and a system for storing them in a mass storage. Readout electronics can be divided into segments collecting data from E and ΔE scintillators, and MWPC. Its schematic diagram is shown in Fig.

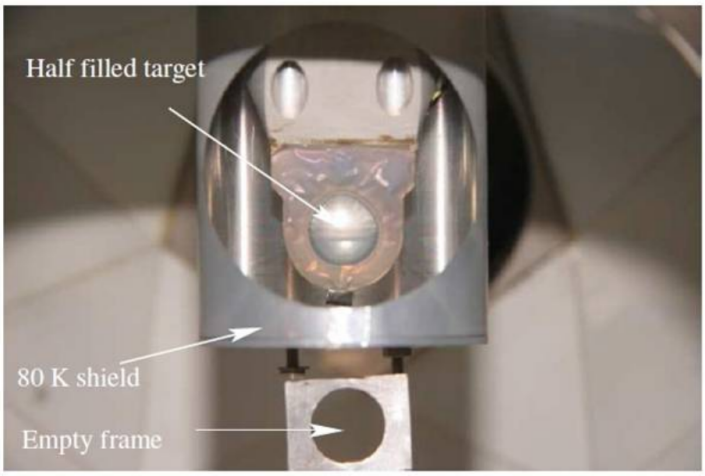

Figure 3.6: Liquid target cell mounted inside the Backward Ball in the middle of filling process.

3.7. The analog signals from E and ΔE detectors were splitted by an active splitter into two branches. The first went to the constant fraction discriminator (CFD). If the signal amplitude was higher than the assumed threshold, the logical signal was generated and propagated through the system. The CFD modules were used to obtain time-walk corrected signals for precise time information for the time-to-digital converter (TDC) LeCroy 3377 modules. Additionally, the CFD produced an OR signal, common for all 16 channels connected to this module, which was further propagated to the trigger logic. The second part of the original signal from the photomultipliers was routed to a 250 ns passive delay line and integrated, within a gate generated by the trigger system, by the analog-to-digital converter (ADC). The conversion was done by the LeCroy 4300B modules. Finally, the information from ADC and TDC was transmitted, via the FERA bus, to the intermediate memory located in the VME crate.

A separate Proportional Chamber Operation System (PCOS-III from LeCroy) was used to readout the multiwire chamber. This system contains all necessary components and modules, such as discriminators, delay lines, memory buffers, etc. The signals from wires were amplified in a dedicated preamplifier cards connected directly to the chamber and transmitted to the discriminators. Each of the 384 channels was connected to a separate analysing unit. The logic signals were internally delayed and saved in the LeCroy 2731A latching module.

When a trigger arrived, the PCOS controller requested the data saved in the latching modules and transferred it to the VME memory, where they were combined with data from scintillators. Optionally, this system could recognize also so-called clusters. These were events for which two or more neighboring wires received a detectable signal. Working in clustering mode allowed not only to significantly reduce the amount of information being transferred, but also improved the resolution of the chamber. For a given hit the values of its centroid and so called half-wire bit were transmitted. The presence of this bit indicated even number of channels activated (most frequently two) and allowed for more precise positioning of the centroid (at a half distance between hitted wires).

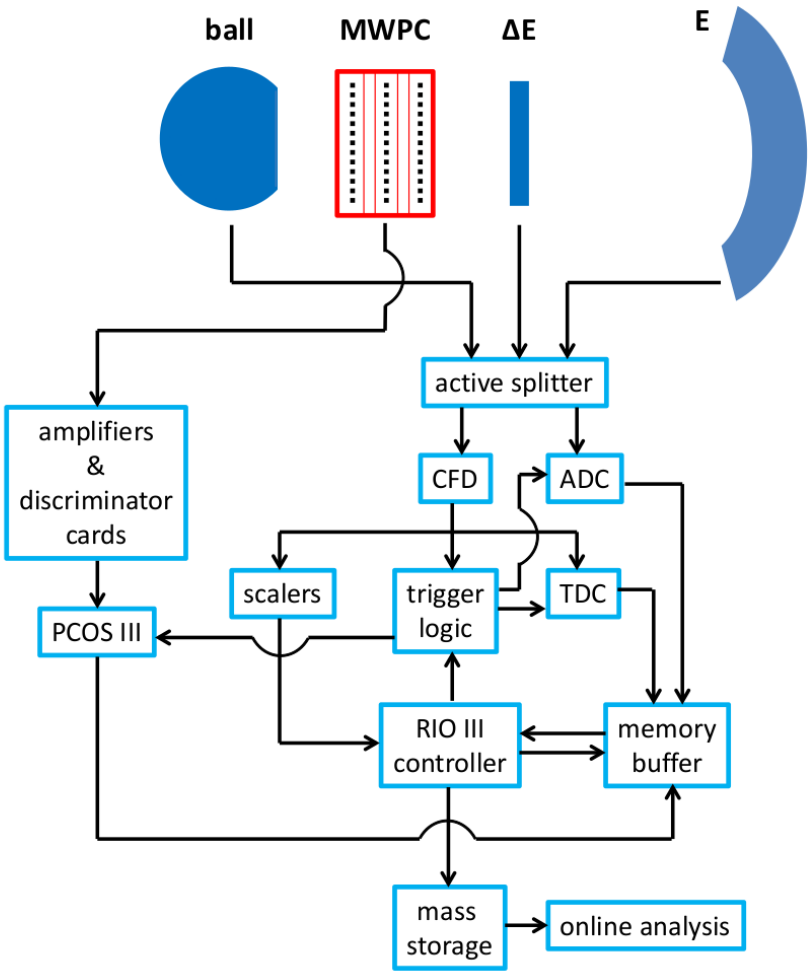

Figure 3.7: The simplified scheme of the readout electronics used for BINA experimental setup.

Chapter 4

Data analysys

In this chapter the data analysis framework is presented. In the first section a brief description of the detection methods used for charge particles is presented. It is largely based on the work carried out as part of previous analyses of breakup reactions [78] [79].

The second section is dedicated to the determination of the integrated over measurement time luminosity based on the *dp* elastic scattering. The luminosity has been finally used to normalize obtained data.

The third section is devoted to the GEANT4 simulations of the BINA detector. The simulations have been used to find the relation between the time-of-flight (TOF) and the energy of charged particles. Such calibration procedure have been performed for the first time with the BINA setup. The simulations were also used to calculate the neutron detection efficiency in plastic scintillators of BINA and the so-called configurational efficiency describing a geometrical acceptance of the detected proton-neutron coincidences.

The fourth and fifth sections constitute the essence of the presented doctoral dissertation. They describe the method of neutron detection and the determination of the efficiency for registration of the proton-neutron pairs, respectively.

4.1 Detection of charged particles

The main tool used in the analysis of the experimental data was a dedicated FBRun sorter. It is a program written in C++, extensively using ROOT [80] libraries. The sorter works in the form of a chain of successively called classes, so that the data processed by one class can be used as an input of the next class. The primary task of the FBRun is to take raw experimental data encoded in a binary form and transform it into physical quantities. At further stages, more advanced data analysis is possible, such as trajectory calculation or extracting coincidence events. The output of this program is saved in the ROOT file in a form of a tree, the structure of which can be modified depending on the needs. Later analysis is based on these sorted files, but is carried out by separate programs dedicated to a specific problem, such as the determination of cross sections or detector efficiency calculations.

The information obtained from the detectors was collected and digitized by the acquisition system (see Sec. 3.3) and stored on hard disks. During the experiment, 149 data files of *dp* reaction were collected, with a total size of approximately 150 GB. At the initial stage of the data selection, time periods which displayed unstable operation of the cyclotron or detectors were identified and removed. This selection was made by checking the information from scalers monitoring the rates of signals registered by individual detectors. Such periods can easily be located by a rapid change of the ratio of corresponding scaler value to the beam current monitor.

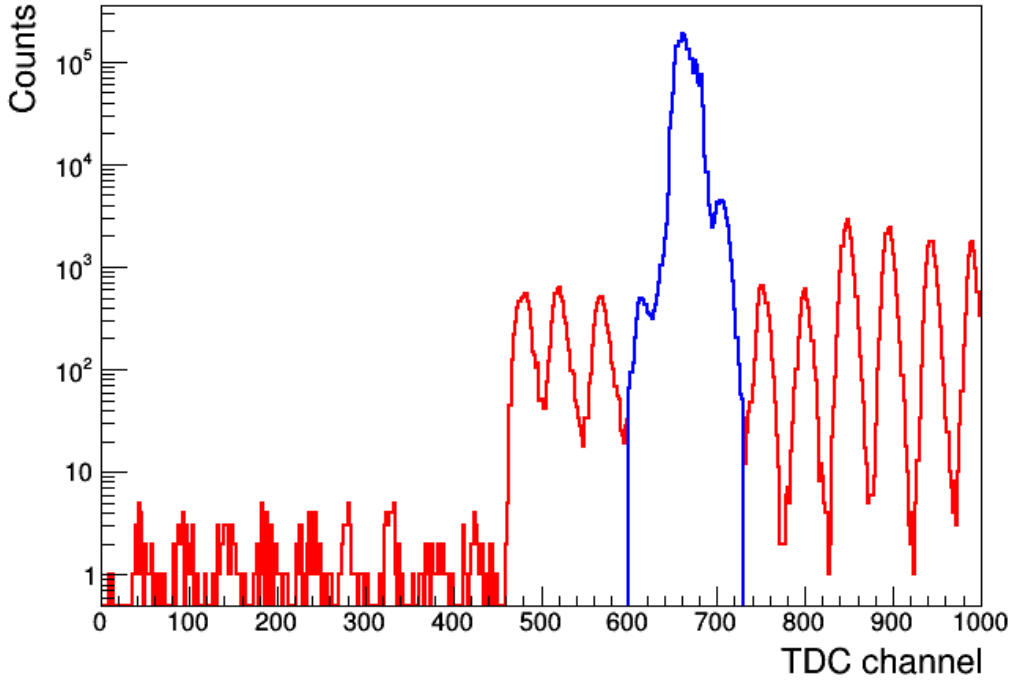

Figure 4.1: A sample of TDC distribution for one E-scintillator is shown (red line). The blue region represents the data within the TDC gate accepted for further analysis.

The next step was to determine the proper time gates for the registered signals. The deuteron beam from the cyclotron was not emitted continuously but in the form of separate bunches. These packages were emitted with a constant cyclotron frequency, which in the case of the AGOR cyclotron was about 40 MHz. Based on the TDC [1] time spectra of different

[1] Time-to-digital converter supplied the arrival times of signals from all E and ΔE detectors with respect to the common trigger signal.

detectors, the gates widths were set in a way to accept only those events which came from the same cyclotron pulse, as it is shown in Fig. 4.1. This significantly reduced the number of random coincidences.

4.1.1 Trajectory reconstruction

Charged particles during their flight in the Forward Wall detector are registered successively in MWPC, *Delta*E and E hodoscopes. Based on the information recorded by these detectors, trajectory can be reconstructed. The wire chamber was used to precisely determine the particle's position. Charged particles moving through the MWPC ionize the gas inside the chamber, generating an electrical signal in the nearest anode wires. When the induced signals are large enough for the readout electronics to accept them, the "hit" is registered in that particular channel. Since the wire chamber consists of three planes of wires tilted relative to each other, the position through which the particle has passed (x, y) can be determined as the intersection point of the wires it activates. The particle trajectory can be approximated by a line which starts in the geometrical center of the target and passes through this identified point in the chamber plane. On this basis, we determine the polar and azimuthal angles (θ, ϕ):

$$\theta = \frac{180^\circ}{\pi} \arctan\left(\frac{\sqrt{x^2+y^2}}{Z_Y}\right), \tag{4.1}$$

$$\phi = \frac{180^\circ}{\pi} \text{atan2}(y, x), \tag{4.2}$$

where the Z_Y is the distance of the projection plane from the target center. The atan2(y,x) function calculates the principal value of the arctan $\left(\frac{y}{x}\right)$, using the signs of two arguments to determine the quadrant of the results [81].

In the analysis we use two classes of tracks, the so-called weak-tracks and full-tracks. Full-track refers to events for which the particle produced a signal in all three (XYU) detection planes. The extra U-plane, in addition to increasing the accuracy of the particle position reconstruction, also plays an important role in the detection of coincident events. When detecting more than one particle, the use of only two detection planes would lead to ambiguity in the choice of a correct intersection and in consequence in the determination of particle position. Adding an another plane, inclined relative to the previous two, gives additional information and allows to resolve such ambiguity.

In the case of full-track, the activated wires, or more generally cluster centroides, form a right-angled triangle (see Fig. 4.2). The reconstruction procedure assumes that the distance between the XY intersection point and the line representing U-plane centroid must be smaller than 7 mm. A circle is inscribed in the resulting triangle (assuming equal position resolution of all planes). The center of this circle indicates the particle's track position. The maximal position resolution obtained along the x and y axis was approximate 2.5 mm [57]. Only events for which track from MWPC can be matched with the signals from ΔE and E hodoscopes are considered in further analysis. The obtained trajectory must intersect with a given accuracy the surface of both activated detector segments. Events without information from ΔE, or some MWPC planes were collected separately and used for the purpose of efficiency calculations.

In the case of the weak-tracks, the possibility that one of the MWPC planes does not register a signal was allowed. The most common reason were the regular inefficiency of the gas detector (in this case on the level of 4 percent) or non-functioning channels, which could

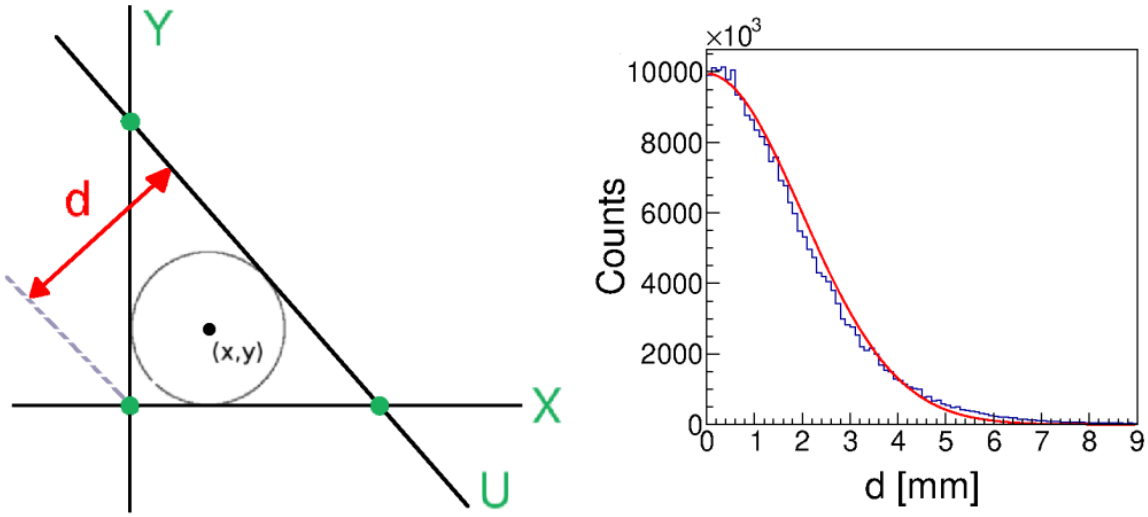

Figure 4.2: *Left panel*: Reconstruction of the particles position based on the information from XYU planes. The green dots show possible positions of weak-tracks. *Right panel:* Distribution of the matching distance d, defined in left panel. Applied limit of 7 mm for d corresponds to about 3σ of fitted Gaussian distribution.

be caused, for example, by bad contact between the chamber and readout cards, or damage in the electronics of this channel. In such a situation, the intersection of the two other active planes was taken as the reconstruction point. In presented analysis weak-tracks were used for the determination of the wire chamber efficiency (Sec. 4.1.4) and for the estimation of the systematic uncertainty connected with this efficiency.

4.1.2 Energy reconstruction and detector calibration

In the presented experiment, kinetic energy of charged particles can be determined by measuring the amount of energy deposited in the E detector. Part of this energy, converted into light is then registered by photomultiplier tubes. The output signal from the PMTs was in analog form and must been digitized by specialized ADC modules (see Sec. 3.3). In order to find the relationship between the value recorded by the ADC and the actual energy deposited by particles Monte-Carlo simulations have been used, as described in Sec. 4.3. Simulated spectra of the deposited energy have been correlated with analogous spectra obtained in the experiment. For the calibration procedure only protons from the *dp* elastic scattering were used. They are especially suitable for this task because of relatively large cross section of this process resulting in sufficient proton statistics over the entire angular range of the Forward Wall. The elastic protons, at given θ angle, have higher energy than protons from breakup reactions and due to kinematical restriction, they produce very clean spectra with a distinct peak. In order to extend the range of kinetic energies available for calibration, a specially designed degraders were inserted between the ΔE detector and the E detector. The use of degraders of various, precisely defined thicknesses allowed to extend the energy of protons suitable for energy calibration down to about 50 MeV.

Precise knowledge of charge particles energy is crucial for the analysis of the ^{1}H(d,pn)p reaction, as the energy of protons is also used to determine the energy of accompanying neutrons (see Sec. 4.4). As a measure of the amount of light produced in the scintillator the

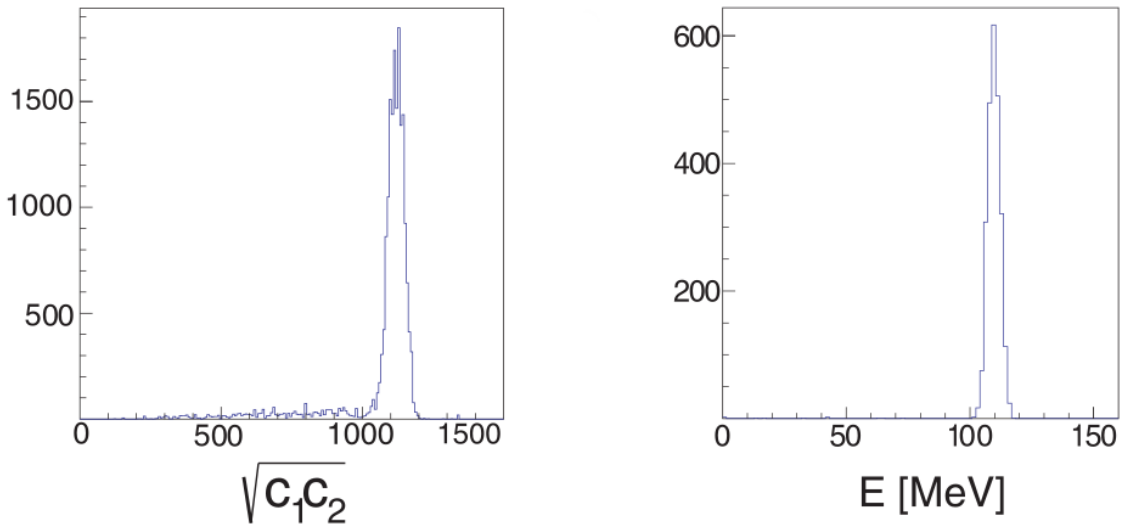

Figure 4.3: An example distribution of registered signals from protons (*left panel*) and deposited energy obtained from simulations (*right panel*). Protons were scattered at the same θ angle $24^\circ - 27^\circ$ and were registered in the same E segment. A 1 mm thick degrader was used.

geometric mean value $C = \sqrt{c_L \cdot c_R}$ of ADC signals corresponding to left and right PMTs was used. This suppresses, to large extent, positional dependence of measured signals c_L and c_R, caused by light attenuation on the way to photomultipliers. In the case of the two central segments, the arithmetic mean $C = c_L + c_R$ was used instead, because the hole for the beam pipe hindered the light transmission to the farther PMT, significantly influencing light distribution between both photomultipliers. The use of the arithmetic mean allows also to avoid vanishing the C value in the absence of any of the component signals. In Fig. 4.3 two raw spectra, one for the simulated energy deposition and one for measured C value are presented side by side. For each E detector segment and θ angle, a non-linear function was fitted:

$$E_p^D(\theta, \mathrm{E}, s) = a(\theta, \mathrm{E}, s) \cdot C(\mathrm{E}) + b(\theta, \mathrm{E}, s) \cdot \sqrt{C(\mathrm{E})}, \tag{4.3}$$

where: E_p^D is the simulated deposited energy in a given E scintillator, s is left or right side of the detector, a and b are fit parameters. An example of such function is presented in Fig. 4.4, left panel.

Having reconstructed particle trajectory, from the deposited energy one can also calculate its initial energy. For this purpose, realistic Monte-Carlo simulation of particle passage through the detector were used. Taking advantage from the azimuthal symmetry of the problem, the deposited energy E_p^D vs the initial energy E_p spectra were constructed for each angular bin and an 8th degree polynomial was fitted. An example of such function is presented in right panel of Fig. 4.4.

In order to illustrate the quality of the energy reconstruction method, an example of a coincidence spectrum of proton-proton pairs from the breakup reaction *dp* is shown in Fig. 4.5. As expected, the experimental data follow the kinematical curve. The energy resolution reaches 2.1% for 123 MeV protons, and decrease for lower energies in accordance with photon statistics [57]. More details on detector calibration and the proton energy reconstruction can be found in the dissertations [78] and [79].

Proton calibration curves have also been used to determine the energies of a deuterons. For this purpose, a correction factors for particle dependent light output provided by scintil-

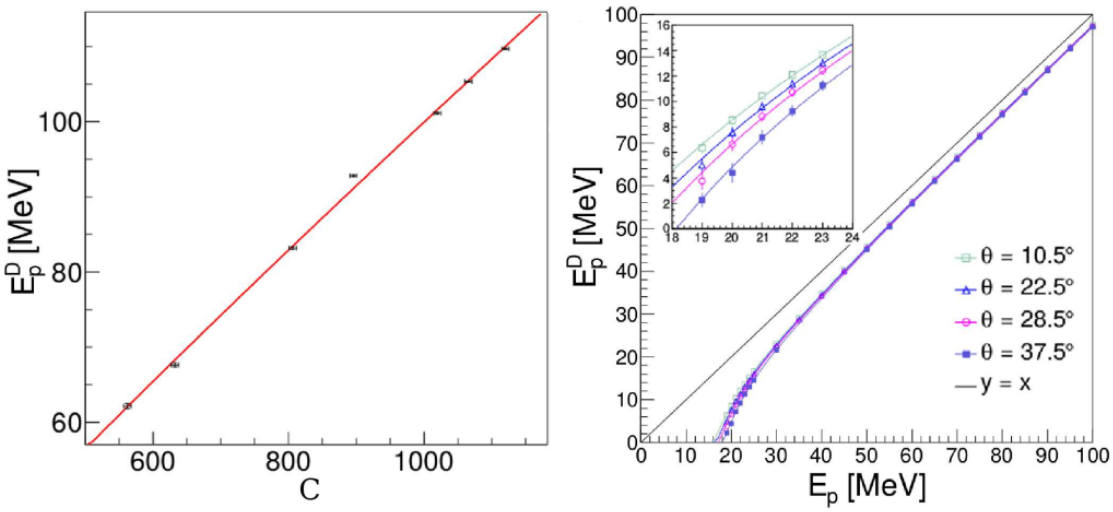

Figure 4.4: *Left panel:* An example of correlation between simulated deposited energy and collected light output C in a single E segment, together with fitted function defined in Eq. 4.3. *Right panel:* A set of functions transforming energy deposited by protons E_p^D to their initial kinetic energy at the reaction point.

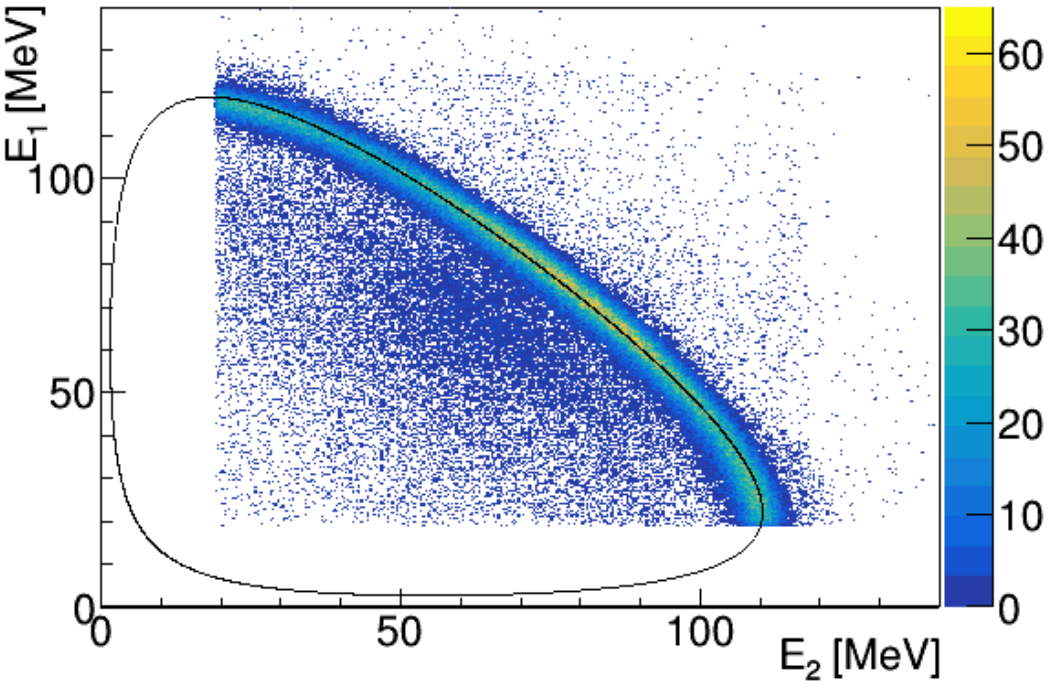

Figure 4.5: E_1 vs E_2 energy spectra of proton pairs from the deuteron breakup reactions, for the angular configuration of $\theta_1 = 25°, \theta_2 = 21°$ and $\Delta\phi_{12} = 160°$. The kinematical curve shown as a black line.

lator manufacturer company, BICRON, were applied. These values have also been veryfied within our experiment in a dedicated study as a part of the doctoral dissertation focused on the *dd* reaction [82] and [79].

4.1.3 Particle identification

Identification of particle types in the experiment was carried out using standard E-ΔE technique. As it was mentioned in Sec. 3.2, the segments of E and ΔE were arranged perpendicularly to each other forming rectangular grid of virtual telescopes. For each telescope, a two-dimensional spectrum of the energy deposited in ΔE and in E detector, respectively has been created. According to the Bethe Bloch formula, different types of particles, depending on their mass and charge, in such a plot group together in the form of characteristic bands, as it is shown in Fig. 4.6. For particle identification, graphical cuts were used for each E-ΔE telescope separately. Areas corresponding to specific particles, frequently referred to as gates, were determined arbitrarily from experimental spectra, to be wide enough to avoid excessive particle loss, while in the same time narrow enough to avoid mixing different particles types. These cuts have been adopted from the previous works [79] and have been checked and fine tuned for the analysis presented in this thesis.

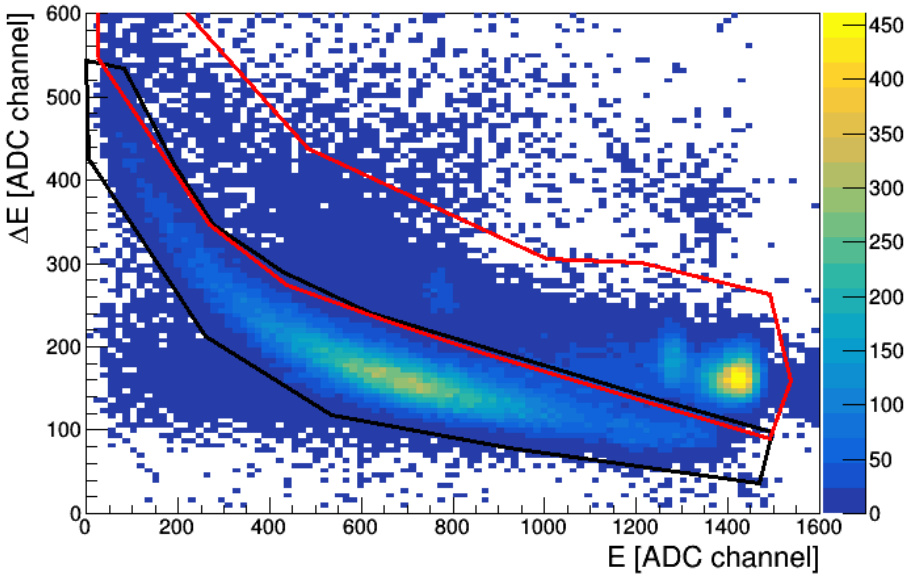

Figure 4.6: An example of the identification spectrum for a one E-ΔE telescope. The graphical cut for protons is marked black while the cut for deuterons in red.

4.1.4 Forward Wall efficiency

For the determination of the cross sections, it is necessary to know the efficiency of the detection system. The probability of registering a particle may depend on many factors, for example: imperfections in the detector design, such as gaps between the scintillation segments or non-functioning wire chamber channels. Since the main detectors (MWPC, E, ΔE) work independently of each other and information from all detectors is needed to correctly reconstruct the particle trajectory, the Forward Wall efficiency can be determined as a product of the individual efficiencies of all detectors. The obtained total efficiency:

$$\epsilon_{\mathrm{total}} = \epsilon_{\mathrm{MWPC}} \cdot \epsilon_{\Delta\mathrm{E}} \cdot \epsilon_{\mathrm{E}} \tag{4.4}$$

will be used as a correction factor scaling the number of registered particles.

ΔE efficiency

The efficiency of the ΔE detector was determined directly by the ratio of particles reconstructed with the matched signals from MWPC, ΔE and E to those that were reconstructed regardless of the presence of information from ΔE. Only single events (with one particle seen in MWPC and E hodoscope) were selected for this analysis. Having the position information from the MWPC, the efficiency can be calculated as a function of particle emission angles:

$$\epsilon_{\Delta \mathrm{E}}(\theta, \phi) = \frac{N_{\Delta \mathrm{E}}(\theta, \phi)}{N_{all}(\theta, \phi)}, \tag{4.5}$$

where $N_{\Delta \mathrm{E}}(\theta, \phi)$ corresponds to the number of events registered in the ΔE detector, while $N_{all}(\theta, \phi)$ to reference number of events, registered regardless of the ΔE information.

Due to the lack of the possibility of identifying the particles (no signal from the ΔE detector), the determination of the efficiency was based on all registered particles, regardless of their type. The results are presented in the form of an efficiency map in Fig. 4.7.

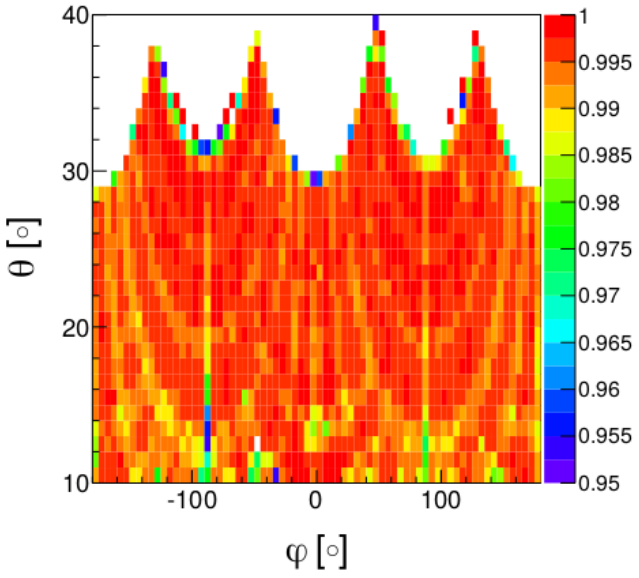

Figure 4.7: Map of the ΔE detector efficiency, presented as a function of ϕ and θ angle of registered particles. Figure adopted from [78].

MWPC efficiency

This efficiency can be obtained for each of detection planes separately. For this, only events with a single particle seen in both E and ΔE hodoscopes were used. The single plane efficiency was calculated in a similar way as the efficiency for the ΔE detector, as the ratio of the number of events with the signal in a given plane to the total number of events. The particle position was determined on the basis of information from the other two detection planes. The total wire chamber efficiency can then be calculated in two ways, depending whether strong (Eq. 4.6) or weak-tracks (Eq. 4.7) are used:

$$\epsilon^{full}_{\mathrm{MWPC}}(\theta, \phi) = \epsilon_X(\theta, \phi) \cdot \epsilon_Y(\theta, \phi) \cdot \epsilon_U(\theta, \phi), \tag{4.6}$$

$$\begin{aligned}\epsilon^{weak}_{\mathrm{MWPC}}(\theta,\phi) = \epsilon^{strong}_{MWPC}(\theta,\phi) \\ + \epsilon_X(\theta,\phi)\cdot\epsilon_Y(\theta,\phi)\cdot(1-\epsilon_U(\theta,\phi)) \\ + \epsilon_X(\theta,\phi)\cdot(1-\epsilon_Y(\theta,\phi))\cdot\epsilon_U(\theta,\phi) \\ + (1-\epsilon_X(\theta,\phi))\cdot\epsilon_Y(\theta,\phi)\cdot\epsilon_U(\theta,\phi).\end{aligned} \tag{4.7}$$

The efficiency of the chamber depends on the amount of energy a particle losses for primary ionization when passing through the gas mixture, which in turn depends on the type of particle and its kinetic energy. In order to account for this effect, a new variable was introduced:

$$E_{loss} \sim q^2\frac{m}{E}, \tag{4.8}$$

where q and m are the particle charge and mass, and E is its kinetic energy. The whole sample of registered particles was split into 3 groups, according to its E_{loss} values, in the way to maintain sufficient statistics in each group. Then, a separate efficiency map was calculated for each group. This division and the energy dependent efficiency maps for the MWPC detector are shown in Fig. 4.8.

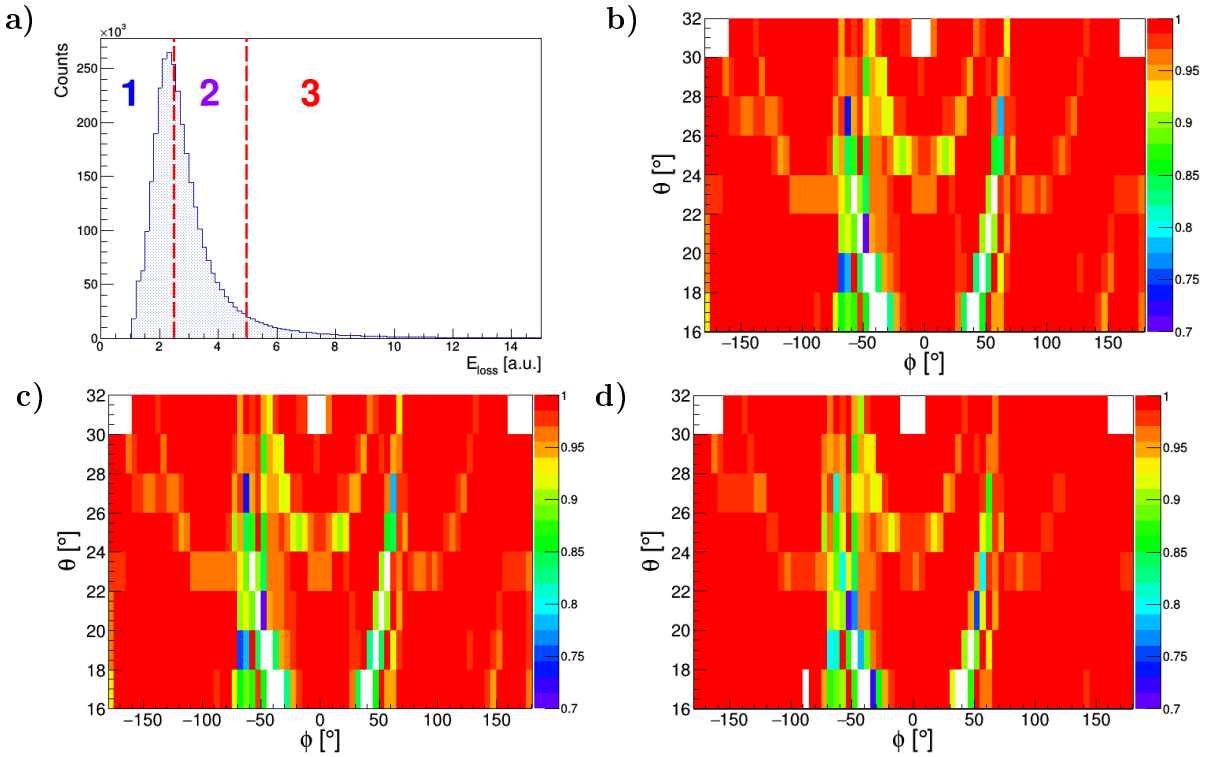

Figure 4.8: *Panel a:* Distribution of events as a function of the energy loss in wire chamber. *Panel b,c and d:* The full-track position dependent MWPC efficiency calculated for E_{loss} regions 1,2 and 3 respectively.

E detector efficiency and hadronic corrections

The problem of E hodoscope efficiency can be reduced to particle type dependent energy threshold. The gap between adjacent scintillators is defined by the thickness of the scintillator wrapping foils and is smaller than 50 μm. Due to lateral straggling and secondary ionization processes, even particles pointing exactly at this gap have little chance to produce no signal in E hodoscope. In consequence the efficiency was assumed to be exactly 100%.

Another effect that can be treated in a similar way as the efficiency is the loss of events due to the hadronic reactions. When the measured particle undergoes a hadronic reaction in the detector, a large part of its energy can be absorbed without producing light in the detector. This way, the reconstructed particle energy is underestimated, which may result in its rejection from the analysis at the identification stage. Detector E is particularly exposed to this phenomenon simple because of its large thickness. To determine the probability of hadronic interaction, once more detector simulations were used (see Sec. 4.3). A set of simulations for various proton energies in the range from 20 to 150 MeV were performed. For a given initial energy of protons, the percentage of events which underwent a hadronic interaction with the detector material has been estimated by the ratio of the number of events in the monoenergetic peak N_{peak} to the number of events in the tail N_{tail} of obtained energy distribution. This allowed to determine the relationship, presented in Fig 4.9, used for the correction of experimental events. The efficiency for hadronic processes was calculated by the formula:

$$\epsilon_{\mathrm{E}} = 1 - \frac{N_{\mathrm{tail}}}{N_{\mathrm{peak}} + N_{\mathrm{tail}}}. \tag{4.9}$$

More details about the efficiency for hadronic interaction can be found in [83].

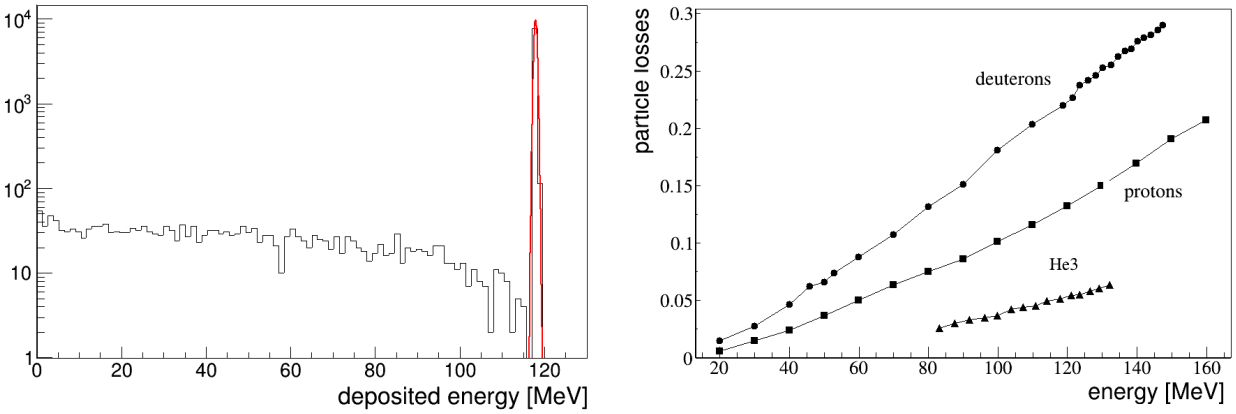

Figure 4.9: *Left panel:* Distribution of deposited energy simulated for 120 MeV deuterons in the thick E scintillator. The red line is a Gaussian distribution fitted to the main peak. Events which undergo hadronic interaction are located to the left of the peak. *Right panel:* Simulated loss of events due to hadronic interactions in the E hodoscope, presented as a function of particle initial energy. Figure adopted from [83].

4.2 Normalization

The luminosity can be determined knowing the thickness and density of a target, the electronic deadtime and the total accumulated beam current. However, due to technical problems with the Faraday cup, it was not possible to reliable measure beam current during the experiment. In addition, the formation of bubbles of hydrogen gas inside the liquid target was observed, which made it difficult to estimate its actual thickness. To avoid these problems, it was decided to use a relative normalization instead.

Since the elastic deuteron-proton scattering was measured simultaneously with the breakup reaction, its known cross-section can be used to determine the luminosity $\widetilde{L}$ using the formula:

$$\widetilde{L}(\theta_p) = \frac{N_{pd}(\theta_p)}{\sigma(\theta_p) \cdot \Delta\Omega \cdot \epsilon(\theta)}, \tag{4.10}$$

where N_{pd} is the number of elastic protons registered in the solid angle $\Delta\Omega$, $\epsilon(\theta)$ is the detector efficiency and $\sigma(\theta)$ is the absolute differential cross section of deuteron-proton elastic scattering. As there was no former measurement of the *dp* elastic scattering cross section at 160 MeV, interpolation has been performed based on the existing experimental data in the energy range 65-190 MeV. A result of the interpolation procedure is presented in Fig. 4.10. More details on the luminosity determination procedure can be found in [57]. The final value of the integrated luminosity was found to be $\widetilde{L} = (19.68 \pm 1.12) \cdot 10^6 [mb^{-1}]$. To calculate the normalization factor the luminosity has to be multiplied by a prescaling factor, which depends on a trigger type. For the portion of the data used for breakup analysis, only the T1 coincidence trigger was active. This trigger was downscaled by a factor 2. Thus the normalization was equal to:

$$L(\theta_p) = 2 \cdot \widetilde{L}(\theta_p) \tag{4.11}$$

and it was used to obtain the absolute five-fold differential ^{1}H(d,pn)p cross-section values presented in this doctoral dissertation.

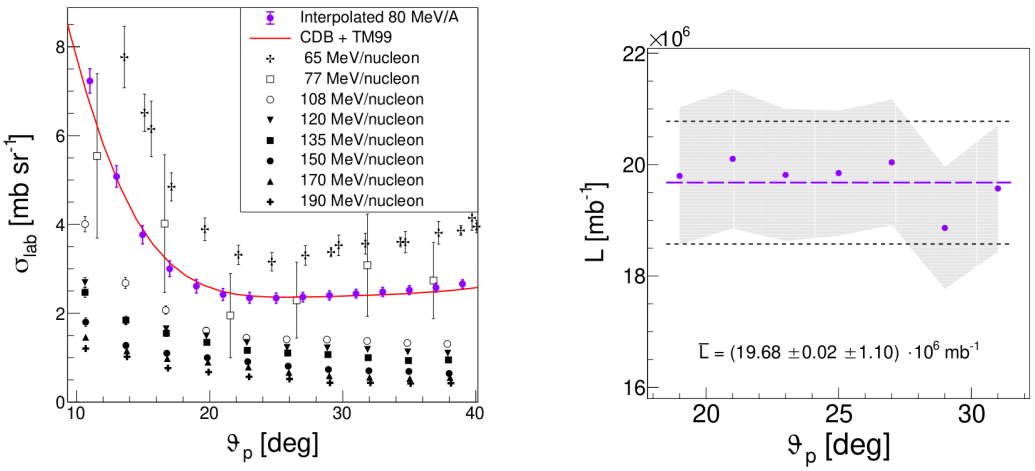

Figure 4.10: *Left panel:* Interpolated cross section for deuteron-proton elastic scattering at 80 MeV/A, together with the full experimental data set and the theoretical calculations. *Right panel:* Luminosity integrated over time determined independently for each proton polar angle. The grey shaded area corresponds to the range of systematic errors of individual points. The average value of luminosity is marked with purple dashed line and its uncertainties with dashed black lines. Figures adopted from [57].

4.3 Simulations framework

Simulations were extensively used during the analysis of the deuteron breakup reaction for various purposes. The simulation code, originally prepared for the previous detection setup, the SALAD experiment [50], was written in the Frotran-based Geant3 framework. Later, the program has been adapted to the new geometry of the BINA detector. The whole simulation program was rewritten in the C++ and based on Geant4 [84] and originally utilized the 3-body kinematics to generate events for the breakup process. This was the starting point for further development, performed by the author of this thesis. In view of extensive simulations expected for the analysis of the ^{1}H(d,pn)p reaction, in the initial phase a large effort was focused on the improvement of the overall simulation performance.

The goals have been achieved by the use of a much faster and more versatile Pluto++ event generator [85] in a first step of the simulations. The code was also adapted for multi-thread computing and the output format was also modified. As a result the time needed for simulations has been reduced by a factor of 10-20 (depending on the reaction type).

The simulation software has also been modified with respect to the following aspects:

- use of realistic models of neutron interaction with matter,
- acquisition and storing of the time information required for a TOF method calibration,
- obtaining of the configurational efficiency for the proton-neutron pair detection,
- calculation of the neutron detection efficiency in the thick E scintillator.

The details of the conducted modifications as well as the simulation program are presented in the following sections.

4.3.1 Pluto++ event generator

Pluto is a Monte Carlo event generator [85], used mostly for hadronic-physics up to energies of a few GeV per nucleon. It was developed for the HADES [86] experiment at GSI. The framework is entirely based on the ROOT package [80] and uses the C++ interpreter. Pluto covers wide range of physics processes, like the models of resonance production with the mass-dependent Breit-Wigner sampling.

The package allows to generate up to 7 particles in a final state and, as such, is well suited to simulate 3- and 4-body breakup processes. Particles are distributed according to the reaction phase space, or as an option, it is also possible to sample the events with an angular distribution and cross sections. Another possibility is to use the dedicated sampling model of momentum distribution of nucleons inside the deuteron [87]. This enables Pluto to simulate quasi-free scattering, which is particularly interesting when considering few-body reactions. The usage of Pluto package is also very user friendly. The reactions can be set up with just a few lines in a ROOT macro code without detailed knowledge of the simulation framework. It uses a specially designed build-in scripting language, which provides an easy way to deal with the reaction process, histogram filling, event filtering and output file format handling. However, Pluto does not allow to track the particles through the detector, that is why its output is usually chained for further processing with Geant4. This strategy was also applied in the presented work.

4.3.2 Geant4

Geant4 is a toolkit for nuclear and high-energy physics simulations, developed and maintained by a broad worldwide community of physicists [84]. It provides full handling of detector simulation: geometry, tracking, detector response, event and track management, visualization and user interface. The multi-disciplinary nature of this toolkit requires that it supplies a large set of physics processes to handle diverse interactions of particles with matter over a wide energy range. Moreover, large database of cross sections is included like nucleon-nucleon interaction (SAID, [88]) and for hadronic processes (INCL [89], binary cascade, Bertini cascade [90]).

4.3.3 Experimental geometry in simulation

The detector geometry, as described in Chapter 3, has been implemented in the Geant4 framework. Some of the passive elements, like the target holder or detector support frames were not included into the simulation. The target was represented by a cylinder made of liquid hydrogen, surrounded by an aluminum ring. It was situated inside the scattering chamber and separated from the vacuum by a 4.5 µm thick Aramica foil. Other parts of the target system like cooling system, solid target holder etc. were not implemented. An exit window of scattering chamber was made of a single foil sheet without a support of Kevlar fabric, however of equivalent thickness (100 µm). There was no proper digitizer included in the simulation. All obtained signals were based on the physical interactions of particles with matter (hits and energy deposition in all detector parts). The digitizer part, handling energy and angular smearings, not working wires in MWPC or energy thresholds are implemented in the further steps of the analysis.

4.3.4 Time-of-flight calibration

One of the most crucial steps in the analysis of the experimental data of the ^{1}H(d,pn)p breakup reaction is the reconstruction of neutron energy with the time-of-flight method (TOF). In order to determine the neutron time of flight it was necessary to calculate the reaction time as precisely as possible. This was done by calculating the time-of-flight of the accompanying particle, which in the case of analysed reaction was a proton.

To determine the time-of-flight of a given particle, its trajectory and the energy (or equivalently -velocity) along the whole trajectory, must be known. The trajectory was assumed to be a straight line given by the target center and the position reconstructed by the MWPC. Considering a minimum energy threshold for protons and deuterons this assumption seemed to be justified. Different strategies can be applied for accessing the velocity distributions along the trajectory in this particular detection system:

- no energy losses,
- simplified, two-step interaction with detector,
- realistic Monte Carlo simulations of energy deposition.

All these approaches are schematically presented in Fig. 4.11.

The first case was used for neutron TOF. In the considered energy region, neutrons virtually do not lose their energy when passing through inner layers of the detection setup and their movement can be approximated as constant, from the moment of their generation in the target, to the final interaction with the E detector.

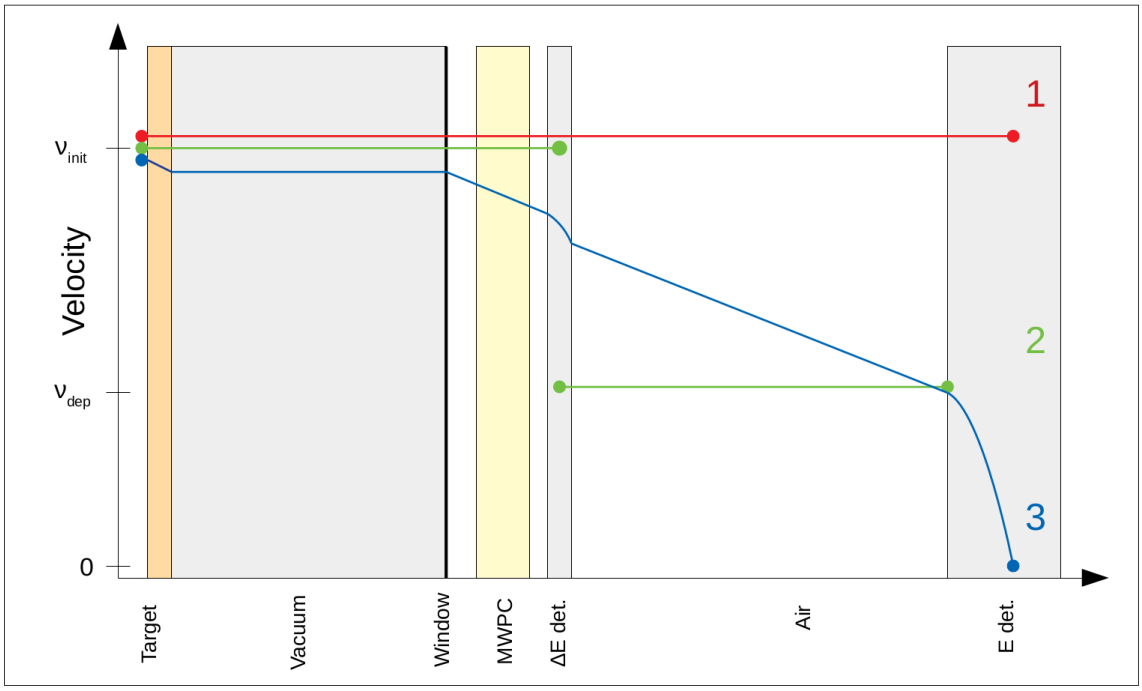

Figure 4.11: A schematic 1-D view (not to scale) comparing three different models of particle movement considered in this analysis. A strategy number 1. assumes no energy dissipation along the trajectory beside the final interaction in the E scintillator and was used for neutron TOF calculation. The second one is a simplified two-steps model, a composition of two uniform, rectilinear motions. The third one is based on the realistic simulations of particle interaction with the matter.

The second method can be applied for charged particles, since it accounts approximately for their specific energy losses along their way to the E-detector. In this two-steps model, we assume that from the moment of production, the charged particle moves to ΔE detector with constant velocity corresponding to its initial energy. From this point a particle continues its motion with constant velocity, but obtained based on the energy deposited in the E detector. This approach takes advantage from the fact, that most of material between target and the E-hodoscope is concentrated in a relatively thin layer of the ΔE scintillator. This method was used at the very beginning of the analysis and also in the final estimation of systematic uncertainties.

On the other hand, the exact particles motion through the detector can be directly calculated step by step. This is particularly important for low energy particles since they lose relatively large fraction of their energy before reaching the detector, which significantly extends their flight time. Particle energy losses due to the ionization of matter are very well known and can be calculated using the Bethe-Bloch formula with the sufficient precision for simple application. But for the more complicated systems, such as BINA, it is more convenient to take advantage from the existing Monte Carlo simulation. The simulations allow one to determine the time of flight of charged particles in the full range of the available energy. Approximately $5 \cdot 10^7$ ^{1}H(d,pp)n breakup reactions have been generated using the PLUTO software. Only events for which both charged particles hit the Forward Wall detector (i.e. the polar angle θ from 10° to 40°, and in the full range of the azimuthal angle ϕ) were accumulated. These events were then used as an input to the GEANT4 simulations. To obtain energy losses in each detector part the standard, natively provided in GEANT4 physics model (*G4EmStandardPhysics_option4*), characterised by accurate electromagnetic

intercations in a given energy range [91] was used. For each simulated particle, its time-of-flight to the E detector and the energy losses in each part of the detector, as well as the total energy lost before reaching the last detector, were recorded. The output of the simulations was saved in the ROOT tree structure, with each branch representing a given variable like: particle kinetic energy, θ, ϕ angles etc. This structure (shown in Appendix B) was the same as for the experimental data, except some additional extra information available only in the simulations. In this way the simulated data can be processed by exactly the same programs as the experimental data in further analysis.

The acceptance of the Forward Wall detector is usually presented as a function of XY position in a middle plane of the MWPC detector where its position resolution reaches its maximum. In order to determine the relation between particles energy and their TOF, the active area of the detector was divided into evenly distributed, rectangular bins. The analysis was carried out for three different XY granulations: 10x10, 40x40, and 80x80. This allowed one to estimate the systematic uncertainties associated with the bin size used for the energy calculation (see Sec. 5.4).

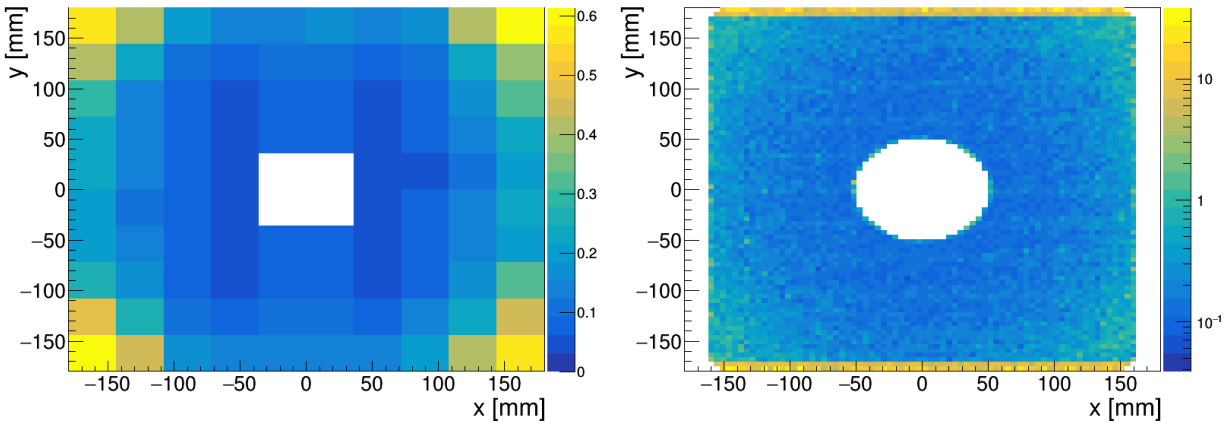

Figure 4.12: The distribution of the $\chi^2/d.o.f$ of fitted $t^k_{\mathrm{TOF}}(E)$ function for each segment of the detector. *Left panel:* with 10x10 segments, *Right panel:* higher granularity of 80x80 segments. The visible horizontal stripes with large discrepancies at the top and bottom of the detection plane are caused by the MWPC aluminum frame. The simulated acceptance was slightly higher than observed in the experiment, allowing particles to actually pass through the edge of the frame.

For each of XY bin, particles registered in all Forward Wall detectors were selected. Then the correlation between the TOF and the particle initial energy has been plotted for each segment (Fig. 4.13, left panel) and fitted with the function of the form:

$$t^k_{\mathrm{TOF}}(E) = a^k + b^k/E + c^k/E^2 + d^k/E^3, \tag{4.12}$$

where k corresponds to the segment number. One example of the obtained fit is presented in Fig. 4.13, right panel. This parameterization reflects underlying physical model dependence and allows for very good description of the data (see Fig. 4.12). Obtained functions were further applied to calculate the moment of reaction in the target t_0.

For most of the detection plane obtained functions vary only slightly between various segments. Larger discrepancies occur near the corners and edges of the plane. With increasing θ angle, particles effectively encounter increasing detector thickness. This results in increased smearing of energy losses in these areas and, as a consequence, a higher fit error. Particles which passed near the top and bottom edges of the detection plane can hit the aluminum

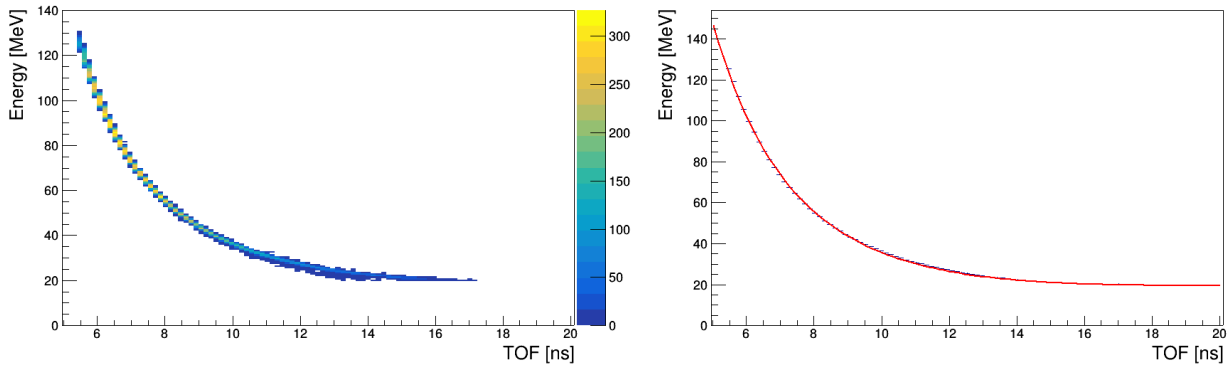

Figure 4.13: *Left panel:* Histogram of the energy vs time-of-flight for simulated protons. Data from 40x40 granulation for one selected segment. *Right Panel:* The t^k_{TOF} function (marked in red) fitted to profiles obtained from the distribution presented in left panel.

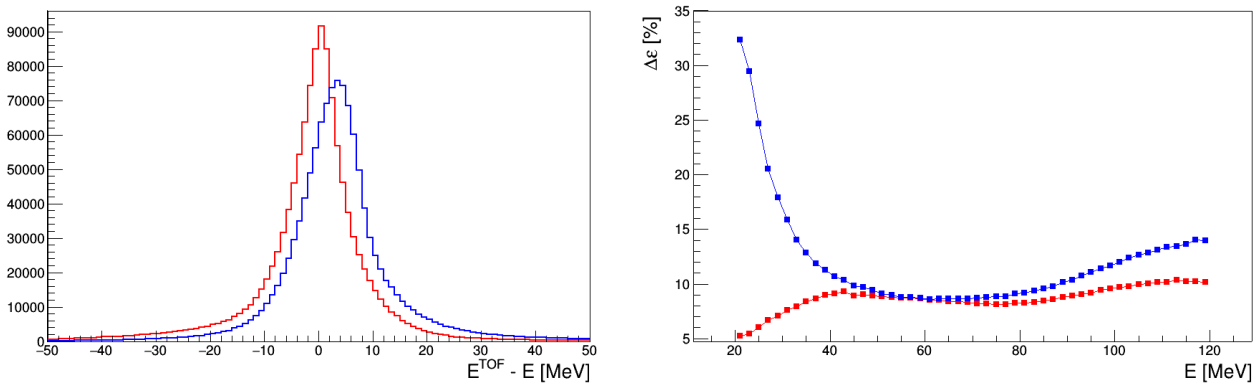

Figure 4.14: *Left panel:* The accuracy of proton energy reconstruction using the TOF method, defined as a difference between the initial energy E and the energy obtained from its time of flight E^{TOF}. The red line represents the TOF energy distribution obtained from the 40x40 segments simulation while the blue line refers to the approximate two-step model. *Right panel:* The mean difference (relative to the initial proton energy) between the proton energy obtained from the energy deposition and TOF, calculated from the simulation (red) and from the simplified model (blue).

frame of the MWPC detector, causing a significantly larger energy losses, resulting in even higher error.

For the cross-check of the method the inverse function, $E^k(t_{\mathrm{TOF}})$ has also been found in a way analogous to the one presented above. This function was used to calculate charged particle energy at the reaction point based on its TOF and eventually to determine the precision of the TOF energy reconstruction method. For this purpose, events with two registered charged particles have been used. One of these particles has been used to obtain the reaction time, while the energy of the second particle has been calculated from the TOF method. This value can then be compared to the energy obtained with a standard energy reconstruction method based on known energy deposition in the scintillator and known energy losses, as presented in Sec. 4.1.2.

Fig.4.14 and 4.15 present the comparison between two methods of time-of-flight calculation: one based on the realistic Monte Carlo simulations and the second based on the simplified, two-step model. As expected the Monte Carlo simulations offer better TOF reconstruction precision than simple model in the entire energy range. This can be seen

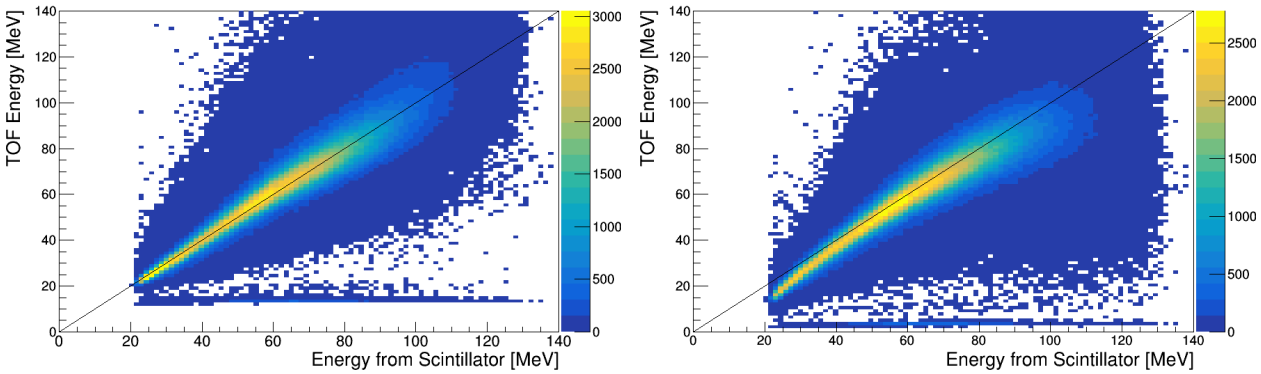

Figure 4.15: Scatter plot of proton energy obtained by energy deposition in scintillators vs. energy from time-of-flight measurement based on the 40x40 segment simulation (right) and the simplified two-step model (left). Correlation plots of energies reconstructed based on TOF and the deposited energy in the E-scintillator. *Left panel:* results from the 40x40 segment simulations. *Right panel:* results from the simplified two-step model.

especially in Fig. 4.14 where both methods applied to the proton-proton coincidences from the *dp* breakup are compared. The data were sorted according to the initial proton energy, E_i, obtained in a standard way, from the energy deposited in the thick scintillator. For each energy interval, the average, relative difference between the energy calculated based on TOF E_i^{TOF} and E_i was calculated using the formula:

$$\Delta\mathcal{E} = \frac{1}{N}\sum_{i=0}^{N}\frac{|E_i^{\mathrm{TOF}} - E_i|}{E_i}\cdot 100\% \tag{4.13}$$

For the simplified method, there is a larger deviation at both the low and high energy regions. Only within a narrow energy range of 55-60 MeV both methods are almost equivalent.

4.4 Neutron detection

Since the BINA detector was designed and used for the detection of charged particles, for the analysis of the ^{1}H(d,pn)p breakup channel a development of a special approach to reconstruct neutrons in the final state was necessary.

The neutron detection method requires registration of at least one additional charged particle. This particle is necessary to calculate neutron time-of-flight and its kinetic energy. We required that between the E segment, which detected neutron, and the one responsible for proton detection, there was at least one non active E-hodoscope segment. The requirement of such a gap prevents from misidentification of neutron with cross-talks between the neighboring detector elements.

Only the E detector, with its 12 cm thick plastic scintillators, can be efficiently used for the neutron detection. The remaining Forward Wall detectors were used as an active veto for charged particles. Since both, the ΔE and MWPC detector overlap and have very high efficiency for charged particles detection, their combination suppresses virtually all charged particles originating from the target. In this analysis, we assumed that efficiency of veto was 100 %. Therefore a valid hit in the E detector with missing signals in *Delta*E and MWPC detectors, remaining after reconstruction of coincident charged particle can indicate a possible neutron interaction. Such neutral track with very high probability is a good candidate to origin from the ^{1}H(d,pn)p reaction.

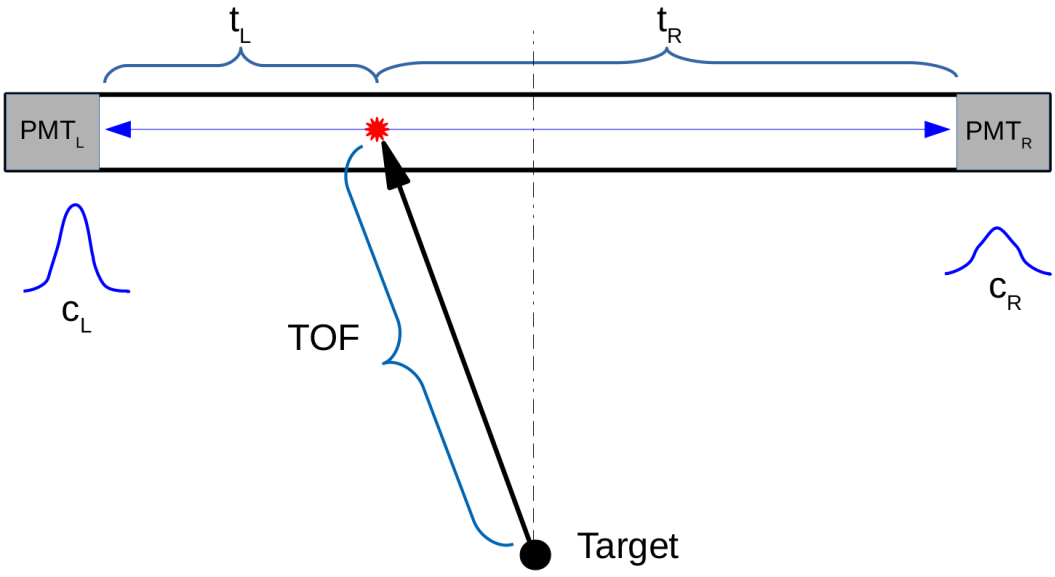

Figure 4.16: The schematic drawing of neutron detection with E-detector.

4.4.1 Neutron momentum reconstruction

Position reconstruction from TDC information

Energy deposited by a particle in the E scintillator is converted into light, which then is collected by photomultipliers at its both ends (Fig. 4.16). They produce signals which are further analysed by corresponding channels of the TDC 3377 module. This module worked in a common-stop mode in which the start signals come from the PMT and the stop is obtained by a trigger logic. As a consequence, time differences measured by the left (t_L) and

right (t_R) PMTs depend on particle position along the scintillator:

$$t_L = t_{\text{int}} + \frac{n_{\text{eff}}\left(\frac{L}{2} + x_T\right)}{c} + \tau_L^i, \quad t_R = t_{\text{int}} + \frac{n_{\text{eff}}\left(\frac{L}{2} - x_T\right)}{c} + \tau_R^i, \tag{4.14}$$

where L is the total length of the E slab, t_{int} is the particle interaction time with the detector, x_T is position along the scintillator, c is the speed of light in vacuum and n_{eff} is effective refraction index of the scintillator medium. The τ_L^i and τ_R^i account for other delays, e.g. caused by different cable length for the i-th E segment. Solving this equation for the variable x_T one can extract the horizontal position of a hit as a function of the difference between left and right TDC signals:

$$x_T = \frac{c}{2n_{\text{eff}}}(t_L - t_R) + \tau_{L-R}^i. \tag{4.15}$$

It should be stressed that the left and right time offsets do not necessarily cancel. Their difference, however, can be calculated taking advantage from precise position information available for charged particles. After this procedure left and right time offsets are reduced to common value τ_{L+R}^i which depends only on a scintillator element. The determination of these values is described in Sec. 4.4.3. The position information which is based on this method is much less accurate than the position information obtained from the MWPC, however it can be applied for events (like neutrons) with no signal in MWPC.

In order to test this approach, the TDC-based position reconstruction method has been applied to charged particles. x_C position, obtained from MWPC for protons, was compared to the position x_T determined with the TDC method (Fig. 4.18). As expected both variables are strongly correlated and follow linear dependence. Quite large effects of granularity due to the finite TDC resolution (0.5 ns) can be seen in the x_T variable. The distribution of the differences between x_T and x_C allows one to obtain the effective refractive index n_{eff} (Fig. 4.17). For further analysis a value of $n_{\text{eff}} = 2.055$ estimated from the data was used, which is significantly larger than a typical value for organic scintillator materials. This is due to the fact that most of the produced light undergoes multiple reflection from the scintillator walls before it reaches the photomultiplier. Using the refractive index $n = 1.58$ of BC-408 scintillator provided by manufacturer one can calculate the average reflection angle $\Theta = 39.7°$. The $x_T - x_C$ distribution can also be used to estimate the position resolution of TDC method, see Fig. 4.19.

Position reconstruction from ADC information

Another method of reconstruction of the horizontal position is based on the asymmetry of the signal magnitudes measured by left and right photomultipliers, a_L and a_R, respectively. Assuming simple model of light attenuation on its way to photomultipliers, the position along the scintillator should depend linearly on the logarithm of the ratio between these magnitudes.

$$a_L \simeq E_D \cdot e^{\left(\frac{L}{2} + x_A\right)/\lambda}, \quad a_R \simeq E_D \cdot e^{\left(\frac{L}{2} - x_A\right)/\lambda}, \tag{4.16}$$

$$x_A = \frac{\lambda}{2} \cdot ln\left(\frac{a_L}{a_R}\right). \tag{4.17}$$

The E_D is energy deposited by particle while λ is the attenuation length of the scintillator. In contrast to the TDC-based method, the x_A position was not calculated directly from Eq. 4.17. Instead, this position has been calibrated using charged particles and the position

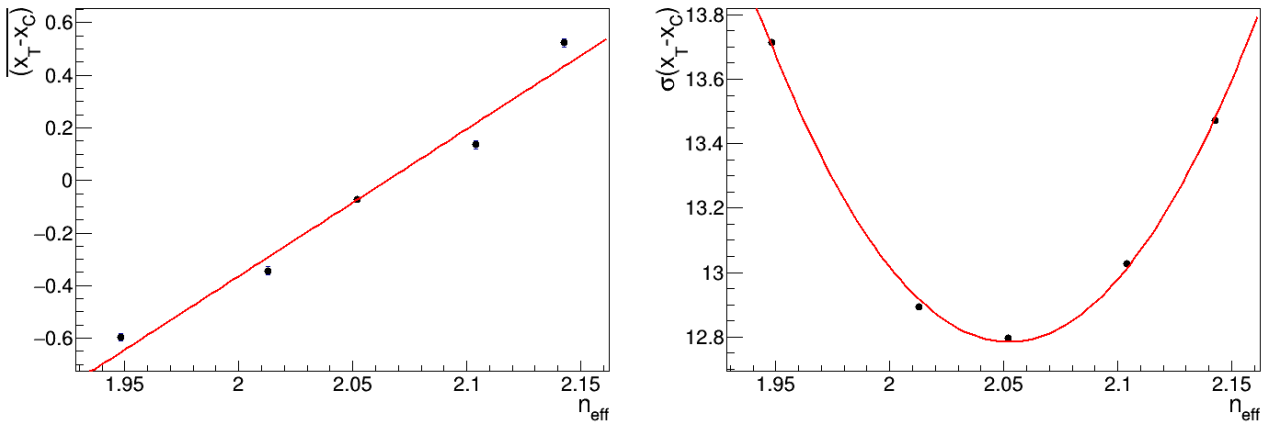

Figure 4.17: *Left panel:* The mean value of the $x_T - x_C$ distribution, presented as a function of effective refractive index. The linear function was fitted to the data. Minimal difference was obtained for the refractive index $n_{eff} = 2.06$. *Right panel:* Similar as left panel but for width (as a standard deviation) of the $x_T - x_C$ distribution, with a parabola fitted to the data. The minimum of the function is at $n_{eff} = 2.05$. The mean of this two value was taken as the final n_{eff}.

information from MWPC. This is due to the fact that the condition of a simple attenuation does not necessarily have to be met, e.g. the effective attenuation length may vary with the distance from scintillator center. The calibration procedure used a portion of the experimental data delivering the correlation plots and finally the calibration of the $ln\left(\frac{a_L}{a_R}\right)$ vs. x_C, as shown in Fig. 4.18 right panel, for each E detector segment. Results of position reconstruction x_A given by this method are shown in Fig. 4.19, right panel.

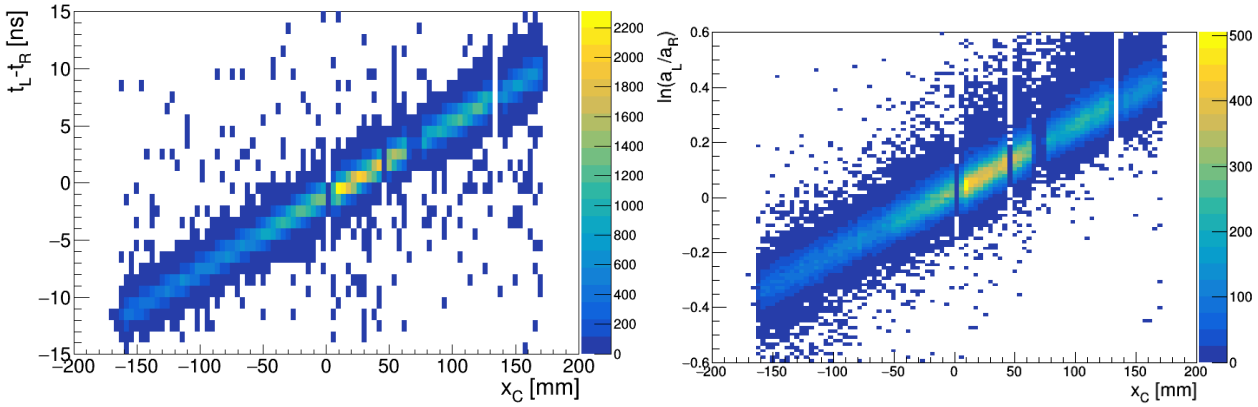

Figure 4.18: *Left panel:* The difference between TDC of left and right PMTs in one E detector segment, as a function of measured position x_C in the MWPC. *Right panel:* The logarithm of left and right PMTs signal ratio, for the same E detector as a function of MWPC position x_C.

Both methods, ADC- and TDC-based, provide independent measurement of particle's position, and combined together, with weights defined by their respective precisions, result in an improved position ($x_{T,A}$) reconstruction for events with no information from MWPC available (Fig 4.20). The final resolution of combined methods, based on the analysis of charged particles data, is $\sigma = \sqrt{\sigma_{T,A}^2 - \sigma_C^2} = \sqrt{11.6^2 - 2.5^2} = 11.3$. This value provides also a good estimation of neutron position reconstruction accuracy. The preliminary results of

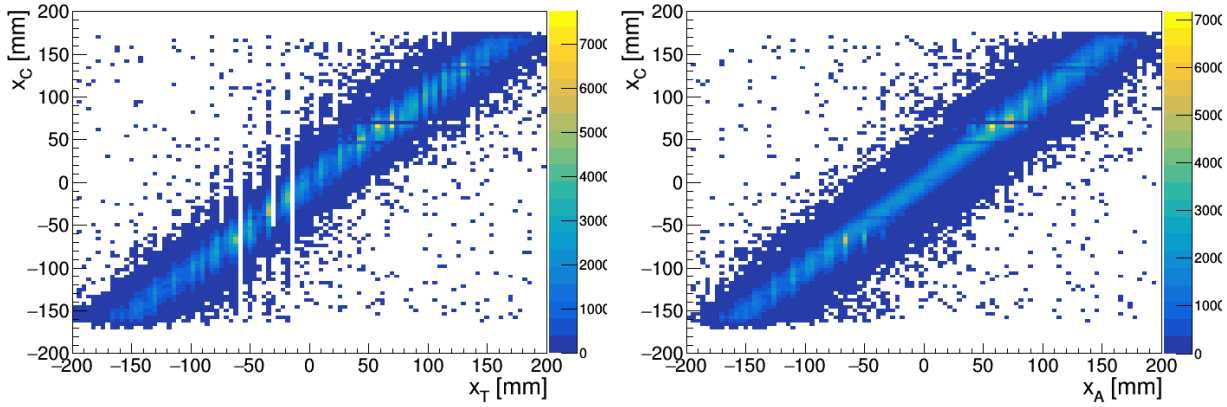

Figure 4.19: *Left panel:* The horizontal x-coordinate reconstructed from the TDC information (x_T) plotted versus the x-coordinate obtained from MWPC (x_C). *Right panel:* The horizontal x-coordinate reconstructed from the ADC information (x_A) plotted versus the x-coordinate obtained from MWPC (x_C).

the both reconstruction methods have been published in [92].

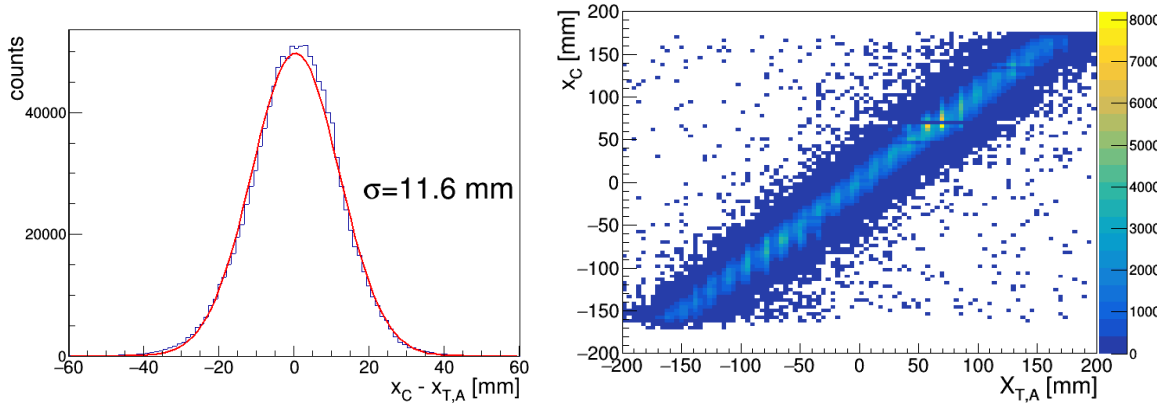

Figure 4.20: *Left panel:* The precision of combined ADC- and TDC-based method, presented in the form of the difference between the MWPC position and TDC-ADC method. *Right panel:* The horizontal x-coordinate reconstructed from the combined ADC- and TDC-based information ($x_{T,A}$) plotted versus the x-coordinate obtained from MWPC (x_C).

4.4.2 Energy reconstruction

The determination of neutrons energy was one of the main challenges facing this doctoral dissertation. The TDC information was previously utilized for particle identification in the analysis of earlier BINA experiments which were performed without ΔE detector. However, the presented analysis was the first to use the particle's flight time to obtain its energy in this experimental setup. Originally, the BINA detector was not designed to detect neutral particles (relatively small distance between the target and the E detector and its low granularity). For this reason, a lot of work had to be done for this method in order to be used reliably with a satisfactory accuracy.

Neutrons deposit their energy in scintillators in a much different way than charged particles - solely by hadronic interactions. Often a large portion of this energy escapes the active volume of the detector in a form of secondary particles, mainly other neutrons and photons.

As a consequence, deposited energy cannot be used as a measure of neutron kinetic energy. Instead the TOF method was used. The energy was calculated using the neutron's flight distance s_n and time t_{TOF}.

$$E_n = m_n c^2(\gamma - 1) = \frac{m_n c^2}{\sqrt{1 - (\frac{s_n}{t_{\mathrm{TOF}} \cdot c})^2}} - m_n c^2, \tag{4.18}$$

where m_n is the neutron mass and c is the speed of light. The distance can be calculated assuming that neutron was produced in the target center and entered given E-detector segment at the position calculated by formula:

$$x_{\mathrm{E}} = x_n \cdot \frac{z_{\mathrm{E}} + \epsilon}{\sqrt{z_0^2 + y_n^2}}. \tag{4.19}$$

The x_{E} and x_n are the horizontal position of neutron interaction in the E detector and wire chamber plane respectively, while the y_n is the vertical position of neutron in MWPC. z_{E} is the radius of the E-detector curvature and the z_0 is the distance from the target center to the center of MWPC. Unlike charged particles, which starts to deposit their energy from the front face of the scintillator, neutrons can initiate the reaction with a probability distributed almost uniformly along their flight path in scintillating material. This difference is accounted for by a small correction ϵ. In order to obtain this value, we have performed scan over ϵ range, minimizing the deviation of the experimental data from the kinematic curve. The results of this procedure are presented in Fig. 4.21. The value has been found to be slightly smaller, 45 mm, than the half of the scintillator thickness (60 mm).

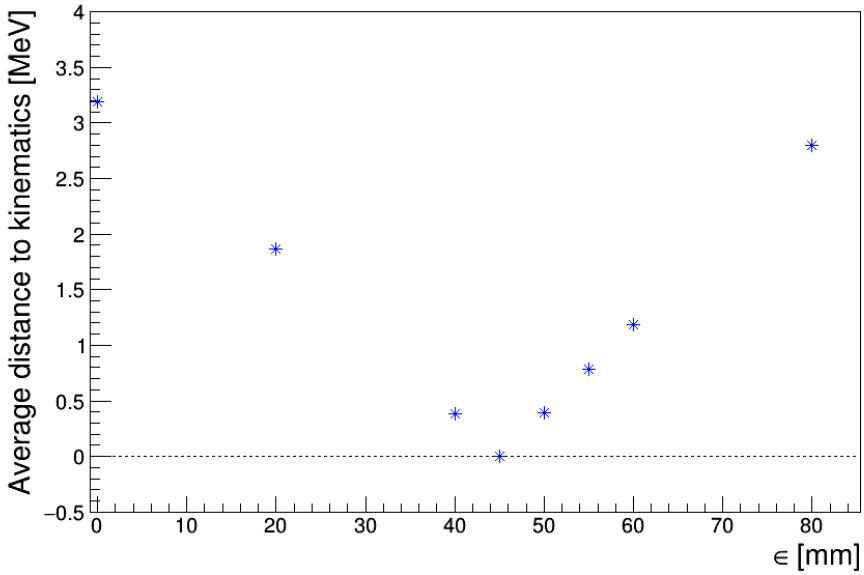

Figure 4.21: The average distance of experimental points to its kinematical curve in a function of a distance, ϵ, added to the neutron flight path length in Eq. 4.19.

Taking advantage of the fact that the E detector has cylindrical symmetry, only the position of the interaction along the horizontal X-axis is needed to finally calculate neutron flight path length:

$$s_n = \sqrt{x_E^2 + (z_E + \epsilon)^2}. \tag{4.20}$$

Time of flight is defined as the difference between the neutron interaction time t^n_{int} with the E scintillator and the reaction time t_0 in the target. To obtain the reaction time, it is necessary to detect at least one proton in a coincidence with the neutron, as explained in Sec. 4.3.4. Having the information about the kinetic energy and the trajectory of accompanying proton, one can calculate its time of flight. In order to properly account for energy loss along the trajectory, the simulation has been used, see Sec. 4.3 for details. Having protons time of flight t^p_{TOF}, one can determine the reaction time $t_0 = t^p_{\mathrm{int}} - t^p_{\mathrm{TOF}}$. Using this information, the neutron time of flight can be calculated according to the formula:

$$t^{\mathrm{n}}_{\mathrm{TOF}} = t^{\mathrm{n}}_{\mathrm{int}} - t^{\mathrm{p}}_{\mathrm{int}} + t^{\mathrm{p}}_{\mathrm{TOF}}. \tag{4.21}$$

Similarly as in the case of position reconstruction, information from TDC modules was used to determine the interaction time. Using the sum of the TDC signals from the left and right PMTs allows to remove position-dependent part of signal:

$$t_L + t_R = t_{int} + \frac{n\left(\frac{L}{2} + x\right)}{c} + \tau^i_L + t_{int} + \frac{n\left(\frac{L}{2} - x\right)}{c} + \tau^i_R, \tag{4.22}$$

$$t_{int} = \frac{1}{2}\left(t_L + t_R - \tau^i_{L+R} - \frac{nL}{c}\right). \tag{4.23}$$

Symbols description can be found in Eq. 4.14. Combining together Eq. 4.21 and Eq. 4.23 the neutron time of flight can be calculated:

$$t^{\mathrm{n}}_{\mathrm{TOF}} = \frac{t^n_L + t^n_R}{2} - \frac{t^p_L + t^p_R}{2} + t^{\mathrm{p}}_{\mathrm{TOF}} + \frac{\tau^i_{L+R} - \tau^j_{L+R}}{2}. \tag{4.24}$$

Eq. 4.24 shows that the TOF method is in fact based on the time difference between the registration of both particles. This difference can be very small, for extreme cases even comparable with the resolution of TDC modules itself. This again clearly indicates at the importance of the precision in estimation of proton time of flight and even small corrections τ_{L+R}. Therefore, a solid calibration of τ_{L+R} has been performed (see Sec. 4.4.3) and also detailed check on reconstructed t^p_{TOF} have been done. In the second case it was necessary to introduce extra correction to the proton calibration, see Sec. 4.4.4.

Events with two coincident protons can be used to test the accuracy of this method. One proton was used for calculation of the reaction time while the other was treated as if it was neutron. Its position has been obtained using combined TDC and ADC method. Because the formula 4.18 does not applied for charged particles, the $E^k(\tau_{\mathrm{TOF}})$ functions obtained from simulations (Sec. 4.3.4) were used instead. The obtained energy from TOF was compared with its energy based on standard energy reconstruction method (Fig. 4.22). The obtained energy resolution reaches minimum of 10.9% at about 80 MeV.

As a cross-check of this method one can compare the neutrons deposited energy with the energy obtained from the time-of-flight method. The value of the energy deposited in the scintillator is always lower than the actual kinetic energy neutron. As shown in Fig. 4.23, the neutron deposited energy E_D in the E-scintillator (treated as if it would be a proton) in the vast majority of events is significantly lower than the obtained from TOF method. It clearly shows that the procedure of identifying and reconstructing neutron position and energy described in this section works correctly.

4.4.3 Time calibration

In the analysis of previous experiments, there was no need to perform a time calibration of the BINA detection setup. However, due to the fact that the neutron detection methods

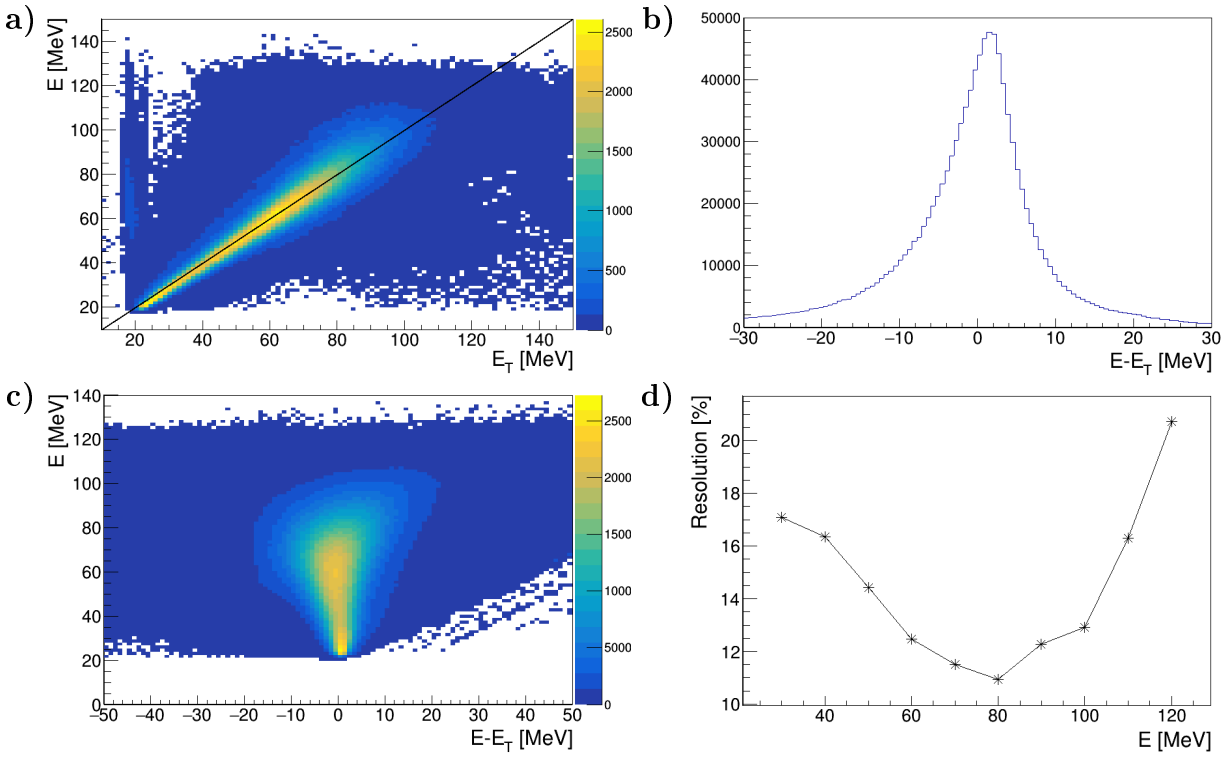

Figure 4.22: *a)* Energy obtained from the TOF method (E_T) vs energy reconstructed based on the deposited energy in scintillator (E) for protons.
b) Distribution of the differences between E and E_T. *c)* Difference between E and E_T in a function of the initial proton energy E. *d)* Resolution (in %) of TOF method, based on the proton-proton events, calculated in a function of the initial proton energy E.

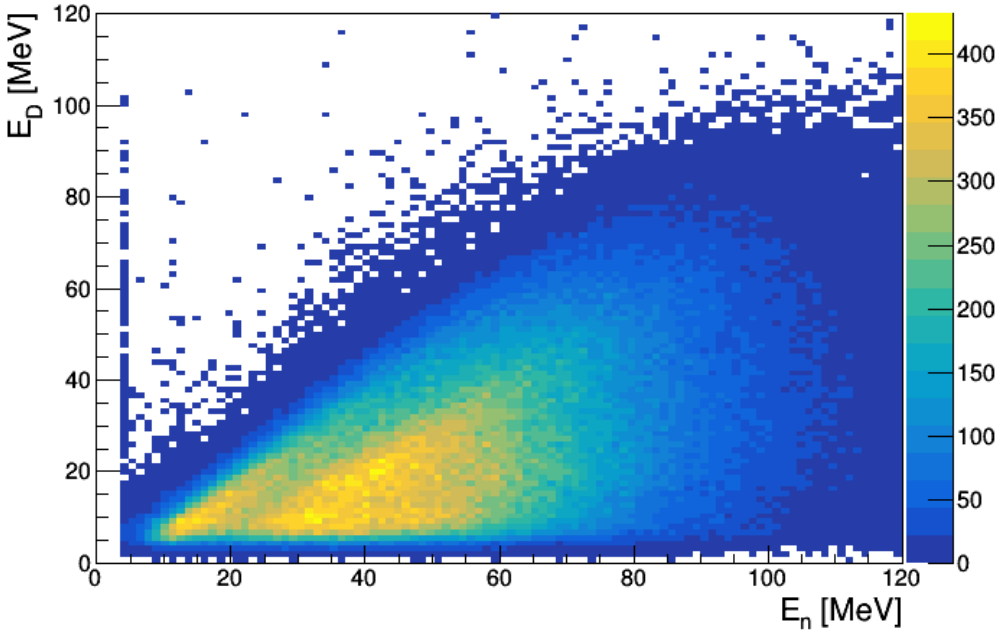

Figure 4.23: Neutron energy reconstructed from light generated in E hodoscope (E_D) vs. time-of-flight method (E_n).

strongly depend on TDC information this time it was necessary to do this for the E detector. The used LeCroy's TDC 3377 modules measured the time difference between individual hits

and common triggering signal with high precision and do not need calibration itself. Since the signals from different detector channels are used in the analysis, all kinds of delays resulting from the difference in cables, or electronics path lengths or electronic thresholds (time walk effect), for different detector channels, affect the time reading. These delays were identified by a common name τ^i in Eqs. 4.14 or 4.15.

In order to reach ultimate precision it was necessary to determine them and correct accordingly. This has been accomplished using events with two coincident protons. For such events momenta of both particles were reconstructed with maximum accuracy provided by the BINA setup. This allowed us to determine trajectories, positions and energies. Comparing it with the values reconstructed by the TDC method allowed to determine a set of necessary corrections for all E-detector elements. The calibration was performed in two steps. In the firsts step a relative calibration of left and right channels, for each E-segment separately, was carried out. Then, a global calibration between the different segments of the E detector was performed.

Correction for single E segment

To find the difference between the left and right offsets τ^i_{L-R} the precise proton position obtained from MWPC, x_C was used and compared with the independent TDC-based position x_T from Eq. 4.14. Then the τ^i_{L-R} was found in a way to reduce the difference between those positions to zero. The obtained corrections are presented in App. B.1 and were used in the final analysis. The effect of this correction is shown in Fig. 4.24.

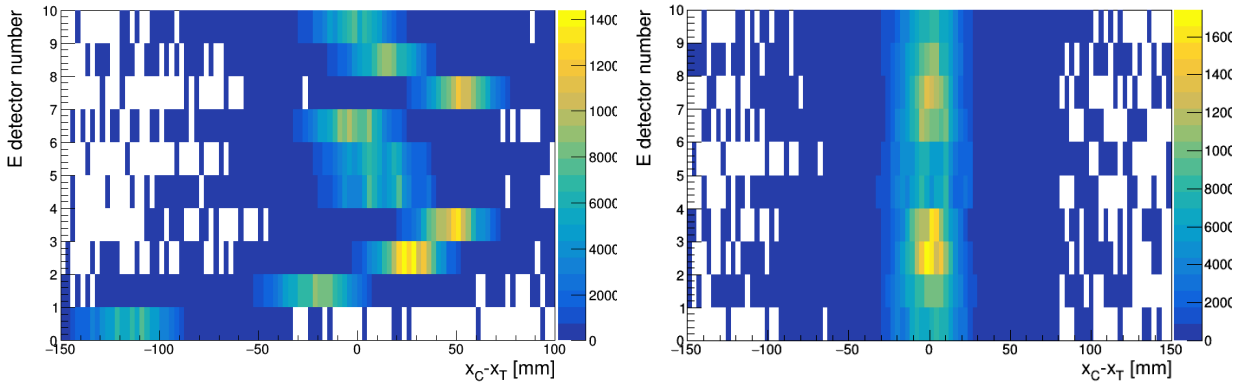

Figure 4.24: *Left panel:* The difference between the x-position for protons, obtained with the use of MWPC information and TDC method, for each of the E detector segment. *Right panel:* The same as on the left panel but after applying the corrections for τ^i_{L-R} offsets.

Global time correction for E detector

In the case of TOF measurement, the correction factors $\tau^{i,j} = \frac{\tau^i_{L+R} - \tau^j_{L+R}}{2}$ between different modules were needed. In order to find them we again have used events with two protons from which the first one was used to get the reaction time, while for the second we calculated its energy from TOF method. In a similar way as in the previous case, the corrections were obtained by minimizing the difference between the energy of the second proton obtained from the time-of-flight (E_T) and from standard energy calibration method (E). The effect of global correction factor can be seen in the Fig 4.25. The obtained $\tau^{i,j}$ corrections can be found in App. B.2.

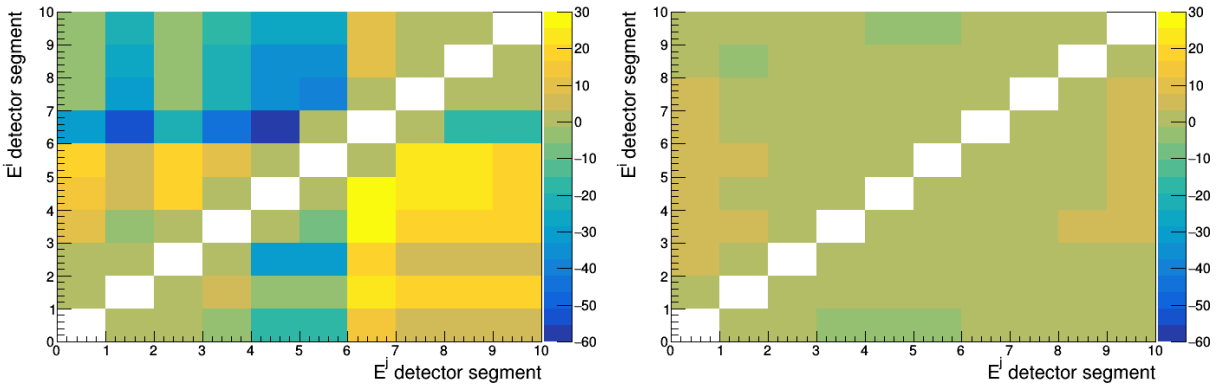

Figure 4.25: The mean difference between TOF-based energy E_T and standard calibration E, presented for all combinations (i, j) of E detector segments, before (left panel) and after applying the $\tau^{i,j}$ corrections (right panel). Observed differences are reduced by a factor of ten.

4.4.4 Proton energy calibration correction

Comparing obtained events distributions around corresponding kinematical curves a strong hints have been observed indicating that the method described above leads to an underestimation of the neutron energy, especially for higher-energy neutrons. Such neutrons are produced predominantly in coincidence with low-energy protons. Fig. 4.26, left panel, shows an example of angular configuration for which a clear deviation from the kinematical curve is visible at the lowest values of the proton energy. Such a behavior is caused by systematic shift in energy calibration of protons. Since calibration data with degraders for low-energy protons were not available, the energy calibration in this region is entirely based on extrapolation. A small change of this calibration, insignificant from the point of view of the proton-proton coincidence analysis, significantly affects the obtained time of flight of the neutron and thus its energy.

To correct for this effect, a simple linear correction was applied to the energy E_p of the registered protons:

$$E_p^{\mathrm{cor}} = \begin{cases} E_p - 0.075 \cdot E_p + 4.5 & \text{for } E_p \leq 60 \text{ MeV} \\ E_p & \text{for } E_p > 60 \text{ MeV} \end{cases} \tag{4.25}$$

The correction increase of about 10% the lowest registered proton energies and does not change the proton energies above 60 MeV. As can be seen in Fig. 4.26, right panel, after applying the correction, the events at the lowest proton energies follow the kinematics. The area between the red and green lines represents the rough estimate of the expected experimental smearing due to the angular bin widths (see Sec. 5.1) and the TDC resolution (0.5 ns). After applying the correction, the obtained events are within the expected limits. Although quite simple in form, this experimental calibration correction works well properly for all tested angular configurations.

4.4.5 Efficiency of the neutron detection

As it was pointed out in Sec. 4.1.4, one of the most important steps in the cross section evaluation is the determination of the detection efficiency. Neutron interacts with the nuclei in the material almost exclusively via hadronic processes. This leads to significantly lower detection efficiency compared to charged particles. The efficiency depends strongly on the

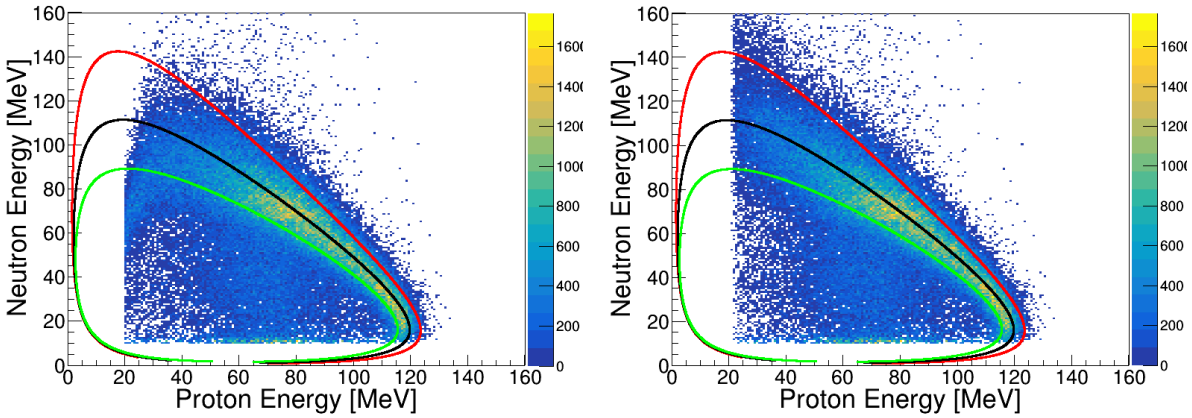

Figure 4.26: E_p vs. E_n energy spectra of proton-neutron pairs, without (*left panel*) and with (*right panel*) the proton calibration correction. The kinematical curve is shown as a black line, while the red and green lines limit the expected smearing of the breakup events.

detector geometry (this effect scales mainly with the neutron path length inside the detector volume), the atomic composition of the material and the neutron energy. In this section we will describe two approaches for the determination of the neutron detection efficiency. The first method is based on the Monte-Carlo simulations and the second one was developed with the use of the experimental data.

Efficiency from the simulation

The detection efficiency of neutrons can be estimated using the Geant4 simulations. For this goal, a dedicated geometry has been implemented in Geant4, consisting only of the thick E detectors and thin ΔE detectors. For each simulated event, one neutron is generated at the target position, with a given kinetic energy and at various angles with respect to the E - ΔE system. In order to simulate the interaction of neutrons as accurately as possible, a very good knowledge of the material used is needed. As a detector material a polyvinylotoluene organic compound, with the atomic ratio of H:C 1:1.1 has been used. This material was selected to imitate the chemical composition and density of the Bicron-408 scintillator. Neutrons can interact with it via many different reactions, predominantly elastic and inelastic processes with nuclei. The primary neutron deposits a portion of its initial energy, mainly in a single hadronic interaction in the scintillator. Such interaction may create many particles, predominantly neutrons, protons and delta electrons, but also recoil nuclei, deuterons, alphas and other light particles. In Fig. 4.28 the particles multiplicities produced in the scintillator are shown. These secondary particles travel through the material, further interact and deposit their energy. In a real situation, the deposited energy in scintillator is emitted in a form of visual and near-UV photons. The amount of produced light is specific for a given scintillator type and strongly depends on particle type and its energy [93]. For strongly ionizing particles (alphas, etc.) a saturation (quenching) effect, which leads to the reduction of photon yield, must be taken into account. When the signal exceeds certain threshold level, the readout electronics records hit in the detector. In the case of our simulations, the light production and transfer through the scintillator has not been modeled. Only a quenching effect was introduced into the simulations, which modifies the amount of light generation from the deposited energy. The quenching effects was parameterized by a set of particle and energy dependent functions, presented in Fig. 4.27.

The absolute value of the electronical threshold (defining the energy threshold) is not

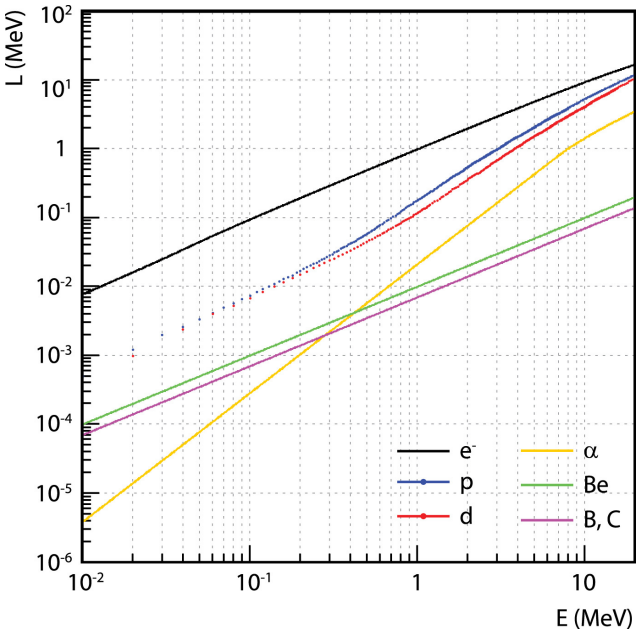

Figure 4.27: Quenching factor for a few particles and light nuclei in a function of their kinetic energy. Figure adapted from [93].

known. In the experiment it was set manually in a relative units of CFD[2] range, during the preparation phase of the experiment for each photomultiplier separately to reduce electronic noise as much as possible without affecting the efficiency for a real particles. From the off-line analysis of the experimental data we know, that the energy threshold for proton detection was about 20 MeV (initial energy). This value corresponds to the energy deposition in the E detector of about 8 MeV, what was established based on the simulations (see Fig. 4.29, right panel). This energy was used as an effective threshold in the simulations. When the total deposited energy, corrected by a quenching factor, in a given E detector segment, exceeded this threshold, the event was counted as detected. In the opposite case we assumed that the detector was inefficient.

It frequently happens that some of secondary particles leave the detector element and hit a neighboring detector segment, which in consequence may create false signals. In order to take into account such process in the simulations, two additional detector segments, one below and one above the investigated segment, have been added in simulations, see Fig. 4.29. The top and bottom E scintillators act as a veto detectors for the middle E slab, while ΔE positioned in front of the E detector is used to registered backscattered particles. The central E detector was illuminated perpendicularly with neutrons, so that each generated particle saw the same effective thickness of the scintillator. When a secondary particle entered one of veto detectors and deposited enough energy to exceed threshold level in it (so-called cross-talk event in a real experiment), such an event was rejected from the analysis, by analogy to the conditions applied for the experimental data.

The Geant4 framework offers a variety of interaction models. It constitute a suitbale tool for modeling and simulating neutron interaction within the energy range used in this experiment. Many authors have reported on its excellent accuracy in the simulation of neutron interaction with plastic scintillators at the intermediate energy [93]. Although end-user can freely combine different models, appropriate for his application, the Geant4 provides also the predefined Reference Physics Lists[91]. These lists are well-maintained, tested and recommended by the Geant4 collaboration for the most applications. In our simulations, we

[2]CFD-Constant fraction discriminator

decided to use 2 different physics lists, QBBC[94] and QGSP-BERT-HP[95]. The QGSP-BERT-HP states for quark gluon string model with Bertini Cascade model and high precision neutron model. QBBC model is recommended for medical and space physics simulations, where accurate simulation for low-energy (below 1 GeV) transport of protons and neutrons is needed. QBBC got its name from QGSC, Binary cascade, Bertini cascade and CHIPS models.

The simulation was performed with the monoenergetic neutrons, for several energies from 10 to 160 MeV. For each of those energies, 1 million events was generated. The obtained efficiency is presented in Fig. 4.30. Each line represents a different value of energy threshold. For comparison, the efficiency calculated from the experimental data (see Sec. 4.4.5) is also included. The obtained values for various interaction models differ quite significantly from each other. It is especially visible for higher energies, where the threshold value does not significantly influence the efficiency. Nevertheless, the results of the simulation as well as the efficiency known from the other experiments [96] [97] support the obtained experimental efficiency.

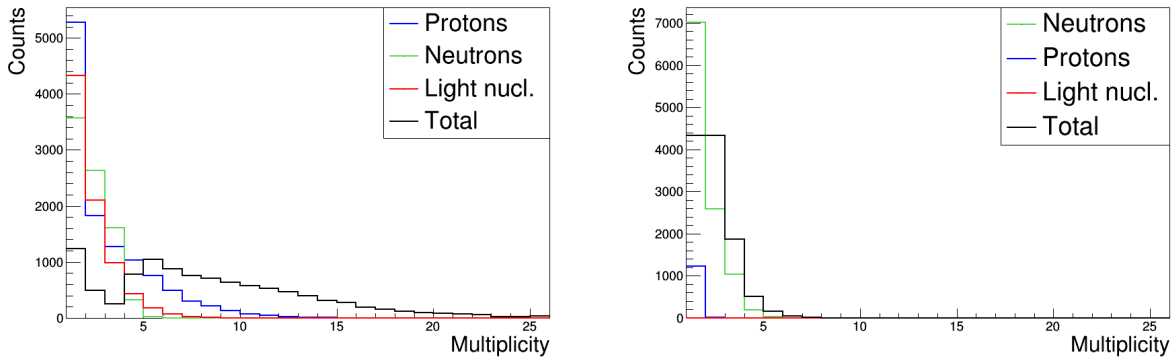

Figure 4.28: *Left Panel*: The multiplicity of secondary particles generated in the scintillating material of the central E detector by neutrons of energy 120 MeV. Different colors represent different particles type, according to the legend presented in figure. *Right Panel*: The same as on the left panel but the multiplicity is presented only for particles leaving the central E detector.

Neutron detection efficiency from the experimental data

The neutron efficiency has also been studied with the experimental data. A measurement of energies and scattering angles of the two breakup protons in the Forward Wall detector provides complete information on the kinematics of the reaction, as it was shown in 2.1.3. This allows to calculate, using the momentum and energy conservation laws, the direction and energy of the remaining neutron. Having these values, one can find how many of the neutrons which were emitted towards E-hodoscope actually produced detectable signals in this detector. Neutron detection efficiency ϵ_n can be expressed as a simple ratio of the number (N_{reg}) of neutrons which were registered in the E detector to the number of all neutrons (N_{tot}) incident in the same detector area, calculated based on information from the two coincident protons:

$$\epsilon_n = \frac{N_{reg}}{N_{tot}}. \tag{4.26}$$

From the whole data sample, a subset has been selected according to the following criteria:

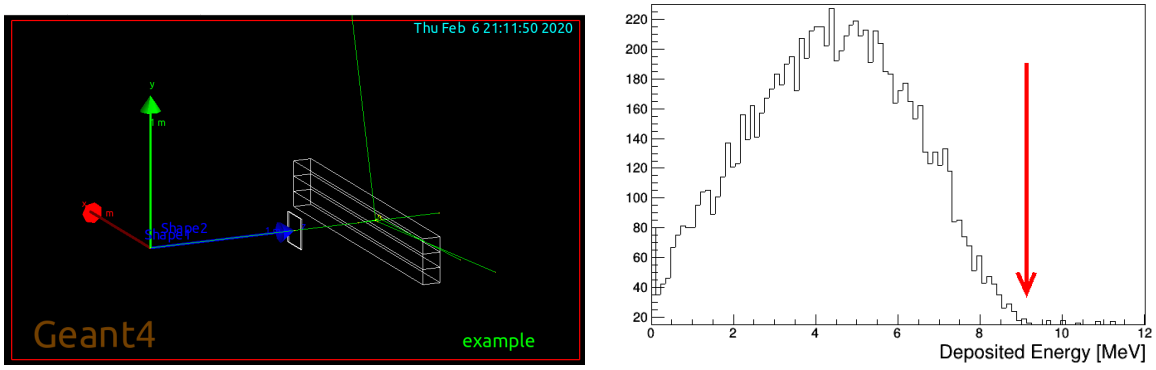

Figure 4.29: *Left panel:* Scheme of geometry used in the Monte-Carlo simulations of the neutron detection efficiency of the E detector. Three scintillator bars are placed one on another as in the experiment. The central one is being irradiated by the neutrons. In front of the segments the scintillator imitating ΔE detector is placed. Green lines represent neutrons, hardly visible yellow and red lines corresponds to electrons and protons or light nuclei, respectively. *Right panel:* Simulated deposited energy in one E detector segment by protons with the initial kinetic energy lower than 20 MeV (full BINA setup simulations). Energy of 20 MeV for protons corresponds to the lowest observed in experimental setup. The maximal value of their deposited energy (indicated by an arrow) corresponds to the effective threshold applied by the discriminators.

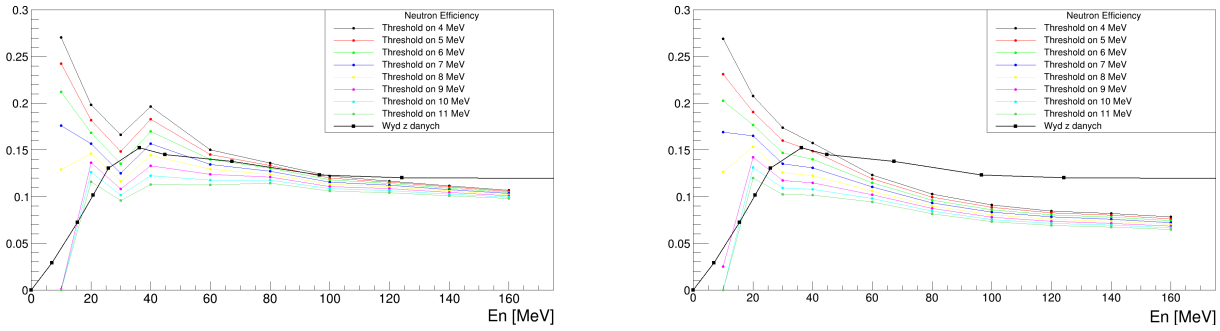

Figure 4.30: *Left panel:* The efficiency of the neutron detection in the BINA detector as a function of the neutron energy. The color lines and dots represent the simulated efficiency, with different threshold parameter, based on the QBBC model. Black line and squares are the efficiency calculated from the experimental data. *Right panel:* The same as on the left but based on QGSP-BERT-HP physics list.

- two tracks found in MWPC, both with all of three detection planes being activated (strong track, see 4.1.1),
- corresponding hits in E and ΔE hodoscopes, matching these tracks, were found,
- both tracks identified as protons,
- no additional hits in ΔE or MWPC - veto condition,
- neutron reconstructed with the use of the breakup kinematics, points to a selected E hodoscope segment,

- separation of at least one not activated scintillator element must be provided between selected segment and elements which detected both protons.

The above conditions allow to identify events of the 3-body breakup for which all three particles can be detected by Forward Wall. As it was mentioned at the beginning of Sec. 4.4, the gap between E segment prevents from counting cross-talks between the elements. The calculated neutron detection efficiency depends on various quantities, like the neutron energy, position in the detector or scintillator thickness, which will be discussed in a following sections.

To check the above neutron identification method the missing mass technique has been used. In Fig. 4.31 the obtained missing mass spectra for proton-proton and proton-neutron pairs are presented. As can be clearly seen the peaks correspond to the rest masses of the neutron (red line) and the proton (blue line) respectively. On an average both proton and neutron masses are very well reproduced what enhances our confidence in energy and position reconstruction of both: protons and neutrons in the BINA detector. It is also clear that the method of determining the position and energy of the neutrons, which was described in detail in the previous sections, offers overall worse resolution than methods used for charged particles. Therefore, the proton-proton missing mas is much better reconstructed than the missing mas of the neutron-proton pair (corresponding red peak is narrower and imposed on a smaller background than the blue one).

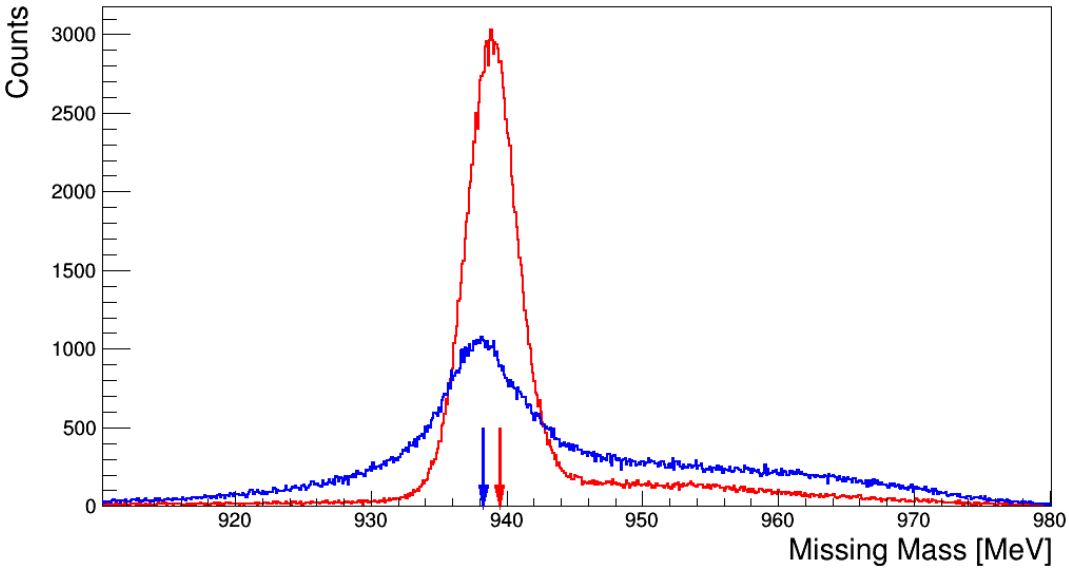

Figure 4.31: Missing mass spectrum of events used for determination of the neutron detection efficiency. The blue distribution represents the spectrum of proton-neutron missing mass, while the red one missing mass for the proton-proton pair. Neutron (939,56 MeV) and proton (938,27 MeV) rest mass were correctly reconstructed (as marked by the red and blue arrow respectively).

Efficiency as a function of the neutron energy

Since the cross section for neutron interaction with a matter depends strongly on its energy one may expect such dependence also for the neutron detection efficiency. As it is know from the previous studies, the cross section for fast and ultrafast neutrons (above few MeV)

should steadily decrease with rising energy. On the other hand, the cross sections for low-energy neutrons exhibits more complex structure associated with a large number of possible inelastic processes. Another very important aspect influencing the efficiency is related to the detector geometry and its readout electronics. After initial interaction with the detector material, neutron usually escapes from the active volume of detector, leaving only portion of its kinetic energy in collisions with medium. Part of it is further lost for production of secondary neutrons or photons, which again may escape from the detector. The deposited energy must be large enough to ensure, that despite the loss of photons due to inefficient light collection and attenuation, the signal from the photomultipliers exceeds the threshold for detection. This leads to a significant decrease in the efficiency for low energy neutrons.

The efficiency obtained in this analysis as a function of the neutron energy is shown in Fig. 4.32. The distribution clearly shows expected significant drop of efficiency for low neutron energy. In average the obtained efficiency is $\epsilon_N = 11.0 \pm 0.1\%$. This value is also in agreement with simulations made for previous BINA experiments [17] and other experimental results [97].

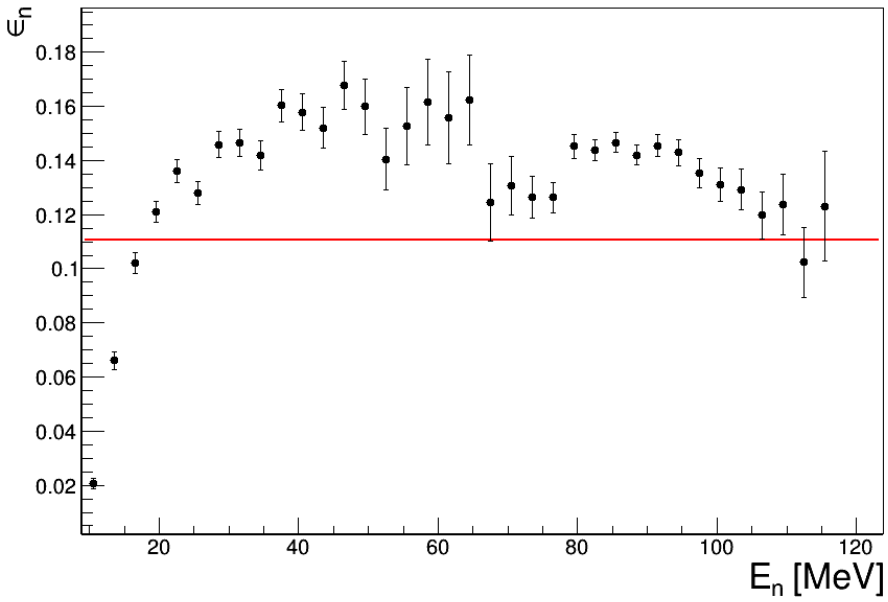

Figure 4.32: Neutron detection efficiency of the BINA detector as a function of the neutron energy.

Efficiency as a function of scintillator thickness

Another important parameter that may have impact on neutron detection efficiency is the detector thickness. As described in Sec. 3, the central part of the E hodoscope is built in a cylindrical geometry and, as a consequence, the path length inside the scintillator for particles emitted from the target depends mostly on the horizontal x coordinates of its trajectory. This effective thickness d can easily be calculated according to the following formula (see also Fig. 4.33):

$$d = d_0 \cdot \sqrt{\frac{x^2 + y^2 + z_0^2}{y^2 + z_0^2}}, \tag{4.27}$$

where x and y are coordinates of intersection of particle's trajectory and the middle MWPC plane, and z_0 is the distance between this plane and the target center. Value $d_0 = 120mm$ is

the nominal thickness of the E scintillator. For this analysis only the neutrons with energies from 60 to 100 MeV were selected. The calculated efficiency shows only slight dependence on the scintillator thickness as expected in the very narrow range of this parameter (Fig. 4.33, right panel). On average the obtained efficiency for the selected neutron sample was $\epsilon_n = 12 \pm 1\%$.

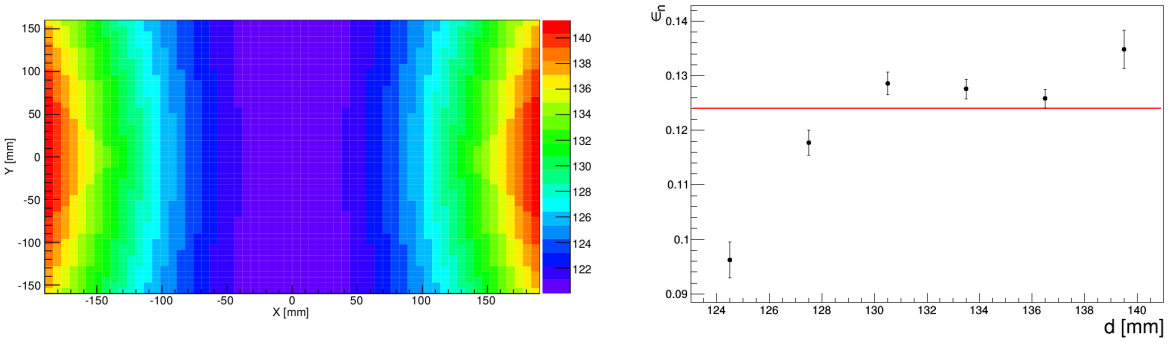

Figure 4.33: *Left panel*: Effective thickness of the E scintillator seen by a particle. *Right panel*: The neutron detection efficiency of the BINA detector as a function of scintillator thickness.

4.4.6 Comparison with the data

The techniques for the position and energy reconstruction of a neutron (see Sec. 4.4.1 and 4.4.2) can be verified using the events with all three particles registered in the Forward Wall detector. Such events have can not be used to determine the cross sections because they have been used to find the efficiency for neutron detection (Sec. 4.4.5). As it was mentioned before, detection of both protons from the breakup reaction allows for the determination of the missing momentum of neutron, which can be used to obtain the position x_{calc} and the energy E_{calc} of the neutron. These values can be compared with those obtained by the neutron detection methods described earlier. Such a comparison is presented in Figs. 4.34 and 4.35 for neutron energy and position, respectively. Both distributions (right panels) reach a maximum near zero, which proves the correctness of the energy and position reconstruction. The obtained width at half maximum is equal to 10.67 MeV for the energy reconstruction and $\sigma = 22.8mm$ for the position reconstruction. As it turned out both, the position and energy reconstruction are worse than obtained for protons, 20% larger for energy and 94% larger for position.

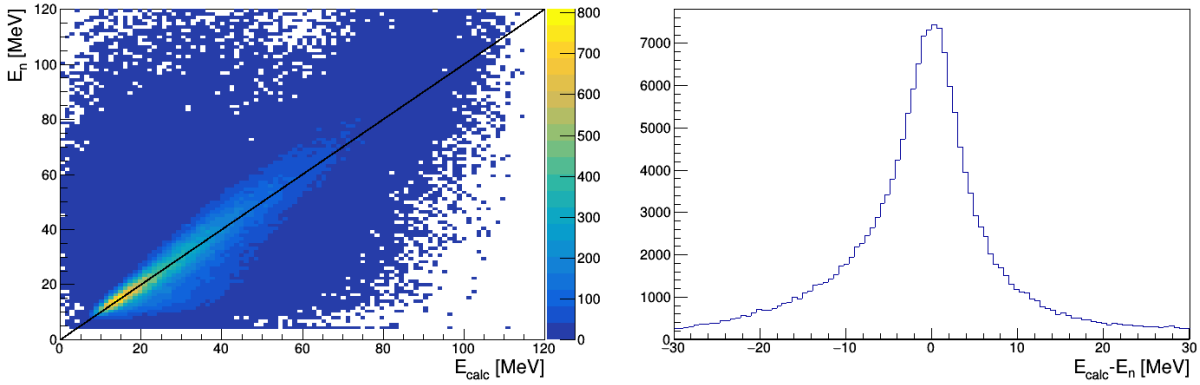

Figure 4.34: *Left panel:* The neutron energy obtained from the TOF method (E_n) versus the energy calculated from the momenta of the two protons by the missing momentum method (E_{calc}). *Right panel:* Distribution of the differences between E_n and E_{calc}.

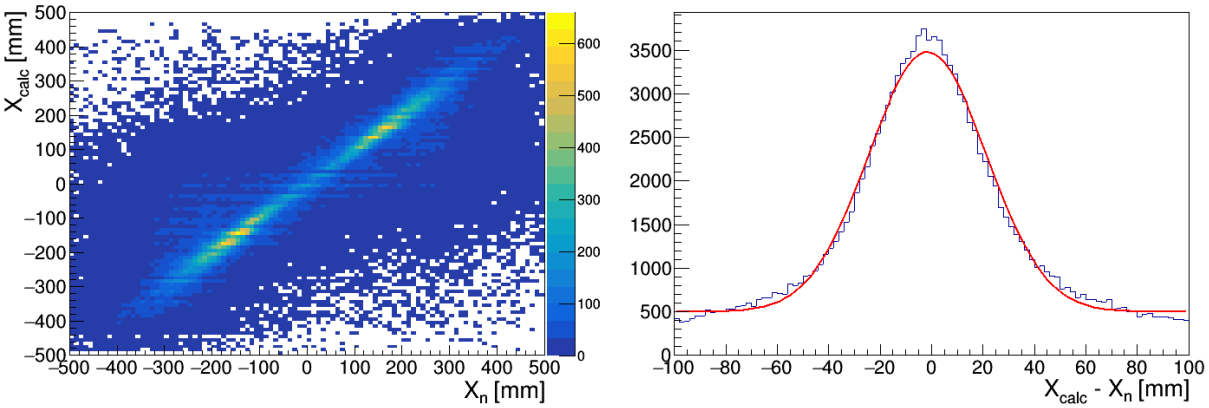

Figure 4.35: *Left panel:* The neutron horizontal x-coordinate registered in the detector (x_n) versus the position calculated from the momenta of the two protons the by missing momentum method (x_{calc}). *Right panel:* Distribution of the differences between x_n and x_{calc}.

4.5 Configurational efficiency

The configurational efficiency account for the influence of the geometrical acceptance on the detection of two coincident particles in the BINA setup. The analysis presented in this thesis is focused on detection of proton-neutron coincidences. If two or more particles hit the same active channel of the detector (the same E-detector slab, ΔE-detector strip or MWPC wire), neither position nor energy can be properly reconstructed and in consequence such event was removed from the analysis. It is clear that the probability of such situation depends strongly on relative configuration of trajectories of both particles with respect to each other and to the detector. In order to reconstruct the actual number of coincidences it was necessary to account for this effect, which in the following sections will be referred to as the configurational efficiency $\epsilon_C(\xi, S)$. Combined together with a single particle detection efficiency $\epsilon_{p,n}(\theta, \phi, E)$ it creates total efficiency for the breakup event detection:

$$\epsilon_{\mathrm{tot}}(\xi, S) = \epsilon_p(\theta_p, \phi_p, E_p) \cdot \epsilon_n(\theta_n, \phi_n, E_n) \cdot \epsilon_C(\xi, S). \tag{4.28}$$

The analysis was performed separately for two cases, one for the charged particles coincidences and the other for the proton-neutron coincidences. Since the configurational efficiency strongly depends on the emission angles of both particles and complicated geometry of the detector, the GEANT4 based simulations of the detector were used for its determination (Sec. 4.3). The ability to generate a large statistics of events for all available phase-space configurations allowed us to reduce the statistical uncertainties to minimum, thus the only significant uncertainties may follow from the inaccuracies of the simulated experimental setup.

4.5.1 Configurational efficiency for charged particles

Procedures applied for calculation of the configurational efficiency for two charged particles were developed for the previous analyses of ^{1}H(d,pp)n [78, 99] and ^{2}H(d,dp)n [82, 100] breakup reactions. Proper registration of a pair of protons required signals from two separate elements of the E detector, two signals in ΔE and two reconstructed hits in MWPC. If two or more particles hit the same E detector segment, information about their individual energies is lost. Similar situation occurs for the ΔE detector - in this case affected is the information about specific energy loss of particle, which precludes their proper identification as proton or deuteron. The configurational efficiency is calculated for each of angular configuration separately, as a ratio of the number of events which fulfill the above conditions to the total number of simulated events. The obtained results for four sample θ_1, θ_2 combinations are presented as a function of the $\Delta\phi_{12}$ angle in Fig. 4.36.

A noticeable local minima can be observed, which reflect the geometrical structure of the E detector. For a coplanar events, in which the $\Delta\phi_{12}$ is close to 180°, only a small portion of events, emitted very close to the horizontal plane, have a chance to hit the same E scintillator. As expected, the efficiency generally rises with the $\Delta\phi_{12}$ angle, as it becomes less likely that both particles hit the same E detector. In the case of ΔE detector, effects of the configurational efficiency are not so much pronounced. The granularity of the detector is more than twice larger and the individual segments cover only half of the length of the entire detector, however, the effect may still be visible, especially in the range of low $\Delta\phi_{12}$.

The same effects can also be observed for the multiwire proportional chamber. Due to much finer granularity of the MWPC corresponding inefficiency is even smaller than for the ΔE hodoscope. During their movement through the MWPC, particle can produce signal in two or even more neighboring channels in the same detection plane. The readout electronics

interprets this as a cluster. When the clusters created by two particles overlap, the electronics cannot separate these particles. Such events were rejected from the analysis. The wires which passed through the center of the chamber, where the hole for the beamline was located, were separated. This cause that each side of the chamber form different detection channels and clusters created by coplanar events practically have no possibility to overlap. The sample of configurational efficiency obtained for pairs of two protons, accounting for different detectors, are presented in Fig. 4.36.

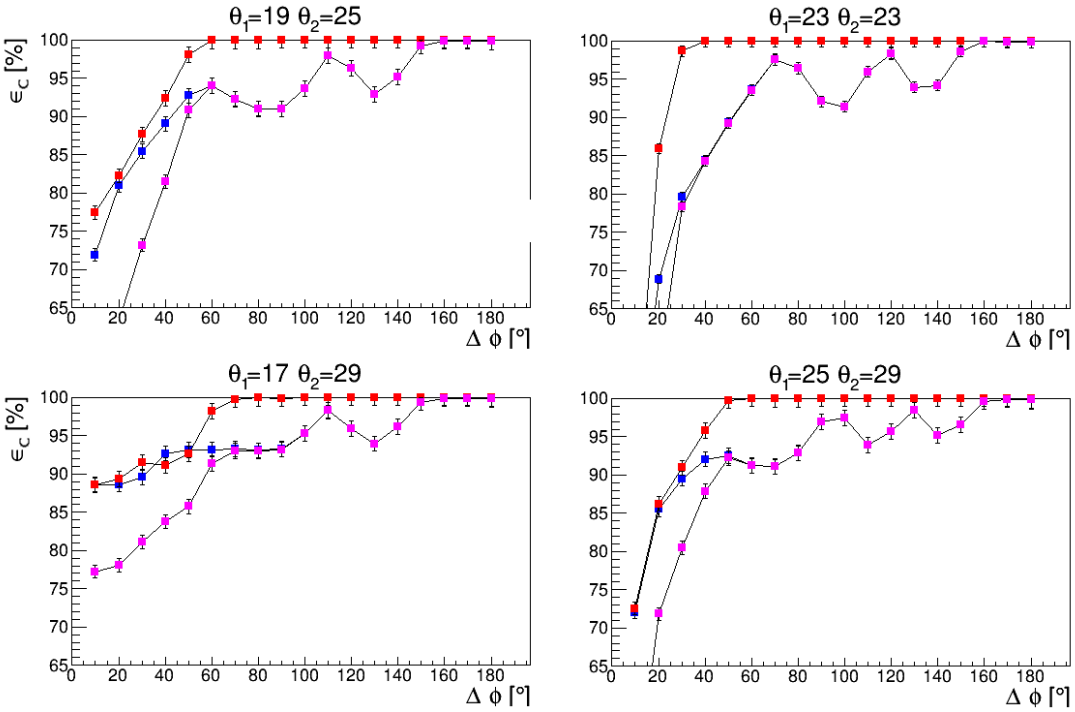

Figure 4.36: Configurational efficiency for the two protons from the breakup reaction as a function of $\Delta\phi$, for selected angular configurations. The efficiency has been calculated separately for the E and ΔE detectors, blue and red points, respectively. <Magenta points refer to the total efficiency.

In the case of ^{1}H(d,pp)n reaction there are three particles in the exit channel. The existence of unobserved neutron has been neglected in all previous analysis. This has been motivated by small interaction probability of neutrons with the detectors. While this is true for ΔE and MWPC, in the case of thick E detector for selected configurations associated effects could reach up to about 10% of calculated configurational efficiency.

4.5.2 Configurational efficiency for neutrons

Configurational efficiency for events with the neutron-proton pair detection is conceptually similar to that for events with two charged particles. However, there are also very significant differences, making its influence much more important and difficult to comprehend. Unlike in the case of configurational efficiency for the two charged particles, the neutrons practically do not interact with neither the MWPC nor the ΔE. Therefore, any inefficiency which may come from these detectors are negligible and only the E detector was responsible for all the effects associated with this efficiency. Even if this particular effect increases the efficiency, additional requirements, necessary for neutron identification, by far surpass this gain.

Detection of a single charged particle in the E hodoscope in some cases leads to the production of pulses in two neighboring scintillator segments. Probability of such events,

called cross-talks, increases for particles hitting a segment close to its edge, They can also be produced by light leaking between photomultipliers at both ends of the scintillators. Though this problem has been corrected for in BINA detector installation at CCB, for data collected at KVI it was not negligible and would greatly disturb analysis of neutron data. In order to suppress misidentification of such cross-talks with neutron interaction we set very stringent condition of separation by at least one inactive E segment between detected p-n pairs. Such requirement eliminates this problem, but significantly diminish configurational efficiency.

Another important ingredient in the $p-n$ configurational efficiency comes from the effect connected with the veto condition used for neutron identification. As explained in Sec. 4.4, the veto was applied to reject events in which the third particle from the reaction (proton), hits the active area of the Forward Wall detector. If the third particle (which should not be observed) was emitted towards the Forward Wall, the event should be rejected from the analysis[3]. This reduces the available phase space considerably. Since the position of the third particle strictly depends on the position and energy of the two detected particles, for a given angular configuration ξ, the configurational efficiency for proton-neutron coincidences has to additionally depend on the S variable, the arc-length along the kinematics.

To include these conditions as accurate as possible, the full phase space of the breakup reaction with all three particles is taken into account in the simulations. This allowed us to determine the areas available for our detection method, to calculate associated efficiency and identify regions where it changes rapidly. Fig. 4.37 presents a sample of obtained configurational efficiency with clear dependence on the S-variable. Since the configurational efficiency was based on the Monte Carlo simulations, its uncertainties can be calculated as:

$$\Delta\epsilon_c(\xi, S) = \sqrt{\left(\frac{\sqrt{N_E}}{N_A}\right)^2 + \left(\frac{\sqrt{N_A}N_E}{N_A^2}\right)^2}, \tag{4.29}$$

where the N_A is the total number of simulated events in a given angular configuration and a given S range, while the N_E is the number of those which fulfilled previously described criteria. As one of the crucial step in the analysis of deuteron breakup reaction, this method has also been described in a separate publication [101].

Simulation smearing

The configurational efficiency for the proton-neutron coincidences is in general much lower than for the proton-proton pairs due to the much more stringent condition.

In order to determine this efficiency, it was necessary to introduce additional energy and position smearing into the simulations, which originate from a finite detector resolution. Such smearings are not caused by the physics of interaction, but rather by detector readout response and the analysis methods specific for neutron reconstruction.

Based on the experimental data the distributions of the reconstructed neutron position and energy have been included into the simulations. The obtained neutron horizontal x position distribution is characterized by a relatively low resolution as compared to the one for charged particles. In addition, it exhibits a semi-discrete behavior, caused by the finite resolution of TDC information, as can be observed in Fig. 4.24. The vertical y coordinate is given by the center of the E detector and is limited to only 10 positions, according to E detector number. Relatively large smearing of the obtained x and y neutron positions affects the obtained azimuthal and polar angles. This smearing can cause an event migration between adjacent angular configurations.

[3]These events, however, have been used for neutron detection efficiency calculation (Sec. 4.4.5)

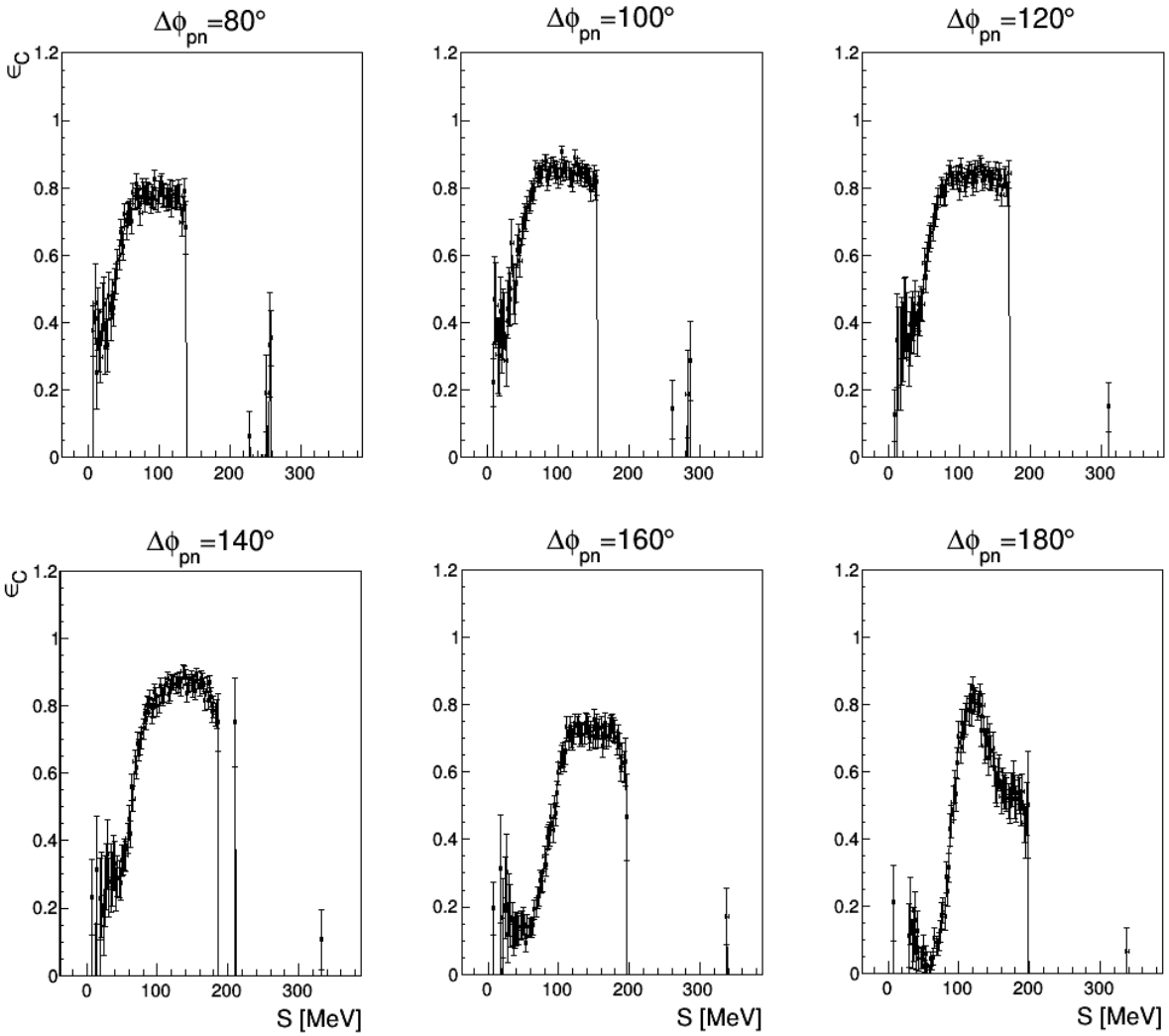

Figure 4.37: The configurational efficiency for proton-neutron coincidences, for the angular configuration of $\theta_p = 23°$, $\theta_n = 27°$ and for 6 relatives azimuthal angles of $\Delta\phi_{pn}$ specified in the figure, as a function of the S variable.

To obtain the energy smearing for the neutron, the experimental data with proton-proton coincidences were used. As a smearing factor, the resolution of time-of-flight method (Fig. 4.22, panel c) was applied. The energy threshold for protons prevents from calculating the smearing factors below 20 MeV. However, neutrons can be observed down to about 5 MeV. Also, above 120 MeV only very few protons can be observed what results in large statistical errors of the smearing factor. Therefore the smearing factor has been extrapolated in these two energy regions.

In the case of protons only the smearing of the kinetic energy has been introduced. It follows from the accuracy of the calibration procedure. Based on the elastically scattered protons, the energy smearing was found to be $\sim 2.1\%$, see Sec. 4.1.2. The angular resolution is quite accurate as the angles are reconstructed with MWPC. As shown in Sec. 4.1.1, it amounts to about 0.4° for polar angle and 0.67° - 1.39° for azimuthal angle.

After applying the position and energy smearing to the simulations, it was possible to reliably calculate the configurational efficiency $\epsilon_C(\xi, S)$ and to compare the experimental data to the simulations. As an example a few kinematical distributions are presented in Fig. 4.38. As one can notice, without the use of smearing, the width of the distributions along the kinematic curve obtained from the simulated data are much narrower than obtained directly

from experimental data. Only the simulations with the smearing included reproduce the experimental distributions reasonably well.

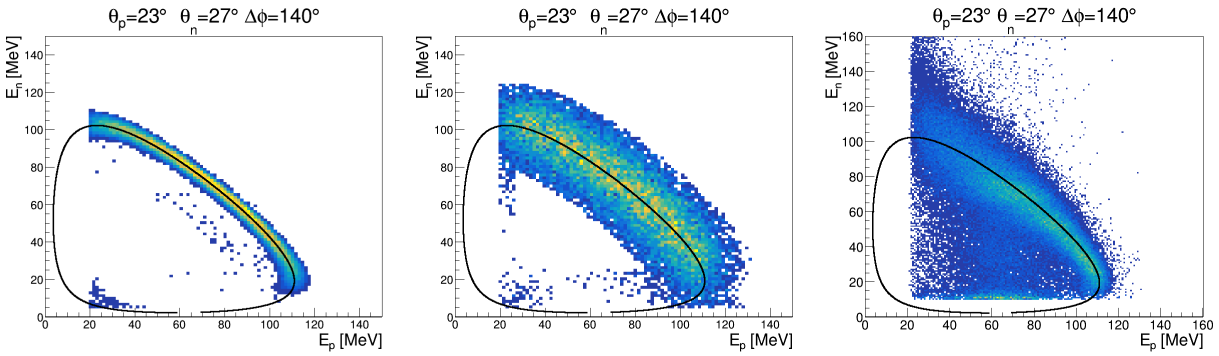

Figure 4.38: Correlation between proton and neutron energies obtained from the Monte-Carlo simulations with and without realistic smearing (middle and left panels), compared to the experimental distribution (right panel) for the same angular configuration of $\theta_p = 23°$, $\theta_n = 27°$, $\Delta\phi_{pn} = 140°$.

Chapter 5

Breakup reaction analysis

5.1 Averaging of the theoretical cross sections

Due to a limited resolution of the detection system, the experimental cross sections are obtained with a certain angular range around the central angular configuration. The width of the angular bin was $\delta\theta = 4°$ for polar angles (θ_p, θ_n) and $\delta\phi = 20°$ for relative azimuthal angle $\Delta\phi_{pn}$. Since the theoretical calculations vary significantly within the chosen angular bin (see Fig. 5.1), it was necessary to account for this effect by averaging of the theoretical cross section. In addition to the cross section calculated for the central configuration, the cross sections have also been calculated for all combinations of angles ($\theta_p^c \pm \delta\theta/2$, $\theta_n^c \pm \delta\theta/2$ and $\Delta\phi_{pn}^c \pm \delta\phi/2$). Each of the configurations is characterized by a different kinematic curve (see Sec. 2.1.3) therefore the cross sections were all projected onto a common, central relativistic kinematics. For each step in the S variable, the weighted average of contributing theoretical cross sections was calculated with the weight being the solid angle of each individual configurations. The obtained averaged theoretical cross sections were later used to compare with the experimental results.

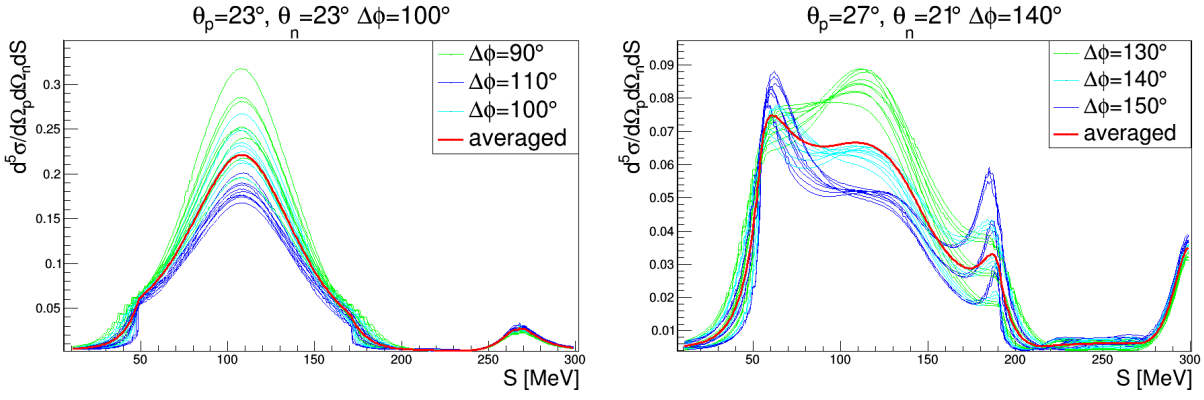

Figure 5.1: Figures present the theoretical 5-fold differential cross section based on the CDB+Δ+C model. All presented theoretical curves are within the averaging limits of the chosen angular configurations described in the picture. Lines marked in green, cyan and blue color refer to different $\Delta\phi$ angle. The thick red lines represent the result of the averaging procedure.

5.2 Differential cross section for deuteron breakup reaction

The main goal of this dissertation was to find experimental differential cross sections for ^{1}H(d,pn)p reaction. For this purpose, the proton-neutron coincidences were identified. The events have been sorted according to their angular configuration ξ. Polar angles ranged from 19° to 27° with step of 4 degrees while the relative azimuthal angles from 80° to 180° every 20 degrees. The obtained data were integrated within the same ranges as defined for the theory averaging. In total, 54 angular configurations were obtained. This binning has been chosen to keep similar angular grid as used in previous analyses of ^{1}H(d,pp)n breakup reaction [57]. Correctly reconstructed events from the breakup reaction should group along the E_p vs. E_n kinematical curve (black line in Fig. 5.2).

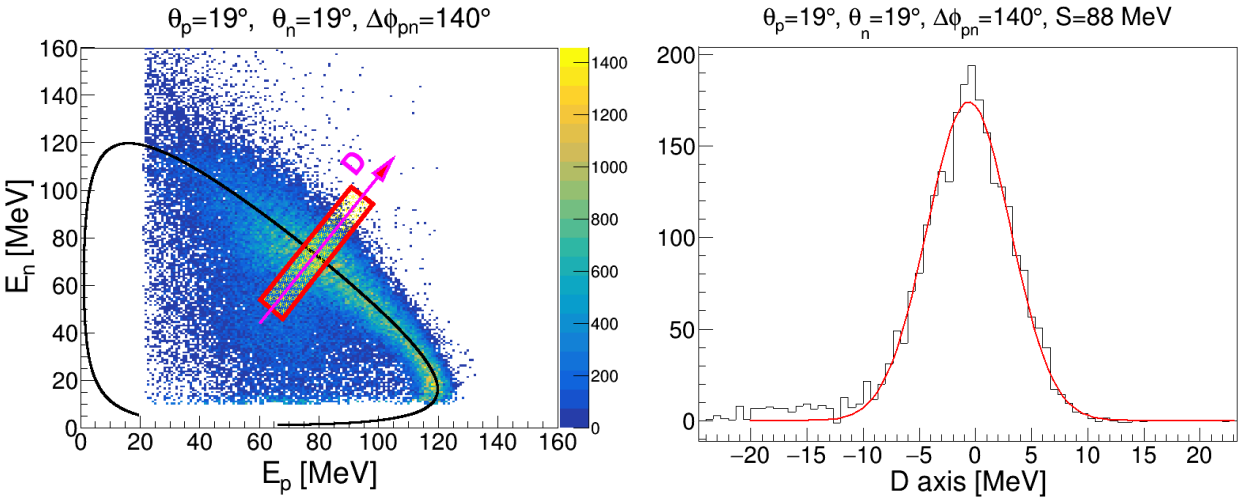

Figure 5.2: *Left panel:* E_n vs. E_p spectrum of the proton-neutron coincidences at $\theta_p = 19°$, $\theta_n = 19°$, $\Delta\phi_{pn} = 140°$ configuration. The solid black line shows kinematical curve calculated for central value of the angular range. The distance from kinematics D and the ΔS bin are presented in a schematic way. *Right panel:* The projection of events corresponding to the same configuration as on the left panel and one S bin onto the D axis with fitted Gaussian distribution.

The kinematical curve was divided along its length into a segments of equal size of $\Delta S = 8$ MeV. For each event, its distance D from the kinematics was calculated, in a way that to the events from inside the kinematics negative D-values were assigned. In the further analysis only events lying within the band of D-values ranging from -40 MeV to 40 MeV were used. For each ΔS segment, a histogram of the D values of the projected events was created as shown in Fig. 5.2. The distribution along D-axis should reach its maximum around zero, which means that the registered events are located centrally around the kinematics and their energy is correctly reconstructed.

For some angular configurations background contribution is quite significant. Since the exact model of background is not known (see discussion in Sec. 5.3), it has been estimated based on the SNIPC algorithm [102]. SNIPC is a tools available in the TSpectrum, a ROOT based library [103]. It allows for modeling of background without making initial assumptions about its nature. After the background subtraction, the Gaussian distribution was fitted to the D distribution. In order to treat all configurations consistently, the obtained Gaussian fit was integrated within the limit of the D variable corresponding to the distance of -3σ to $+3\sigma$ from the maximum of the distribution. The obtained value of the estimated number of

proton-neutron coincidences, N_{pn}, was used to calculate the five-fold differential cross section according to the following formula:

$$\frac{d^5\sigma(\xi,S)}{d\Omega_p d\Omega_n dS} = \frac{N_{pn}(\xi,S)}{L\cdot\epsilon_p(\theta_p,\phi_p,E_p)\cdot\epsilon_n(E_n)\cdot\epsilon_C(\xi,S)\cdot\Delta\Omega_p\cdot\Delta\Omega_n\cdot\Delta S}, \tag{5.1}$$

where L is the luminosity integrated over the measurement time, ϵ_p and ϵ_n account for the total detection efficiencies for protons and neutrons, respectively. The ϵ_C is the configurational efficiency for proton-neutron pairs. The $\Delta\Omega_p$ and $\Delta\Omega_n$ are the proton and neutron solid angles and ΔS is the bin size of the S arc-length. An example of the obtained differential cross-section distributions for one selected configuration of polar angles, together with theoretical calculations is shown in Fig 5.3. For clarity only a few selected models were presented. The results for all configurations are presented in Appendix D.

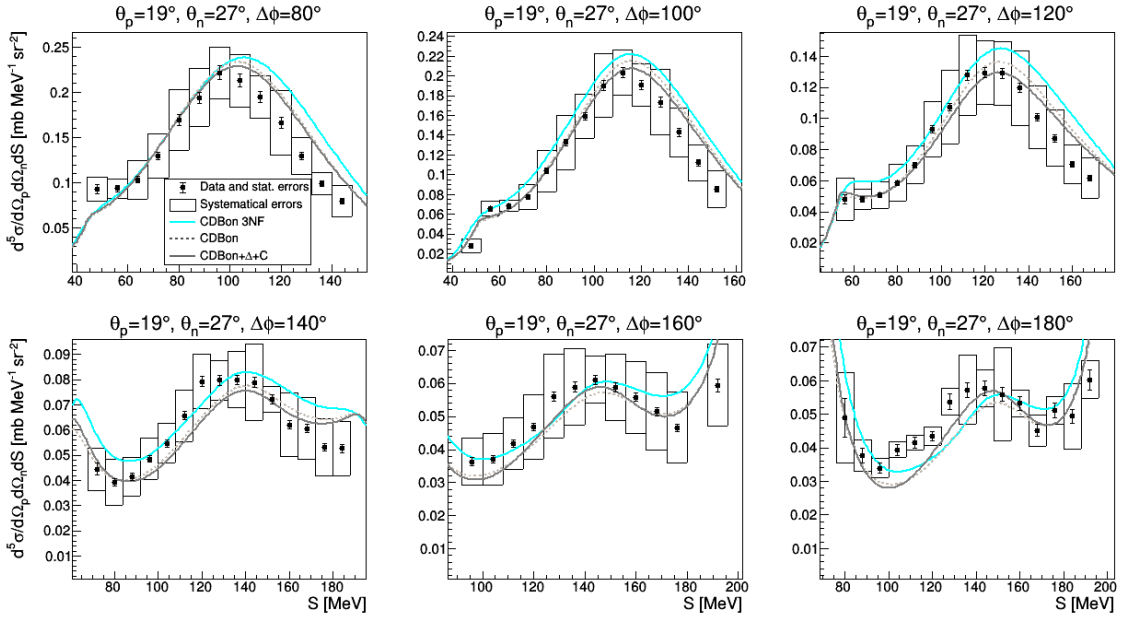

Figure 5.3: An example of the differential cross section distributions for 6 different relative azimuthal angles and a single polar angles configuration, specified in the pictures. The data are plotted together with a few selected theoretical calculations specified in the legend. For each data point statistical (black bars) and systematical (empty box) errors are presented.

5.3 Background estimation

Due to relatively small efficiency of the neutron detection and much smaller precision of measured observables, candidates for proton-neutron coincidences are affected by a much larger background contribution than for the pairs of charged particles. The exact background model is unknown, however, some sources can easily be identified:

- accidental coincidences of one charged particle from the target and any kind of particles produced outside the target - mainly in the beam line and the beam dump,
- accidental coincidences of proton and neutron from two different breakup reactions,
- coincidences of protons and neutrons produced by secondary hadronic interactions of deuterons from elastic scattering, with neutron emission in forward angles.

Veto-based neutron identification presumes that every signal recorded in the E detector in a correct time widow can potentially be classified as a neutron. Such signal can be caused by various particles, for example neutrons and gammas which are a natural background of an operating cyclotron. Even charged particles backscattered from the beamdump or beamline, which can hit the E detector from behind, can bypass the veto. The signals generated by these particles may accidentally be time-correlated with a proton produced in the target.

The second significant background source comes from accidental proton-neutron coincidences. In this case, the registered protons and neutrons come from two different reactions in the target. Particles produced at different time (even from different cyclotron bunches) can still be closely correlated in time due to their different times of flight. They can be accepted by the time gates used in the data analysis and therefore constitute the substantial background source. Such a random background should be distributed relatively uniformly for all angular configurations. The neutron energy is calculated on the basis of the formula 4.18, and due to nonlinear dependence of kinetic energy on time of flight, the magnitude of the background should increase with increasing time difference between the recorded particles. As a result, in the E_p vs E_n spectra, these events should group on the inner side of the kinematics, in the region of low neutron energy.

To investigate this problem, a dedicated, simple simulations were performed. Events with a single proton were uniformly generated in the energy range between 20 and 110 MeV, with additional uncorrelated signal in the E-detector. The left panel in Fig 5.4 shows the simulated distribution of such events for one specific angular configuration, on condition that the proton is in coincidence with a random signals. Non uniform distribution of the background preferring low neutron energy is clearly visible.

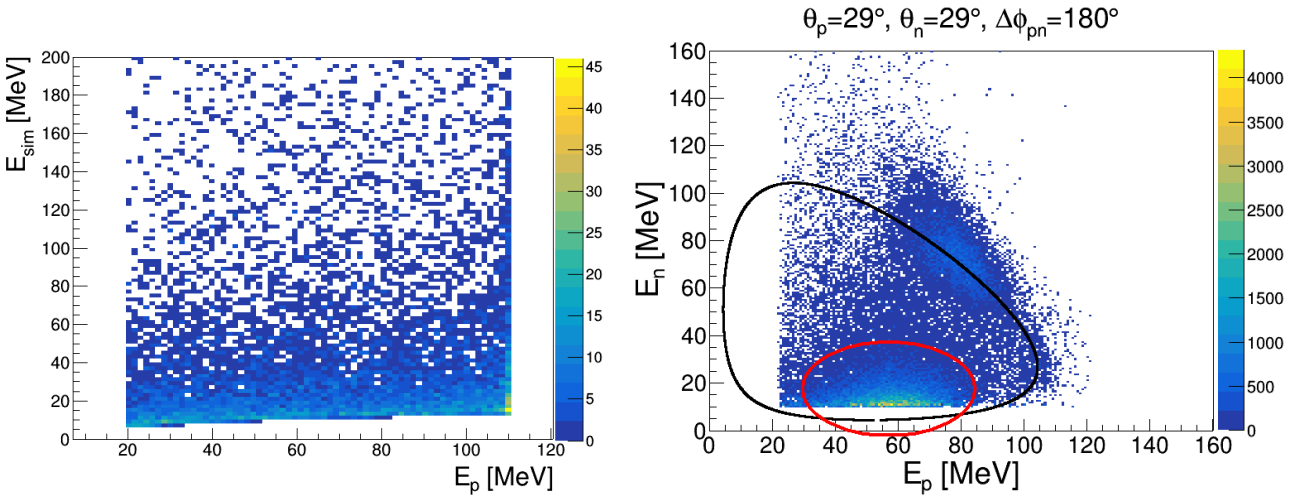

Figure 5.4: *Left panel:* The simulated background, based on the random proton-neutron coincidences. The proton data is correlated with the uniformly distributed time signals, treated as a neutrons. Background energy (E_{sim}) was calculated based on the TOF method. *Right panel:* Sample of E_p vs. E_n distribution for a selected angular configuration with large background contribution (shown in red ellipse).

The last category of background are events that in large amount populate the bottom of the E_p vs E_n spectra (see Fig. 5.4, right panel), at the neutron lowest energies and unlike the previously mentioned sources, their intensity strongly depends on angular configuration, being most visible for the configurations with large θ and $\Delta\phi$ close to 180° (see Fig. 5.5). Although these background events are relatively close to the kinematics, they cannot come from a breakup reaction because of vanishing cross section and configurational efficiency for

this region. The coplanar nature of these events may indicate their origin from *dp* elastic scattering. Indeed, the deuteron produced in the elastic scattering can relatively easy (see. Fig. 4.9) breakup into proton and neutron as a result of secondary nuclear reactions in the target or detector components. Subsequently, the secondary neutron, predominantly flying in the direction of the initial deuteron, can be registered in the detector in coincidence with the elastically scattered proton. In the same time the second proton is not detected.

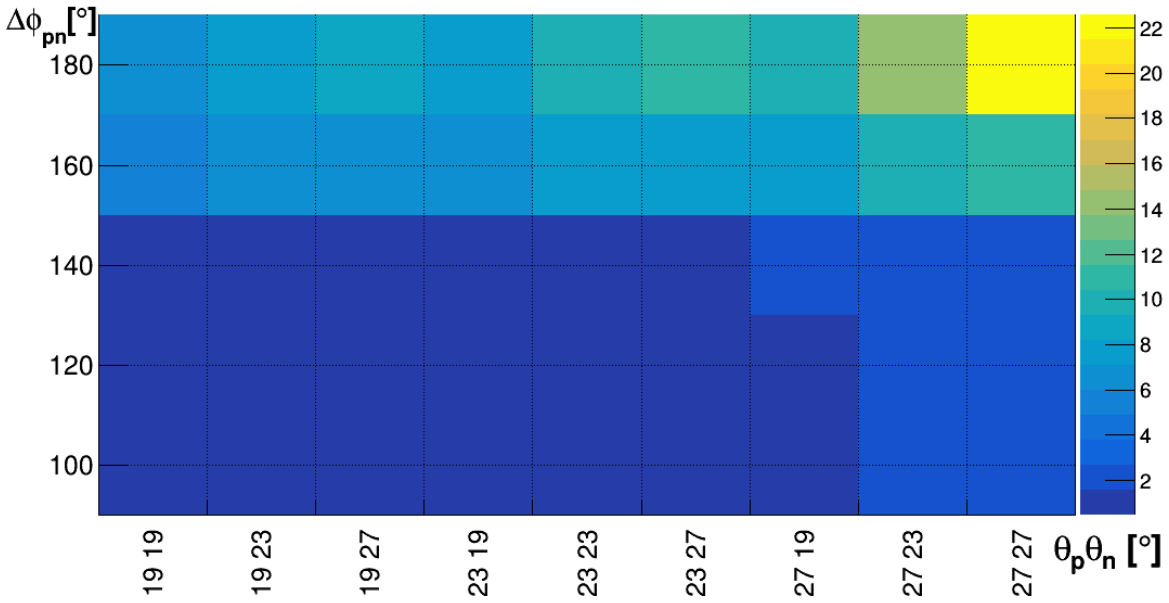

Figure 5.5: Estimated background (see Fig. 5.4 right panel) presented as percentage contribution to total number of events for all analysed angular configurations.

The listed above effects show a complex nature of the experimental background and point at expected difficulties of an attempt to quantify it. The background was finally subtracted subtracted just after projecting the obtained events onto the *D*-axis using the SNIP algorithm (see Fig. 5.6). The SNIP functionality was used to fine tune the amount of subtracted background and to estimate the size of systematic error associated with the background removal, as presented in Sec. 5.4.

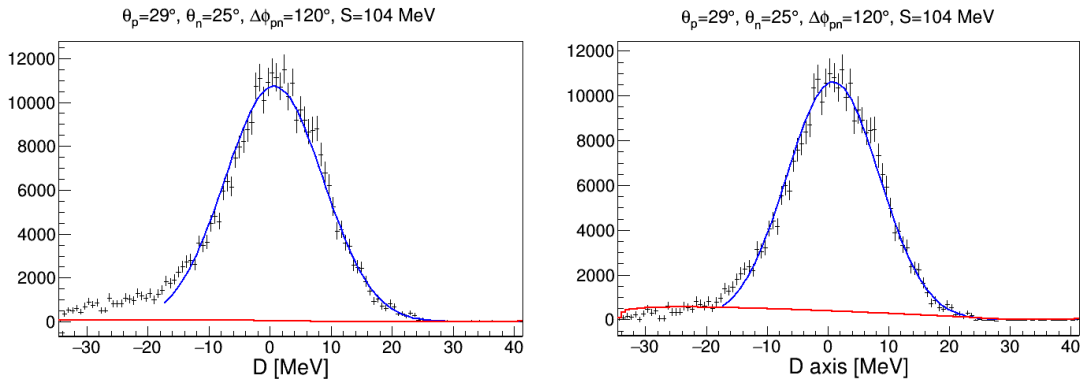

Figure 5.6: An example of background subtraction for one selected *S*-bin used for the estimation of the effect of this procedure on systematic uncertainty of the cross section. The red lines show the estimated background, which is significantly underestimated (left panel) and overestimated (right).

5.4 Possible sources of experimental uncertainties

This section contains a discussion of a possible sources of uncertainties which may influence the obtained values of the absolute differential cross sections. There are two types of uncertainties: statistical and systematical. The systematical uncertainties have been further divided into two categories, global uncertainties which are common for all data points, and point-to-point systematical errors which are calculated for each of the data points separately. Tab. 5.1 summarizes the various types of systematic errors considered in the analysis. The total experimental uncertainties include both systematical and statistical uncertainties added in quadrature.

Source of uncertainty		effect on the cross-section [%]	Comments
Global errors	Particle identification	5%	[78]
	Normalization	4.2%	[57]
	Angle Reconstruction	0.24%	[78]
	Hadronic Reaction	2%	[104]
	Energy calibration	1%	[78]
Point-to-point errors		5% - 30%	
Total systematical uncertainty		8.5% - 30.8%	

Table 5.1: Sources and typical size of systematic effects.

5.4.1 Statistical uncertainties

In order to calculate the statistical uncertainty of the number of registered proton-neutron pairs, we assume that it follows the Poisson distribution and its error is given by $\Delta n = \sqrt{n}$. Since in the experiment the registered coincidence events were prescaled by a factor of two, the final uncertainty was:

$$\Delta N = \sqrt{2n}. \tag{5.2}$$

The total statistical error is also influenced by the uncertainty of the configuration efficiency (more details can be found in Sec. 4.5). Not only the cross section values for the breakup reaction but also the cross sections for the elastic scattering are affected by a statistical error. This uncertainty was included in the luminosity uncertainty ΔL which was used to determine the normalization factor is based on the statistics collected for the *dp* elastic scattering reaction (see Sec. 4.2).

As it is shown in Fig. 5.8 (left panel), the total statistical uncertainties of the ^{1}H(d,pn)p reaction vary between 2% and 8% for most of the obtained experimental points.

5.4.2 Global systematical uncertainties

Due to careful pre-sorting of the data and study of the detection system geometry in the simulations as well as in the experiment, the systematical errors were significantly reduced. The global uncertainties contribute equally to all data points. They include effects related to the normalization, particle identification, angle reconstruction, hadronic interactions or energy calibration. Most of these uncertainties have already been estimated in the previous analyses, see [78, 79]. The potential sources of systematical uncertainties and their impact on the cross sections values are the following:

- **Particle identification.**

Types of particle were identified based on the graphical cuts imposed on the E-ΔE spectra. Since there is no sharp limits between proton and deuteron bands, some level of misidentification are inevitable. The associated systematical effects were estimated by varying the gate sizes and calculating the relative difference between resulting cross sections. The obtained uncertainties were found to be below 5%.

- **Absolute normalization.**

  As shown in Sec. 4.2, the normalization is based on the analysis of the elastic scattering reaction. There are several components that affect the error value. The major part of the uncertainty comes from the interpolation of the elastic scattering cross section due to the lack of experimental data for 160 MeV. Other significant error components were the particle identification and the angle reconstruction. Details about the the error determination of the luminosity can be found in [57]. The total uncertainty resulting from the normalization was estimated to 4.2%.

- **Scattering angle reconstruction.**

  The reconstruction procedure assumes that the particles originate from a point-like target. However, the target thickness and the size of a beam spot has to be taken into account. By varying the position of the target, it has been estimated how it affects the determination of angles of particle's trajectories. The errors obtained by this method are:

  $$\delta\theta \in (0.40^\circ, 0.49^\circ),$$
  $$\delta\phi(\theta) \in (0.67^\circ, 1.39^\circ),$$

  which is significantly smaller than the assumed bin widths of $\delta\theta = 4^\circ$ and $\delta\phi_{pn} = 10^\circ$. The analysis of cross section was repeated with all angles shifted according to their uncertainties. The change of a cross section allowed to estimate the effect to approximately 0.24%.

- **Proton energy calibration.**

  The error in energy calibration may influence particles distributions and ultimately the cross section values. It was estimated by varying the calibration parameters. The influence of this systematic effect on the cross section results was found to be less than 1%.

- **Hadronic interactions.**

  The systematic effects originated from the hadronic reactions was estimated based on the detector simulations (more details in Sec. 4.1.4). The systematic uncertainty due to this effect was estimated to be about 4%.

5.4.3 Point to point systematical uncertainties

One of the main goals of this thesis was to develop a neutron detection methods applicable to the BINA system. In order to estimate the systematic uncertainties related to these methods as accurately as possible, an error analysis for each cross section point was conducted. By changing conditions used in the analysis within the ranges specified below, different values of the differential cross section have been obtained. This procedure assumed varying only one parameter at a time, while all others where kept at their central values. As a result of this procedure a set of differential cross section distributions for the same angular configuration

was obtained (see Fig. 5.7). Having this, one can obtain the mean value and standard deviation for each S-bin separately. Each experimental point was weighted with its statistical error. Assuming that the sources of the uncertainties are uncorrelated, the standard deviation can be considered as a proper estimator of the systematic uncertainty associated with these parameters. The following effects were investigated:

- **MWPC efficiency and resolution**.

  In order to investigate the impact of the MWPC position reconstruction on the final results, data analysis was carried out using also the so-called weak-tracks (see Sec. 4.1.1). Much more limited information in this case results in worse position resolution from one side, but from the other side this analysis allows to test the influence of MWPC efficiency (with weak-tracks included the chamber inefficiency is almost negligible).

- **Background subtraction**.

  To estimate the effect of background subtraction on the cross section, the data analysis was repeated for two different background subtraction strategies. In the first approach one practically removes the entire background, even at the cost of losing events in the signal, while in the second the opposite strategy was applied. Of course the nominal analysis presents an intermediate case.

- **Veto condition**.

  The veto condition is an essential part of the analysis distinguishing signals assigned to neutrons from those produced by charged particles. We have examined how the changing of the veto definition influences the obtained values of the cross section. The analysis was repeated allowing one additional hit or cluster in the MWPC that was not already used for proton position reconstruction.

- **Neutron detection efficiency**.

  The efficiency for the neutron detection (Sec. 4.4.5) is characterized by its own error which, due to the low statistics, is considerable. In order to establish its influence on the obtained results, we have repeated the analysis for the upper and lower efficiency estimation, within its uncertainty.

- **Spatial granulation of time-of-flight simulations**.

  The time-of-flight of charged particles was determined on the basis of the Monte-Carlo simulations, described in Sec. 4.3.4. In the analysis three different MWPC granulations have been taken into account. In the final analysis, a grid of 40x40 elements was selected. In order to check the effect of the grid density, and thus the accuracy of the time-of-flight determination, two additional analysis were carried out for factor of two thinner grid (20x20) and a factor of two denser one (80x80).

- **Size of the angular binning**.

  The chosen bin width of the angles $(\delta\theta_p, \delta\theta_n, \delta\phi_{pn})$ defining a given angular configuration may have significant impact on the obtained values of the cross sections. Due to the relatively small x, y binning obtained for neutrons, events may migrate between neighboring configurations, which only partially was compensated by configurational efficiency. The influence of various bin sizes defining the angular configurations on the final cross sections has also been studied. The analysis was repeated with two different angular binning: the smaller one ($\delta\theta = 1^\circ, \delta\phi = 5^\circ$) and larger one ($\delta\theta = 3^\circ, \delta\phi = 15^\circ$), simultaneously in the data and in the theoretical calculations.

- **Neutron energy calibration**.

  The uncertainty associated with the neutron energy calibration was evaluated by varying the obtained neutron energy. The energy was shifting according to the resolution of the TOF method presented in Fig. 4.22. The analysis were repeated for the two most extreme cases, when the neutron energy was completely overcalibrated and when it was undercalibrated.

As the total systematic uncertainty of the cross section for a given S-value (point-to-point error) the spread of all obtained values for this bin was taken. The distribution of these uncertainties, normalized to the corresponding values of the cross section obtained in nominal analysis (relative errors), for all experimental points is shown in Fig. 5.8, right panel. For most of the configurations this uncertainty is between 8-20%. The points for which the point to point systematic error was determined to be greater than 30% were rejected from further analysis. Comparing the size of the systematic uncertainties to the statistical uncertainties for all points, it is clear that the overall precision of this measurement is determined by systematical effects.

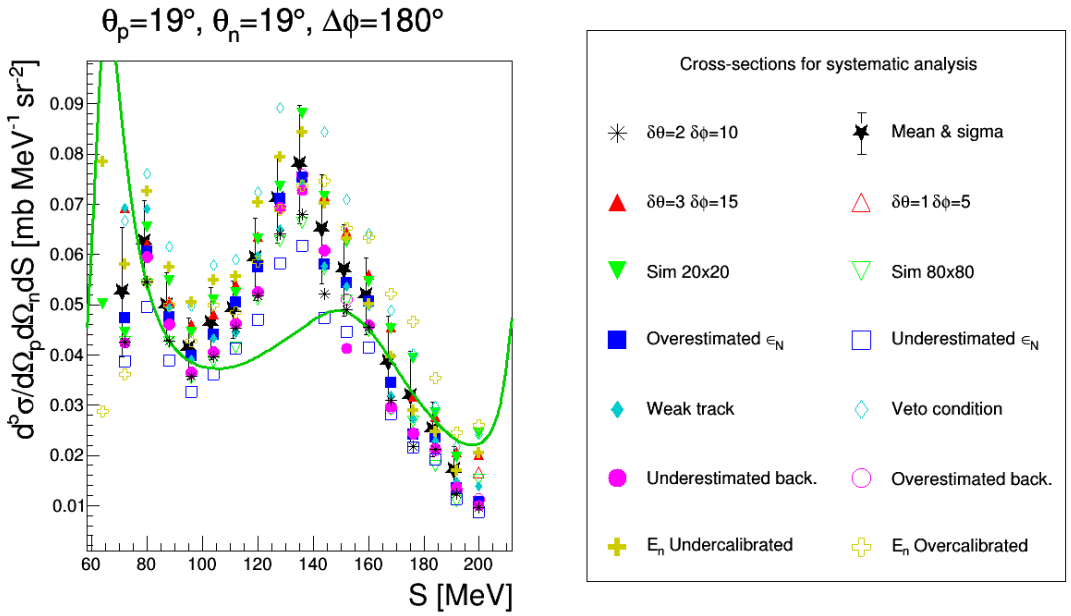

Figure 5.7: Influence of various events selection criteria on the obtained values of the differential cross section for a selected angular configuration. Sample of theoretical calculation is also presented to guide the eye.

5.5 Results and comparison with the theoretical calculations

The experimental cross section data were obtained for 54 individual angular configurations of the proton-neutron pairs from the ^{1}H(d,pn)p breakup reaction at the 160 MeV deuteron beam energy. Considering the dependence on S-variable, this gives in total 765 cross section values, which were compared with the available theoretical calculations, divided into two groups.

The first group comprises calculations performed by Witała et al. and is based on CD-Bonn (CDB) [8] and Argonne v18 (Av18) [7] nucleon-nucleon potentials. For each of these

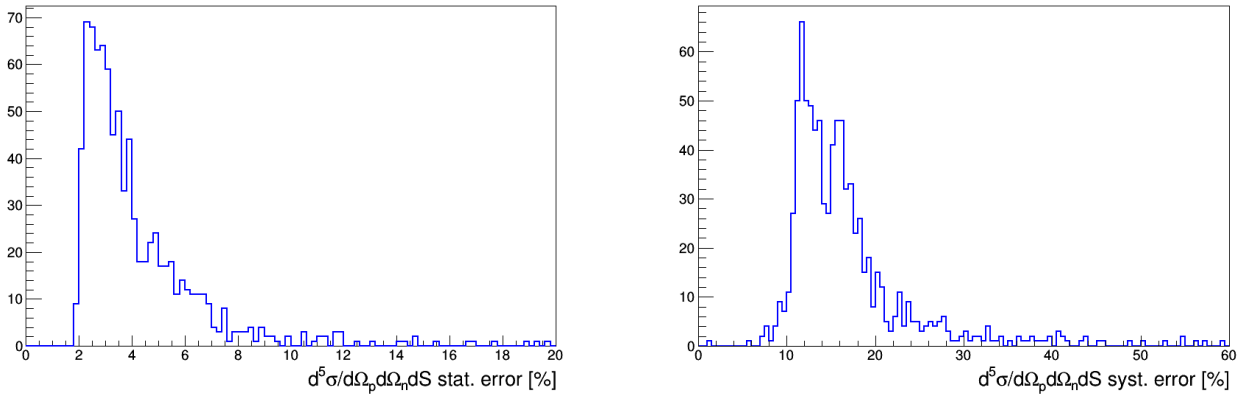

Figure 5.8: The point-to-point statistical (left panel) and systematical (right panel) relative errors distributions for presented analysis of ^{1}H(d,pn)p breakup reaction.

potentials calculations with the Tucsone-Melbeurne 99 [30] 3NF model (2N + TM99) and without this force were performed. The second group comprises the calculations by Deltuva et al. based on the Argonne v18 potential with and without the Urbana-Illinois X [20] 3NF model included, and on the copupled-channel CDB+Δ [3] formalism. Both of these approaches additionally account for the electromagnetic interaction (CDB+Δ+C [38], Av18+UIX+C [39]). Calculations are shown as lines representing the averaged values of the cross sections (see Sec. 5.1).

Due to the relatively large number of the theoretical models used for the comparison, we have introduced a color code (see Fig. 5.9) to facilitate observation of trends. Theories containing only 2N interactions are drawn with solid lines, while those containing the 3NF are drawn with dashed lines. The calculations which take into account the Coulomb interaction use different shade (lighter) of color. The theories provided by Witała et al. use a square marker, while the theories performed by Deltuva use an downward triangle for calculations based on the Argonne v18 potential and a upward triangle for the calculations with CDBonn potential.

5.5.1 χ^2_{red} and A-factor comparison

In order to make a quantitative comparison between the data and the theory, two different approaches were carried out. First was based on the chi-squared per degree of freedom analysis while the second used a statistical deviation A-factor. The reduced-variable χ^2_{red} was calculated for each theoretical model and each geometrical configuration as follows:

$$\chi^2_{\mathrm{red}} = \frac{1}{N-1}\sum_{i=1}^{N}\left(\frac{\sigma_i^{exp}-\sigma_i^{th}}{\Delta\sigma_i^{tot}}\right)^2, \tag{5.3}$$

where $\sigma_i^{exp}(\sigma_i^{th})$ corresponds to the measured (theoretical) value of the cross section, $\Delta\sigma_i^{tot}$ is the total uncertainty of the measured value and the sum runs over all experimental points (N) available for a given data set.

Taking total uncertainty (statistical + systematical) instead of only statistical causes that the analysed quantity does not have a precise statistical meaning. However, it still allowed to test the reproduction of the experimental cross section distributions by different theoretical calculations. We are aware of limited applicability of chi-square test to this comparison. In particular the experimental uncertainties are only roughly estimated and most probably do not follow Gaussian distribution, which is considered as a prerequisite of this test. However

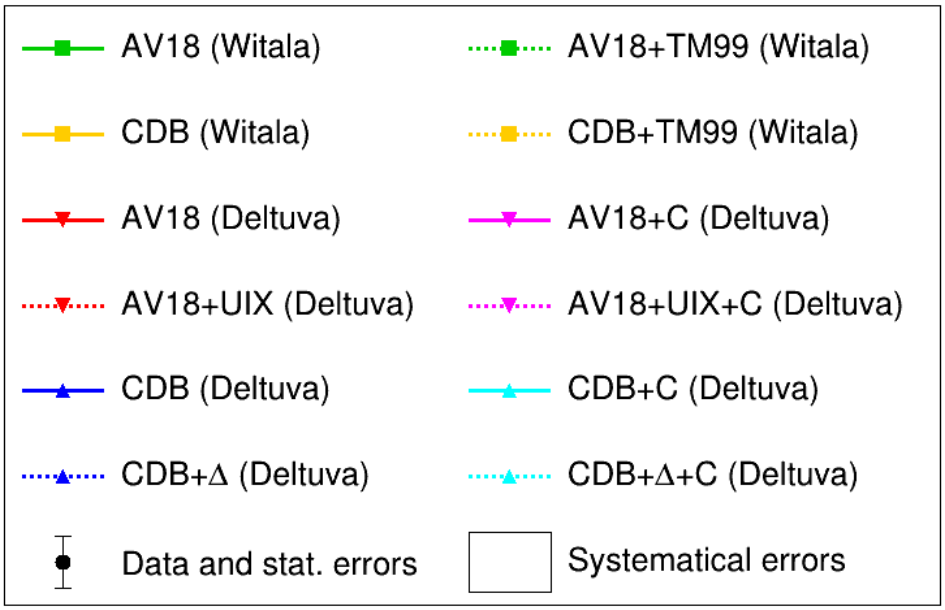

Figure 5.9: The color code used to present the obtained experimental data and the compared theoretical models.

in this analysis we focus rather on comparison of different models then a validation of a particular one.

Due to difficulties in a precise estimation of the experimental uncertainties, quite large dynamic range and discrepancies between data and theories, another method of testing the agreement between the obtained cross section data and the theoretical predictions, the so-called A-deviation factor, has also been used. The A-factor [105] is defined as:

$$A = \frac{1}{N} \sum_{i=1}^{N} \frac{|\sigma_i^{exp} - \sigma_i^{th}|}{\sigma_i^{exp} + \sigma_i^{th}}, \tag{5.4}$$

where symbols meaning is the same as in Eq. 5.3. The A-factor has very useful properties:

- Its value does not depend on the absolute value of the cross section.
- It has the advantage of its simple interpretation. Its value is in the [0,1] range, where zero means perfect agreement between theory and data. With the increasing discrepancies the A-factor approaches to one. For small deviations ($\sigma^{exp} \approx \sigma^{th}$) the A-factor can be interpreted as half of the average relative distance between the experimental results and theoretical cross section. For instance, when $A = 0.05$ then the average relative distance is about 10%.
- It is invariant with respect to exchange of the theoretical and measured cross sections, such that the overestimation of one part of the distribution by the prediction along with the underestimation of the other part does not result in a cancellation of the A-factor.
- It does not depend on the estimated uncertainties of measured values.

Obtained global results of both the χ^2_{red} and the A-factor are collected in Fig. 5.10. The quality of the description for individual configurations is presented in the form of maps (Fig. 5.11 for χ^2_{red} and Fig. 5.12 for A-factor) for three selected cases representing the worst, intermediate and the best agreement between the theory and experiment. The maps for all theoretical models are presented in Appendix C. Fig. 5.13 and 5.14 present the same results, averaged over the relative azimuthal angle, as a function of a combination of proton and neutron polar angles, while in Fig. 5.15 opposite strategy was applied. The quality of the agreement between the experiment and the different theories has also been investigated in a function of neutron and proton energies in Fig. 5.16 and 5.17.

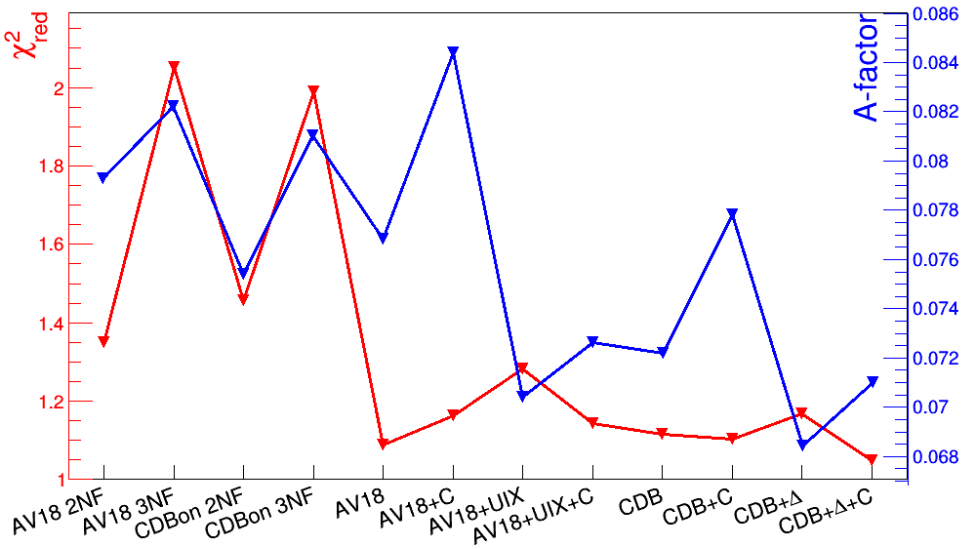

Figure 5.10: Comparison of global χ^2_{red} (red) and A-factor (blue) for the all available theoretical models. Lines connecting points are to guide the eye only.

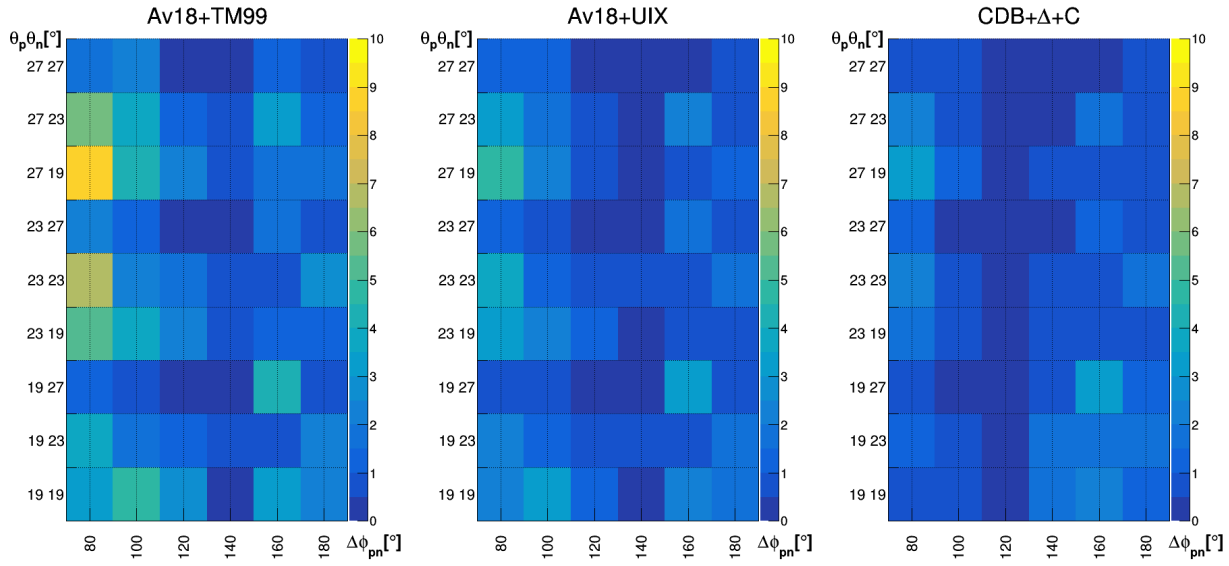

Figure 5.11: Maps of χ^2_{red} for individual configurations of the ^{1}H(d,pn)p reaction defined by polar angles (θ_p,θ_n) on vertical axis and by relative azimuthal angle $\Delta\phi_{pn}$ on horizontal axis. The data are presented for the selected theories with the worst (left), intermediate (center) and with the best agreement (right).

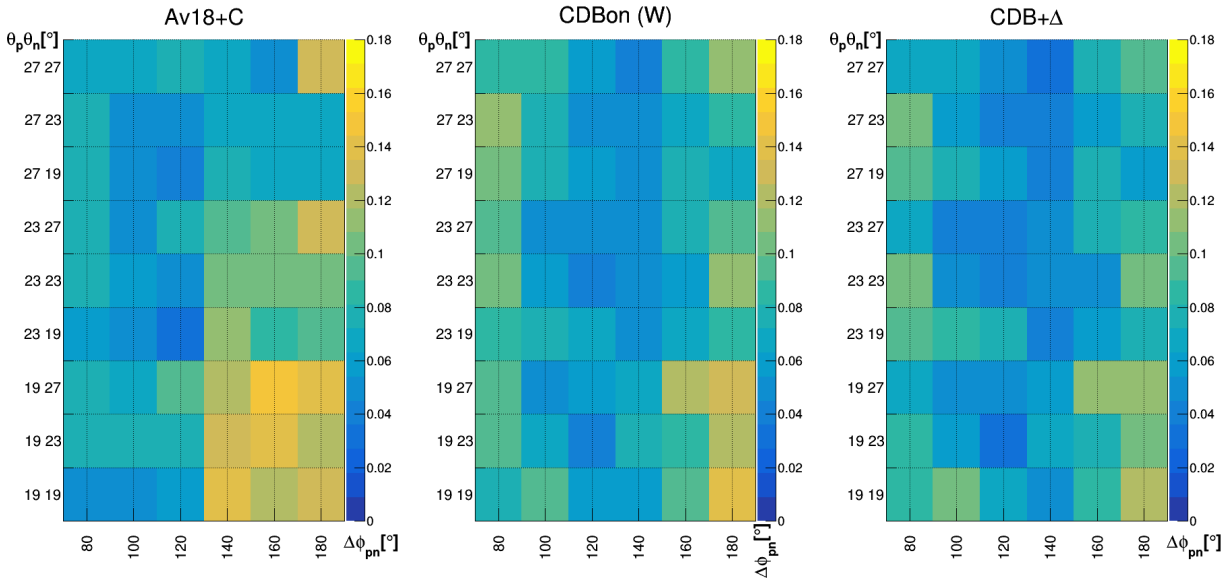

Figure 5.12: Similar as in Fig. 5.11 but for A-factor.

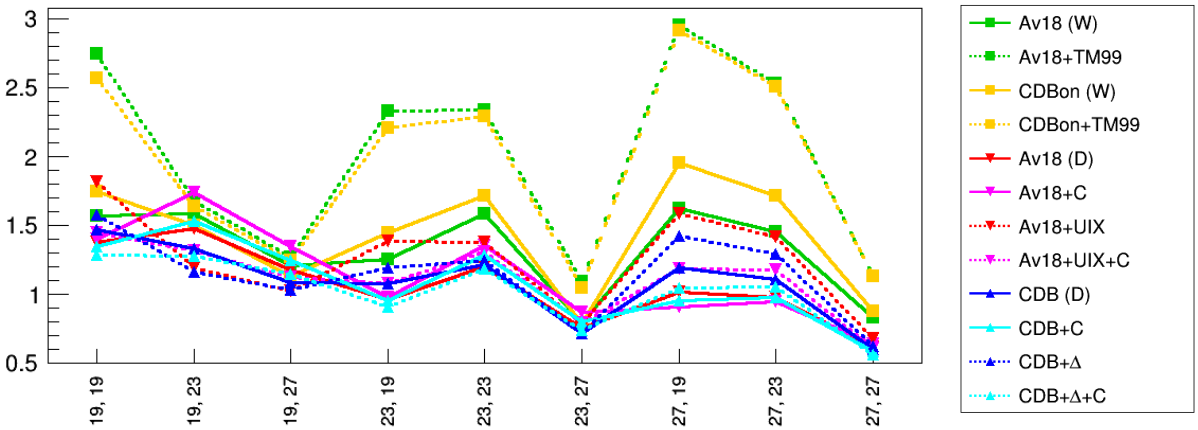

Figure 5.13: The $\chi^2_{\rm red}$ presented as a function of the combination of the proton and neutron emission polar angles (θ_p,θ_n).

Comparing the ^{1}H(d,pn)p breakup reactions data with the theoretical calculations, one can conclude that the obtained results for the proton-neutron coincidences in general are very well reproduced by theoretical models. The obtained global $\chi^2_{\rm red}$ (see Fig. 5.10) ranged from approximately 1.1 to 2.1, depending on the theoretical model. This quite low values can partially be accounted for by conservatively estimated and relatively large systematic uncertainties. Due to a different, more complicated and less accurate analysis method applied for the proton-neutron as compared to the proton-proton coincidences, values of the systematic error are significantly larger, but still comparable (typically 7.5% for proton-proton and 16% for proton-neutron). However, the error independent A-factor ranges between 0.068 and 0.084, which confirms good agreement between the data and models. This strengthens our confidence in the presented analysis.

The results based on the $\chi^2_{\rm red}$ and A-factor analysis are not fully in agreement, as can be easily observed in most of Figs. 5.10 and 5.13 to 5.17. This is due to a fact that A-factor does not take into account experimental errors, only a relative distance between the theory

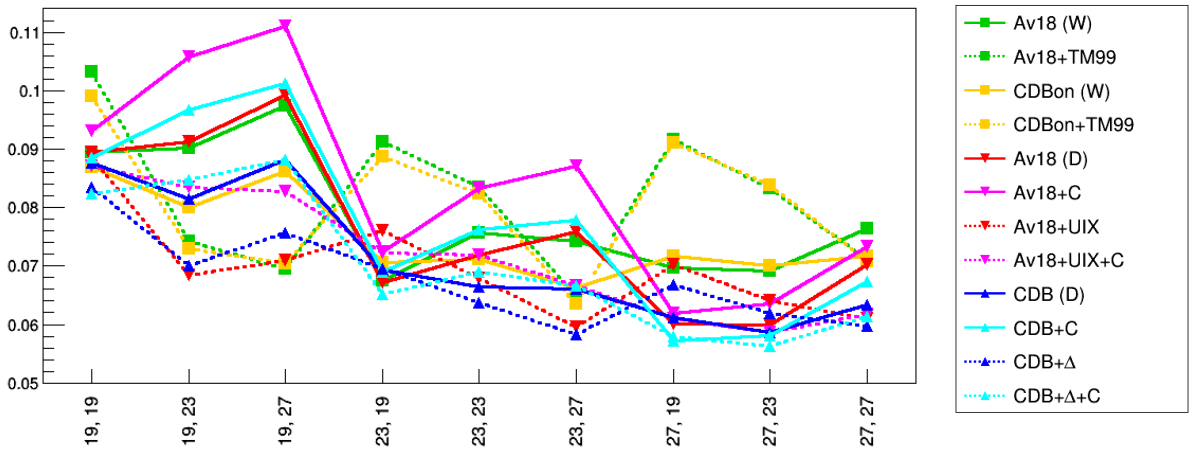

Figure 5.14: Similar as in Fig. 5.11 but for A-factor.

and experimental value at a given point. When A-factor and $\chi^2_{\rm red}$ behave differently (eg. A-factor increases while $\chi^2_{\rm red}$ stays low) it may indicate that for these areas well estimated systematical uncertainties compensate increasing relative discrepancies between theory and the data. Such situation can be observed e.g. in Fig. 5.15 for large relative azimuthal angles.

A global comparison between the ^{1}H(d,pn)p data and theory shows that for calculations performed by Witała et al. both $\chi^2_{\rm red}$ and A-factor analysis reveal that adding 3NF does not improve, but even spoils the agreement between the theory and data. In the case of Deltuva et al. calculations, A-factor and $\chi^2_{\rm red}$ draw different picture. The best agreement for A-factor is obtained for the models with only 3NF while including the Coulomb interaction always spoils the agreement with the experimental data. Except Av18+C and CDB+C calculations, obtained values of A-factors are significantly lower than for calculations by Witała et al. This difference is even more pronounced in the case of $\chi^2_{\rm red}$ calculations. Here the relative differences are much smaller and the situation is almost opposite as for A-factor, with the 3NF models having the worst agreement. Using together Coulomb and 3NF improves reproduction of the experimental data. The best agreement is obtained for the CDB+Δ+C model, followed by pure Av18 potential. Evidently, the addition of the 3NF effects alone spoils the agreement, regardless of the type of applied 2N potential. These findings are very surprising and in fact contradict our expectations based on the previous cross section analysis of the proton-proton coincidences.

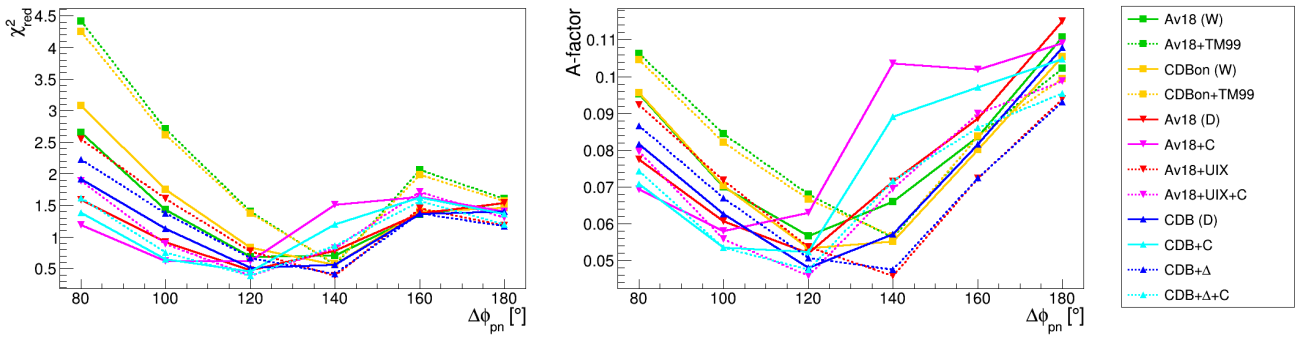

Figure 5.15: The quality of the description of the measured cross sections based on $\chi^2_{\rm red}$ (left panel) and A-factor (right panel) presented as a function of the relative azimuthal angle $\Delta\phi_{pn}$.

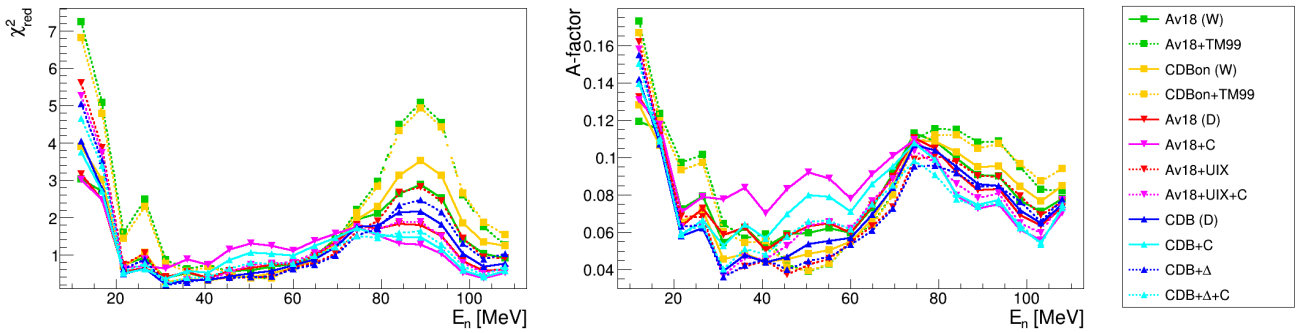

Figure 5.16: Similar to Fig. 5.15 but presented as a function of neutron energy.

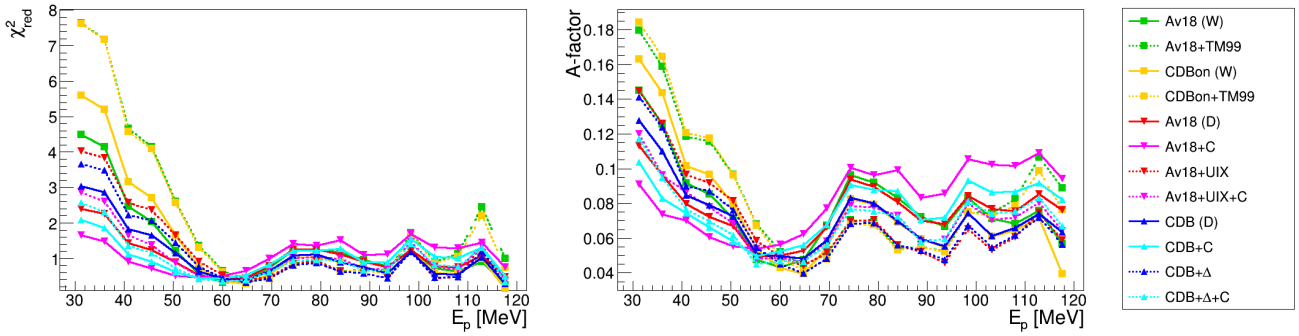

Figure 5.17: Similar to Fig. 5.15 but presented as a function of proton energy.

More detailed inspection of the data sorted according to $\Delta\phi_{pn}$ (Fig. 5.15), reveals that the discrepancies between different models reach their minimum for $120^\circ \leq \Delta\phi_{pn} \geq 140^\circ$. Theories taking into account only the Coulomb interactions achieve the best χ^2_{red} and A-factor for the low values of the $\Delta\phi_{pn}$ angle, while for the higher angles the agreement deteriorates significantly. This region seems to be more sensitive for the 3NF effects. It seams that increasing relative discrepancies between the data and theories, observed for the relative azimuthal angles approaching to 180°, is compensated by larger uncertainties in this region, see the corresponding χ^2_{red} plot (Fig. 5.15). Such compensation is not observed for small angles, which proves that both analysis provide complementary information and are important to get the full picture.

Dependence on the neutron energy E_n (Fig 5.16) shows that both A-factor and χ^2_{red} reach a local minimum in the range of about 40 to 70 MeV. This may be linked to the observation that for this energy range the neutrons detection methods achieve the best accuracy. In this region both analysis show that models with the Coulomb interaction reproduce the data slightly worse while the addition of 3NF improves the description. For the higher energies the opposite behavior is observed. Interesting conclusion can be drawn from the dependence on the proton energy E_p (Fig. 5.17). For almost whole energy range above 60 MeV and all theories the χ^2_{red} value is very low and constant around 1. For lower energies it increases rapidly, however at very different rates for different theories, reaching maximum at the lowest proton energy. Possible explanation could indicate at the accuracy of the proton energy calibration. As it was shown in Sec. 4.4.4, in this low-energy region, as no degrader data was available, only extrapolation has been applied. Even a small error in the determination of the energies of low-energy protons may result in a significant discrepancy in the estimation of their time of flight. Since low-energy protons are accompanied by high-energy neutrons, for which the time of flight can also be poorly determined due to the resolution of TDCs,

the obtained discrepancies are even more significant. This is reflected in a local maximum near the neutron energy of 90 MeV.

5.5.2 Invariant coordinates

Another way of presenting the cross section data is with the use of the Lorenz invariants. The Mandelstam variables for two-body processes can be rewritten for a three-body breakup reaction ($d + p \rightarrow p + p + n$) [66, 67]. Denoting the 4- momenta of the entrance channel by $\mathbf{p_p}$ for proton and $\mathbf{p_d}$ for deuteron, and in the exit channel by ($\mathbf{p_p^{(1)}}$, $\mathbf{p_p^{(2)}}$) for two protons and $\mathbf{p_n}$ for neutron, one can obtain four invariant variables:

$$s_{pp} = \left(\mathbf{p_p^{(1)}} + \mathbf{p_p^{(2)}}\right)^2, \tag{5.5}$$

$$s_{pn} = \left(\mathbf{p_p^{(1)}} + \mathbf{p_n}\right)^2, \tag{5.6}$$

$$t_n = \left(\mathbf{p_d}/2 - \mathbf{p_n}\right)^2, \tag{5.7}$$

$$t_p = \left(\mathbf{p_p} - \mathbf{p_p^{(2)}}\right)^2. \tag{5.8}$$

The s_{pp} and s_{pn} are the relative momenta of proton-proton and proton-neutron subsystems. The $\sqrt{t_n}$ corresponds to the 4-momentum transfer from bound neutron in the entrance channel to a free neutron in the exit channel, while the $\sqrt{t_p}$ corresponds to the 4-momentum transfer from the free proton in entrance channel (target) to the proton in the exit channel, which was not used in the calculation of s_{pn}. For more convenience, these variables can further be redefined in terms of the kinetic energy transfer to a particle and energies of relative motion of nucleons within a pairs:

$$E_{rel}^{pp} = \sqrt{s_{pp}} - 2m_p, \tag{5.9}$$

$$E_{rel}^{pn} = \sqrt{s_{pn}} - m_p - m_n, \tag{5.10}$$

$$E_{tr}^{p} = \frac{-t_p}{2m_p}, \tag{5.11}$$

$$E_{tr}^{n} = \frac{-t_n}{2m_n}, \tag{5.12}$$

where the m_p and m_n are the rest masses of the proton and neutron respectively. This representation has been chosen due to its direct and close relation to the dynamics of the studied reaction. For example the low relative energies E_{rel} can give an insight into the Final State Interaction within a given pair. This turned out to be especially suitable for studying the effects of the Coulomb interaction, which are very pronounced at the small values of E_{rel}^{pp} of proton-proton pair [15]. The relative energy between proton-neutron pair E_{rel}^{pn} does not have as intuitive interpretation but it takes advantage of the fact that in our analysis both particles are directly detected.

Similarly, the energy transfer tells how much a given nucleon is involved in the interaction. When E_{tr} is close to zero, this nucleon acts as a spectator, which corresponds to Quasi-Free Scattering of the two other nucleons. In this analysis we do not present the result for transfer energy to proton because computing this variable by definition would be based solely on the reconstruction of unmeasured proton, which is biased by relatively low accuracy.

The obtained results are presented in a function of E_{rel}^{pn} (Fig. 5.18), E_{rel}^{pp} (Fig. 5.19) and E_{tr}^{n} (Fig. 5.20). Large spread and similar behavior can be observed for χ^2_{red} and A-factor in a function of the relative energy of the proton-neutron pairs (Fig. 5.18). Models with the

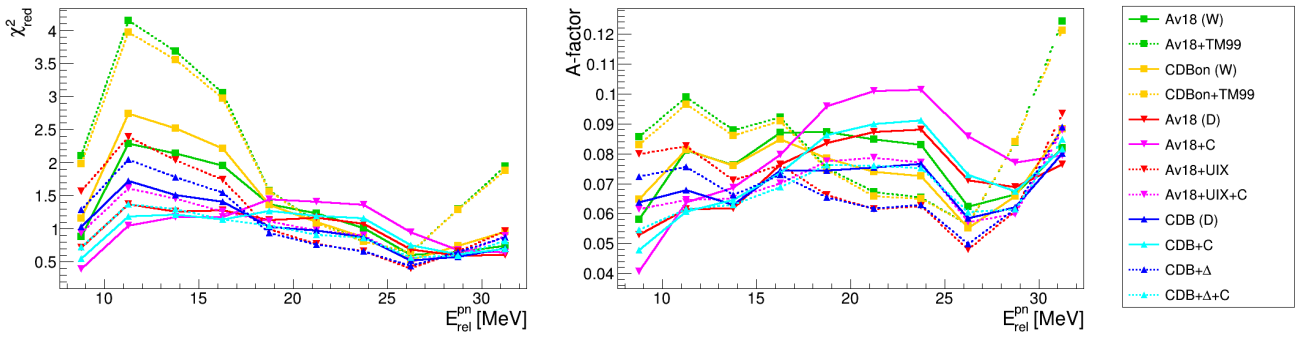

Figure 5.18: χ^2_{red} (left panel) and A-factor (right panel) presented as a function of relative energy of proton-neutron pair E^{pn}_{rel}.

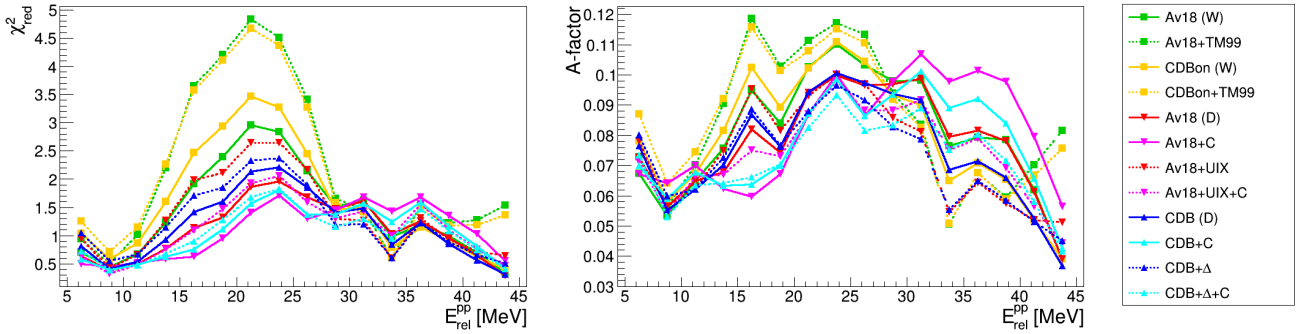

Figure 5.19: Similar to Fig. 5.18 but presented as a function of relative energy of proton-proton pair E^{pp}_{rel}.

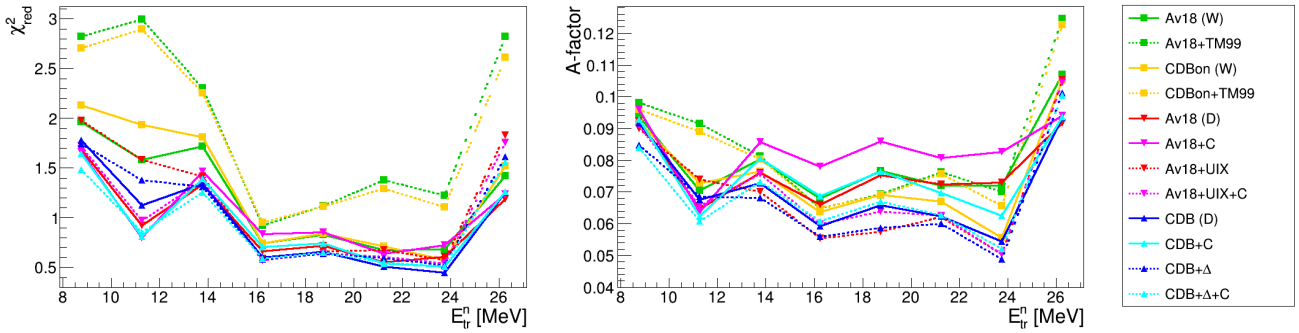

Figure 5.20: Similar to Fig. 5.19 but presented as a function of energy transfer to neutron E^{n}_{tr}.

Coulomb component better describe the experimental data for low energy range, while the predictions with only 3NF better work for higher energies. In the case of χ^2_{red} analysis, the highest discrepancy is obtained for the relative energy of 10-15 MeV and it steadily improves with increasing E^{pn}_{rel} for almost all theoretical models. For the A-factor, this effect is not that visible, as the spread of theories stays the same. For the highest relative energy, for almost all models (except those by Witała et al. with 3NF included) the discrepancies with the data converge to a single value for both χ^2_{red} and A-factor with average relative difference on the level of 16%. The results for E^{pp}_{rel} (Fig. 5.19) show even larger spread of χ^2_{red} values for different theories, creating distinct peak near 20 MeV and two minima. At minimal relative energy of proton-proton pair, both the χ^2_{red} and A-factor converge to low value. At the second minimum near 35 MeV only χ^2_{red} values converge, while for A-factor substantial

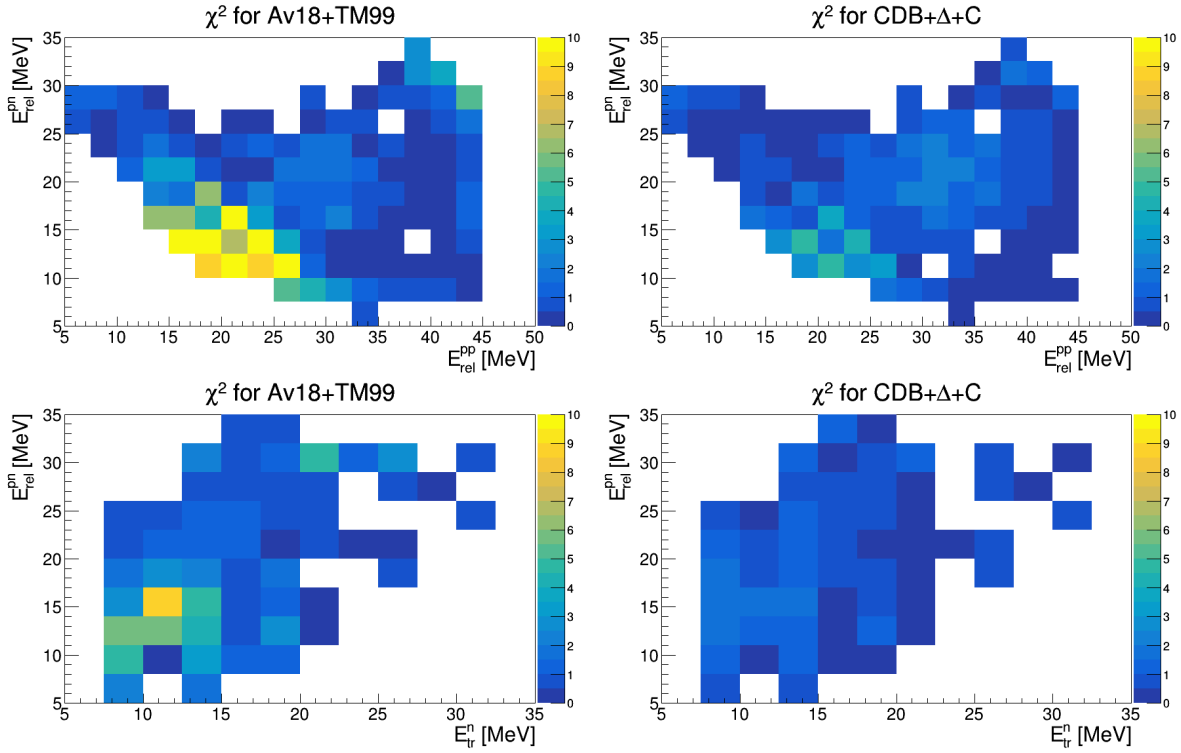

Figure 5.21: The $\chi^2_{\rm red}$ for the correlations of E^{pp}_{rel} vs. E^{pn}_{rel} (top panels) and E^{n}_{tr} vs. E^{pn}_{rel} (bottom panels). Panels on the left presents the results for theory with the worst while on the right with the best agreement.

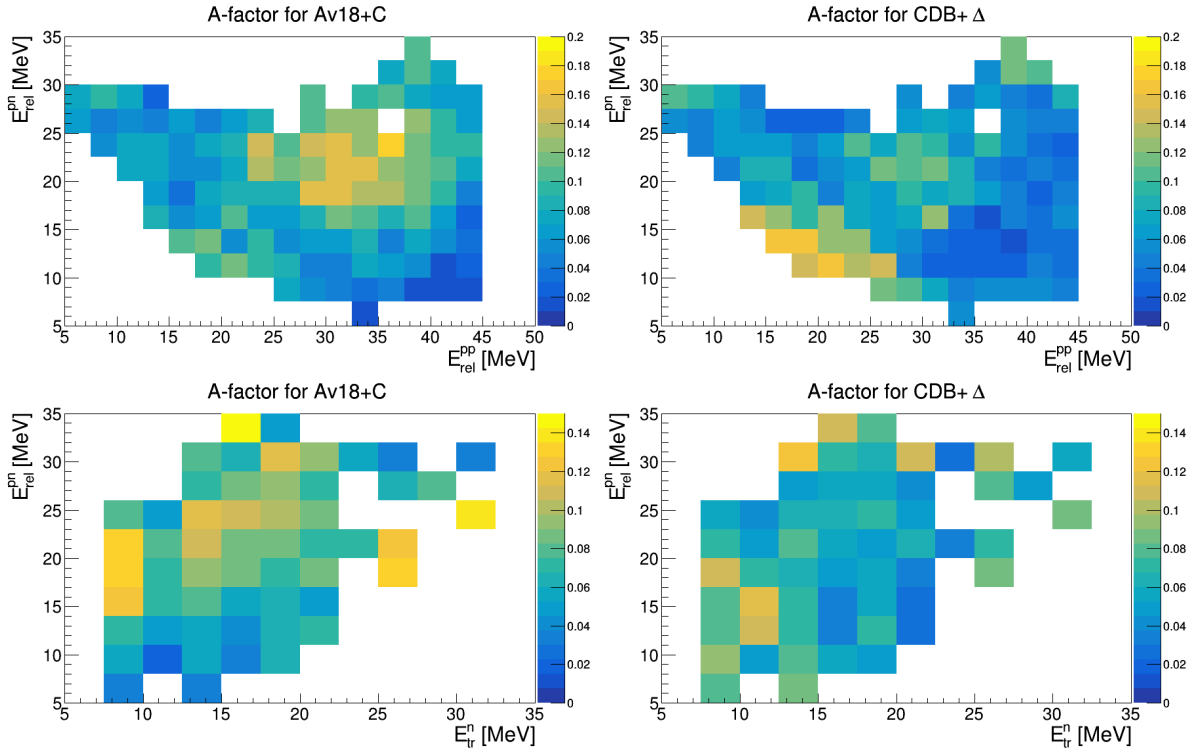

Figure 5.22: Similar as in Fig. 5.21 but for A-factor.

discrepancies remain. Interestingly, the dependence of the $\chi^2_{\rm red}$ on the energy transfer E^{n}_{tr} to the neutron (Fig. 5.20) shows that most theories, except those calculated by Witała et al., with 3NF stay close together, obtaining value lower than one. This may provide a hint

pointing at the main cause of a weak agreement of these models with the data.

For better illustration of the dependencies between new variables, a two dimensional correlations of E_{rel}^{pp} vs. E_{rel}^{pn} and E_{tr}^{n} vs. E_{rel}^{pn} were prepared. The obtained results for the χ^2_{red} and A-factor are presented in Fig 5.21 and 5.22 respectively. In the case of χ^2_{red} the discrepancies clearly form a hot spot around $E^{np}_{\text{rel}} = 15$ MeV and $E^{pp}_{\text{rel}} = 20$ MeV for the Av18+TM99 theory, which is characterized by the worst global agreement among all tested models. The correlations obtained for the CDB+Δ+C theory show good and relative constant agreement for almost the entire studied area. When it comes to the A-factor, the discrepancies are more evenly distributed. This is particularly evident in the E_{rel}^{pp} vs. E_{rel}^{pn} correlations. Although the theory in the pictures on the right offer better reproduction of the experimental data, there are some regions (low E_{rel}^{pp} vs. E_{rel}^{pn} values) where the results get worse. In the case of E_{tr}^{n} vs. E_{rel}^{pn} correlation such an effect is not as pronounced. The whole set of correlations calculated for other models is presented in Appendix E.

5.5.3 Comparison with the latest Chiral EFT

Courtesy of a group of theoretical physicists from the LENPIC Collaboration, we have gained a preliminary access to the latest theoretical calculations using new potentials based on chiral effective field theory (see Sec. 2.2.4). The use of the new SMS-type regularization allowed to determine the interaction potential for next-to-next-to-leading order (N^2LO) chiral expansion in the 3N systems, where three-nucleon forces naturally starts to contribute to the interaction. Fig. 5.23 shows the cross section calculations for the ^{1}H(d,pn)p reaction. Two theories were presented, one calculated using the full SMS potential [36] with the regularization parameter $\lambda = 450$ MeV which naturally includes the 3NF (reffered later as SMS+3NF), and for the potential obtained without the 3NF terms in the chiral expansion [35] (referred to as SMS). Unfortunately, calculations are currently available only for a few selected angular configurations. Thus the presented theories are calculated only for central values of those configurations and they were not averaged over the angular ranges as used in the experiment. For comparison also Av18 and Av18+UIX models calculated by Deltuva's group are plotted. Table 5.2 shows the obtained values of the χ^2_{red} and A-factor analysis for each individual angular configurations as well as a global values integrated over available configurations.

	Theories	Configuration						Global
		$\theta_p = 21°, \theta_n = 27°$			$\theta_p = 23°, \theta_n = 21°$			
		$\Delta\phi = 140°$	$\Delta\phi = 160°$	$\Delta\phi = 180°$	$\Delta\phi = 140°$	$\Delta\phi = 160°$	$\Delta\phi = 180°$	
A-factor	Av18	0.051	0.049	0.071	0.052	0.062	0.080	0.061
	Av18+UIX	0.051	0.036	0.050	0.045	0.053	0.063	0.050
	SMS 2NF	0.055	0.052	0.085	0.046	0.068	0.078	0.064
	SMS 3NF	0.061	0.045	0.084	0.052	0.072	0.081	0.066
χ^2_{red}	Av18	0.28	0.18	0.82	0.50	0.62	1.19	0.61
	Av18+UIX	0.39	0.20	0.41	0.46	0.46	0.79	0.46
	SMS 2NF	0.31	0.21	1.07	0.42	0.68	1.17	0.65
	SMS 3NF	0.47	0.42	1.14	0.56	1.00	1.19	0.80

Table 5.2: Comparison of the χ^2_{red} and A-factor values obtained for the calculations based on the SMS type of the chiral effective field theory, together with Av18 and Av18+UIX potential.

In the case of chiral models, the agreement with the data is slightly worse than for the

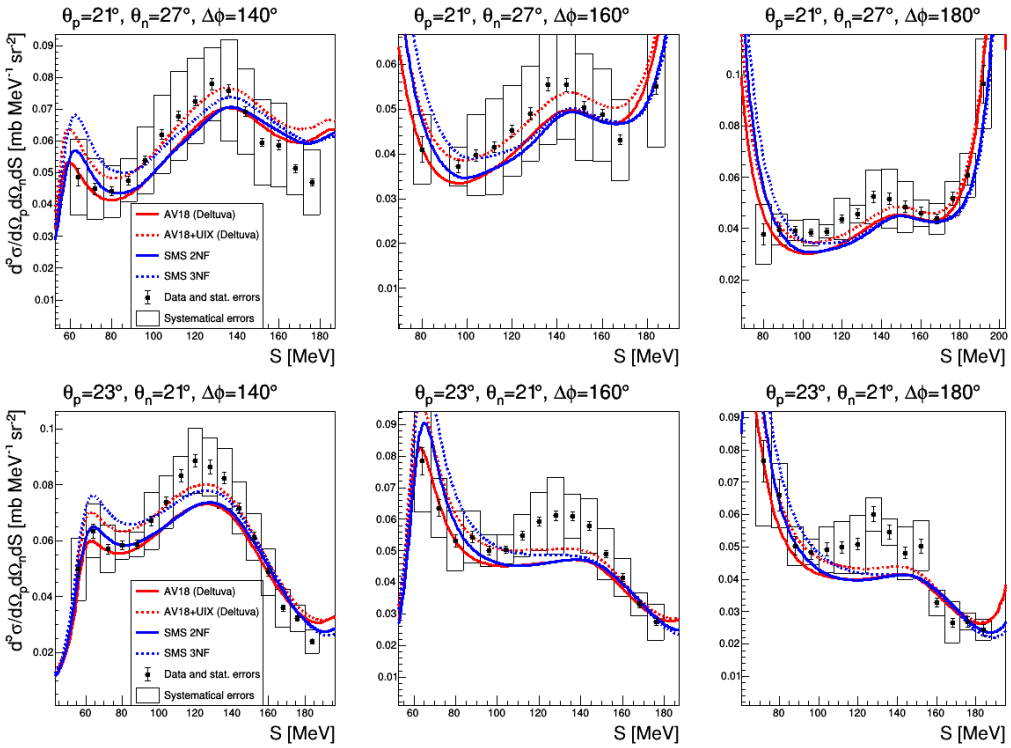

Figure 5.23: The experimental differential cross section distributions compared to the SMS-type calculations (specified in the figure). In addition predictions based on the Av18 and Av18+UIX models are presented.

models with the Av18 potential. Similarly as for the calculations performed by Witała et al., the addition of 3NF spoils agreement even further. However, the number of available configurations is unfortunately too small to draw more global conclusions.

5.5.4 Comments on the proton-proton coincidences data

Taking advantage of the fact that proton-neutron coincidences were measured simultaneously with the proton-proton ones, one can discuss the results obtained in this thesis with the results from the the ^{1}H(d,pp)n analysis [57]. The proton-proton coincidence data has been converted into the new kinematic variables. The χ^2_{red} distributions as a function of the relative azimuthal angle $\Delta\phi_{pn}$ and $\Delta\phi_{pp}$ (Fig. 5.24), relative energy of proton-proton pair E^{pp}_{rel} (Fig. 5.25), and neutron transfer energy E^{n}_{tr} (Fig. 5.26), were selected for comparison. Proton-neutron cross sections caluclations were presented only for the same theoretical models as available in [57] for the proton-proton coincidences.

Analysis of the proton-proton coincidences with respect to the $\Delta\phi_{pp}$ angle (Fig. 5.24) show that the differences between theory and experiment increase with the relative azimuthal angle between the pair of protons. The influence of the Coulomb effects is not as clearly noticeable as in the case of the relative energy, but the addition of the 3NF significantly improves the data description. Since in the case of proton-neutron coincidences, the χ^2_{red} results were presented in a function of the relative azimuthal angle between proton-neutron pair, no Coulomb effect can be expected here. Indeed, the $\Delta\phi_{pn}$ dependence is almost opposite as for $\Delta\phi_{pp}$. Except the Av18+C, obtained discrepancies are larger for the low $\Delta\phi_{pn}$ and inclusion of 3NF always spoils the agreement with the experimental data.

Contrary to the results of the proton-neutron analysis, the obtained χ^2_{red} values for the proton-proton coincidences show a very interesting though predictable behavior. Different

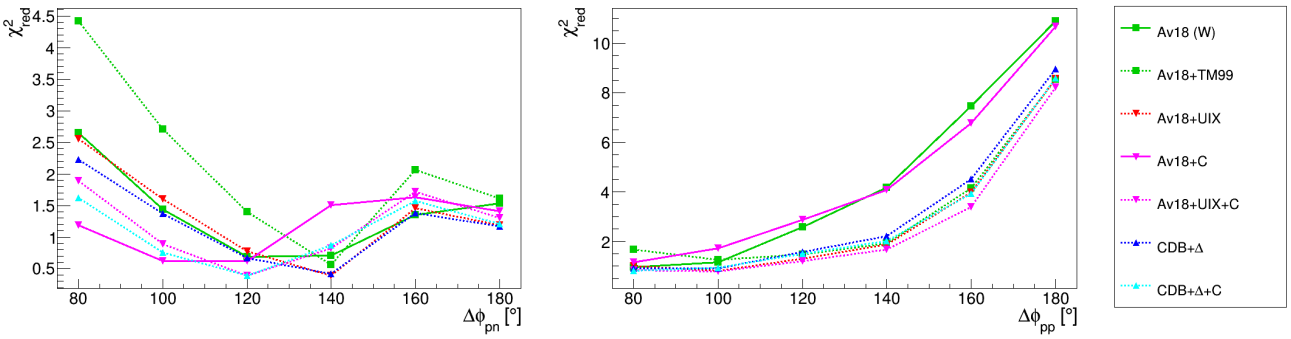

Figure 5.24: Comparison of the χ^2_{red} results in a function of $\Delta\phi_{pn}$ and $\Delta\phi_{pp}$ for selected theoretical calculations for the proton-neutron coincidences (left column) and the proton-proton coincidences (right column).

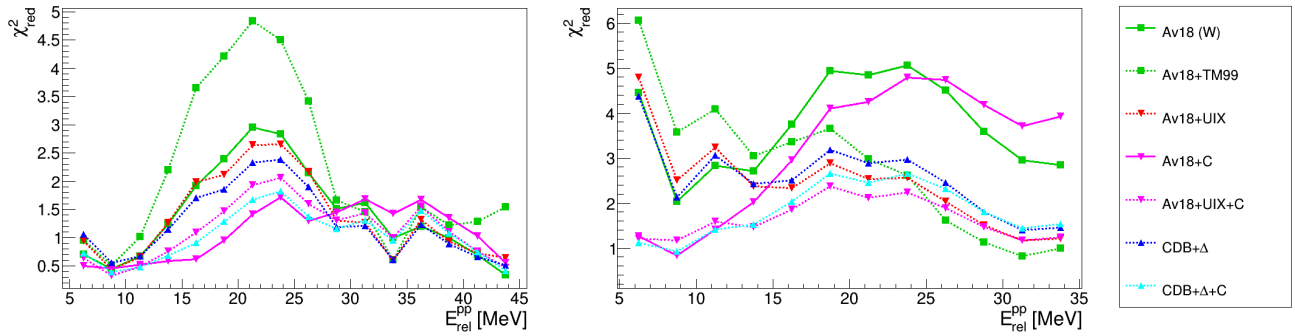

Figure 5.25: Similar as in Fig. 5.24 but presented in a function of E^{pp}_{rel}.

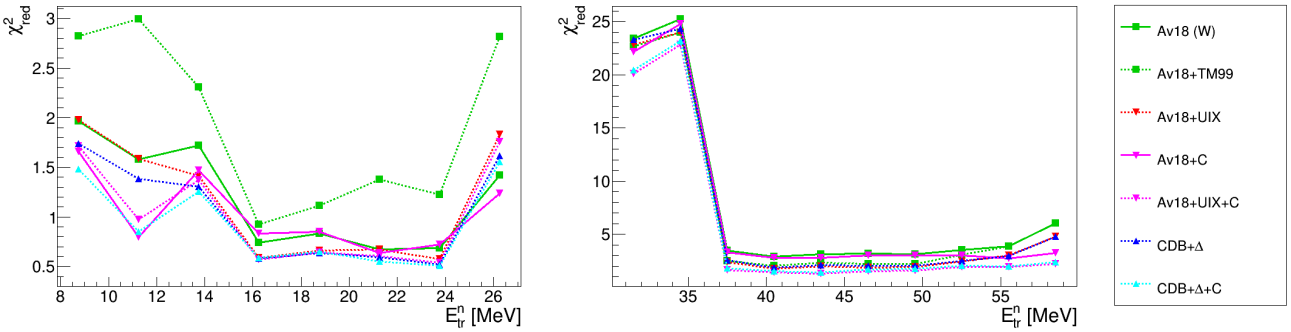

Figure 5.26: Similar as in Fig. 5.24 but presented in a function of E^{n}_{tr}.

aspects of the 3N systems dynamics are visible for different data regions. This is especially well illustrated in the distribution of the relative energy of the proton-proton pairs (Fig. 5.25). Theoretical models which take into account the Coulomb force reproduce much better the experimental data for low E^{pp}_{rel} values. Such a behavior was generally expected. Based on the previous experiments, in these areas a significant influence of the electromagnetic interaction caused by final state interaction in the proton-proton system was anticipated. Slightly less intuitive may be the improvement in the agreement for large values of the relative energy when effect of 3NF are included, while simultaneously deteriorating it for the small E^{pp}_{rel}. In general, the 3NF and the Coulomb force together improve the agreement between the data and theory in a wide range of the available phase space. In the case of proton-neutron coincidences all theories perform almost equally well at the lowest relative protons energy, converging to the local minimum χ^2_{red} value. Second minimum can be observed at maximum

energy, energy which is significantly higher than available for proton-proton coincidences.

It is worth noting that both analysis investigated separate, although kinematically similar, regions of breakup phase space. This is especially well visible for E_{tr}^{n} variable in Fig. 5.26. In the case of proton-neutron coincidences the energy transfer is in the range of 8-28 MeV, while for the proton-proton this value is in the range of 32-57 MeV. When sorted according to this variable, the obtained $\chi^2_{\rm red}$ values for the proton-proton coincidences have a peculiar feature. Very large disagreement between data and all theories is observed for low E_{tr}^{n}, in fact almost factor of ten larger than anywhere else. This, in turn, may manifest itself in other observables, like $\Delta\phi_{pp}$. This effect has been overlooked in publication [57]. This indicates that reanalysis of the proton-proton coincidences using the invariant coordinates can be valuable.

Chapter 6

Summary

The main goal of presented doctoral dissertation was to experimentally investigate the ^{1}H(d,pn)p reaction using a deuteron beam with an energy of 160 MeV impinging a liquid hydrogen target. As a result of the deuteron breakup reaction, three free nucleons were produced. Two of them (proton and neutron), detected by the BINA detection system, were used to determine the five-fold differential cross sections of the breakup reactions. This has become possible with the development of new techniques enabling the registration of neutrons in this detector. The most important and difficult steps in the data analysis was to obtain the neutron emission angles and its energy from the time-of-flight method, and to account for configurational efficiency, related to the detector geometry. This required extensive use of precise Monte-Carlo simulations of the detection system. A total of 765 points were obtained for 54 angular configurations in the range of 19 to 27 degrees in the polar angle and 80 to 180 degrees in the relative azimuthal angle of the detected particles.

The cross section results have been obtained for phase-space regions complementary and with almost no overlap to the standard analysis of proton-proton coincidences performed routinely for several experimental campaigns. They have been compared to the theoretical calculations based on different approaches. We have used calculations based on realistic nucleon-nucleon potentials alone (CDB, Av18) and supplemented with three-nucleon force models (TM99 and UIX). Also calculations based on coupled channel formalism with the Δ isobar degree of freedom (CDB+Δ) alone and with the Coulomb interaction (CDB+Δ+C, Av18+UIX+C) were taken into account. In addition to that, a very recent calculations based on the chiral effective field theory were tested for a selected angular configurations.

In the studied phase-space regions have been identified in which most of the calculations converge with each other, however, not always with the experimental data. There are also quite many places with very substantial discrepancies between different models. In spite of far from optimal for neutron detection experimental setup, the overall quality of the obtained results does not deviate significantly from the standard analysis of proton-proton coincidences. The quality of data reproduction was tested using the χ^2_{red} and A-factor method (see Sec. 5.5.1). Among all of the compared theoretical models, the best agreement was obtained for the models containing 3NF and 3NF with Coulomb interaction, depending on the selected method. The best obtained global χ^2_{red} value for CDB+Δ+C model was 1.05, and the global A-factor for CDB+Δ was 0.071 (see Fig. 5.10). On the other hand, it was somewhat surprising that for the models taking into account the TM99 force, the reproduction of experimental data deteriorated, regardless of the type of the 2N potential model adopted. This is in contradiction to the conclusions drawn from the complementary analysis of the ^{1}H(d,pp)n reaction, in which adding the three-nucleon force generally improved agreement between the data and the theories. The observed disagreement for the case of ^{1}H(d,pn)p cannot be entirely attributed to the non-relativistic calculations because

the reaction energy (80 MeV/nucleon) is too small for this. The discrepancies at this energy, which remain even when Urbana IX or TM99 3NF was included, point to the importance of short-range contributions to the 3NF (like $\pi - \rho$, $\rho - \rho$ exchanges).

An interesting observation is the relatively large discrepancy between the results obtained for the calculations performed by the Witała et al. and the Deltuva et al. This effect revealed in both analysis: with the use of χ^2_{red} and A-factor. Such a large discrepancy between the calculations based on the same 2N potential, even greater than the differences caused by the Coulomb or 3NF effects, significantly hinders drawing conclusions about the dynamics of 3N systems. A similar situation was partially observed in the previous analysis of the proton-proton coincidences [57], but not that pronounced.

The agreement between the theory and the experimental data has also been checked in the function of several kinematic variables. For this purpose, we chose variables such as combination of polar angles (θ_p, θ_n) (Figs. 5.13 and 5.14), relative azimuthal angle $\Delta\phi_{pn}$ (Fig. 5.15), proton E_p (Fig. 5.17) and neutron E_n energy (Fig. 5.16). The analysis showed more complicated structure, with different theories obtaining the best agreement in different regions. This was especially visible between the theories containing the Coulomb interactions and those with 3NF. Similar results were observed in the case of variables, based on the Lorentz invariants (Figs. 5.18 to 5.20). They were also used for comparison with previously published data obtained from proton-proton coincidences [57]. This analysis revealed problems with the accuracy of the energy calibrations of protons. Using the detection methods developed for this thesis the calibration can be improved.

The obtained results indicate that the phase space of the breakup reaction abounds in areas where the dynamics of the interaction is still not fully understood. It reassures us once again that a more complete theory of nuclear interactions is needed.

6.1 Outlook

Since late 2000' there was no major progress or upgrade reported on the improvement of TM99 or other three-nucleon force models. Also the coupled-channel approach is being developed only towards 4-nucleon systems. Currently, the LENPIC collaboration is developing model of 3NF based on the chiral effective field theory. In recent years major problems in the theory development have been overcome and it is a general believe that this is the most proper and most consistent approach to build 3- and many-body forces. We are keen on test future calculations with a proper averaging and for a wider range of angular configurations than presented in this thesis.

One of possible improvement of the presented analysis is the use of the so-called kinematic refit. It is a well-established and widely used method in particle physics experiments, applicable in experiments with redundant kinematical information, allowing for better resolution and more accurate particle reconstruction [106]. It may be especially useful around the "corners" of kinematics, where due to relatively low neutron energy resolution, the projection of more distant points on the kinematics is problematic. These regions turn out to be particularly interesting due to the large discrepancies between the various theoretical predictions, caused by the final state interactions. Taking advantage of the fact that neutrons have a lower energy threshold for the detection than protons, a properly implemented kinematic refit procedure can potentially extend the available cross section range towards lower S values.

The data analysis led to the development of tools allowing to study previously inaccessible areas of the deuteron breakup phase space. The next step could be to use these methods to analyse the data from the deuteron-deuteron reaction. The ^{2}H(d,dn)p breakup cross section

can be directly compared to the ones obtained in the standard ^{2}H(d,dp)n analysis [100], under the same kinematic conditions. The difference between the results can be used to study Coulomb force effects directly.

Moreover, the conducted data analysis showed which areas of the phase space are especially sensitive to various effects of the 3-body dynamics and in which, on the contrary, the addition of other components practically does not affect the obtained theoretical cross sections. This may be helpful in designing future measurements. Research on few-nucleon systems will be continued at the Cyclotron Center Bronowice, also with the use of neutron detection. For this purpose, a dedicated neutron detector [107] is being developed. Also at CCB, an new experiment will be carried out in the near future to investigate the relativistic effects in *pd* collisions, in which the author of this thesis plays the role of PI [59].

Last but not least this analysis showed the need of the reanalysis of proton-proton coincidences, taking advantage from experiences and tools described in this thesis.

Appendix A

Simulation output structure

The table below shows the ROOT-based tree structure used in the simulations output file (see Sec. 4.3.4) developed for this thesis. The # is the particle number.

Branch name	Description
evNum#	Event number #
fPType#	Particle kind (1-protons, 2-deuterons, 3-neutrons) for the particle #
fX#	Position along x axis for the particle #
fY#	Position along y axis for the particle #
fEn#	Initial energy of the particle #
fEd#	Energy deposited in E detector for the particle #
fEddE#	Energy deposited in ΔE detector for the particle #
fE#	E detector number hitted by the particle #
fdE#	ΔE detector number hitted by the particle #
fTh#	θ angle for the particle #
fPhi#	ϕ angle for the particle #
fTOF#	TOF value for the particle #
fFlagMWPC#	Particle # detection in MWPC
fFlagE#	Particle # detection in E
fFlagdE#	Particle # detection in ΔE
fXv#	Initial vertex position x (in the target) for the particle #
fYv#	Initial vertex position y (in the target) for the particle #
fZv#	Initial vertex position z (in the target) for the particle #

Table A.1: Structure of the output file

Appendix B

Time correction values

In this Appendix we present the global ($\tau^{i,j}$) and local (τ^{i}_{L-R}) time corrections values of the i-th and j-th E detector element. The definition of these corrections is explained in Sec. 4.4.3.

i	0	1	2	3	4	5	6	7	8	9
τ^{i}_{L-R}	114,7	20,35	-26,06	-47,66	-12,37	-9,93	3,55	-51,98	-14,01	1,67

Table B.1: τ^{i}_{L-R} correction values, all values are in ns.

$i \setminus j$	0	1	2	3	4	5	6	7	8	9
0	0,0	2,67	-1,2	1,31	3,33	3,70	-4,80	-1,60	-1,29	-1,27
1	-	0,0	-3,81	-1,19	0,66	0,87	-7,58	-4,39	-4,01	-4,19
2	-	-	0,0	2,75	4,67	4,81	-3,96	-0,88	-0,59	-0,75
3	-	-	-	0,0	1,91	2,06	-6,42	-3,51	-3,54	-3,29
4	-	-	-	-	0,0	0,33	-8,29	-5,36	-5,40	-4,94
5	-	-	-	-	-	0,0	-4,46	-5,57	-5,59	-4,91
6	-	-	-	-	-	-	0,0	3,01	3,27	4,10
7	-	-	-	-	-	-	-	0,0	0,107	0,87
8	-	-	-	-	-	-	-	-	0,0	0,66
9	-	-	-	-	-	-	-	-	-	0,0

Table B.2: $\tau^{i,j}$ correction values, all values are in ns

Appendix C

χ^2_{red} and A-factor results

This Appendix contains the obtained χ^2_{red} and A-factor results (see Sec. 5.5.1) collected together for all individual angular configurations. Each of the theoretical model is presented in a separate figure. The abbreviations are explained in Fig. 5.9.

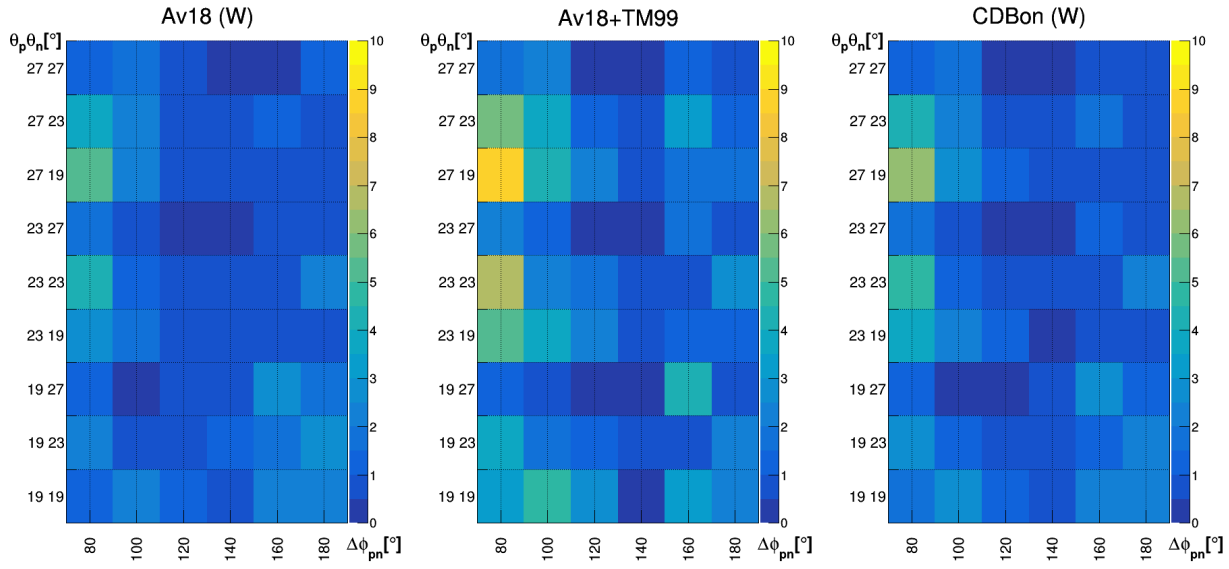

Figure C.1: The χ^2_{red} for individual configurations of the ^{1}H(d,pn)p reaction defined by polar angles (θ_p,θ_n) on vertical axis and by relative azimuthal angle $\Delta\phi_{pn}$ on horizontal axis.

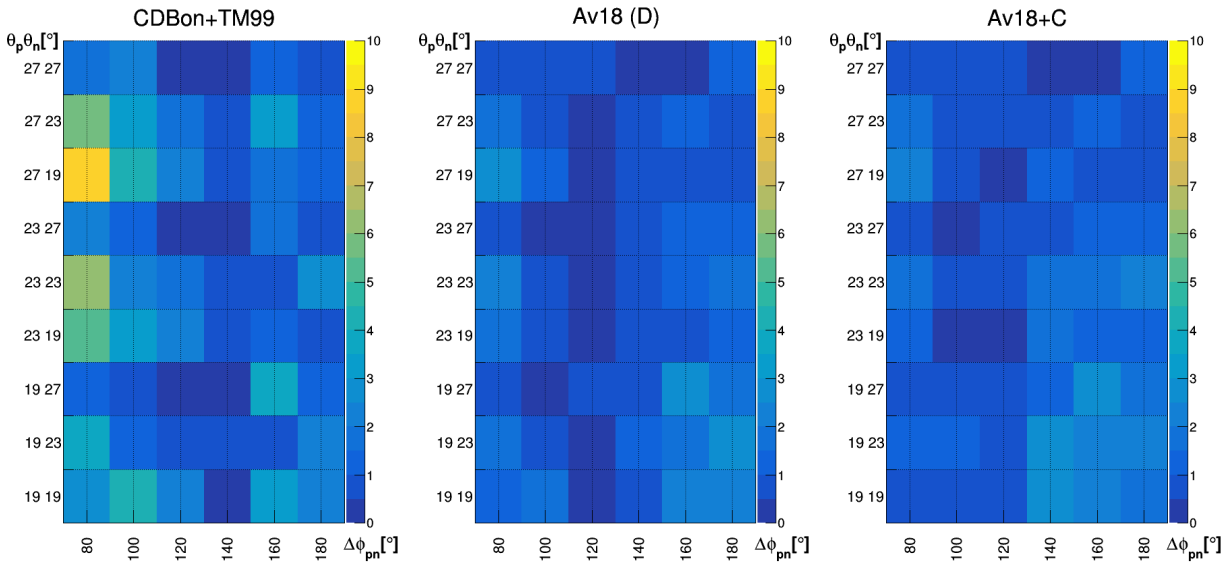

Figure C.2: Similar as in Fig. C.1 but for different theoretical models

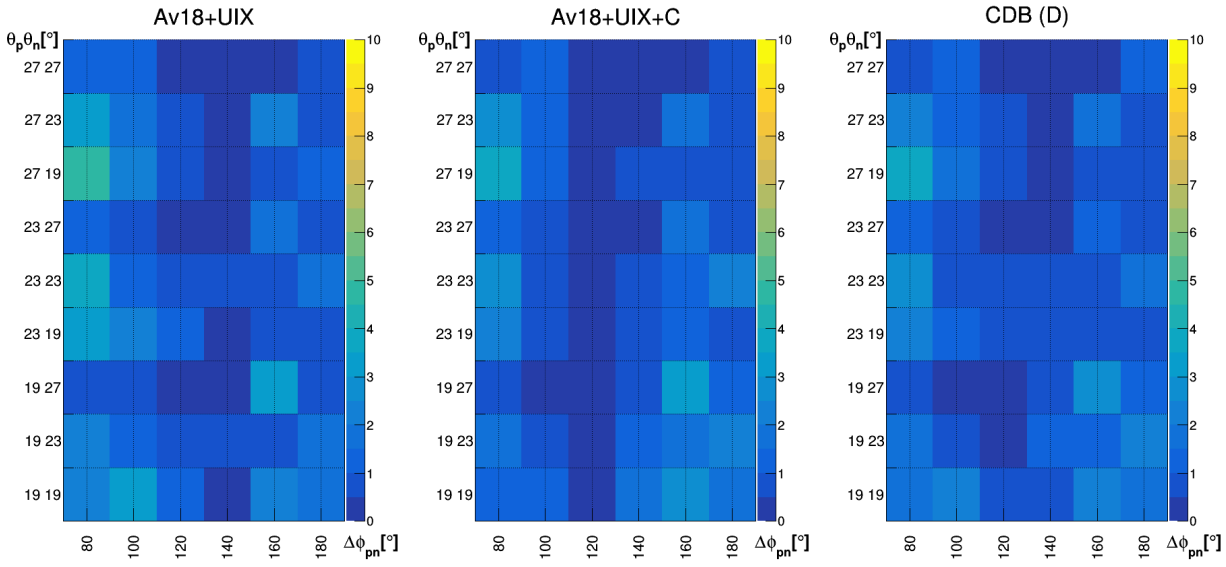

Figure C.3: Similar as in Fig. C.1 but for different theoretical models

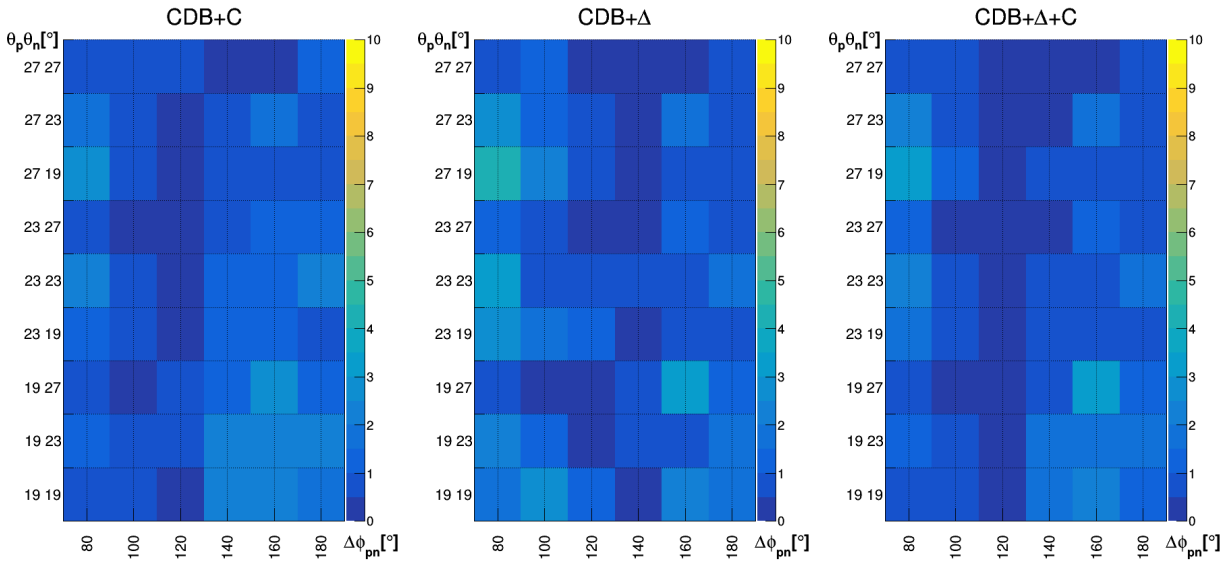

Figure C.4: Similar as in Fig. C.1 but for different theoretical models

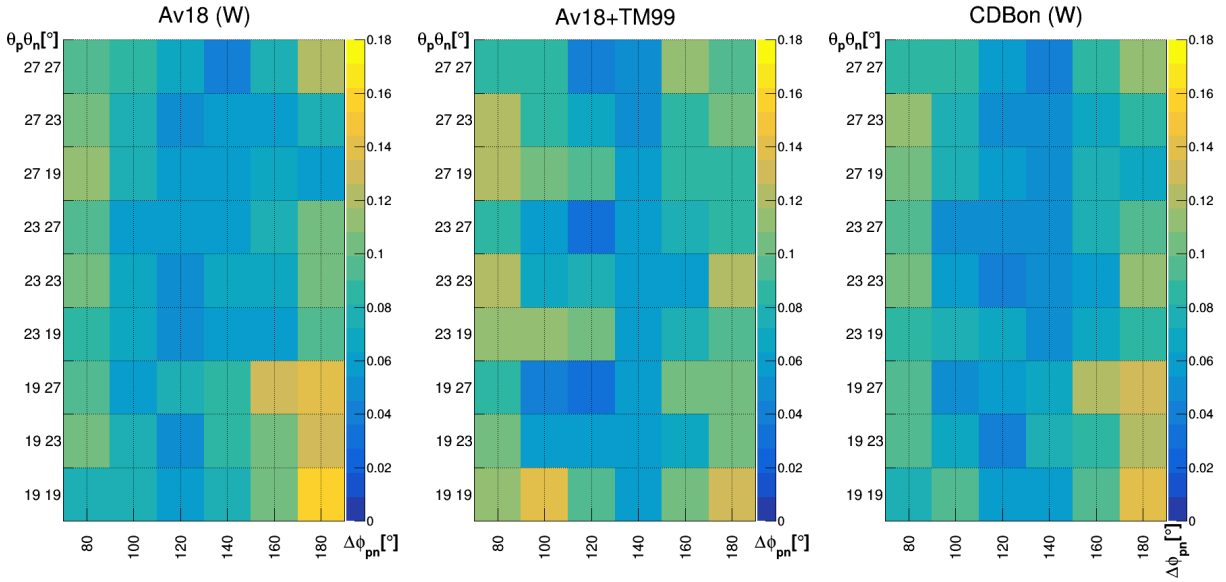

Figure C.5: A-factor for individual configurations of the ^{1}H(d,pn)p reaction defined by polar angles (θ_p,θ_n) on vertical axis and by relative azimuthal angle $\Delta\phi_{pn}$ on horizontal axis.

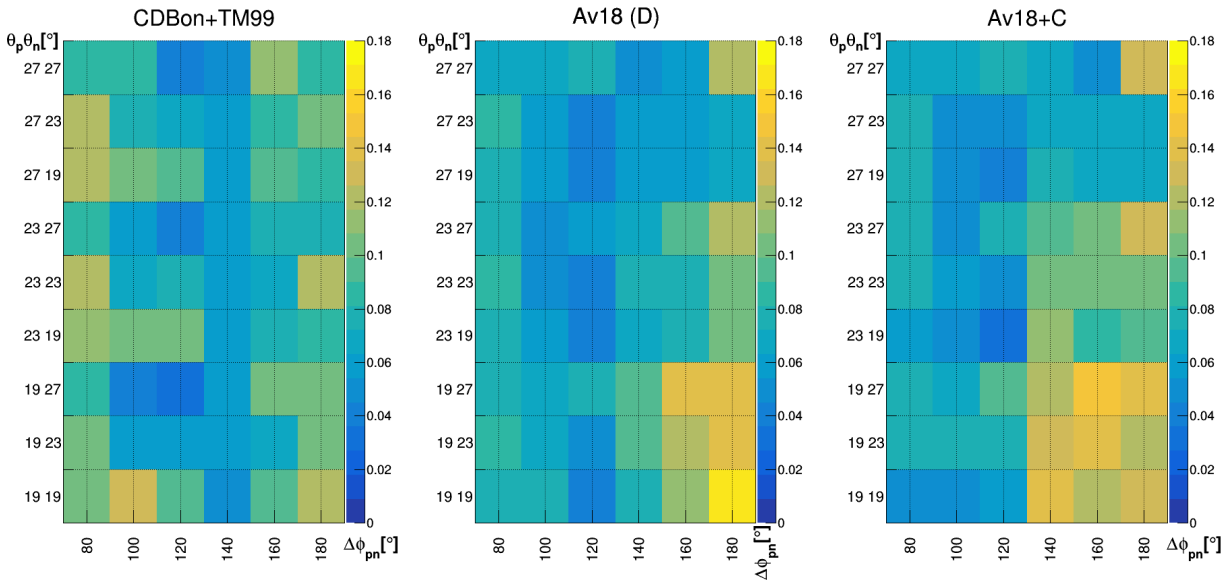

Figure C.6: Similar as in Fig. C.5 but for different theoretical models

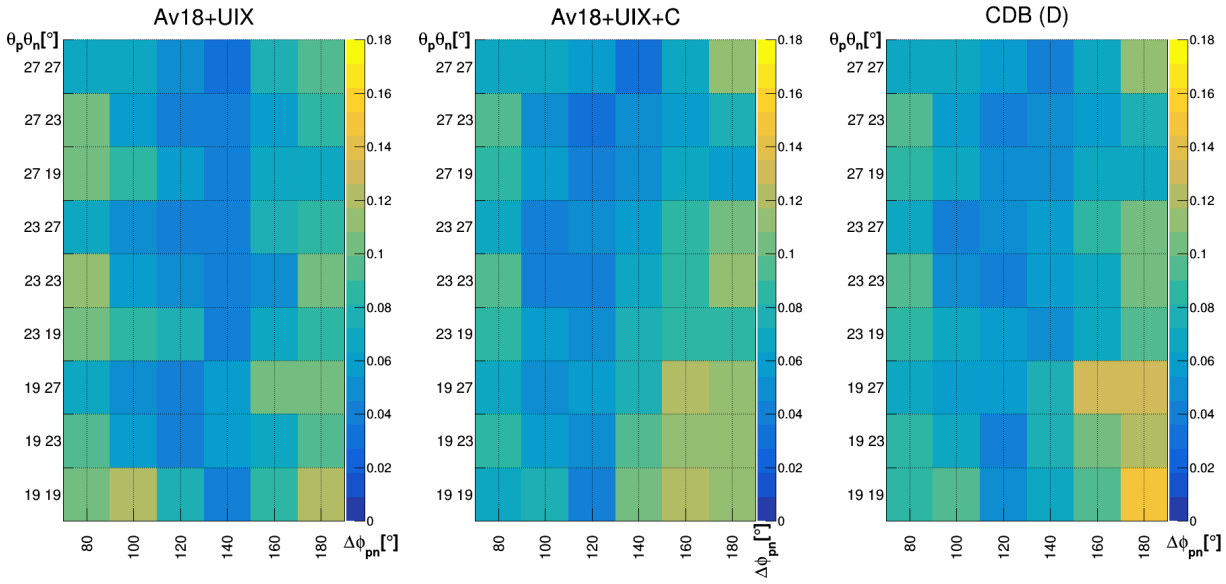

Figure C.7: Similar as in Fig. C.5 but for different theoretical models

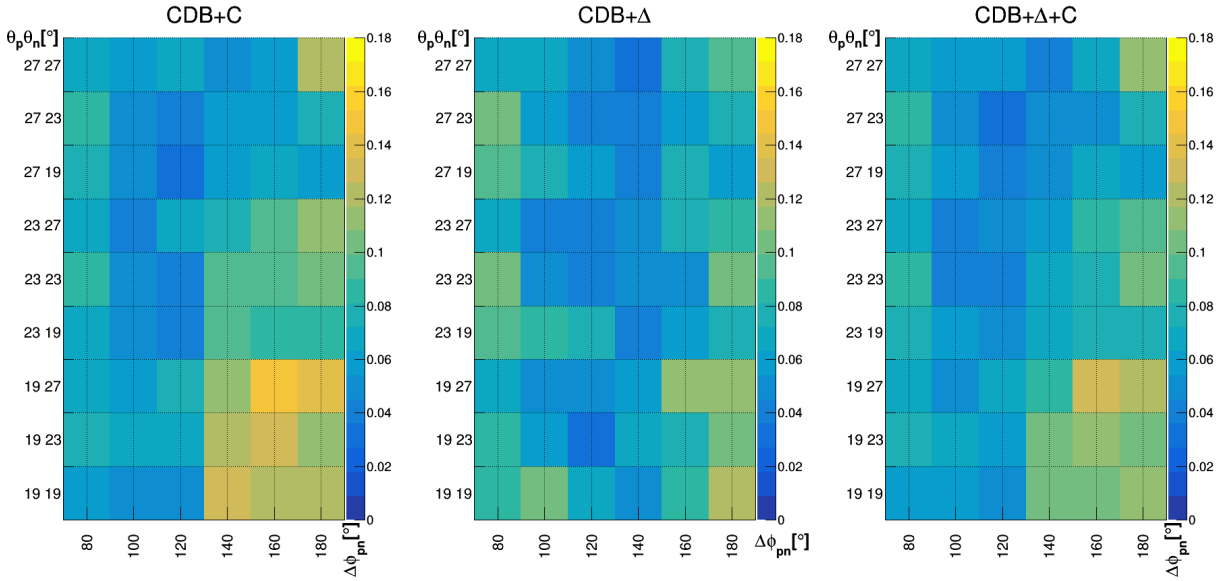

Figure C.8: Similar as in Fig. C.5 but for different theoretical models

Appendix D

Breakup Cross-section Results

This Appendix contains a full collection of the differential cross-section distributions of the ^{1}H(d,pn)p breakup reaction obtained in this analysis. The results are collected in sets with the same θ_p and θ_n, and with different $\Delta\phi_{pn}$ angles. To make the comparison between the data and calculations easier, we have divided the theoretical models into three groups. Each group is focused on different aspects of the few-nucleon dynamics. In each group, calculations based on the pure Av18 and CDB models (by Deltuva et al.) were shown as a reference. For better visibility, each data set has been presented in a separate figure.

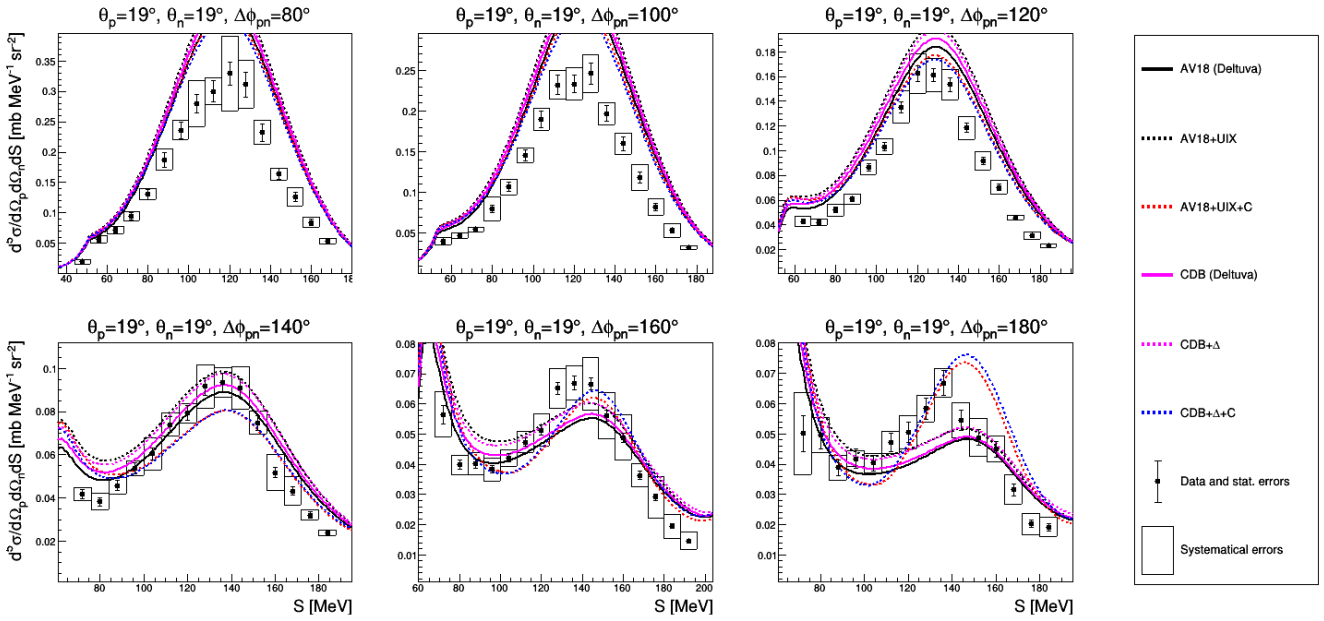

Figure D.1: Results at $\theta_p = 19°, \theta_n = 19°$ and for different $\Delta\phi_{pn}$ lines represent different theoretical models (specified in the legend).

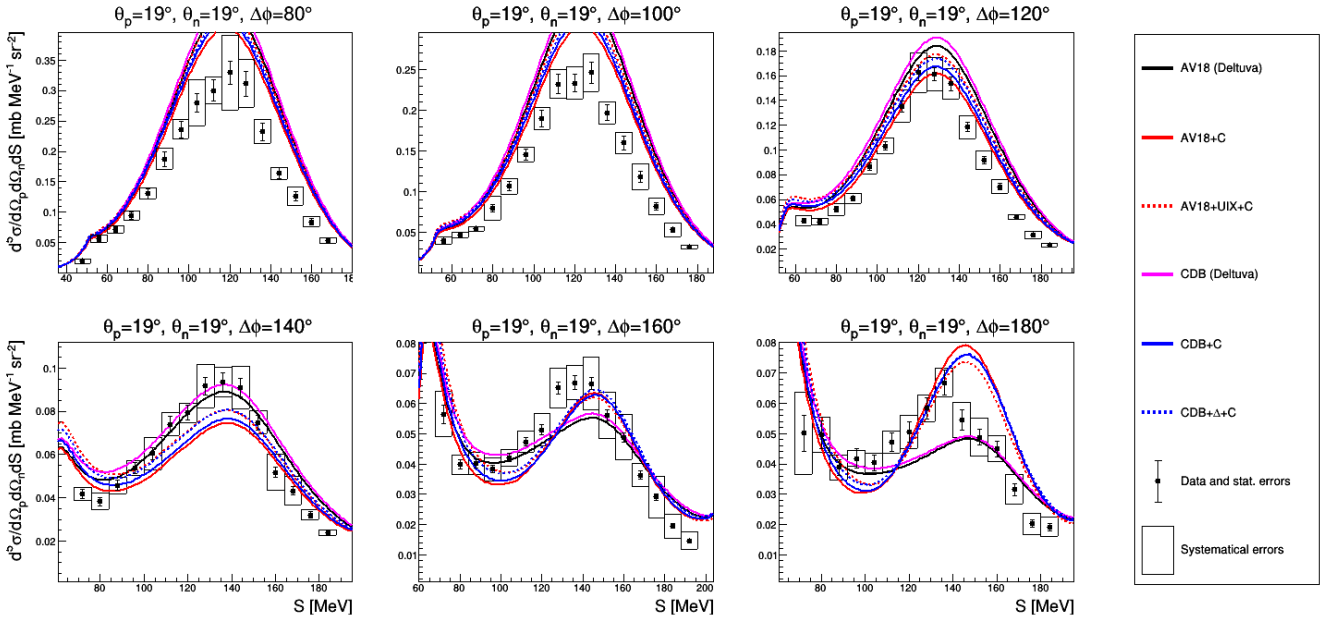

Figure D.2: The same as Fig. D.1 but for different set of theoretical models (specified in the legend).

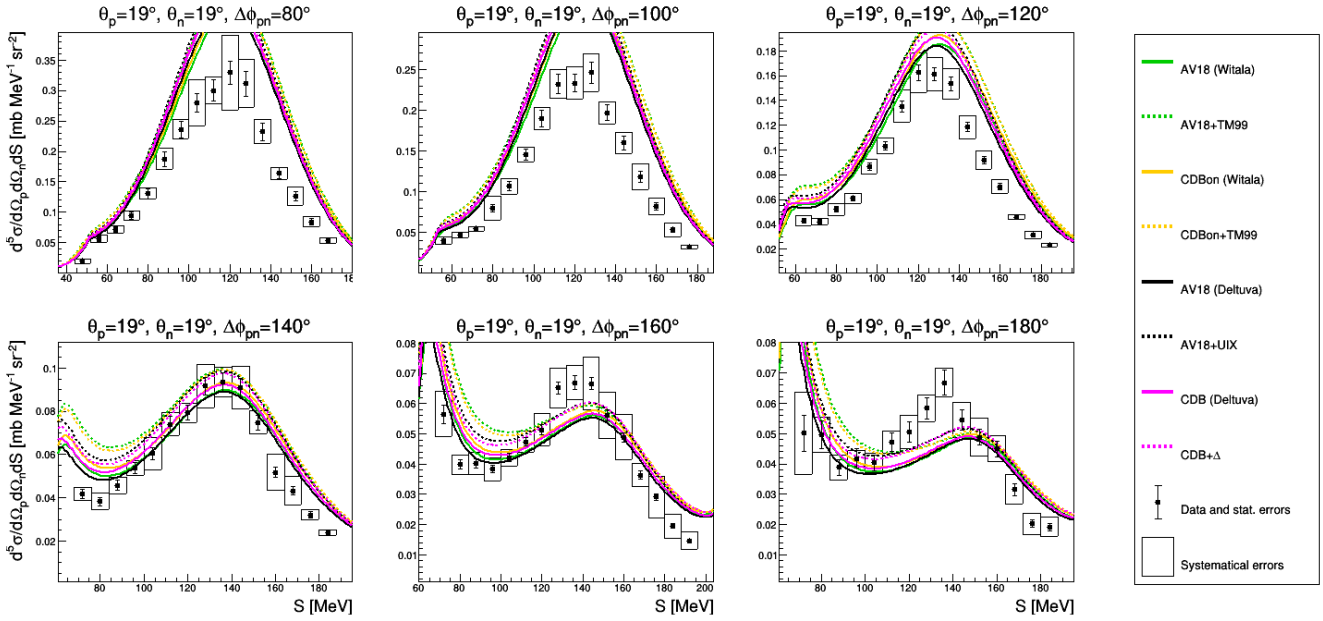

Figure D.3: The same as Fig. D.1 but for different set of theoretical models (specified in the legend).

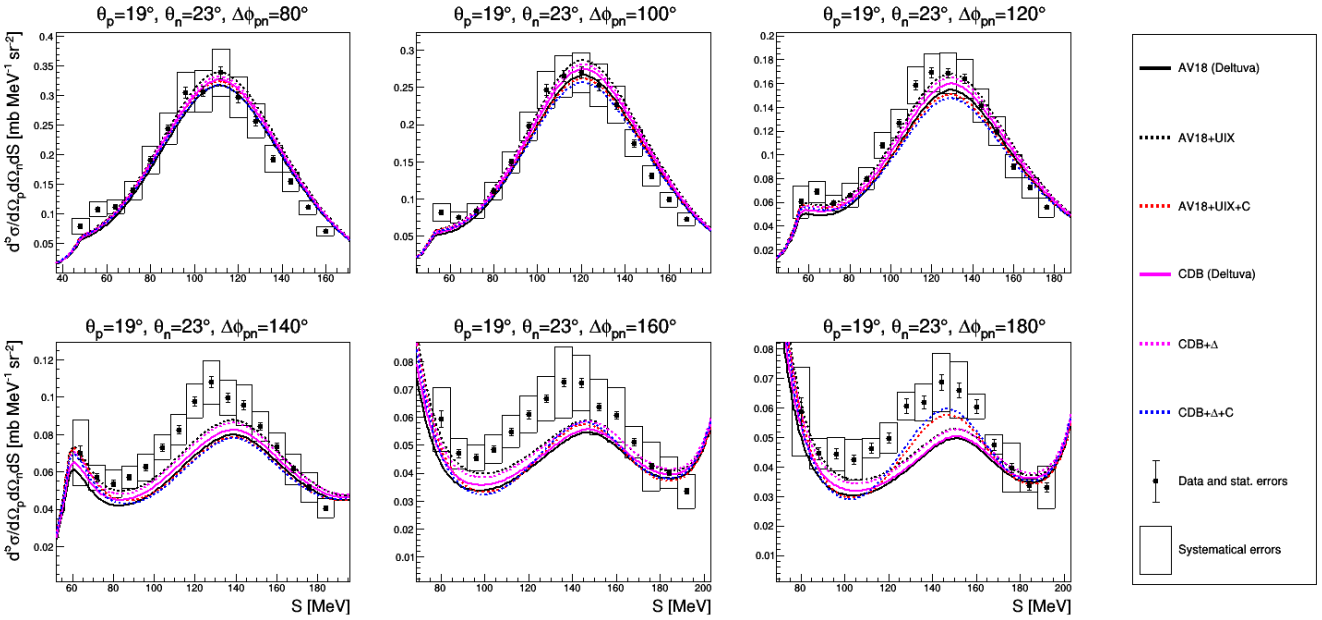

Figure D.4: Results at $\theta_p = 19°, \theta_n = 23°$ and for different $\Delta\phi_{pn}$ lines represent different theoretical models (specified in the legend).

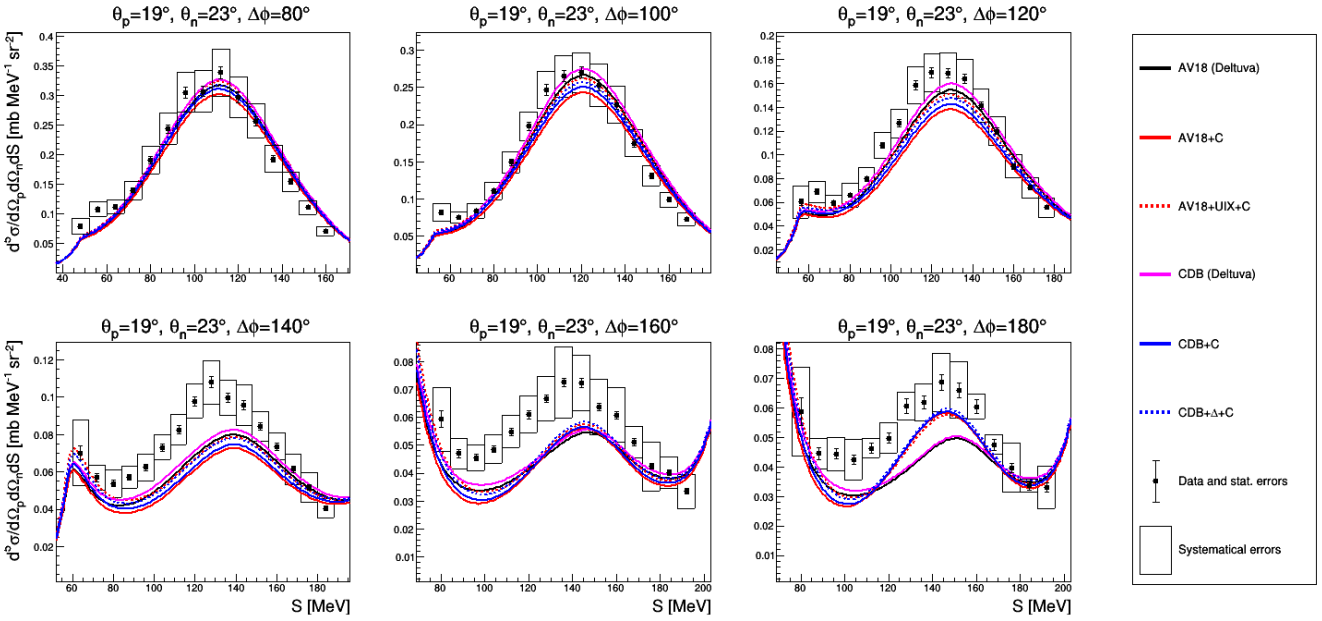

Figure D.5: The same as Fig. D.4 but for different set of theoretical models (specified in the legend).

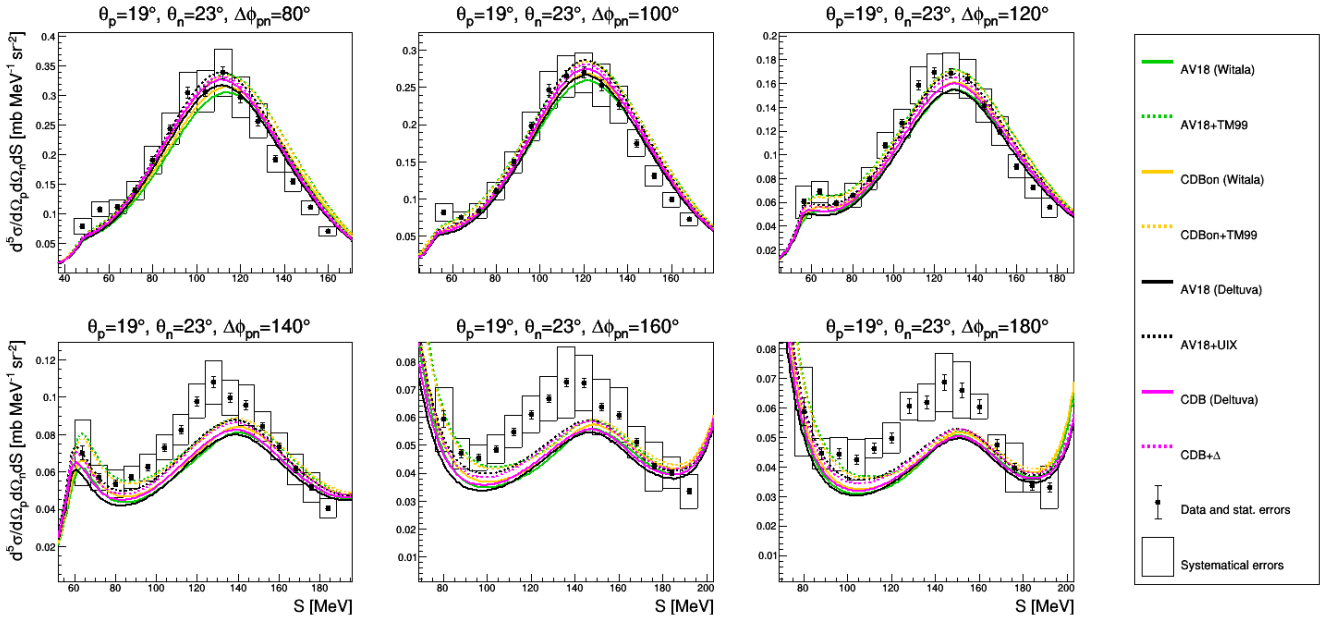

Figure D.6: The same as Fig. D.4 but for different set of theoretical models (specified in the legend).

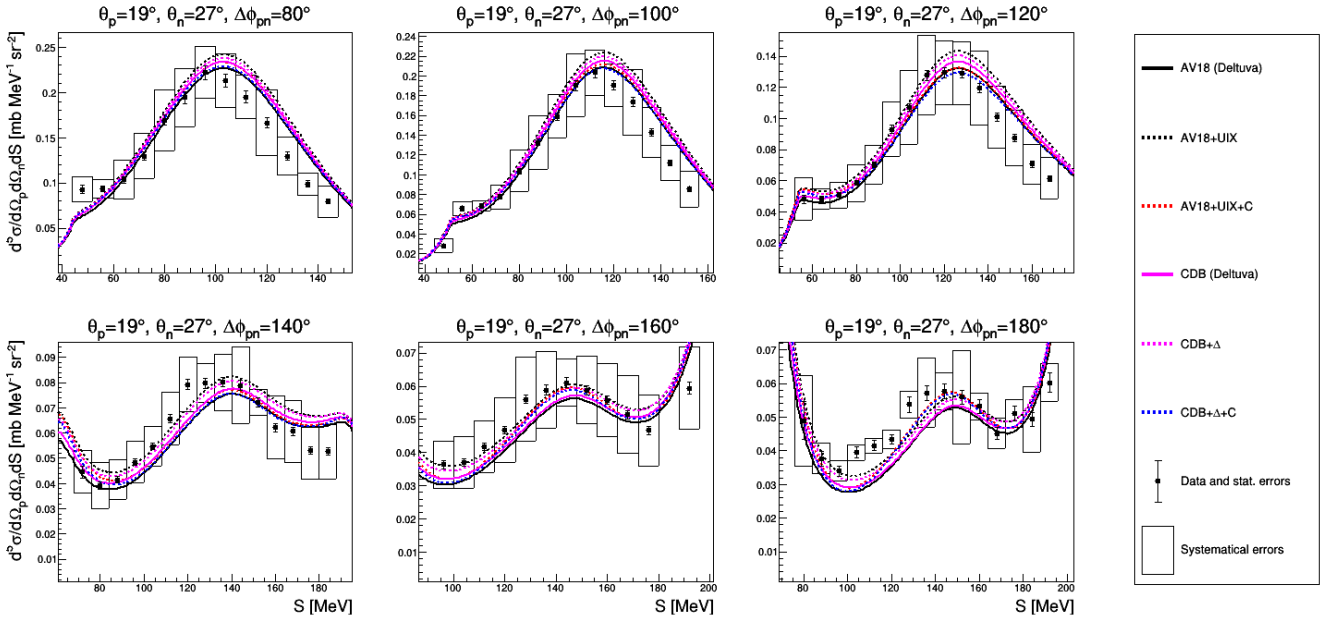

Figure D.7: Results at $\theta_p = 19°, \theta_n = 27°$ and for different $\Delta\phi_{pn}$ lines represent different theoretical models (specified in the legend).

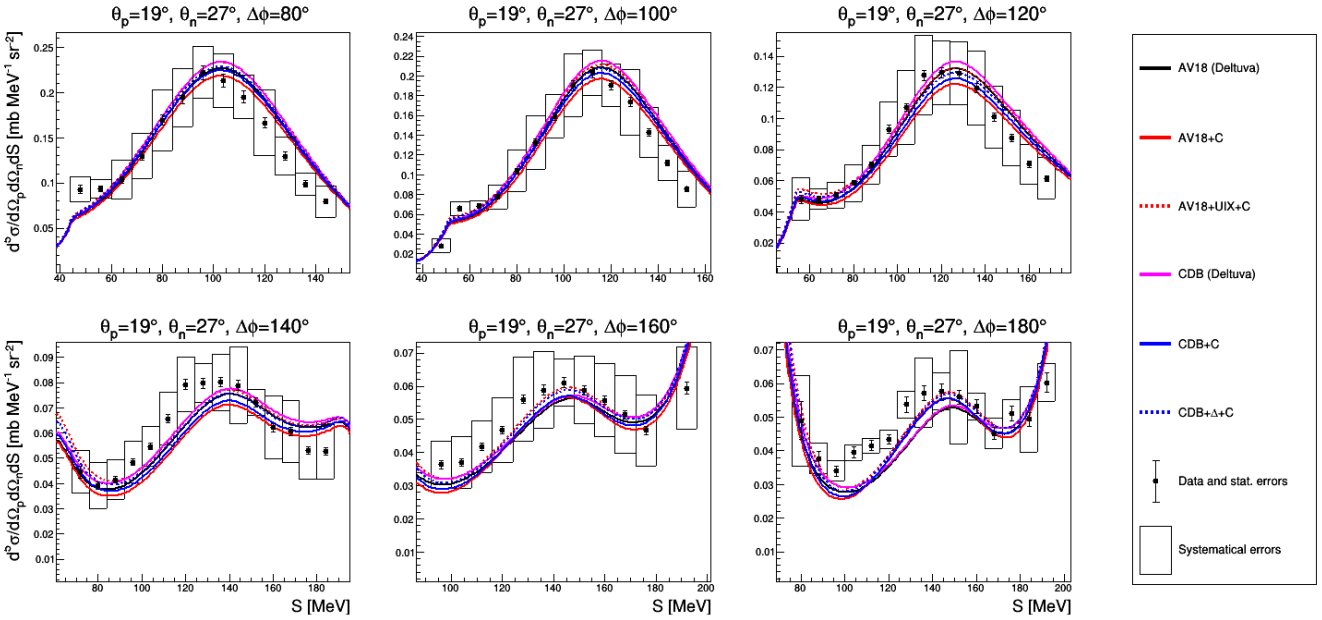

Figure D.8: The same as Fig. D.7 but for different set of theoretical models (specified in the legend).

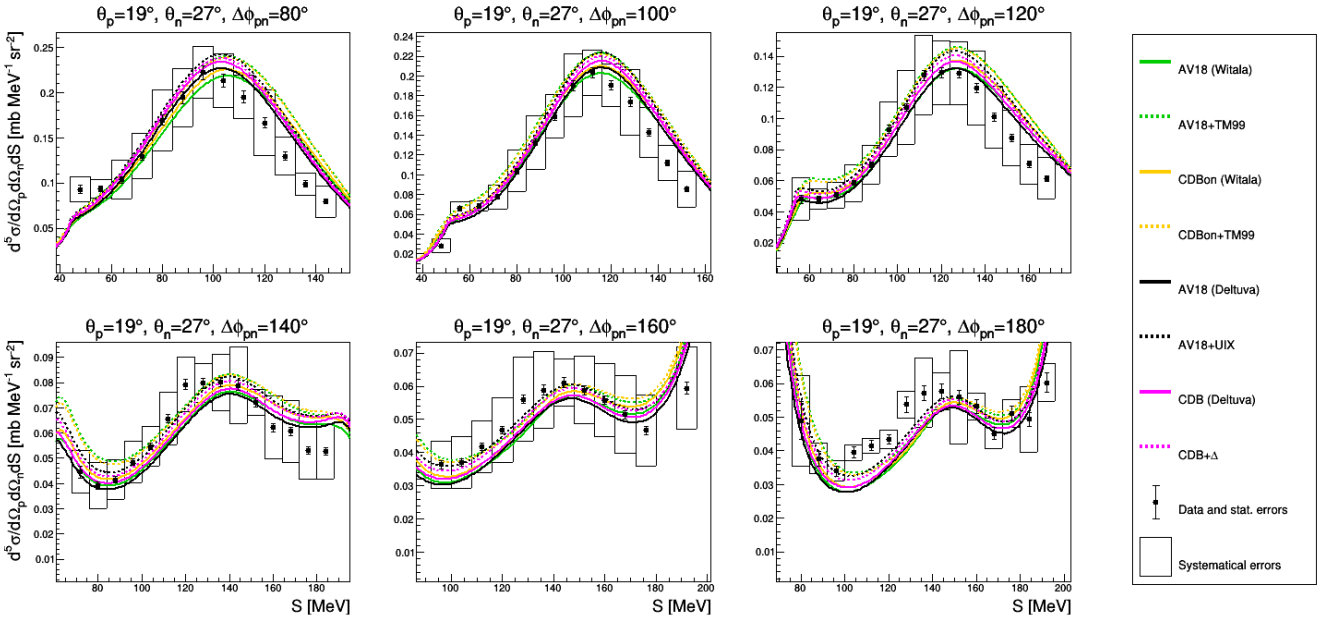

Figure D.9: The same as Fig. D.7 but for different set of theoretical models (specified in the legend).

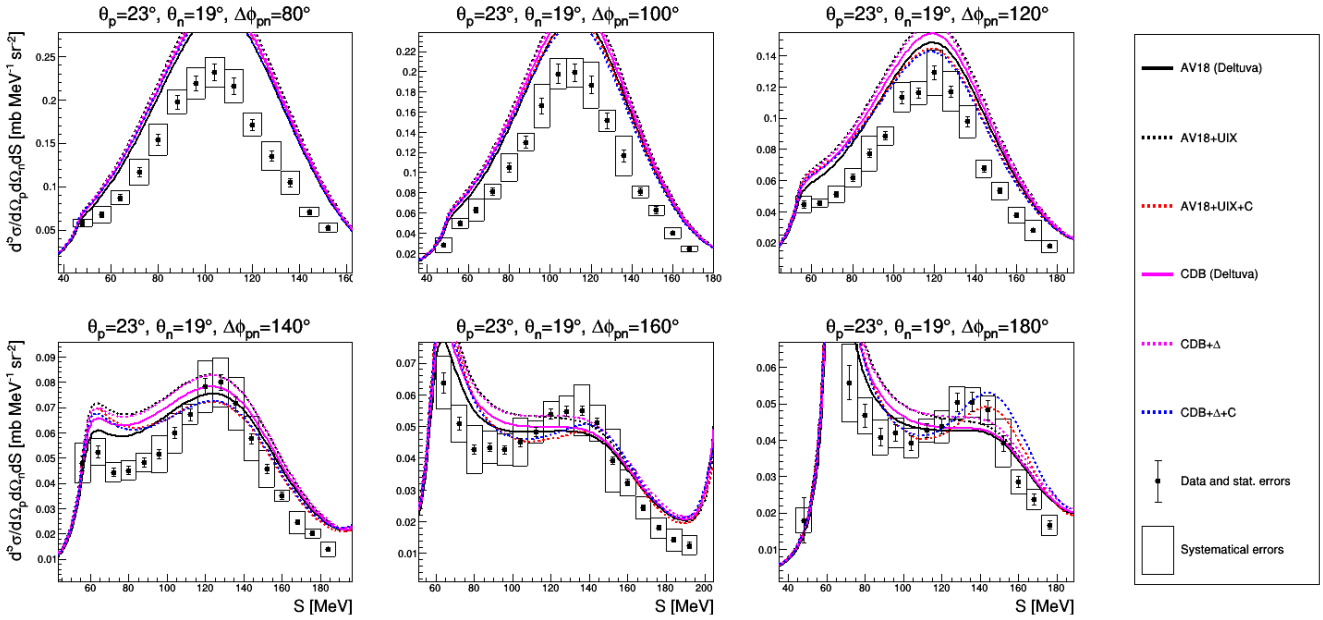

Figure D.10: Results at $\theta_p = 23°, \theta_n = 19°$ and for different $\Delta\phi_{pn}$ lines represent different theoretical models (specified in the legend).

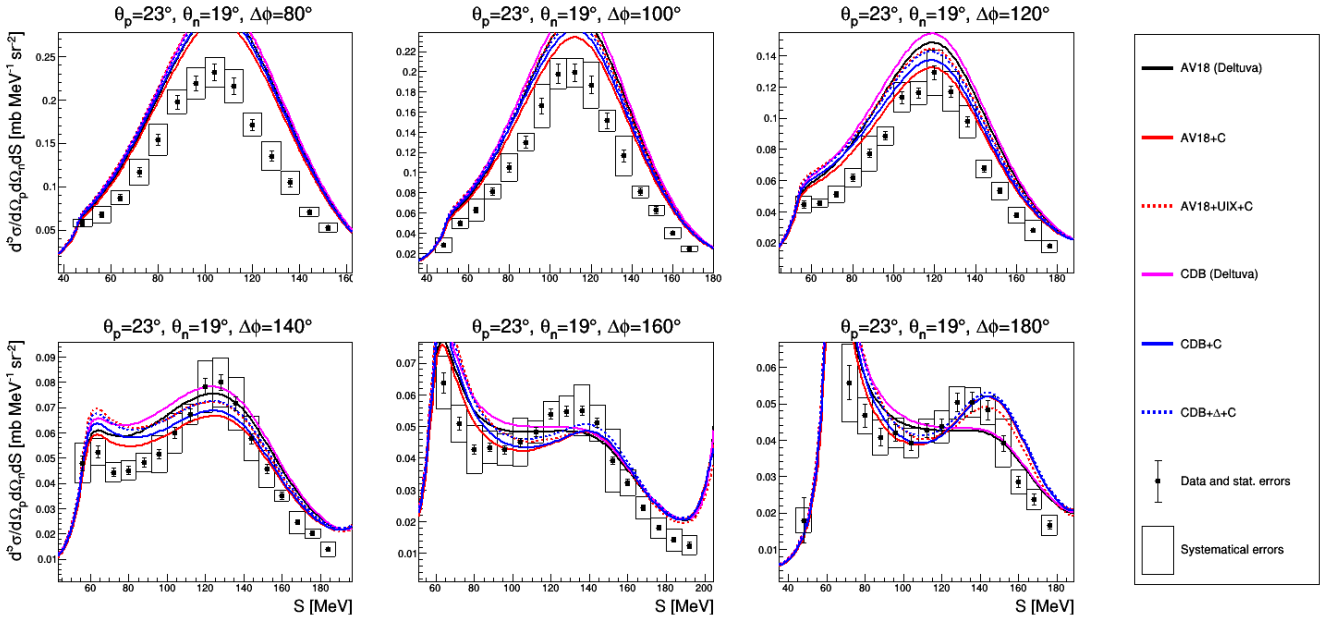

Figure D.11: The same as Fig. D.10 but for different set of theoretical models (specified in the legend).

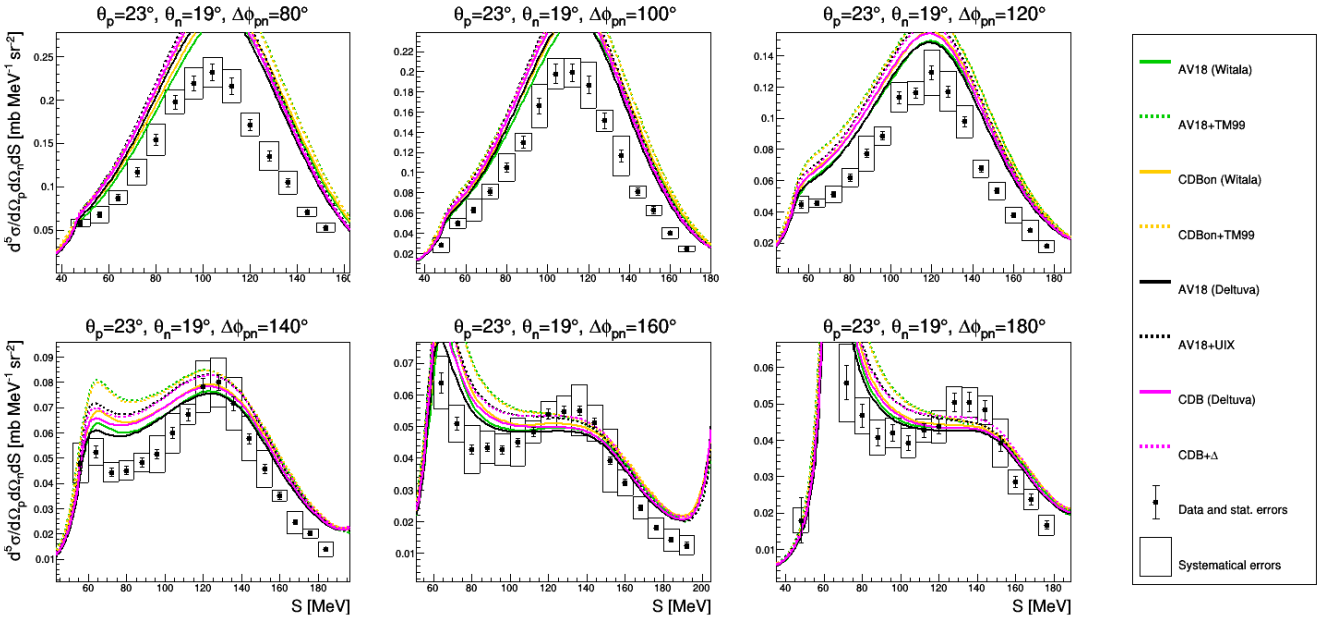

Figure D.12: The same as Fig. D.10 but for different set of theoretical models (specified in the legend).

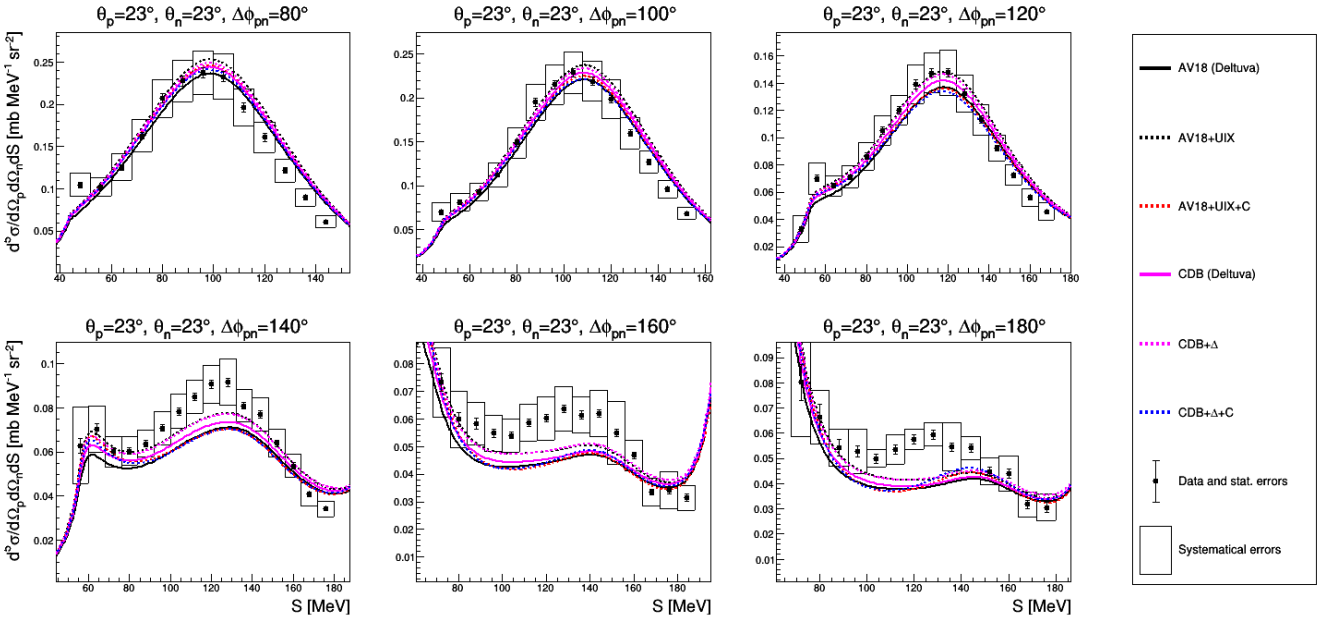

Figure D.13: Results at $\theta_p = 23°, \theta_n = 23°$ and for different $\Delta\phi_{pn}$ lines represent different theoretical models (specified in the legend).

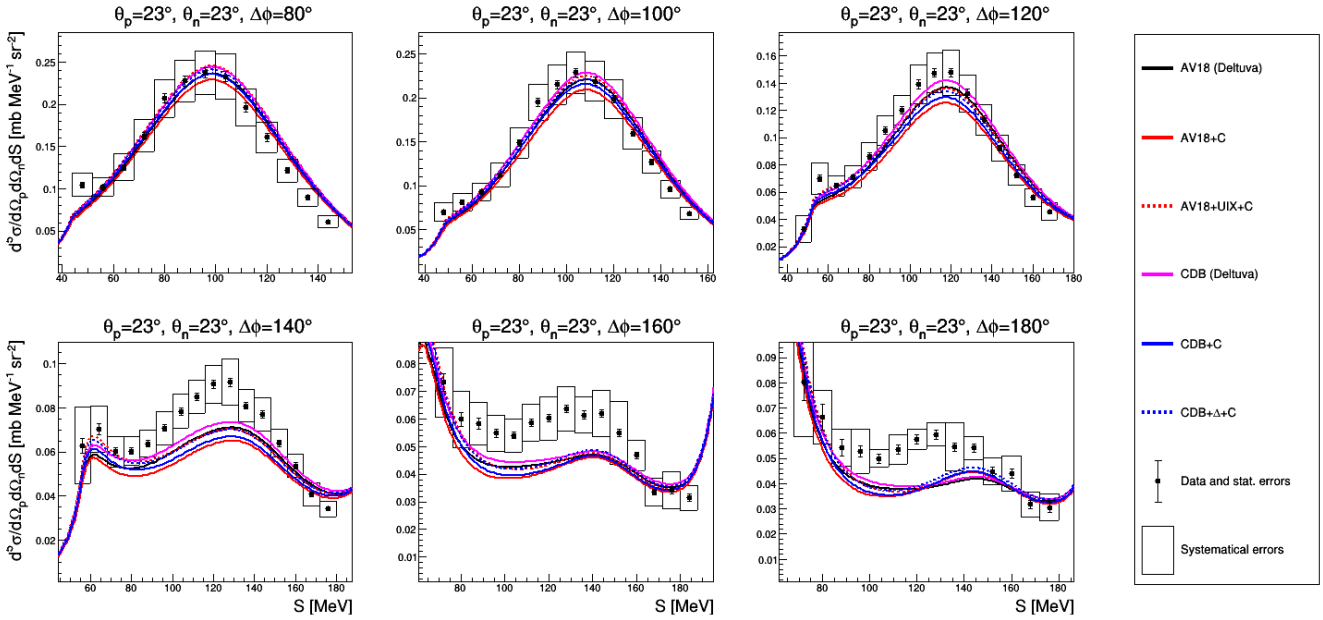

Figure D.14: The same as Fig. D.13 but for different set of theoretical models (specified in the legend).

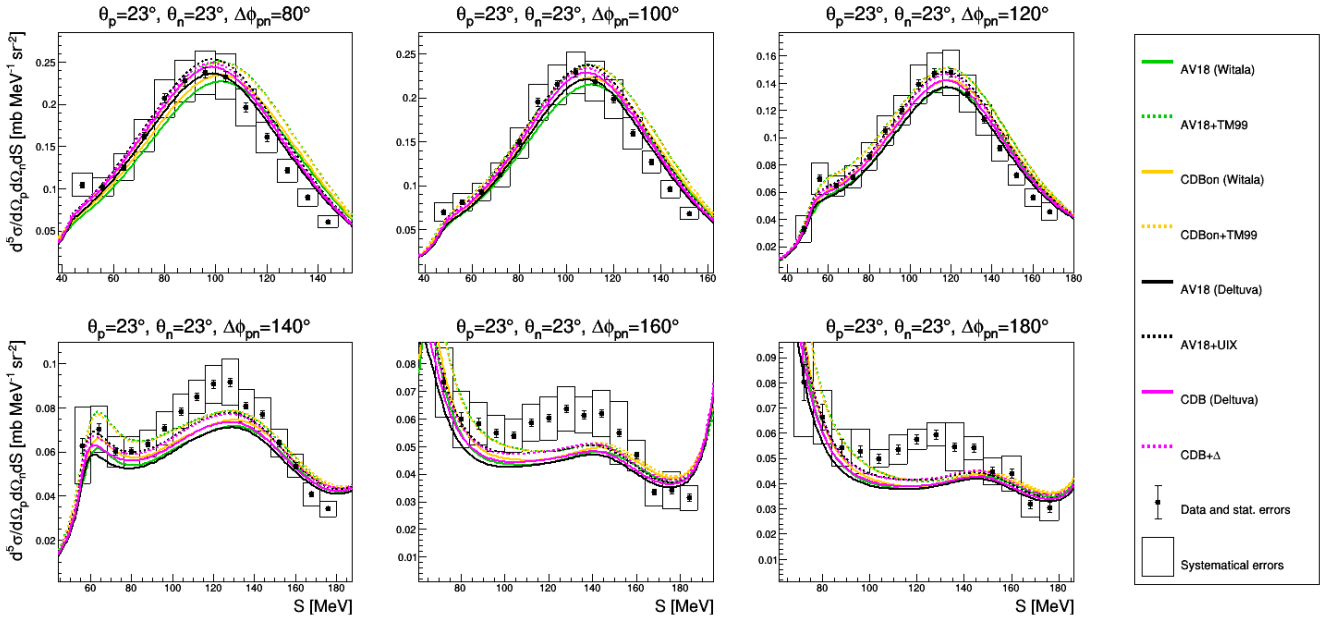

Figure D.15: The same as Fig. D.13 but for different set of theoretical models (specified in the legend).

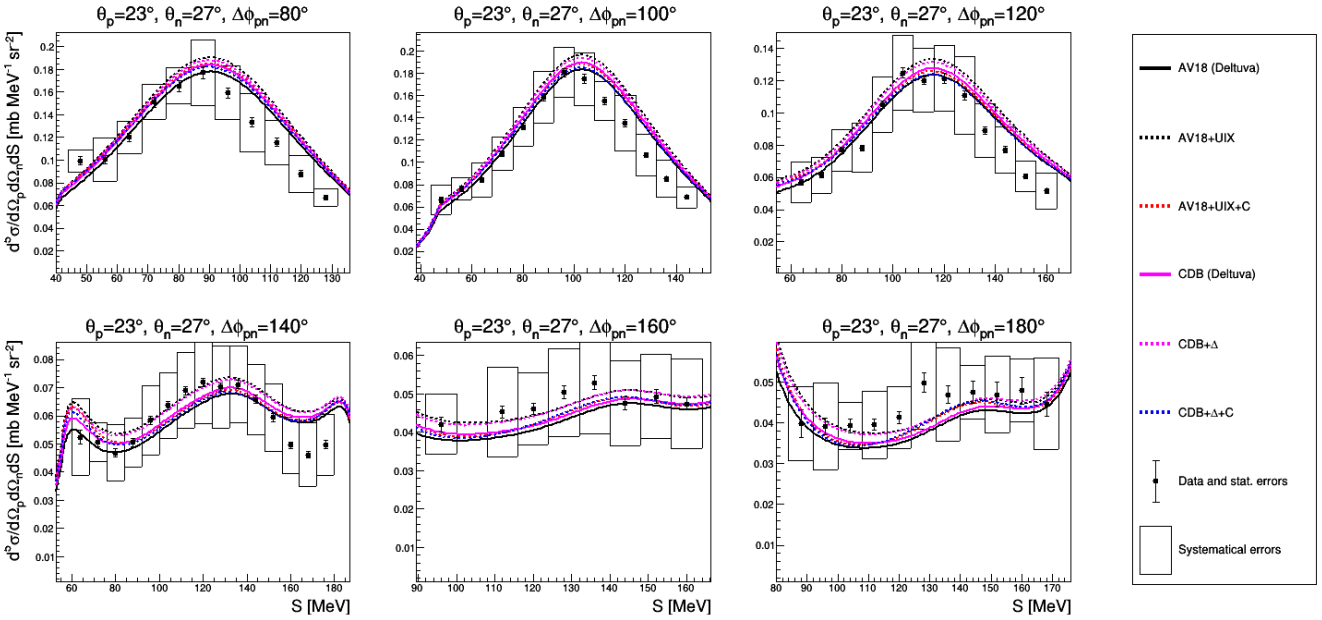

Figure D.16: Results at $\theta_p = 23°, \theta_n = 27°$ and for different $\Delta\phi_{pn}$ lines represent different theoretical models (specified in the legend).

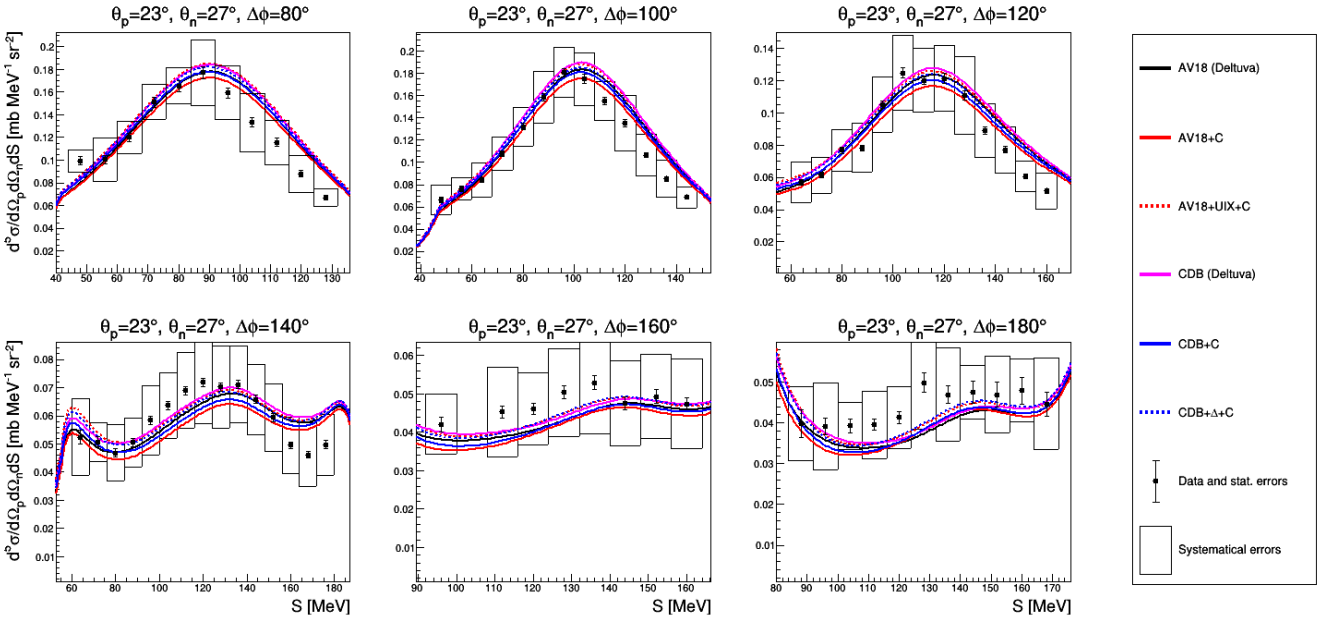

Figure D.17: The same as Fig. D.16 but for different set of theoretical models (specified in the legend).

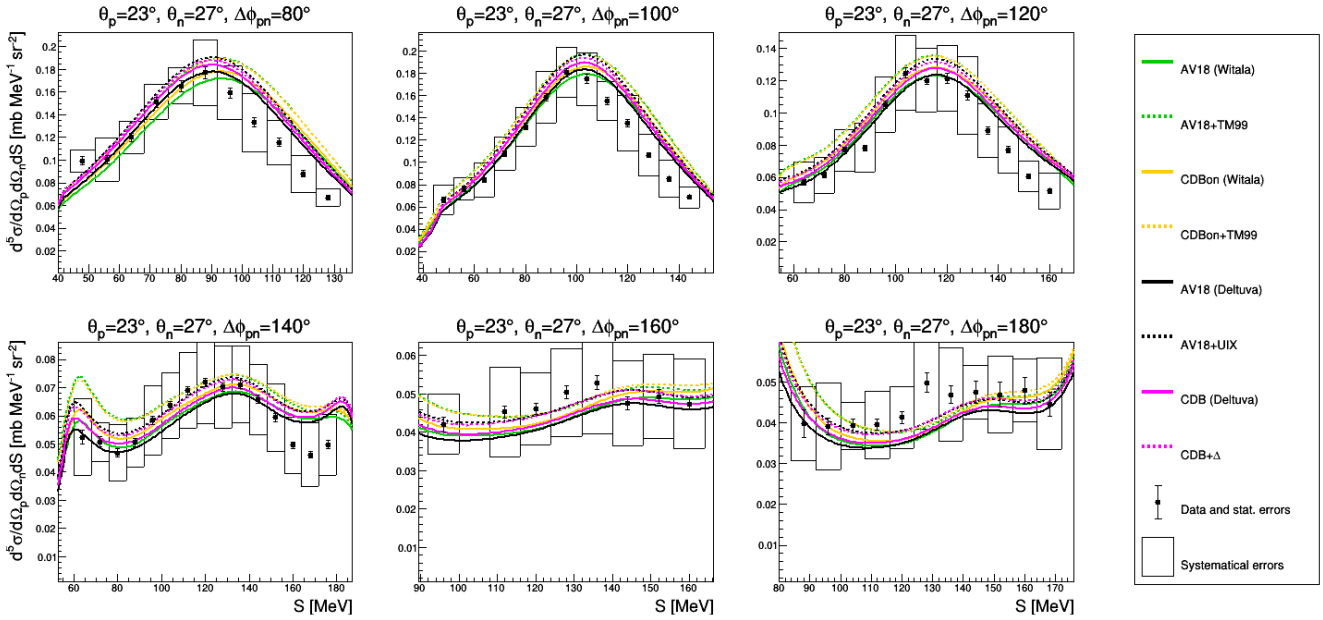

Figure D.18: The same as Fig. D.16 but for different set of theoretical models (specified in the legend).

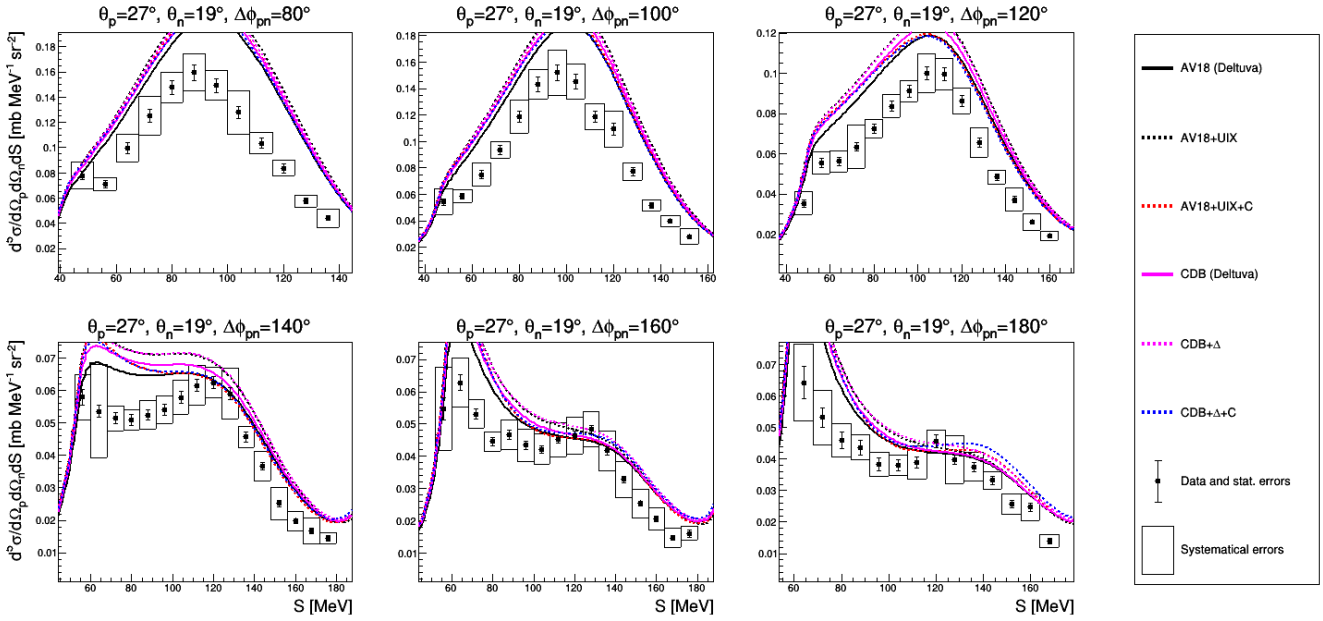

Figure D.19: Results at $\theta_p = 27°, \theta_n = 19°$ and for different $\Delta\phi_{pn}$ lines represent different theoretical models (specified in the legend).

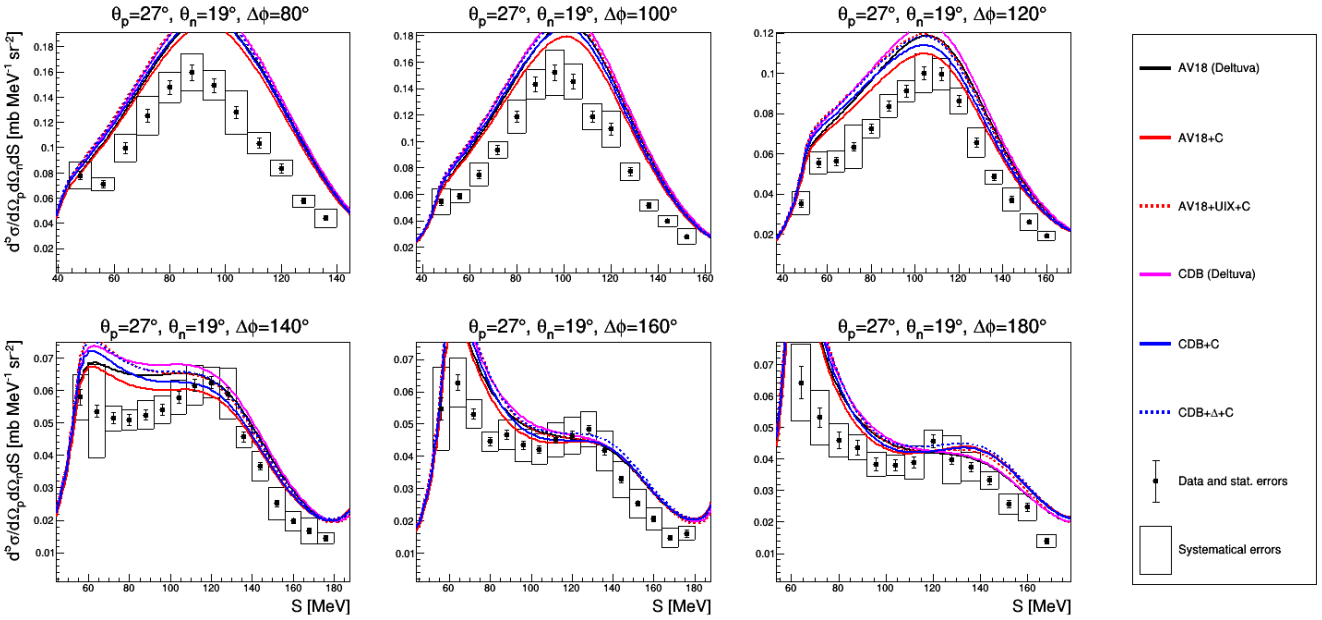

Figure D.20: The same as Fig. D.19 but for different set of theoretical models (specified in the legend).

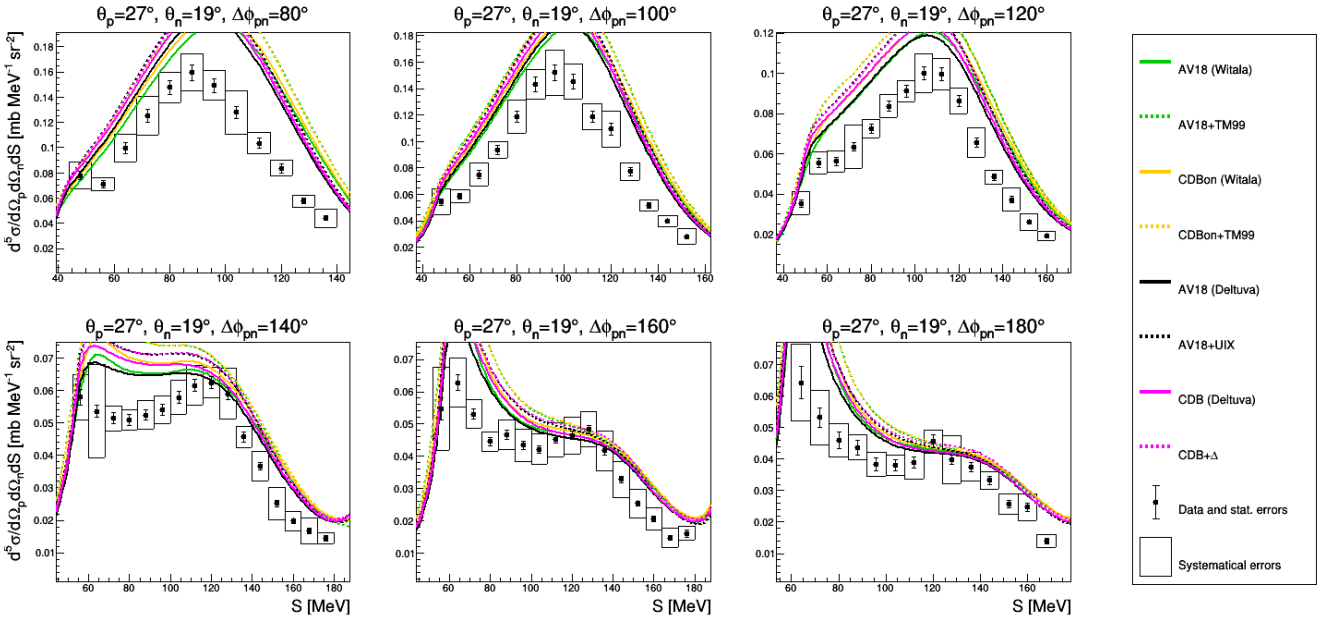

Figure D.21: The same as Fig. D.19 but for different set of theoretical models (specified in the legend).

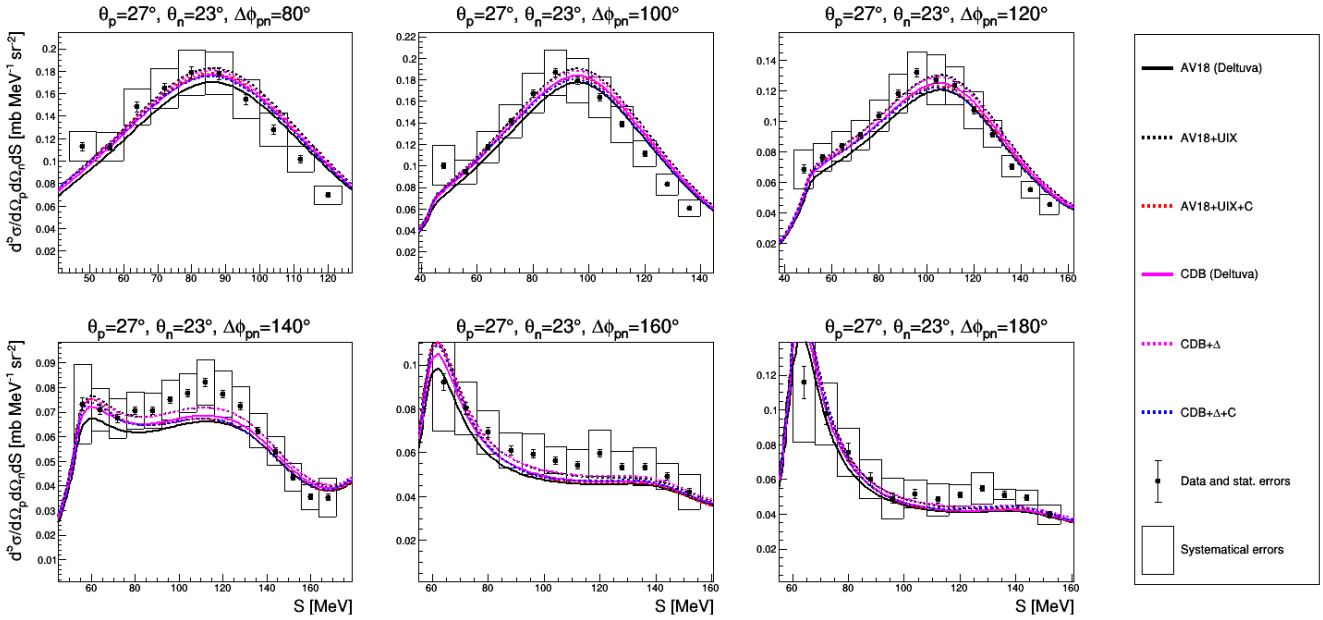

Figure D.22: Results at $\theta_p = 27°, \theta_n = 23°$ and for different $\Delta\phi_{pn}$ lines represent different theoretical models (specified in the legend).

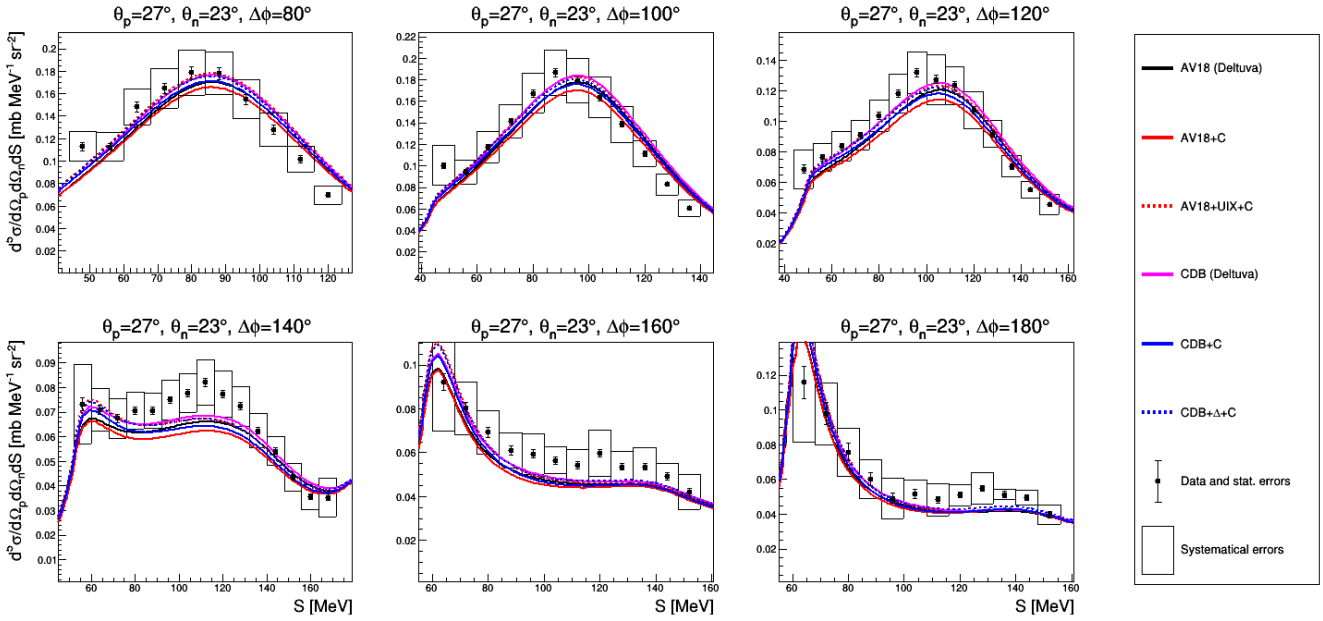

Figure D.23: The same as Fig. D.22 but for different set of theoretical models (specified in the legend).

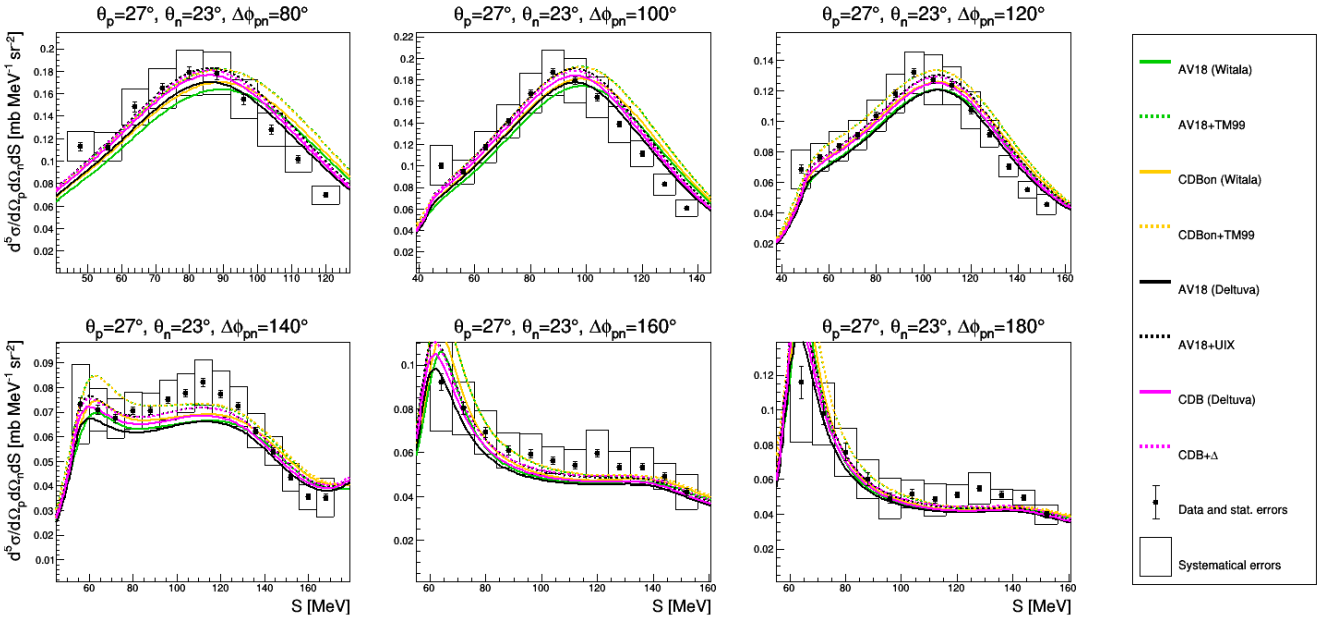

Figure D.24: The same as Fig. D.22 but for different set of theoretical models (specified in the legend).

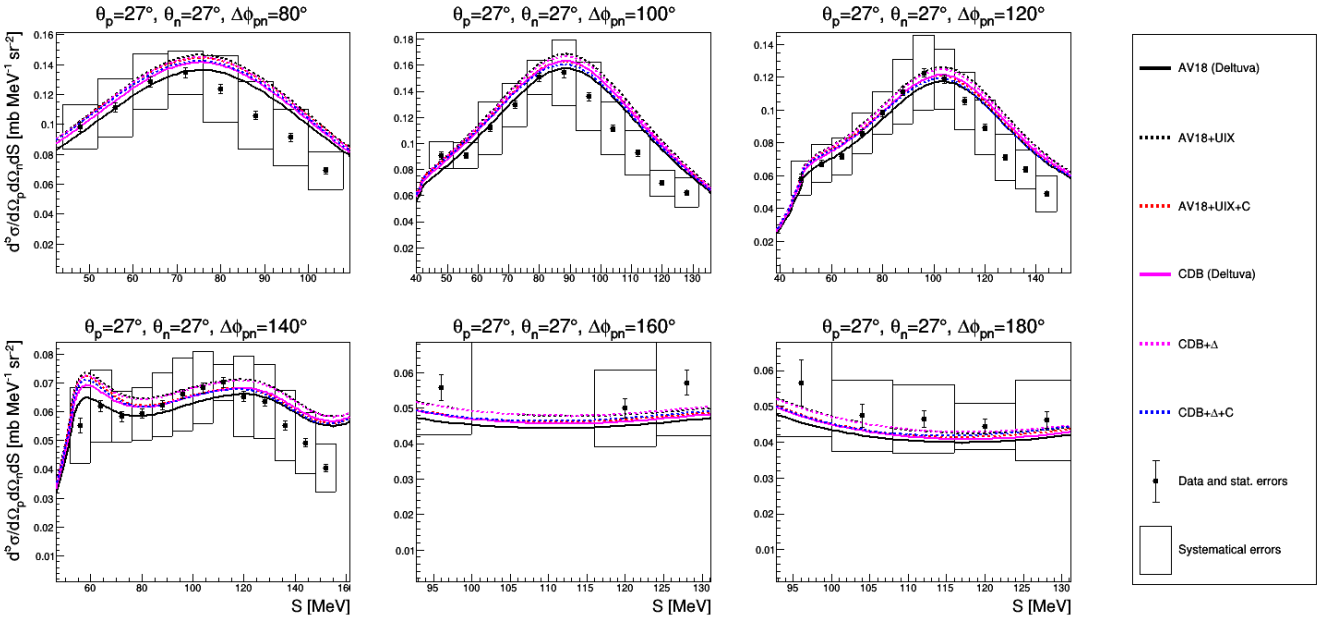

Figure D.25: Results at $\theta_p = 27°, \theta_n = 27°$ and for different $\Delta\phi_{pn}$ lines represent different theoretical models (specified in the legend).

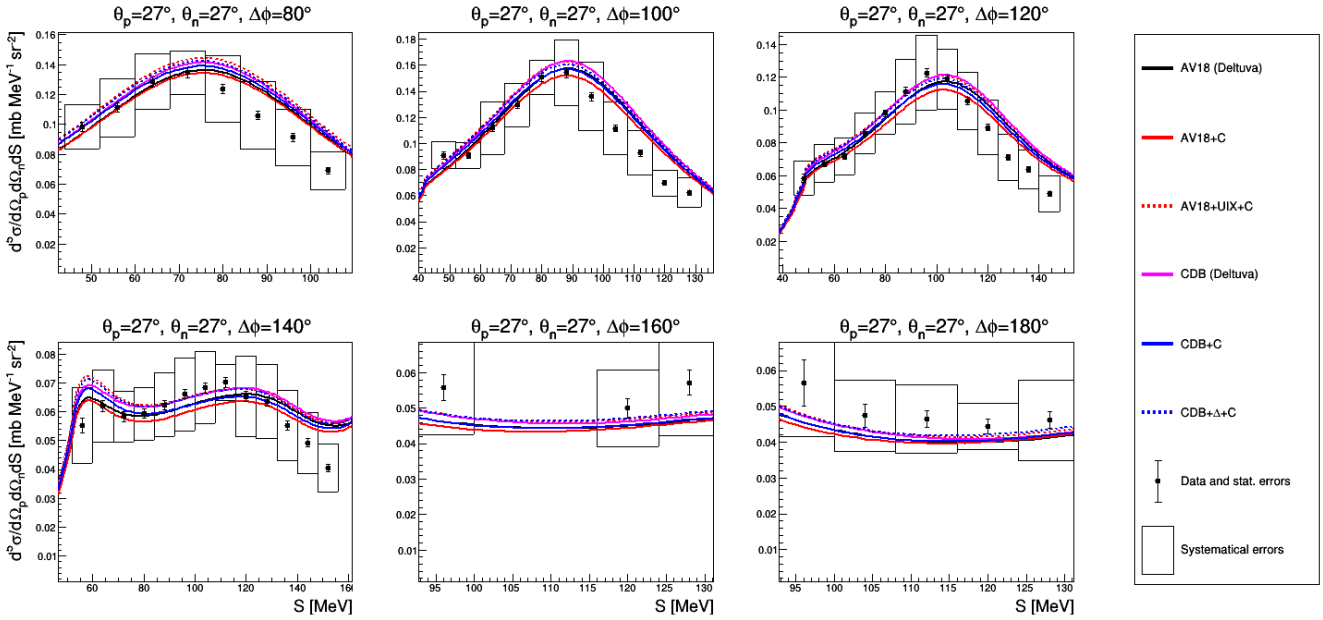

Figure D.26: The same as Fig. D.25 but for different set of theoretical models (specified in the legend).

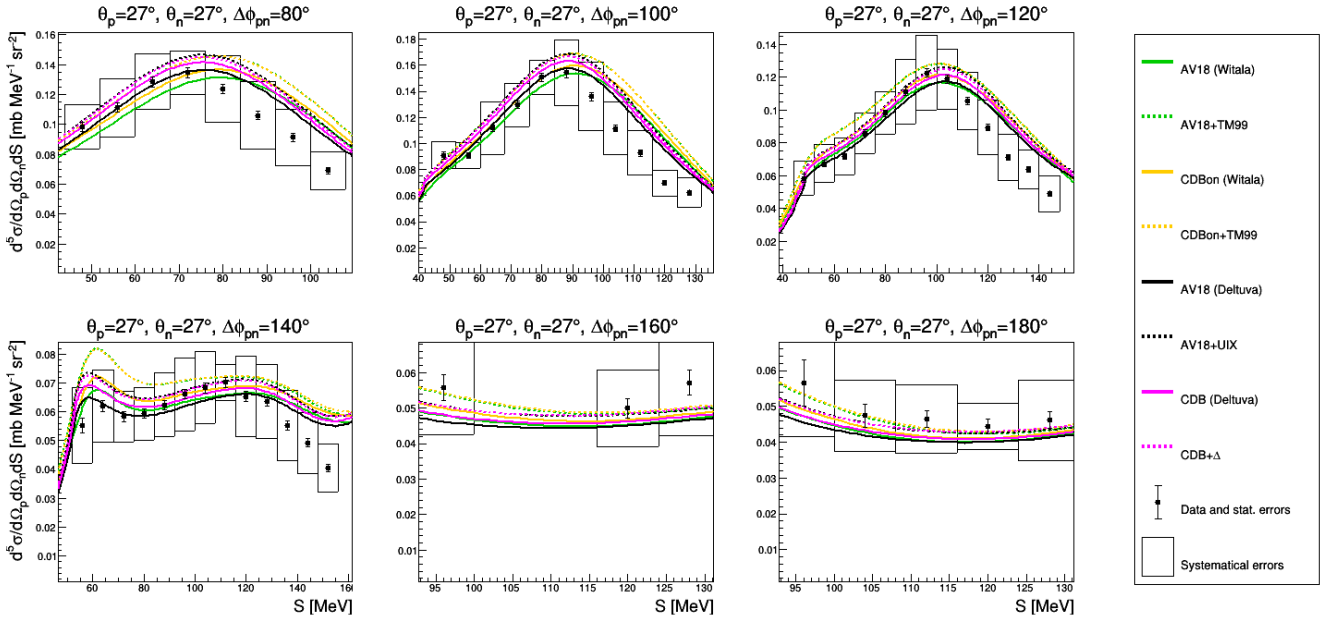

Figure D.27: The same as Fig. D.25 but for different set of theoretical models (specified in the legend).

Appendix E

Correlations between Lorentz invariant kinematical variables

The next pages contains the χ^2_{red} and A-factor results, presented in a form of two dimensional correlations between Lorentz invariants (defined in Sec. 5.5.2). Each of the theoretical model is shown in a separately, and their abbreviations are explained in Fig. 5.9.

(Please go to the next page)

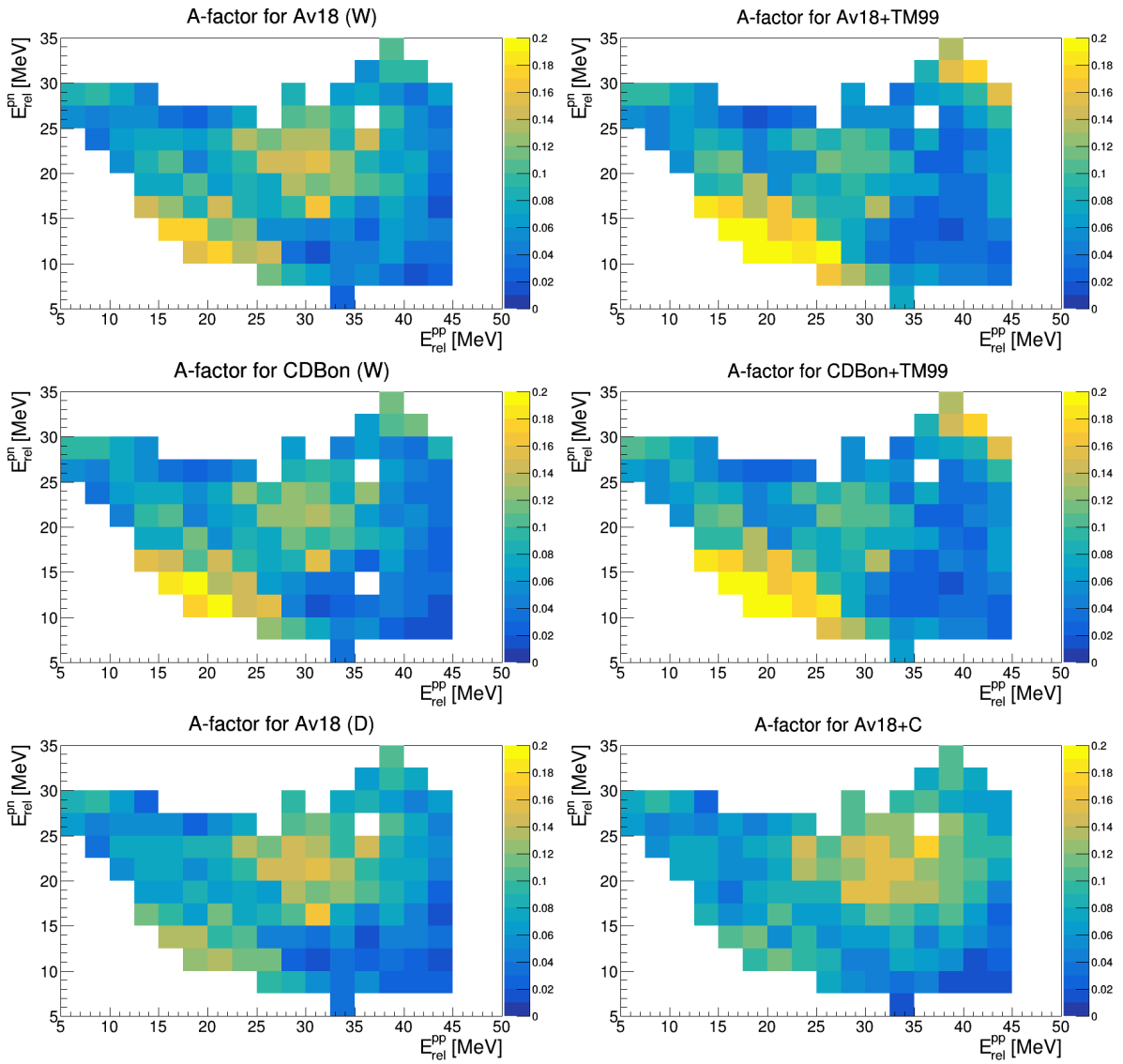

Figure E.1: The A-factor for the correlations of E^{pp}_{rel} vs. E^{pn}_{rel} for different theoretical models (specified in panels).

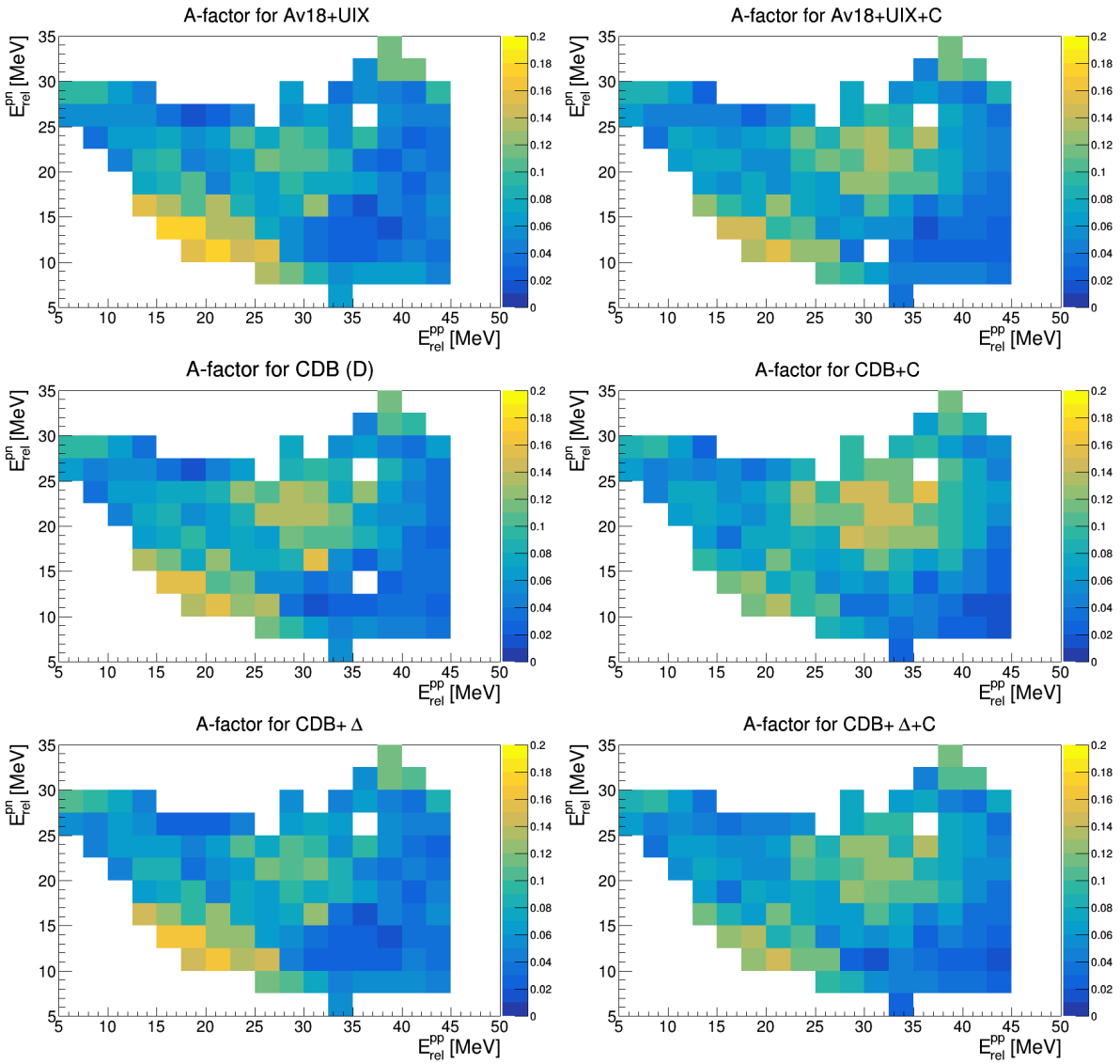

Figure E.2: The A-factor for the correlations of E^{pp}_{rel} vs. E^{pn}_{rel} for different theoretical models (specified in panels).

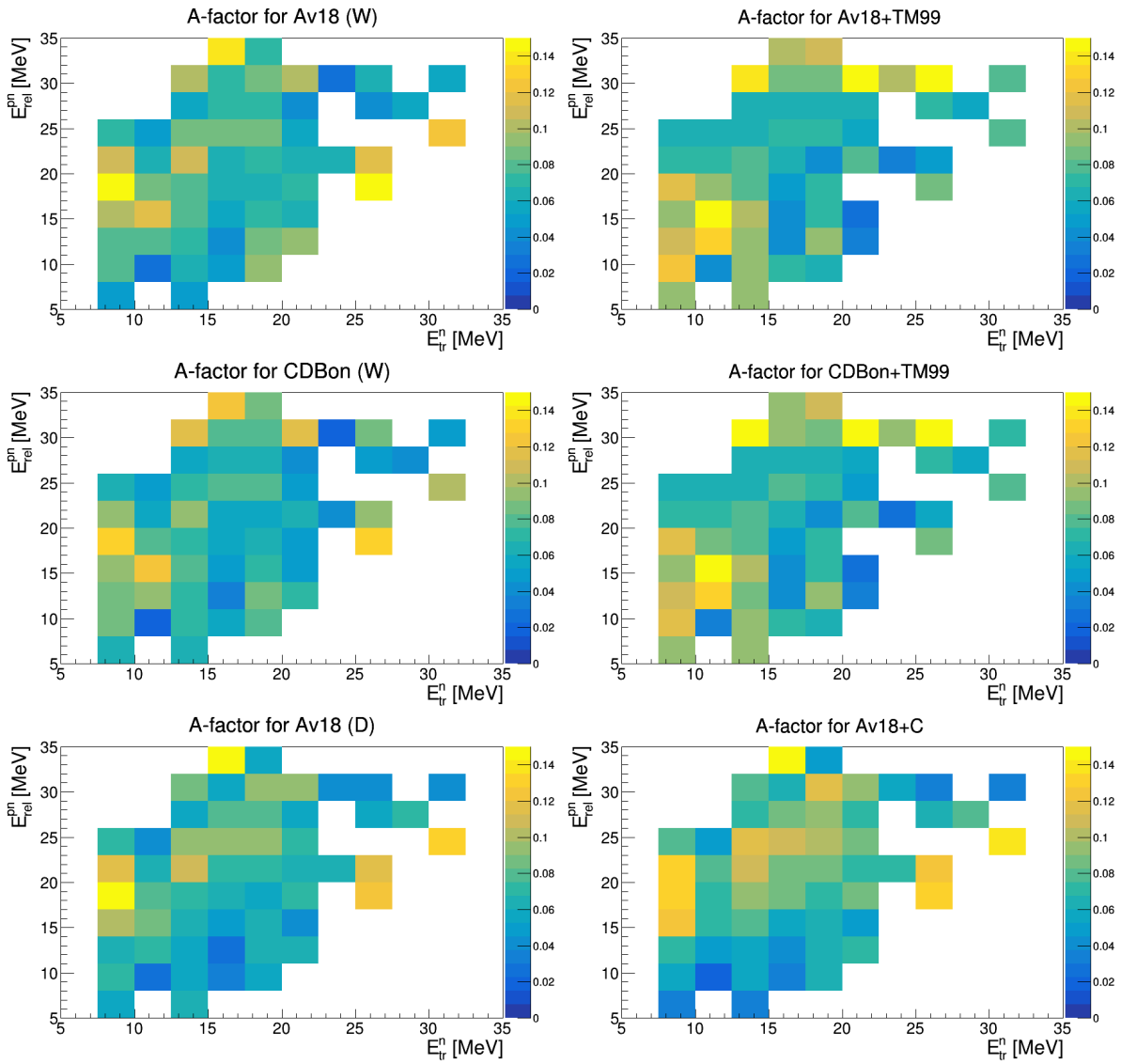

Figure E.3: The A-factor for the correlations of E^n_{tr} vs. E^{pn}_{rel} for different theoretical models (specified in panels).

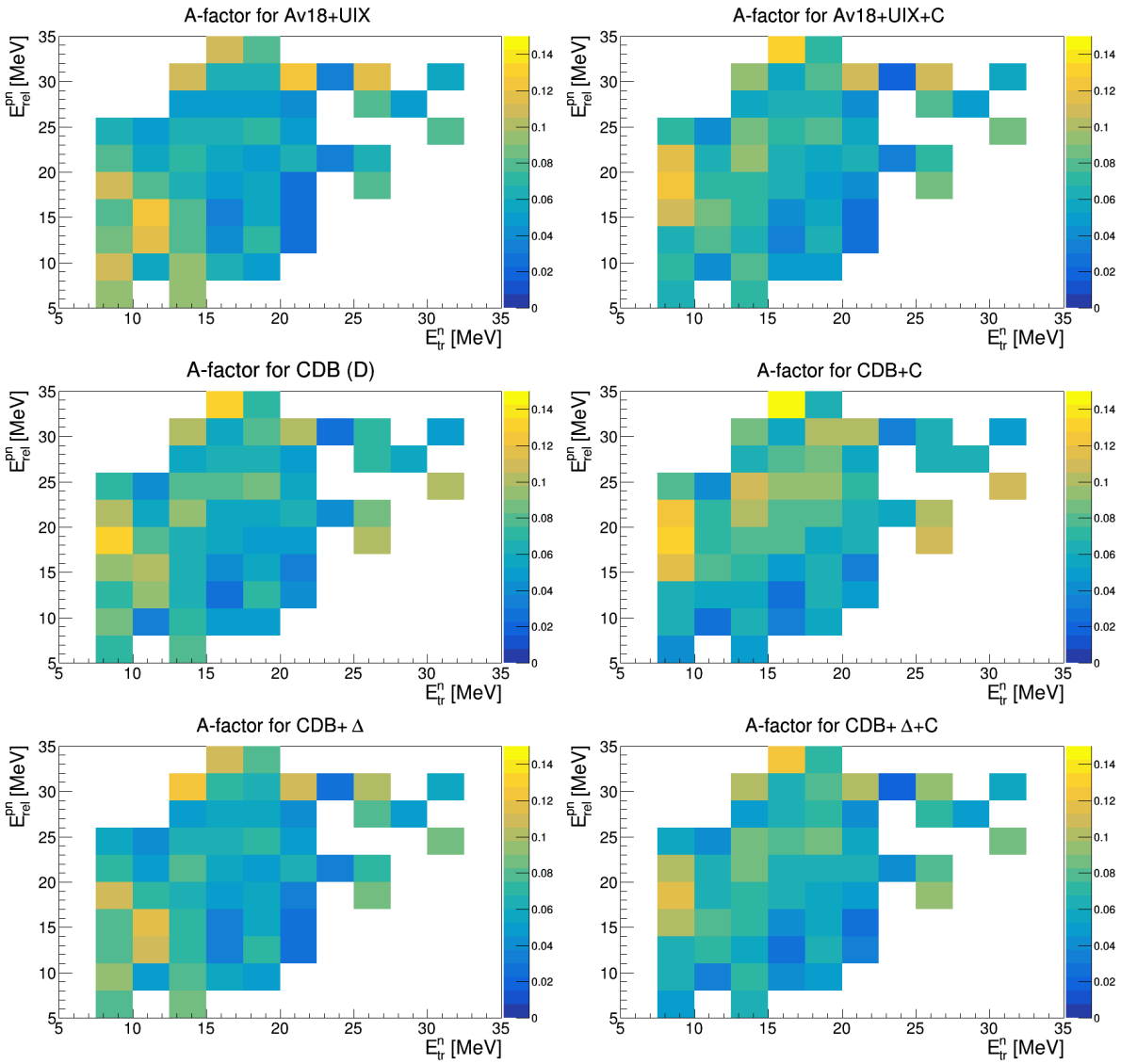

Figure E.4: The A-factor for the correlations of E^n_{tr} vs. E^{pn}_{rel} for different theoretical models (specified in panels).

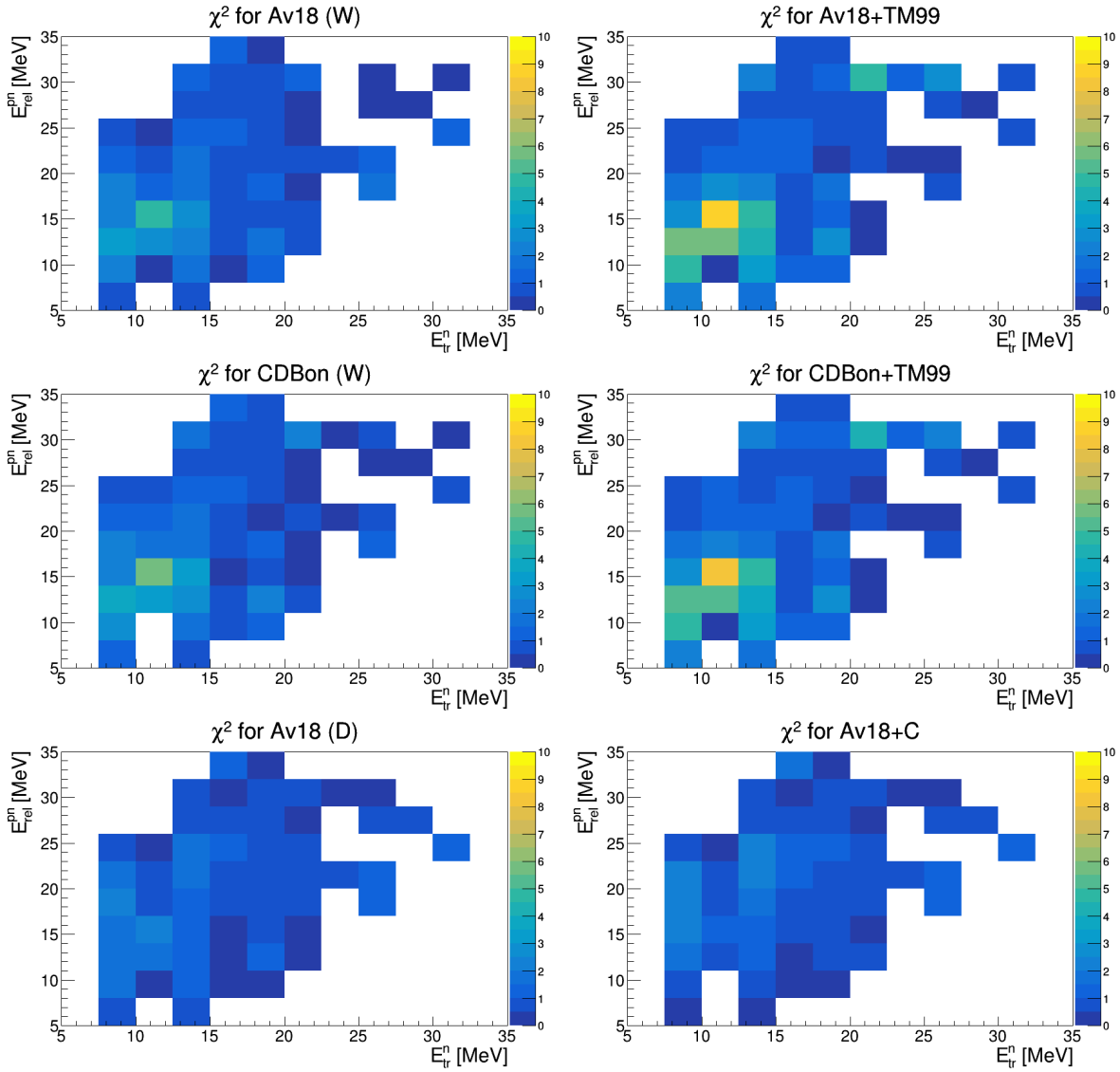

Figure E.5: The χ^2_{red} for the correlations of E^n_{tr} vs. E^{pn}_{rel} for different theoretical models (specified in panels).

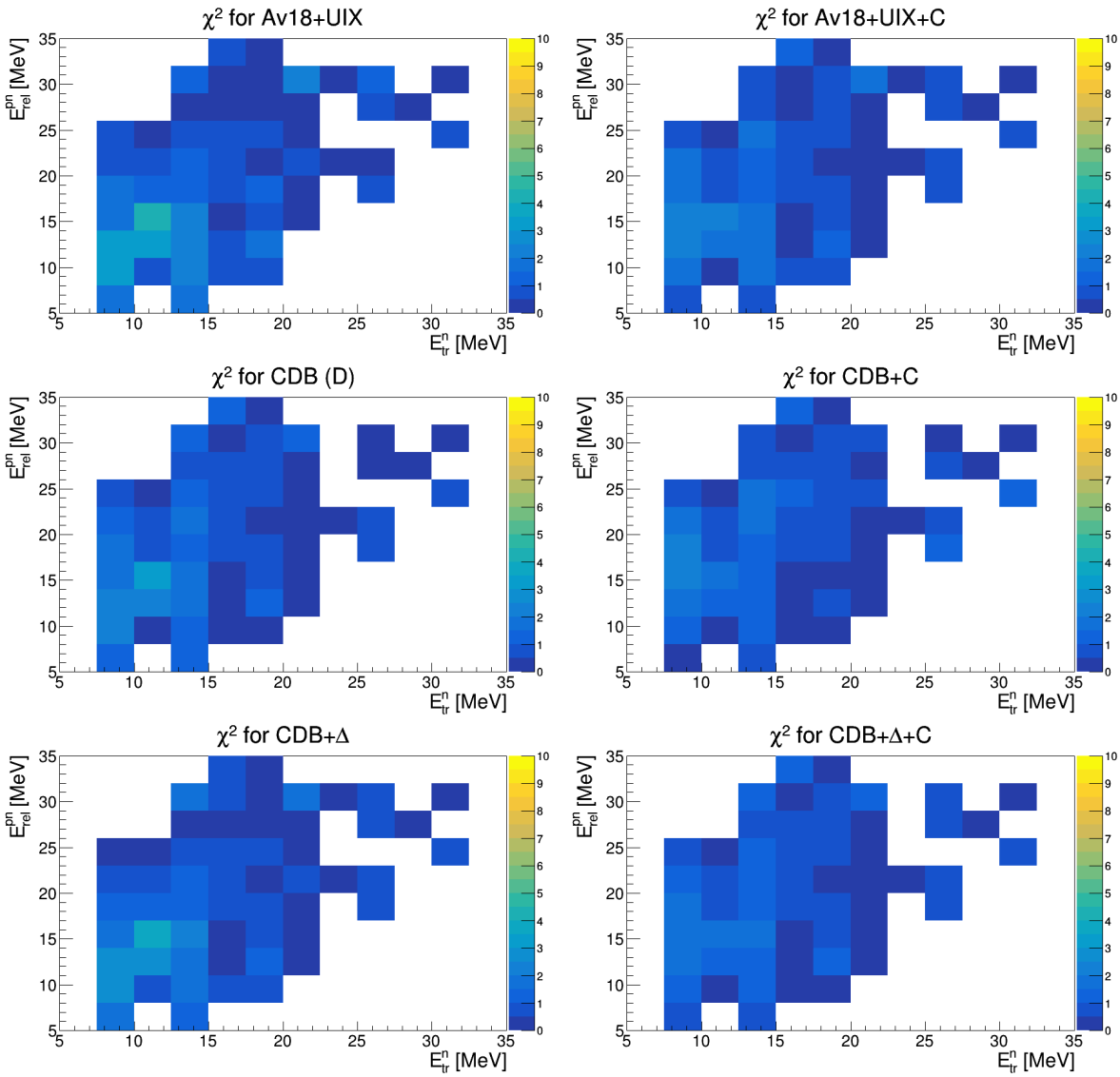

Figure E.6: The χ^2_{red} for the correlations of E^n_{tr} vs. E^{pn}_{rel} for different theoretical models (specified in panels).

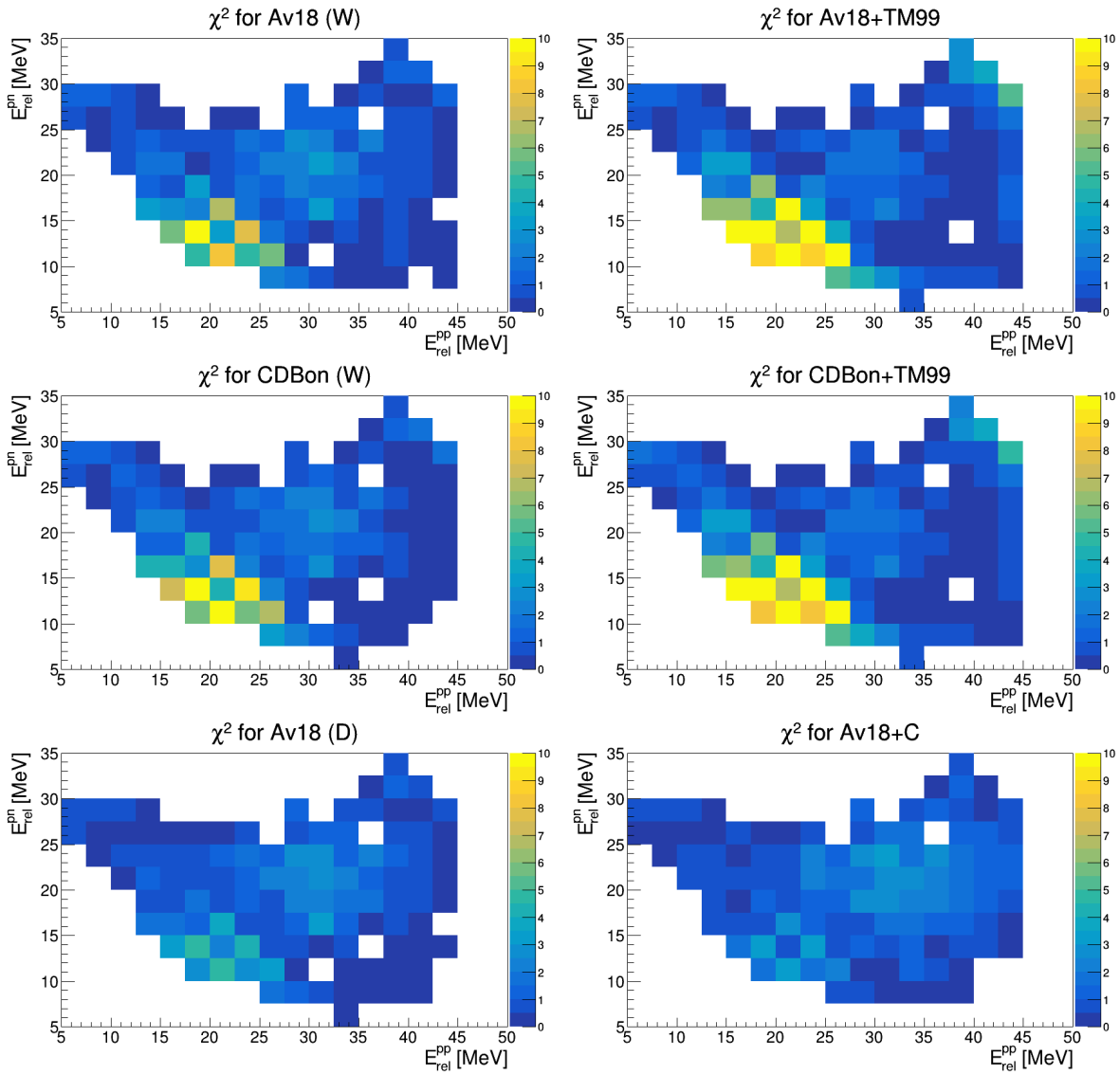

Figure E.7: The χ^2_{red} for the correlations of E^{pp}_{rel} vs. E^{pn}_{rel} for different theoretical models (specified in panels).

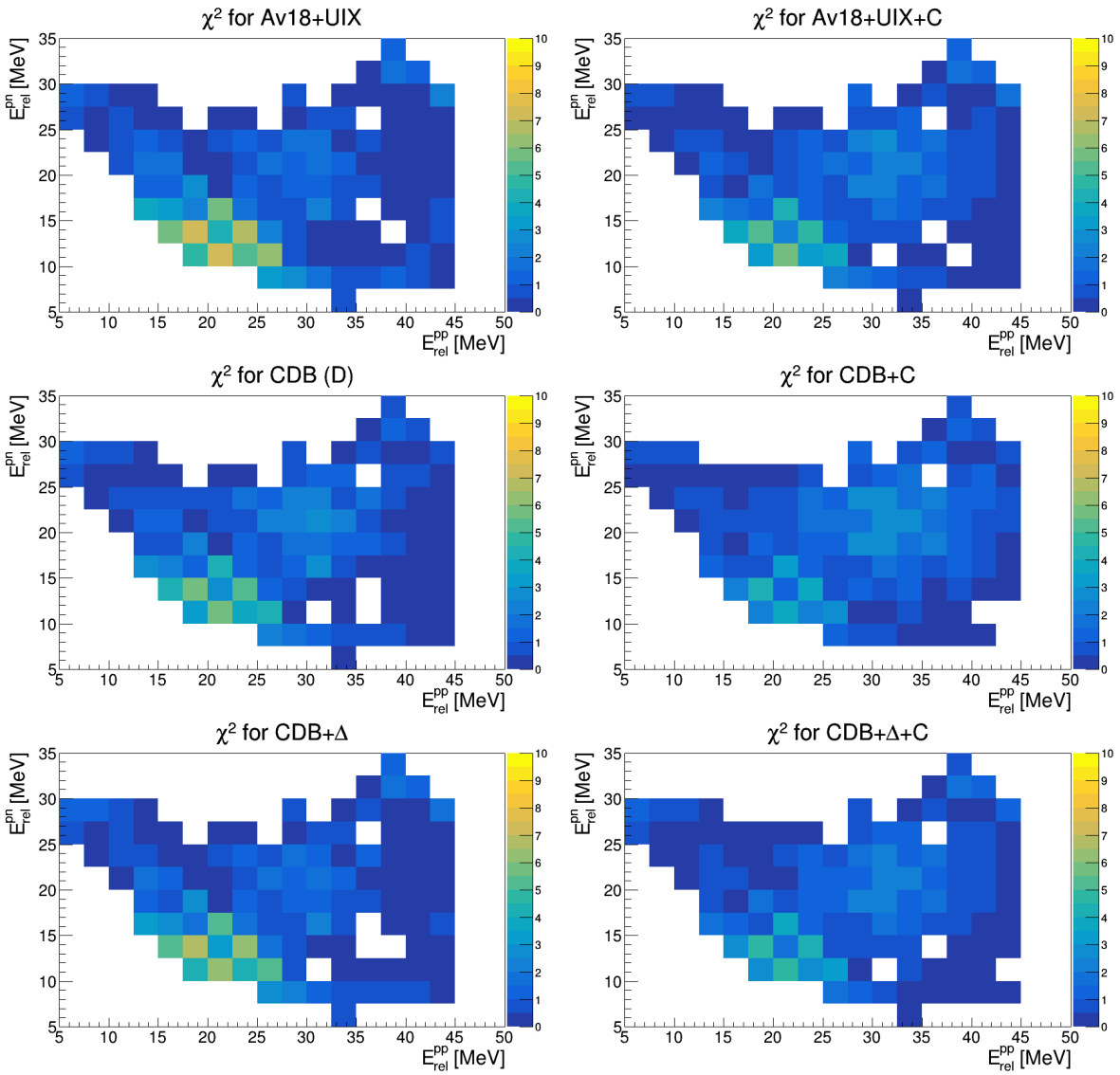

Figure E.8: The χ^2_{red} for the correlations of E^{pp}_{rel} vs. E^{pn}_{rel} for different theoretical models (specified in panels).

Acknowledgements

At this point I would like to sincerely thank everyone who contributed to this work.

First of all, I wish to express my gratitude to my promotor and co-promotor, **Dr. Adam Kozela** and **Dr. Izabela Ciepał**, for guiding and supporting me through all these years from the beginning of my M.Sc. studies to the end of my PhD studies. Your help in preparing and editing this manuscript was invaluable. Without your patience and encouragement I would not have achieved this goal.

I would like to thank all the collaborators with whom I participated in the BINA experiment:
Prof. Dr. Stanisław Kistryn,
Prof. Dr. Nasser Kalantar-Nayestanaki and the whole KVI group,
Dr. Elżbieta Stephan,
Dr. Jacek Zejma,
Dr. Barbara Kłos,
Dr. Paweł Kulessa,
Dr. Izabela Skwira-Chalot,
Dr. Wiktor Parol,
Dr. Andrzej Wilczek,
M.Sc. Angelina Łobejko,
M.Sc. Albert Szadziński,
for the years of working together, for the hundreds of discussions and for the countless emails I received.

I would also like to thank theory group from Jagiellonian University, Lisbon-Vilnius group and LENPIC Collaboration for providing me the theoretical calculations.

This thesis was supported by the Polish National Science Center under Grants No. 2016/21/D/ST2/01173 and 2019/35/N/ST2/03321.

Finally, I want to express my thankfulness to my family, friends and beloved fiancée for their support and motivation during my PhD.

Bibliography

[1] H. Yukawa. Proc. Phys. Math. Soc., Jpn 17, 48, (1935)

[2] C. M. G. Latter, H. Muirhead, G. P. S. Occhialin and C. F. Powell, Nature 159, (1947)

[3] P. U. Sauer, A. Deltuva, R. Machleidt Phys. Rev. C 68, 024005, (2003)

[4] P. U. Sauer, A. Deltuva, K. Chmielewski Phys. Rev. C 67, 034001, (2003)

[5] A. Deltuva, A. C. Fonseca, Phys. Rev. C 95, 024003, (2017)

[6] E. Epelbaum, H.W. Hammer, U.G. Meissner Rev. Mod. Phys. 81, 1773, (2009)

[7] R.B. Wiringa, V.G.J. Stoks, R. Schiavilla, Phys. Rev. C 51, 38, (1995)

[8] R. Machleidt, F. Sammarruca, and Y. Song, Phys. Rev. C 53, R1483, (1996)

[9] V.G.J. Stoks, R.A.M. Klomp, C.P.F. Terheggen, J.J. de Swart, Phys. Rev. C 49, 2950, (1994)

[10] H. Kamada et al., Phys. Rev. C 67, 034004, (2003)

[11] H. Miyazawa J. Fujita. Prog. Theor. Phys. 17, 360, (1957)

[12] S. Oryu P. U. Sauer S. Nemoto, K. Chmielewski, Phys. Rev. C 58, 2599, (1998)

[13] K. Ermisch et al. Phys. Rev. C 68, 051001(R), (2003)

[14] P. Mermod et al. Phys. Lett. B 597, 243, (2004)

[15] I. Ciepał, "Investigation of the Deuteron Breakup on Protons in the Forward Angular Region", PhD thesis, Jagiellonian University, (2010).

[16] St. Kistryn et al. Phys. Rev. C 72, 044006, (2005)

[17] A. Ramazani-Moghaddam-Arani, *Cross section and analyzing-power measurements in three and four-nucleon scattering*, PhD thesis, RUG, (2009)

[18] H. Mardanpour, *Investigation of nuclear forces in d + p elastic and p + d break-up reactions at intermediate energies*, PhD thesis, RUG, (2008)

[19] K. Hebeler, Physics Reports 890, (2021)

[20] J. Carlson, S. Gandolfi, F. Pederiva, Steven C. Pieper, R. Schiavilla, K. E. Schmidt, and R. B. Wiringa, Rev. Mod. Phys. 87, 1067, (2015)

[21] M. Ciemała, et. al., Physical Review C 101, (2020)

[22] P. Demorest, T. Pennucci, S. Ransom, et. al., Nature 467, (2010)

[23] H. T. Cromartie, E. Fonseca, S. M. Ransom, et. al., Nature Astronomy 4, (2020)

[24] M. H. P. M. van Putten, M. Della Valle, Monthly Notices of the Royal Astronomical Society: Letters, Vel. 482, (2019)

[25] F. Sammarruca, R. Millerson, Frontiers in Physics, vol. 10, (2019)

[26] P. Constanca, F. Margane, P. Helena, R. Aziz, Frontiers in Astronomy and Space Science, vol. 6, (2019)

[27] "Partition of forces using Jacobi coordinates". Advanced electromagnetism and vacuum physics. World Scientific. p. 102. ISBN 981-238-367-0

[28] L. D. Faddeev, Sov. Phys. JETP 12, 1014, (1961)

[29] B. S. Pudliner et al., Phys. Rev. C 56, 1720, (1997)

[30] S. A. Coon, H. K. Han, Few-Body Syst. 30, 131, (2001)

[31] S. Weinberg, Physica A 96, 327, (1979)

[32] E. Epelbaum, *The Nucleon-Nucleon Interaction in a Chiral Effective Field Theory*, Berichte des Forschungszentrums Jülich, Juel-3803, (2000)

[33] E. Epelbaum, A. Nogga, W. Glöckle, H. Kamada, U.-G. Meissner, H. Witała, Phys. Rev. C 66, 064001, (2002)

[34] http://www.lenpic.org/

[35] P. Reinert, H. Krebs, E. Epelbaum, Eur. Phys. A 54, 86, (2018)

[36] E. Epelbaum, J. Golak, K. Hebeler, H. Kamada, H. Krebs, U.-G. Meissner, A. Nogga, P. Reinert, R. Skibiński, K. Topolnicki, Yu. Volkotrub, H. Witała, Eur. Phys. J. A 56, 92, (2020)

[37] E. Epelbaum, YKIS2018b Symposium on Recend Developments in Quark-Hadron Sciences June 11 - June 15, YITP, Kyoto, (2018)

[38] P. U. Sauer, A. Deltuva, A. C. Fonseca, Phys. Rev. C 71, 054005, (2005)

[39] A. Deltuva, E. Epelbaum, H. Krebs, U.-G Meiner. Phys. Rev. C 80, 064002, (2009)

[40] H. Witała, R. Skibinski, J. Golak, W. Glöckle, EPJ A, 41, (2009)

[41] I. Ciepał et al., Few-Body Syst. 56, 665, (2015)

[42] K. Hatanaka et al., Phys. Rev. C66, 044002, (2002).

[43] Y. Maeda et al., Phys.Rev. C76, 014004, (2007)

[44] H. Witała, R. Skibiński and J. Golak, Eur. Phys. J. A30, 369, (2006)

[45] H. Witała et al. Phys. Rev., 83:044001, (2011)

[46] WASA Collaboration, Phys. Rev. C 101, 044001, (2020)

[47] W. Parol, I. Ciepał for the WASA-at-COSY Collaboration, Acta Phys. Pol. B 49, 469, (2018)

[48] H.Witala et al., Phys Rev Lett. 81 1183, (1998)

[49] W. Tornow et al., Phys. Rev. C 54, 42, (1996)

[50] N. Kalantar-Nayestanakiet al.,Nucl. Instrum. Methods A444, 591, (2000)

[51] E. Stephan et al., European Phys. Journal A, 49, (2013)

[52] M. Allet et al., Phys. Rev. C 50, 602, (1994)

[53] M. Allet et al., Few-Body Syst. 20, 27, (1996)

[54] J. Zejma et al., Phys. Rev. C 55, 42, (1997)

[55] E. Stephan et al., Phys. Rev. C 82, 014003, (2010)

[56] M. Eslami-Kalantari et al., Mod. Phys. Lett.A 24, 839, (2009)

[57] W. Parol et al., Phys. Rev. C 102, 054002, (2020)

[58] A. Łobejko, et al., Acta Phys. Pol. B, Vol. 50, (2019)

[59] B. Włoch, Preludium NCN:2019/35/N/ST2/03321, `https://projekty.ncn.gov.pl/index.php?projekt_id=464572`

[60] A. Ramazani-Moghaddam-Arani et al., Phys. Rev. C 83, (2011)

[61] R. Ramazani-Sharifabadi et al., Eur. Phys. J. A 56, (2020)

[62] M. Mohammadi-Dadkan et al., Eur. Phys. J. A 56 (2020)

[63] M.T. Bayat et al., Eur. Phys. J. A 56 (2020)

[64] H. Tavakoli-Zaniani et al., Eur. Phys. J. A 56 (2020)

[65] N. Kalantar-Nayestanaki et al., Rep. Prog. Phys. 75, 016301, (2012)

[66] E. Byckling, K. Kajantie, "Particle Kinematics", John Willey & Sons, (1973) ISBN 0471128856

[67] St. Kistryn, E. Stephan, J. Phys. G, Nucl. Part. Phys. 40, 063101, (2013)

[68] E.L Petersen et al., Phys. Rev. Vol. 188, (1969)

[69] R. Plasek, V. Valković, G.C. Phillips, Nuclear Physics A, Vol. 256, Issue 2, (1976)

[70] F. Takeutchi, Y. Sakamoto, Physics Letters, Vol. 41B, (1972)

[71] E.S. Konobeevski Nuclei Experiment DOI: 10.1134/S1063778813110100 (2013)

[72] D. E. Gonzalez Trotter Phys. Rev. C 73, 034001, (2006)

[73] K. Sagaraet al.,Few-Body Syst. 48, 59, (2010)

[74] K. Sagara,Few-Body Syst. 55, 1073, (2014)

[75] A. H. Couture, et al., Phys. Rev. C 85, 054004, (2012)

[76] K. Ohnakaet al.,Few-Body Syst.55, 725, (2014)

[77] R. Openshaw et al., Trans. Nucl. Sci. NS-36, 567, (1989)

[78] W. Parol *Badanie efektów siły trójciałowej w reakcji rozszczepienia deuteronu*, PhD thesis, Jagiellonian University, Kraków, (2015)

[79] G. Khatri, *Investigation of Deuteron Disintegration*, PhD thesis, Jagiellonian University, Kraków, (2015)

[80] Rene Brun and Fons Rademakers, *ROOT - An Object Oriented Data Analysis Framework*, Nucl. Inst. Meth. in Phys. Res. A 389, 81 (1997), See also "ROOT" [software], Release v6.18, https://zenodo.org/record/3895860

[81] M. Kerrisk et al., The Linux man-pages project (2004), http://man7.org/linux/man-pages/man3/atan2.3.html

[82] G. Khatri et al., Acta Phys. Pol. B 47, 411, (2016)

[83] I. Ciepał et al., Few-Body Syst. 60, 2, (2019)

[84] J. Allison et al., Nucl. Inst. Meth. in Phys. Res. A 835, 186, (2016)

[85] I. Fröhlich et al., PoS ACAT 076, (2007)

[86] The HADES Collaboration, Eur. Phys. J. A 41, (2009)

[87] P. Benz et al., Nucl. Phys. B 65, 158, (1973)

[88] http://gwdac.phys.gwu.edu/

[89] http://irfu.cea.fr/dphn/Spallation/incl.html

[90] D. H. Wright, M. H. Kelsey, Nucl. Inst. Meth. in Phys. Res. A, 804, (2015)

[91] "Guide for Physics Lists" https://geant4-userdoc.web.cern.ch/UsersGuides/PhysicsListGuide/html/ind

[92] B. Włoch, Acta Phys. Pol. B 49, 411, (2018)

[93] A.R. Garcia et. al., Nucl. Inst. Meth. in Phys. Res. A 868, 73, (2017)

[94] "QBBC" https://geant4-userdoc.web.cern.ch/UsersGuides/PhysicsListGuide/html/reference_PL/QBI

[95] "QGSP" https://geant4-userdoc.web.cern.ch/UsersGuides/PhysicsListGuide/html/reference_PL/QGS

[96] P. C. Rout, et al., Nucl. Instr. and Meth. in Phys. Re. A, (2018)

[97] C. E. Wiegand, et al., Review of Scientific Instruments 33, 526, (1962)

[98] J. Kuboś, *Wyznaczenie wydajności detektora BINA na rejestracje neutronów w reakcji breakupu dp przy energii 160 MeV,* bechelor thesis, IFJ PAN Kraków, (2015)

[99] W. Parol, B. Włoch et al., Acta Phys. Pol. Proc. Supp., B 10, (2017)

[100] I. Ciepał et al., Phys. Rev. C 100, 024003, (2019)

[101] B. Włoch, Recent Progress in Few-Body Physics, (2020)

[102] M. Morhac et al., Nucl. Inst. Meth. in Phys. Res. A 401, 113, (1997)

[103] https://root.cern.ch/doc/master/classTSpectrum.html

[104] I. Ciepał et al., Phys. Rev. C 99, 014620, (2019)

[105] S. K. Sharma, B. Kamys, F. Goldenbaum, and D. Filges, Eur. Phys. J. A 53, 150, (2017)

[106] D. Soliman, *Hunting the ppK-: A kinematic refit for the exclusive analysis of the reaction pp→pK+Λ*, PhD thesis, TUM Munich, (2012)

[107] A. Łobejko, Preludium NCN:2020/37/N/ST2/02360, `https://projekty.ncn.gov.pl/index.php?projekt_id=485083`